

Measurement of the Charge Asymmetry of W Bosons Produced in pp Collisions at $\sqrt{s} = 7$ TeV with the ATLAS Detector

A dissertation presented

by

Verena Ingrid Martinez Outschoorn

to

The Department of Physics

in partial fulfillment of the requirements

for the degree of

Doctor of Philosophy

in the subject of

Physics

Harvard University

Cambridge, Massachusetts

May 2011

©2011 - Verena Ingrid Martinez Outschoorn

All rights reserved.

Thesis advisor

Author

Professor João Pedro Barreiro
Guimarães da Costa

Verena Ingrid Martinez Outschoorn

Measurement of the Charge Asymmetry of W Bosons Produced in pp Collisions at $\sqrt{s} = 7$ TeV with the ATLAS Detector

Abstract

This dissertation presents a measurement of the muon charge asymmetry from W bosons produced in proton-proton collisions at a center-of-mass energy of 7 TeV. The asymmetry provides information about the momentum fraction of the proton carried by the partons participating in W production, particularly the u and d quarks. It therefore helps understand predictions for the parton distribution functions (PDF) in the colliding protons in a new kinematic regime.

W candidate events are selected in the $W \rightarrow \mu\nu$ decay mode and the asymmetry is measured as a function of the decay muon pseudorapidity. The data were recorded by the ATLAS detector in 2010 and correspond to 31 pb^{-1} of integrated luminosity. The measurement is compared to theoretical predictions based on next-to-leading order QCD calculations and a range of PDF sets. The input of the measurement for the determination of the next generation of PDF sets is expected to bring the different predictions closer together and aid in reducing the uncertainties. This contributes to improving LHC predictions that rely on precise knowledge of the proton PDFs.

Contents

Title Page	i
Abstract	iii
Table of Contents	iv
List of Figures	viii
List of Tables	xii
Acknowledgments	xiv
Dedication	xv
1 Introduction	1
2 Theoretical Overview	5
2.1 W Boson Production in pp Collisions	7
2.1.1 The Proton Structure	7
2.1.2 The Production Cross Section in Hadronic Collisions	8
2.1.3 The W Boson Production Cross Section	10
2.1.4 The Parton Distribution Functions	12
2.1.5 W Decay and the Muon Channel	16
2.1.6 Overview of Past W Cross Section Measurements	17
2.1.7 Predictions of the Inclusive W Production Cross Section in pp Collisions at $\sqrt{s} = 7$ TeV	17
2.2 W Charge Asymmetry and PDF Constraints	20
2.2.1 W Rapidity and Asymmetry	20
2.2.2 The Lepton Charge Asymmetry	21
2.2.3 Past W Asymmetry Measurements. An Overview of Tevatron Measurements	25
2.2.4 Kinematic Constraints from the Charge Asymmetry at the LHC	28
3 The LHC and the ATLAS Detector	30
3.1 The Large Hadron Collider	31
3.2 The ATLAS Detector	37
3.2.1 Coordinate System	42

3.3	Inner Detector	42
3.3.1	Pixel Detector	44
3.3.2	Semiconductor Tracker	45
3.3.3	Transition Radiation Tracker	45
3.4	Calorimeters	46
3.4.1	Electromagnetic Calorimeter	48
3.4.2	Hadronic Calorimeter	50
	Tile calorimeter	50
	LAr hadronic end-cap calorimeter	51
	LAr forward calorimeter	51
3.5	Muon Spectrometer	52
3.5.1	Chamber Layout	53
3.5.2	Monitored Drift Tubes	55
3.5.3	Cathode Strip Chambers	58
3.5.4	Resistive Plate Chambers	59
3.5.5	Thin Gap Chambers	59
3.5.6	Overview of MDT Readout Electronics	60
3.6	Trigger and Data Acquisition	61
3.6.1	Trigger System Overview	63
3.6.2	Muon Trigger	65
3.6.3	Data Acquisition	67
4	Muon Reconstruction and Performance Studies with Cosmic Rays	68
4.1	Muon Reconstruction Overview	70
4.2	Muon Charge Ratio in Cosmic Rays	71
4.2.1	Analysis Techniques and Measurement Outline	73
4.3	Dataset and Reconstruction Configuration	74
4.4	Event Selection Criteria	77
4.5	Acceptance Correction	80
4.5.1	Mirror Track Validation	82
4.6	Muon Trigger Efficiency	84
4.7	Detector Efficiencies	88
4.8	Muon Reconstruction Efficiency	89
4.9	Selected Muon Sample	93
4.10	Surface-Cavern Energy Correction	94
4.11	Uncertainty Estimation	99
4.11.1	Momentum Scale and Resolution, Charge Misidentification and Bin Migration	101
4.11.2	Surface-Cavern Correction	106
4.11.3	Tracking Efficiency	106
4.11.4	Selection Criteria	107
4.12	Results	107

4.13	Conclusions	109
5	$W \rightarrow \mu\nu$ Event Selection and First Asymmetry Measurement	110
5.1	Event and Object Reconstruction	112
5.1.1	Inner Detector Tracking	112
5.1.2	Primary Vertex Reconstruction	113
5.1.3	Combined Muon Reconstruction	114
5.1.4	Alignment Status of the ID and MS Trackers	115
5.1.5	Missing Transverse Energy Reconstruction	117
5.2	Data and Simulated Monte-Carlo Samples	119
5.3	Event Selection	120
5.4	Background Estimation	125
5.4.1	Electroweak and $t\bar{t}$ Backgrounds	126
5.4.2	QCD Background	127
5.4.3	Cosmic Ray Background	129
5.5	Muon Reconstruction Efficiency	129
5.6	Trigger Efficiency	132
5.7	Muon Momentum Scale and Resolution	133
5.8	The W Cross Section Measurement	134
5.8.1	Cross Section Results	138
5.9	The W Charge Asymmetry Measurement	139
6	Differential W Charge Asymmetry Measurement	146
6.1	Data and Simulated Monte-Carlo Samples	147
6.2	Event Selection	149
6.3	Trigger and Reconstruction Efficiencies	150
6.3.1	Trigger Efficiency	152
6.3.2	Reconstruction Efficiency	155
6.3.3	Muon Isolation Efficiency	158
6.4	Pileup Simulation	159
6.5	Muon Momentum Scale and Resolution	160
6.5.1	Muon Momentum Resolution	161
6.5.2	Muon Momentum Scale	163
6.5.3	Charge Misidentification	171
6.6	Background Estimation	172
6.6.1	EW and $t\bar{t}$ Backgrounds	173
6.6.2	QCD Background	175
6.7	Uncertainty Estimation	180
6.7.1	Impact of the Trigger and Reconstruction Efficiencies	182
6.7.2	Impact of the Muon Momentum Scale and Resolution	183
6.7.3	Impact of Backgrounds	187
6.7.4	Impact of Theoretical Modeling	188

6.8 Results	189
7 Conclusions	195
Bibliography	204

List of Figures

2.1	Measurements of α_s as a function of the energy scale Q .	6
2.2	Diagram for Particle Production in Hadronic Collisions.	9
2.3	Feynman diagram for W production.	11
2.4	Flavor decomposition of W boson production.	12
2.5	Kinematic constraints provided by different datasets on NNPDF PDF sets.	14
2.6	PDFs of the proton for MSTW 2008 at NLO.	16
2.7	Feynman diagrams for W production and decay in the muon channel.	17
2.8	W Cross Section as a Function of Energy and Comparison to Past Measurements.	18
2.9	W^+ and W^- cross section for available PDF sets at NLO and NNLO.	19
2.10	W Production and Decay Diagram.	22
2.11	Rapidity and asymmetry distributions for the W Boson and pseudo-rapidity and asymmetry distributions for the decay lepton.	23
2.12	W and decay lepton asymmetries with various p_T requirements	24
2.13	W and the decay lepton rapidity and asymmetry distributions in $p\bar{p}$ collisions.	26
2.14	DØ W lepton asymmetry measurement results.	26
2.15	CDF direct W asymmetry measurement results.	27
2.16	Comparison of Valence, Sea and Gluon PDFs and Asymmetries for CTEQ and MSTW.	28
3.1	Diagram of an LHC dipole magnet.	32
3.2	CERN Accelerator Complex.	33
3.3	ATLAS pp luminosity for 2010.	35
3.4	Overview of the ATLAS detector.	39
3.5	Layout of the ATLAS Inner Tracker.	43
3.6	Overview of the ATLAS Calorimeter System.	46
3.7	Material in ATLAS.	48
3.8	Field Integral for Toroidal Magnet System.	52

3.9	Overview of the ATLAS muon spectrometer.	54
3.10	Overview of the Monitored Drift Tube Chamber and Tube.	56
3.11	Example TDC and $r - t$ relation.	58
3.12	The MDT readout electronics scheme.	60
3.13	Overview of the Trigger and Data Acquisition Systems.	62
3.14	Overview of the Muon Level 1 Trigger.	66
4.1	MDT hit multiplicity for cosmic ray muon tracks per barrel station.	78
4.2	RPC hit multiplicity for cosmic ray muon tracks.	78
4.3	Track χ^2 and segment multiplicity per sector for cosmic ray muons.	79
4.4	Diagram of the cosmic ray muon trajectory in ATLAS.	81
4.5	Event display of real and mirror track illustrating the acceptance correction technique used in the cosmic charge ratio measurement.	82
4.6	Validation of the ATLAS extrapolator for MDT hits.	83
4.7	Validation of the ATLAS extrapolator for RPC hits.	83
4.8	Comparison of muon tracks and their mirror track at the tube level.	85
4.9	Comparison of muon tracks and their mirror track at the chamber level.	86
4.10	RPC low- p_T trigger coverage for the run used in the cosmic charge ratio analysis.	87
4.11	MDT single tube efficiency.	89
4.12	RPC single panel efficiency.	90
4.13	MDT hit multiplicity for extrapolated tracks and the corresponding number of matched hits.	91
4.14	MDT hit multiplicity for raw hits along the path of extrapolated tracks and the number of matched hits on track.	92
4.15	Tracking efficiency based on the matching of raw MDT hit combinations to reconstructed standalone MS tracks.	93
4.16	Distribution of cosmic ray muon track z before and after applying the cosmic charge ratio selection criteria.	95
4.17	Charge ratio in cosmic ray muons in the ATLAS cavern.	96
4.18	Diagram of the ATLAS cavern and shafts.	97
4.19	Profile of the rock layers above the ATLAS cavern.	98
4.20	Surface-to-cavern momentum correction for cosmic ray muons.	99
4.21	Surface-to-cavern momentum correction for cosmic ray muons as a function of various track parameters.	100
4.22	Momentum distribution of muons from cosmic rays used in the charge ratio measurement before and after applying the surface-to-cavern momentum correction.	100
4.23	Muon track multiplicity in cosmic ray events.	102
4.24	Curvature measurement comparison in the top and bottom of the MS for positively charged tracks.	103

4.25	Curvature measurement comparison in the top and bottom of the MS for negatively charged tracks.	104
4.26	Curvature scale and resolution as a function of momentum for cosmic ray muons.	105
4.27	Systematic uncertainties on the muon charge ratio associated with the surface-to-cavern momentum correction.	106
4.28	Systematic uncertainty on the muon charge ratio associated with the track reconstruction efficiency correction.	107
4.29	Robustness tests of the selection criteria used for the muon charge ratio measurement.	108
4.30	Charge ratio in cosmic ray muons using MS standalone tracks in ATLAS and past measurements performed by other experiments.	109
5.1	W Boson Candidate Event Display.	111
5.2	Primary vertex distributions from first pp collision data.	114
5.3	Muon p_T distribution.	123
5.4	Muon isolation and E_T^{miss} for events with a high- p_T muon.	124
5.5	Transverse mass distribution before and after the E_T^{miss} requirement.	125
5.6	Distributions for cross checks of QCD background estimation.	129
5.7	Muon reconstruction efficiency measurement using 310 nb^{-1} of data.	131
5.8	Muon trigger efficiency measurement using 310 nb^{-1} of data.	133
5.9	Muon momentum scale and resolution from Z peak using 310 nb^{-1} of data.	135
5.10	W production cross section results using 310 nb^{-1} of data.	140
5.11	W production cross section as a function of the center-of-mass energy, comparing the ATLAS result to past measurements.	141
5.12	W candidate distributions by charge using 310 nb^{-1} of data.	143
5.13	W asymmetry results using 310 nb^{-1} of data.	145
6.1	Muon selection criteria to reject π/K decays in flight.	151
6.2	Trigger efficiency turn-on curves for 31 pb^{-1} of data.	154
6.3	Trigger efficiency as a function of muon η in data for positive and negative charges.	155
6.4	Data over MC trigger efficiency scale factors for 31 pb^{-1} of data.	156
6.5	Muon reconstruction and identification efficiency using 31 pb^{-1} of data.	158
6.6	Muon isolation efficiency in data for positive and negative muons using 31 pb^{-1} of data.	159
6.7	Number of primary vertices in data and W MC for 31 pb^{-1} of data.	160
6.8	Comparison of the W transverse mass distribution before and after applying muon momentum smearing corrections.	164
6.9	Examples of fits to the muon curvature distribution.	167

6.10	Muon momentum scale parameter fit results for the combined track and its ID and MS components.	169
6.11	Ratio of muon momentum scale first results for positive and negative muon η	170
6.12	Muon momentum scale fit results as a function of the muon ϕ	171
6.13	Muon charge asymmetry using the momentum measurement from the CB track and its ID and MS components.	172
6.14	Muon charge asymmetry using the momentum measurement from the ID and MS components of the CB track after applying momentum scale and resolution corrections.	173
6.15	Muon momentum scale fit results in the charge asymmetry $ \eta $ bins.	174
6.16	Muon p_T distribution for positive and negative W candidates using 31 pb ⁻¹ of data.	174
6.17	QCD prediction for positive and negative muons in measurement $ \eta $ bins.	179
6.18	Absolute uncertainties on the differential W lepton charge asymmetry measurement using 31 pb ⁻¹ of data.	182
6.19	Toy Monte Carlo studies for the muon momentum scale parameter fitting method.	185
6.20	Comparison of muon p_T distributions at truth level.	189
6.21	Muon η distribution for positive and negative W candidates using 31 pb ⁻¹ of data.	190
6.22	W fiducial cross section results and W lepton charge asymmetry measurement stages using 31 pb ⁻¹ of data.	192
6.23	Differential W charge asymmetry result using 31 pb ⁻¹ of data.	194
7.1	Comparison of valence quark, sea quark and gluon predictions from HERA PDF 1.5 after the inclusion of the ATLAS asymmetry data.	197
7.2	Comparison of valence quark, sea quark and gluon predictions from HERA PDF 1.5 after the inclusion of the ATLAS asymmetry data and additional Tevatron measurements.	198
7.3	Valence quark, sea quark and gluon predictions and uncertainties from HERA PDF 1.5 with Tevatron data before and after the inclusion of the ATLAS asymmetry measurement.	199
7.4	Comparison of ATLAS asymmetry data with NNPDF2.1 predictions.	200
7.5	Comparison of NNPDF2.1 prediction uncertainties before and after including the ATLAS asymmetry measurement.	202
7.6	Absolute uncertainties on the differential W lepton charge asymmetry result scaled to 1 fb ⁻¹ of data.	203

List of Tables

2.1	Main processes included in the MSTW 2008 PDF sets.	15
2.2	W Cross Section Predictions at NNLO.	20
3.1	LHC parameters for the nominal design and the pp runs in 2010.	37
3.2	ATLAS Performance Design Specifications.	41
3.3	ATLAS sub-detector uptimes for 2010 pp collision running.	41
3.4	Main lowest threshold L1 triggers in the commissioning menus and their allocated bandwidth.	64
4.1	Selection requirement efficiencies for the cosmic charge ratio analysis.	80
4.2	Summary of systematic uncertainties for the muon charge ratio measurement.	101
4.3	Curvature scale and resolution parameters for cosmic ray muons.	105
5.1	Expected muon resolution for different regions of the MS.	117
5.2	Signal and background MC samples used in the W measurements.	121
5.3	Event selection used for W candidates.	122
5.4	Summary of observed W candidates, expected background and signal yield for 310 nb^{-1} of data.	126
5.5	Efficiency correction and acceptance factors used in W production cross section and charge asymmetry measurements.	137
5.6	Systematic uncertainties on the efficiency and acceptance correction factors used in the W production cross section and charge asymmetry measurements.	137
5.7	W fiducial cross section results using 310 nb^{-1} of data.	138
5.8	W total production cross section results using 310 nb^{-1} of data.	139
5.9	W total production cross section results for the combination of the electron and muon channels.	139
5.10	W charge asymmetry measurement using 310 nb^{-1} of data.	144

6.1	Lepton pseudorapidity bin ranges used in the differential asymmetry measurement.	147
6.2	Triggers and corresponding integrated luminosities for the dataset periods used in the differential charge asymmetry analysis.	148
6.3	Event selection for W candidates used in the differential charge asymmetry measurement.	149
6.4	Selection criteria used for the trigger efficiency measurement based on Z candidate events.	153
6.5	Selection criteria used for the muon reconstruction efficiency measurement based on Z candidate events.	157
6.6	Pileup event weights used to correct the number of vertices in simulation to that in data.	160
6.7	Muon momentum smearing parameters used to improve the agreement of the resolution in data and MC.	162
6.8	Summary of expected background events per $ \eta $ bin and charge for 31 pb^{-1} of data.	175
6.9	Expected background events from EW and top processes per $ \eta $ bin and charge for 31 pb^{-1} of data.	176
6.10	Absolute systematic uncertainties on the differential W lepton charge asymmetry measurement.	181
6.11	Summary of observed W candidate events, expected background and acceptance and efficiency correction factors used in the differential W charge asymmetry measurement.	191
6.12	Differential $W \rightarrow \mu\nu$ charge asymmetry measurement using 31 pb^{-1} compared to various theoretical predictions.	193

Acknowledgments

Many people have made my graduate studies and this dissertation possible. I am particularly grateful to João Guimarães da Costa, my advisor, for providing continuous support and for being so generous with his time and advice. The other members of the Harvard ATLAS group during my graduate years, particularly Melissa Franklin, John Huth, Masahiro Morii and George Brandenburg, have always been extremely encouraging and have constantly been available to answer my questions. I would also like to thank Kevin Black and Alberto Belloni, for working closely with me and for being so patient in doing so, as well as Corrinne Mills and the other postdocs in the group for being so helpful and understanding. My profound gratitude goes to Srivas Prasad, my fellow student throughout graduate school, who is one of the most wonderful people I have met. It has been a pleasure to work with Ben Smith, Michael Kagan and all the other graduate students. I am also very thankful to the undergraduates who have been involved in the Harvard ATLAS group, particularly Tomo Lazovich, Maximilian Swiatlowski and Jack Kearney. I am extremely grateful to many people at Harvard, particularly in the Physics department, who have made these years such a memorable experience. A special mention to Howard Georgi for providing advice through my studies and being on my thesis committee. Many thanks also to Frank Taylor, Giora Mikenberg and Maarten Boonekamp for being so supportive of my future plans. I would additionally like to express my gratitude to ATLAS and CERN who have enabled this work to go forward.

Most important of all I would like to thank my family and friends for always making me happy. I am extremely fortunate to have you.

Dedicated to all my family.

Chapter 1

Introduction

W bosons are produced abundantly at the Large Hadron Collider (LHC), allowing for detailed measurements of their production properties in a new kinematic regime. This thesis describes the first measurements of the W production charge asymmetry performed in ATLAS, corresponding to the first precision physics measurements using pp collisions at $\sqrt{s} = 7$ TeV. In pp scattering, W^\pm bosons are mainly produced by the annihilation of a u or d (valence or sea) quark in one proton with the \bar{d} or \bar{u} (sea) quark in the other. The asymmetry in the W^+ and W^- rapidity distributions is the result of the difference between the u and d distributions in the proton, so a measurement of the charge asymmetry provides constraints on these distributions. Since the longitudinal momentum of the neutrino is not measured experimentally, the W rapidity is not reconstructed. The lepton charge asymmetry is measured instead, where the information of the W rapidity is preserved in the decay lepton pseudorapidity (η). The studies presented in this dissertation constitute measurements to test perturbative QCD and provide new constraints on the parton distribution functions.

The parton distribution functions at the new energy range of the LHC are indispensable to accurately characterize background predictions and thus establish new physics discrepancies, including searches for the Higgs Boson and physics beyond the Standard Model such as Supersymmetry.

W bosons in the muon decay channel provide a well characterized event topology. Experimentally they constitute a “benchmark” process to study LHC collision data and detector response. In particular, W bosons, in conjunction with Z bosons, are a major source of high transverse momentum (p_T) muons, providing a sample to examine calibrations of the detector momentum scale and resolution, and the reconstruction and identification efficiencies. Another aspect is the requirement of large missing transverse energy E_T^{miss} corresponding to the neutrino from the W decay. The selection of $W \rightarrow \mu\nu$ events presents an opportunity to study this complex experimental variable. The comparison with simulations based on Monte Carlo allows for validation of the detector simulation and the optimization of selection strategies. Finally, an understanding of the backgrounds, particularly the QCD background, both in terms of the overall normalization and the relative shapes, as a function of variables such as muon p_T and η , is another crucial step towards a precision measurement using W bosons. A good characterization of high- p_T muons and E_T^{miss} is important for a wide array of physics analyses that include these objects.

This dissertation is organized as follows. Chapter 2 presents the theoretical motivation for the measurement, describing the available theoretical predictions for W^\pm production and the impact of the W charge asymmetry on the parton distribution

functions. Chapter 3 introduces the LHC and the ATLAS detector, including the performance and operational parameters, and provides a brief description of the various detector components used in the measurement of $W \rightarrow \mu\nu$ events.

Prior to collision data-taking in 2008 and 2009, millions of cosmic ray events were acquired, which served to commission the experiment, including the trigger, the data acquisition, the various sub-detectors and the reconstruction software. Chapter 4 describes some of the studies with cosmic rays performed as part of this effort, in order to characterize and contribute to the improvement of the Muon Spectrometer (MS) capabilities ahead of collisions. A measurement of the muon charge ratio in cosmic rays using MS tracks is presented which served to study the detector performance and allowed for the development of analysis techniques used in the first collision data.

Chapter 5 presents the first published measurement of the W charge asymmetry in ATLAS [1]. It starts with a description of the object reconstruction, focusing particularly on the muon track reconstruction, the definition of missing transverse energy associated with the decay neutrino, and the reconstruction of the collision vertex. It then describes the selection of $W \rightarrow \mu\nu$ events in the context of the first W cross section measurement, used in the definition of the charge asymmetry measurement, with a dataset corresponding to an integrated luminosity of about 310 nb^{-1} . The measurement of the W charge asymmetry with this dataset established an overall asymmetry in the rate of W^\pm production. These measurements have been crucial to define the objects used in the selection of W candidates, develop techniques for characterizing the object performance in data, validating the detector simulation and

understanding the background rates, particularly for QCD which is relatively poorly modeled in simulation. These are important steps towards understanding the major sources of systematic uncertainties for the W charge asymmetry and establishing the analysis strategies for subsequent measurements.

Chapter 6 describes the differential charge asymmetry measurement in the production of $W \rightarrow \mu\nu$, performed as a function of the decay muon pseudorapidity. It uses the full pp collision dataset from 2010, corresponding to an integrated luminosity of about 31 pb^{-1} , one hundred times larger than that used for the first measurement. This measurement has been accepted for publication [2]. A detailed discussion of the event selection, the background estimations, the main sources of systematic uncertainties and the final result are presented. Chapter 7 concludes with a summary of the asymmetry result and a preliminary discussion of the impact of the differential measurement on the parton distribution functions.

Chapter 2

Theoretical Overview

Scattering processes at hadron colliders are described in the Standard Model of particle physics by Quantum Chromodynamics (QCD) [3]. QCD is a gauge field theory that characterizes the strong interactions of colored quarks and gluons. A crucial property of strong interactions is asymptotic freedom, whereby the interaction strength decreases with energy. This implies that in high energy collisions, quarks and gluons may be treated as effectively free particles, allowing for perturbative QCD (pQCD) calculations. Conversely, at low energies quarks and gluons interact strongly, binding in combinations forming hadrons such as the proton. A fundamental parameter of QCD is the strong coupling constant α_s , that depends on the energy scale, typically the scale Q of the momentum transfer for a given process, indicating the effective strength of the strong interaction in the process. Figure 2.1 summarizes the measurements of α_s as a function of Q , providing compelling evidence for the accurate prediction of the scale dependence in QCD.

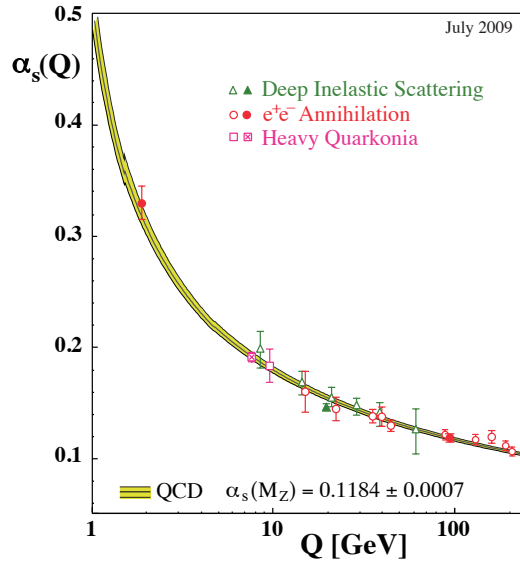


Figure 2.1: Measurements of the strong coupling constant α_s as a function of the energy scale Q . Note the uncertainty on the value best value of $\alpha_s(M_Z)$ is 0.6%, from [4].

Particles such as the W boson are produced in high energy hadronic collisions from the hard scattering of the incident partons (quarks and gluons). However, since the initial state particles are hadrons, in order to relate theoretical calculations to experimental measurements it is necessary to know the momentum distribution of the partons inside the colliding hadrons. This information is non-perturbative and must be extracted from data.

This thesis describes the first measurements of the production of W bosons in high energy proton-proton collisions at the LHC with the ATLAS detector. The main emphasis is placed on the study of the production properties of W s and the information they provide about the description of the proton. This chapter reviews the theoretical background and presents the motivation for the measurements described in the subsequent chapters.

2.1 W Boson Production in pp Collisions

2.1.1 The Proton Structure

The proton is a composite object and its structure depends on the energy scale Q with which it is probed. Here the ability to resolve the constituents increases with the momentum transfer between the proton and the probe used to study it. At low energies, $Q \lesssim 1$ GeV, the proton behaves like a point-like particle and its substructure cannot be resolved. Its static properties such as electric charge and quantum numbers [5] are determined by the three valence quarks: two up-type and one down-type quark, forming the proton bound state. These valence quark point-like constituents were first postulated, and experimentally confirmed, in the sixties and seventies [6, 7], giving rise to the quark parton model of the proton [8, 9, 10].

This picture of the proton was further refined when it was realized that these valence quarks produce gluons g , that additionally split into $q\bar{q}$ pairs: the sea quarks. At higher energies, $1 < Q \lesssim 100$ GeV, the proton structure is resolved, including contributions from the valence quarks, the sea quarks and the gluons. The dynamics of the proton can be understood in terms of how the proton momentum is distributed among the constituent partons. Formally, the fraction of the momentum carried by a given parton is expressed as a probability distribution, called a parton distribution function, PDF [11], see Section 2.1.4. At low energies, the momentum of the proton is primarily distributed among the three valence quarks. As the energy increases, the emission of gluons is more probable and these gluons carry some of the initial momentum of the quarks. As a result the gluons and the sea quarks arising from

gluon splitting, are increasingly important at small momentum fractions. Since the sum of all the momentum fractions is normalized to unity, in order to yield the total momentum of the proton, as the energy increases, the distribution of momentum fractions for the valence quarks correspondingly shifts towards lower values.

2.1.2 The Production Cross Section in Hadronic Collisions

The factorization theorem, first proposed by Drell and Yan [12], postulates that in hadronic collisions, the cross section of a hard scattering process can be separated into a partonic cross section, which is process-dependent and calculable in pQCD, and a universal part corresponding to the distribution of partons inside the colliding hadrons, given by the PDFs. The factorized hard-scattering process is shown schematically in Figure 2.2. If hadrons A and B interact to produce X , the cross section for the process $\sigma_{AB \rightarrow X}$ can be determined from the convolution of the cross section of the intervening partons a and b , $\hat{\sigma}_{ab \rightarrow X}$, and the PDFs of the hadron, $f_{a/A}(x_a)$, for parton a in hadron A , and similarly $f_{b/B}(x_b)$ for parton b in hadron B :

$$\sigma_{AB \rightarrow X} = PDF \otimes \sigma_{ab \rightarrow X} = \sum_p \int dx_a dx_b f_{a/A}(x_a) f_{b/B}(x_b) \hat{\sigma}_{ab \rightarrow X}, \quad (2.1)$$

where x_a and x_b are the momentum fractions of hadrons A and B carried by partons a and b respectively. The partonic cross section $\hat{\sigma}_{ab \rightarrow X}$ may be expressed as a power series expansion in the coupling α_s , where each order of the strong coupling corresponds in perturbation theory to contributions from higher order emissions. It may thus be written in terms of leading order (LO), next-to-leading order (NLO), next-to-next-to-leading order (NNLO) and so on processes, as

$$\hat{\sigma}_{ab \rightarrow X} = [\hat{\sigma}_{LO} + \alpha_s \hat{\sigma}_{NLO} + \alpha_s^2 \hat{\sigma}_{NNLO} + \dots]_{ab \rightarrow X} \quad (2.2)$$

where α_s depends on the scale of the process.

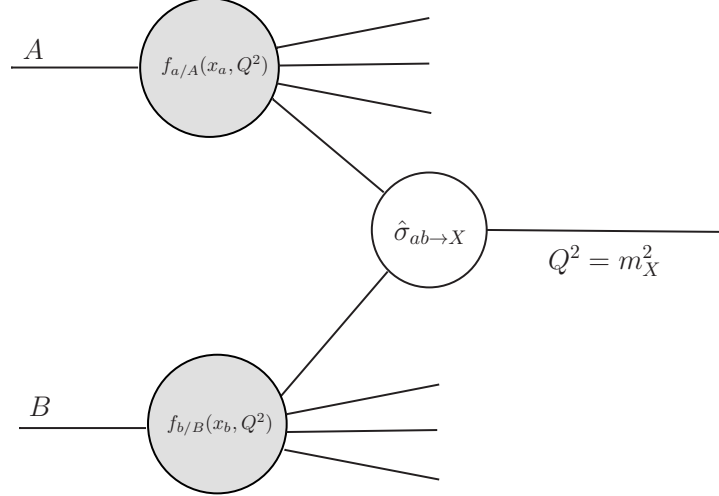


Figure 2.2: Schematic diagram for particle production in hadronic collisions.

Terms beyond leading order, the higher order corrections in Equations 2.1 and 2.2, give rise to logarithmic divergences due to soft and collinear gluon emissions [13]. These logarithms can be absorbed into the definition of the PDFs, and the factorized cross section can be re-written in terms of renormalized PDFs, depending on the scale of the hard-scattering process Q^2 , as

$$\sigma_{AB \rightarrow X} = \sum_p \int dx_a dx_b f_{a/A}(x_a, Q^2) f_{b/B}(x_b, Q^2) \hat{\sigma}_{ab \rightarrow X}. \quad (2.3)$$

The scale Q is referred to as the factorization scale μ_F . This is understood to be the scale separating the long and short-distance physics, where perturbative and non-perturbative calculations apply. Similarly the scale dependence of α_s can be explicitly written as

$$\hat{\sigma}_{ab \rightarrow X} = [\hat{\sigma}_{LO} + \alpha_s(\mu_R^2) \hat{\sigma}_{NLO} + \alpha_s^2(\mu_R^2) \hat{\sigma}_{NNLO} + \dots]_{ab \rightarrow X} \quad (2.4)$$

where μ_R is the renormalization scale for the strong coupling. The full cross section calculation, completely describing the physical scattering process, includes all orders of α_s and does not depend on unphysical scales. In practice only finite-order calculations can be performed. As a result the cross section depends on the scales μ_F and μ_R , giving rise to a theoretical uncertainty from higher order contributions.

2.1.3 The W Boson Production Cross Section

The W boson production cross section can thus be calculated using QCD with the factorization theorem, by convoluting the partonic cross section with the parton distribution functions. The total inclusive W cross section can be written as

$$\begin{aligned} \sigma(pp \rightarrow W + X) &= \sum_{n=0}^{\infty} \alpha_s^n(\mu_R^2) \sum_{a,b} \int dx_a dx_b f_{a/A}(x_a, \mu_F^2) f_{b/B}(x_b, \mu_F^2) \\ &\quad \times \hat{\sigma}_{ab \rightarrow W+X}^{(n)}(x_a x_b s, \mu_R^2, \mu_F^2) \end{aligned} \quad (2.5)$$

where s is the center-of-mass energy of the collision squared and A and B are the two protons. For this process, calculations are available up to NNLO or $\alpha_s^2(\mu_R^2)$. Note that the choice of scales typically used is the W mass: $\mu_F = \mu_R = m_W$. The overall theoretical uncertainty comes from higher order QCD and EW¹ contributions and the PDF uncertainties.

In pp collisions, W bosons at leading order are produced from the annihilation of a quark-antiquark pair, as shown in Figure 2.3. Charge conservation requires an up-type and a down-type quark to interact. In the case of resonant scattering, the scale

¹The most precise calculations are available to NLO in QED.

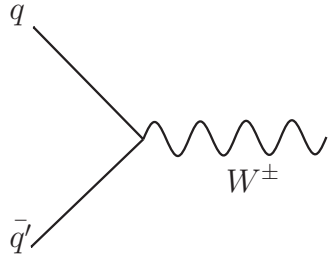


Figure 2.3: Feynman diagram for W production. The W charge depends on the incident partons. For example, a $u\bar{d}$ annihilation produces a W^+ boson and a $d\bar{u}$ annihilation a W^- boson.

of the process is directly related to the momenta of the incoming partons and the W mass

$$Q^2 = sx_a x_b = M_W^2 \quad (2.6)$$

where \sqrt{s} is the center-of-mass energy of the colliding beams. Since u quarks in the proton carry more momentum than d quarks, due to the presence of an additional valence quark, $x(u) > x(d)$, it is kinematically more likely for a $u\bar{d}$ combination to satisfy Equation 2.6 than a $d\bar{u}$ combination. As a result more W^+ relative to W^- are produced.

The parton decomposition of the W^+ and W^- total cross sections as a percentage of the total cross section is shown in Figure 2.4. The dominant mechanism for W production in pp collisions is valence-sea scattering of u and d quarks, where $u\bar{d} \rightarrow W^+$ and $d\bar{u} \rightarrow W^-$. At the LHC energy of $\sqrt{s} = 7$ TeV, about 10% of the total is associated with charm-strange scattering. These sea-sea processes dominate over the valence-sea contributions like up-strange, that are across families and hence Cabibbo suppressed, and contribute at the percentage level.

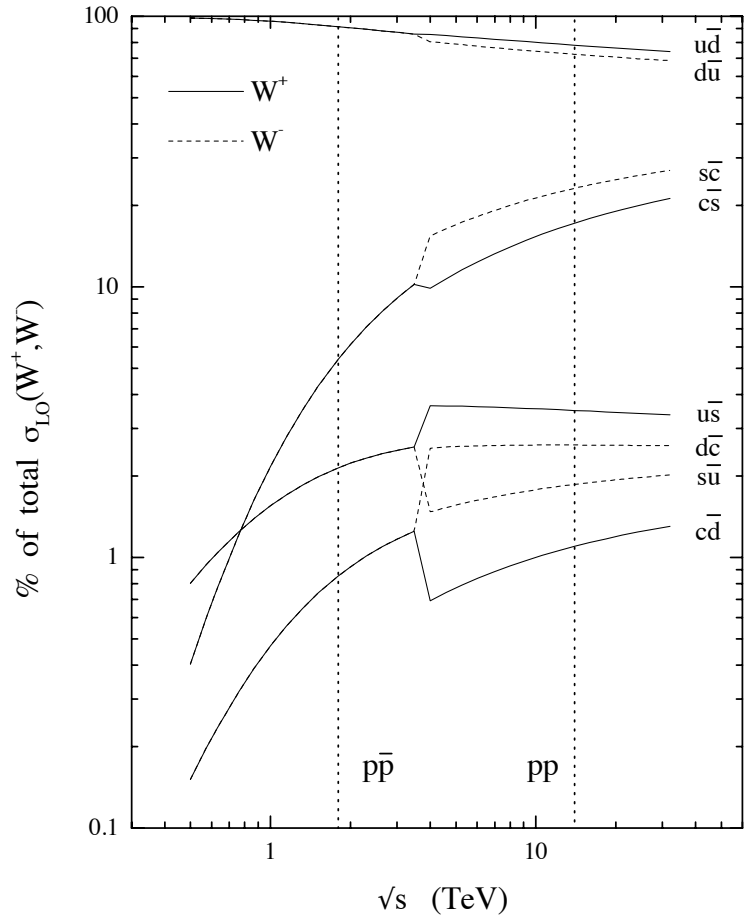


Figure 2.4: Parton flavor decomposition of the W^+ (solid line) and W^- (dashed line) total cross sections in $p\bar{p}$ and pp collisions as a function of the center-of-mass energy, from [14].

2.1.4 The Parton Distribution Functions

In the parton model, the proton structure is described by parton distribution functions (PDFs) that provide the probability for a given parton type to carry a fraction x of the proton's momentum. Integrating over all the parton contributions, the quan-

tum numbers of the proton should be recovered

$$\begin{aligned}
 \int_0^1 [u_v(x) + u_s(x) - \bar{u}_s(x)] dx &= 2 \\
 \int_0^1 [d_v(x) + d_s(x) - \bar{d}_s(x)] dx &= 1 \\
 \int_0^1 [s_s(x) - \bar{s}_s(x)] dx &= 0
 \end{aligned}
 \tag{2.7}$$

where the subscripts v and s denote the valence and sea quarks respectively.

The PDFs contain non-perturbative physics and so are not entirely derived from theoretical calculations. In practice they are obtained from fits to experimental data from fixed target experiments, deep inelastic scattering (DIS)², Drell-Yan (DY) and jet production. The scale Q^2 dependence is known analytically in pQCD, but the x dependence is determined mainly from the data. Each experiment provides information about a range of x and Q^2 , and this is combined in fits that provide predictions over a large kinematic range. The fits are parametrized at a starting scale Q_0^2 and the distributions are evolved to higher scales Q_1^2, Q_2^2, \dots where they are compared with data. The typical procedure used is based on adjusting the initial parameters, in order to obtain the best fit to the data.

Various collaborations provide PDF sets, particularly the CTEQ [15, 16], MSTW [17] and NNPDF [18] groups. These are based on global fits to fixed-target, DIS, DY and Tevatron data. The ABKM [19] group provides PDF sets using all the types of datasets except for the Tevatron data. Finally, there are additional sets provided by

²Deep inelastic scattering refers to processes in which the structure of hadrons such as the proton is probed by colliding them with leptons.

the two HERA experiments [20] based only on the DIS measurements³.

The $Q^2 - x$ range probed by the input experimental datasets is shown graphically in Figure 2.5. It may be noted that while much of the kinematic plane is covered by experimental input, not all parton types are covered equally. The processes used in the current MSTW PDF fits [17], including the partons that are probed in each process and the approximate ranges of x that are constrained, are listed in Table 2.1. The fixed target experiments populate the large x low Q^2 region, and the DIS experiments probe a diagonal band (see Figure 2.5) from low x and low Q^2 up to large x and large Q^2 . Finally the Tevatron inclusive jet and W/Z measurements, probe large x at larger Q^2 .

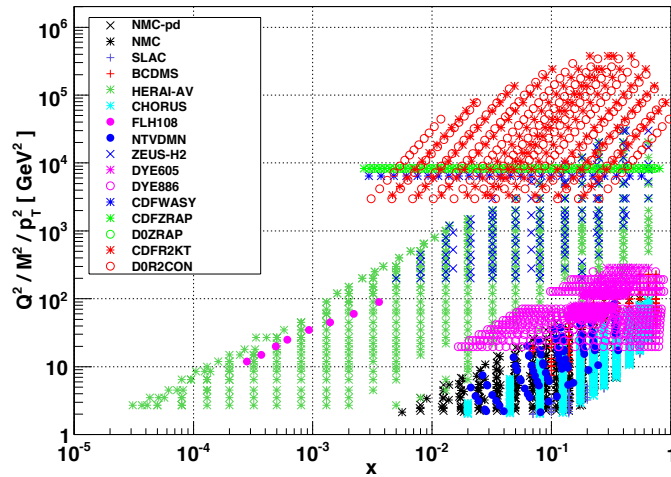


Figure 2.5: Kinematic regions of experimental data used in NNPDF2.0 set in terms of x and Q^2 from Tevatron $p\bar{p}$, HERA ep and a variety of fixed target experiments. The x -values of the two intervening partons are included in the plot, from [18].

³As will be discussed in Chapter 7, the HERA PDF fits are now adding Tevatron and LHC data.

Process	Subprocess	Partons	x range
$l^\pm \{p, n\} \rightarrow l^\pm X$	$\gamma^* q \rightarrow q$	q, \bar{q}, g	$x \gtrsim 0.01$
$l^\pm n/p \rightarrow l^\pm X$	$\gamma^* d/u \rightarrow d/u$	d/u	$x \gtrsim 0.01$
$pp \rightarrow \mu^+ \mu^- X$	$u\bar{u}, d\bar{d} \rightarrow \gamma^*$	\bar{q}	$0.015 \lesssim x \lesssim 0.35$
$pn/pp \rightarrow \mu^+ \mu^- X$	$(u\bar{d})/(u\bar{u}) \rightarrow \gamma^*$	\bar{d}/\bar{u}	$0.015 \lesssim x \lesssim 0.35$
$\nu(\bar{\nu}) N \rightarrow \mu^-(\mu^+) X$	$W^* q \rightarrow q'$	q, \bar{q}	$0.01 \lesssim x \lesssim 0.5$
$\nu N \rightarrow \mu^- \mu^+ X$	$W^* s \rightarrow c$	s	$0.01 \lesssim x \lesssim 0.2$
$\bar{\nu} N \rightarrow \mu^+ \mu^- X$	$W^* \bar{s} \rightarrow \bar{c}$	\bar{s}	$0.01 \lesssim x \lesssim 0.2$
$e^\pm p \rightarrow e^\pm X$	$\gamma^* q \rightarrow q$	g, q, \bar{q}	$0.0001 \lesssim x \lesssim 0.1$
$e^+ p \rightarrow \bar{\nu} X$	$W^+ \{d, s\} \rightarrow \{u, c\}$	d, s	$x \gtrsim 0.01$
$e^\pm p \rightarrow e^\pm c\bar{c} X$	$\gamma^* c \rightarrow c, \gamma^* g \rightarrow c\bar{c}$	c, g	$0.0001 \lesssim x \lesssim 0.01$
$e^\pm p \rightarrow \text{jet} + X$	$\gamma^* g \rightarrow q\bar{q}$	g	$0.01 \lesssim x \lesssim 0.1$
$p\bar{p} \rightarrow \text{jet} + X$	$gg, qg, qq \rightarrow 2j$	g, q	$0.01 \lesssim x \lesssim 0.5$
$p\bar{p} \rightarrow (W^\pm \rightarrow l^\pm \nu) X$	$ud \rightarrow W, \bar{u}\bar{d} \rightarrow W$	u, d, \bar{u}, \bar{d}	$x \gtrsim 0.05$
$p\bar{p} \rightarrow (Z \rightarrow l^+ l^-) X$	$uu, dd \rightarrow Z$	d	$x \gtrsim 0.05$

Table 2.1: The main processes included in the global MSTW 2008 PDF analysis ordered in three groups: fixed-target, HERA and Tevatron experiments. For each process an indication of their dominant partonic subprocesses, the primary partons which are probed and the approximate range of x constrained by the data are provided, from [17].

The PDF sets provided by the MSTW 2008 fitting group, at two different energy scales $Q^2 = 100 \text{ GeV}^2$ and $Q^2 = 10000 \text{ GeV}^2$, are shown in Figure 2.6. As discussed previously, the structure of the proton depends on the energy scale. As the energy increases, the sea and the gluon contributions to the PDFs increase, mainly at low x . It may be noted, that even at LHC energies, in order to produce a W where $Q \sim m_W \sim 80 \text{ GeV}$, at least one of the partons typically carries a significant fraction of the proton's momentum, so the process often involves a valence quark.

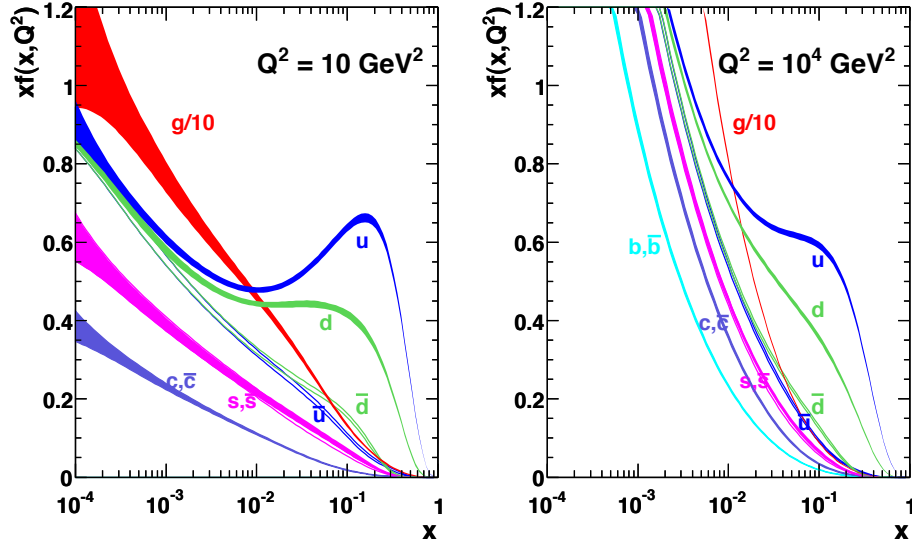


Figure 2.6: The parton distribution functions of the proton at next-to-leading order (NLO) for two values of Q^2 calculated by the MSTW collaboration. The shaded regions correspond to the band that includes one standard deviation around the most probable value, representing the 68% confidence level (C.L.) bands, from [17].

2.1.5 W Decay and the Muon Channel

In practice, the W decay products are measured instead of the W itself. This thesis is concerned with the leptonic decay of the W into a muon and a neutrino $W \rightarrow \mu\nu$. In pp collisions, it is beneficial to reconstruct the W in the leptonic decay modes since the hadronic modes suffer from large backgrounds due to jets. In particular, since events with a high energy muon are relatively rare, the muon decay channel where $W \rightarrow \mu\nu$, provides a clean signature. The branching fraction to each lepton flavor is $(10.80 \pm 0.09)\%$, compared to that of hadrons $(67.60 \pm 0.27)\%$ [11]. The leading order Feynman diagrams for W production in pp collisions and the corresponding muon decay are shown in Figure 2.7.

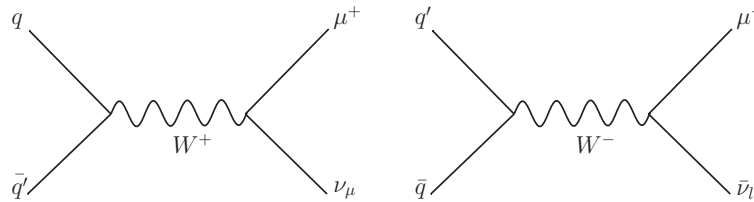


Figure 2.7: Feynman diagram for W production at leading order in pp collisions and decay into a muon and a neutrino.

2.1.6 Overview of Past W Cross Section Measurements

The W production cross section has been measured previously at $p\bar{p}$ colliders by the UA1 [21] and UA2 [22] experiments at the CERN $S\bar{p}pS$, and by the CDF [23, 24] and DØ [25, 26] experiments at $\sqrt{s} = 1.8$ TeV and $\sqrt{s} = 1.98$ TeV at the Fermilab Tevatron. The RHIC collider experiments [27, 28] have recently reported a measurement of the W cross section in pp collisions at $\sqrt{s} = 0.5$ TeV. Theoretical prediction curves at NNLO for the inclusive cross section, obtained with the ZWPROD [29] and FEWZ [30, 31] calculation using the MSTW 2008 NNLO PDF set, are shown in Figure 2.8. All measurements are in good agreement with the theoretical expectations of energy dependence.

2.1.7 Predictions of the Inclusive W Production Cross Section in pp Collisions at $\sqrt{s} = 7$ TeV

A variety of predictions have been made for the W boson production cross section in pp collisions at the center-of-mass energy of $\sqrt{s} = 7$ TeV. The W boson cross sections at NNLO, calculated with ZWPROD [29] and FEWZ [30, 31] using the PDF sets available at NNLO, are listed in Table 2.2 and constitute the most precise

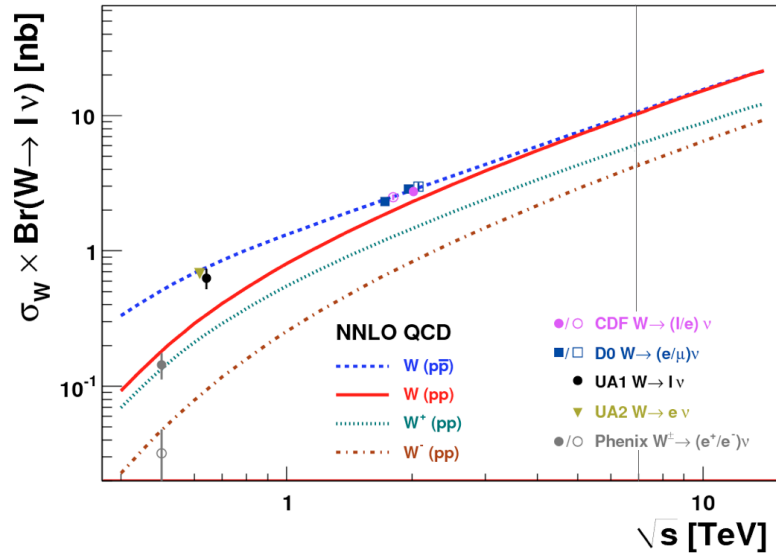


Figure 2.8: W boson production cross section predictions at NNLO, including curves for W^+ and W^- , in $p\bar{p}$ and pp collisions as a function of the center-of-mass energy. Past measurements from the S $\bar{p}p$ S, Tevatron and RHIC colliders, including the total experimental uncertainties, are also shown. The vertical line indicates the LHC energy of $\sqrt{s} = 7$ TeV, modified from [1].

calculations available. Using the MSTW08 PDF set, the NLO prediction is 3% lower compared to the NNLO one and similar variations can be seen in the comparisons shown in Figure 2.9. It may also be noted that at higher order, the theoretical uncertainty also decreases, particularly dependence on the renormalization (μ_R) and factorization (μ_F) scales. The theoretical uncertainty associated with higher order contributions, estimated by varying μ_R and μ_F independently up-and-down by a factor of two around their central value m_W , with the constraint $0.5 < \mu_R/\mu_F < 2$, yields 3% for the NLO prediction and a 0.6% variation at NNLO.

The W^+ and W^- cross section prediction for various PDF sets available at NLO and NNLO are compared in Figure 2.9 and show agreement between them within the

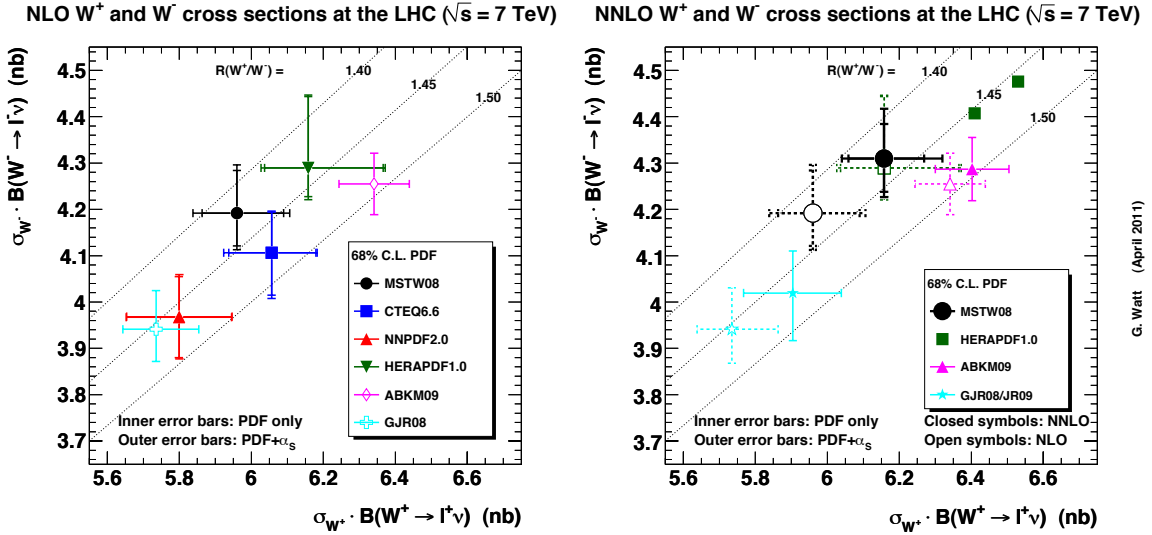


Figure 2.9: Predictions for the W^+ and W^- cross sections at $\sqrt{s} = 7$ TeV for the available PDF sets with the uncertainties from the PDFs and α_s at NLO (left) and NNLO (right). The comparison corresponds to differences between PDFs alone, since the different predictions are performed with otherwise identical code and settings. Theoretical uncertainties are not included and the scale is fixed at $\mu_R = \mu_F = m_W$, from [32].

uncertainties. The predictions for the total W cross section do not depend strongly on the choice of PDF set, but the separate W^+ and W^- predictions show larger differences between them. This is also indicated in Figure 2.9 by the diagonal bands corresponding to the W^+ to W^- cross section ratio. While the NNLO predictions for the cross section are a few percent larger than the NLO ones, the W^+ to W^- cross section ratio is relatively insensitive to NNLO corrections. The charge dependence of W production is further discussed in Section 2.2.

	MSTW08	ABKM09	HERA	JR09
W^+	6.16 ± 0.11	6.42 ± 0.09	6.42 ± 0.16	5.92 ± 0.12
W^-	4.30 ± 0.08	4.29 ± 0.07	4.42 ± 0.10	4.03 ± 0.08
W	10.46 ± 0.18	10.71 ± 0.15	10.84 ± 0.26	9.94 ± 0.19

Table 2.2: Cross section times leptonic branching ratio in NNLO QCD, for W^+ , W^- and W production using various PDF sets. The units are nb. The uncertainties in the predictions are only the PDF uncertainties at 68% C.L. The additional uncertainty associated with α_s (about 2% uncertainty for a 1% error on α_s) is not included.

2.2 W Charge Asymmetry and PDF Constraints

2.2.1 W Rapidity and Asymmetry

In the leading order case, for incoming partons with momenta p_a and p_b the four-momenta in the center-of-mass frame may be expressed as

$$p_a = \frac{\sqrt{s}}{2}(x_a, 0, 0, x_a), \quad p_b = \frac{\sqrt{s}}{2}(x_b, 0, 0, -x_b). \quad (2.8)$$

The rapidity y_W , a measure of the longitudinal boost, may be expressed from its definition as

$$y_W = \frac{1}{2} \ln \left(\frac{E + p_z}{E - p_z} \right) = \frac{1}{2} \ln \left(\frac{x_a}{x_b} \right) \quad (2.9)$$

and for $m_W = \sqrt{s}x_ax_b$ the following relations are obtained

$$x_a = \frac{m_W}{\sqrt{s}} \exp(y_W), \quad x_b = \frac{m_W}{\sqrt{s}} \exp(-y_W). \quad (2.10)$$

As a result, the W rapidity provides information about the quark and anti-quark distribution functions (x -dependence) of the colliding protons.

Since the valence quarks typically carry more momentum than the sea quarks $x(u) > x(\bar{d})$, W^+ bosons are produced preferentially in the direction of the u quark,

and similarly W^- bosons in the d quark direction. Since on average $x(u) > x(d)$, from Equation 2.9, the W^+ bosons tend to be produced at larger y_W compared to W^- . Moreover, the difference in production rates for W^+ and W^- increases with rapidity y_W , and is directly related to the difference in the u and d PDF curves.

The W rapidity asymmetry, defined as

$$A_W(y) = \frac{d\sigma_{W^+}/dy - d\sigma_{W^-}/dy}{d\sigma_{W^+}/dy + d\sigma_{W^-}/dy}, \quad (2.11)$$

depends on the x of the intervening partons and as a result provides a measure of the relative u and d quark distributions as a function of x [33]. For the case of pp collisions, using the notation $q(x) = f_q(x)$, the asymmetry may be expressed in terms of the dominant production mechanism at LO as

$$A_W(y) \approx \frac{u(x_a)\bar{d}(x_b) - d(x_a)\bar{u}(x_b)}{u(x_a)\bar{d}(x_b) + d(x_a)\bar{u}(x_b)}, \quad (2.12)$$

showing the dependence of the asymmetry on the u and d quark PDFs. For small values of x , where $\bar{u} \sim \bar{d} \sim \bar{q}$, the dependence may be simplified as

$$A_W(y) \sim \frac{u - d}{u + d} \sim \frac{u_v - d_v}{u_v + d_v + 2\bar{q}}, \quad (2.13)$$

which indicates that the asymmetry at low x is sensitive to the valence quark PDFs.

2.2.2 The Lepton Charge Asymmetry

The lepton decay mode provides experimental measurements with a relatively pure sample of W s to measure the charge asymmetry. However, since the z -component of the neutrino is not determined experimentally, it is difficult to reconstruct the

W boson. As a result, the charge asymmetry can be more readily measured as a function of the decay lepton pseudorapidity η . In analogy with the asymmetry from Equation 2.11, the lepton asymmetry is defined as

$$A_l(\eta) = \frac{d\sigma_{W^{l+}}/d\eta_{l^+} - d\sigma_{W^{l-}}/d\eta_{l^-}}{d\sigma_{W^{l+}}/d\eta_{l^+} + d\sigma_{W^{l-}}/d\eta_{l^-}}, \quad (2.14)$$

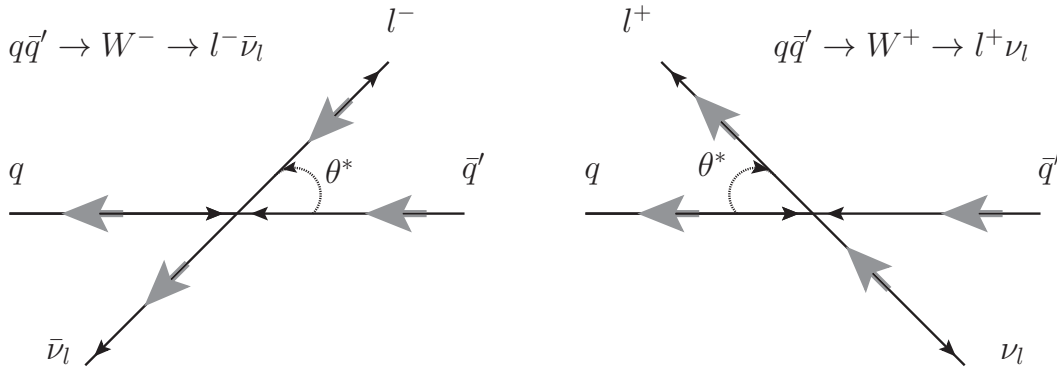


Figure 2.10: W production and decay diagram showing the favored opening angle at the LHC between the quark q and the lepton l in the rest frame of the W for $q\bar{q}' \rightarrow W^- \rightarrow l^- \bar{\nu}_l$ (left) and $q\bar{q}' \rightarrow W^+ \rightarrow l^+ \nu_l$ (right). The small black arrows correspond to the momentum while the large grey arrows indicate the spin.

This asymmetry corresponds to the convolution of the W production and the $V - A$ (vector - axial vector) decay of the W . The $V - A$ structure implies that the decay of the charged lepton is not isotropic. In particular, the parton-level cross section, in terms of the angle between the W and the decay lepton, in the rest frame of the W , is given by

$$\frac{d\sigma}{d\cos\theta^*} \propto (1 \pm \cos\theta^*)^2 \quad (2.15)$$

where the sign depends on the W and the decay lepton helicities. The preferred angular decay configuration for W^- and W^+ is shown schematically in Figure 2.10. The W

couples to negative-helicity fermions and positive-helicity antifermions. By angular momentum conservation, the outgoing fermion or anti-fermion, l or \bar{l} , preferentially follows the direction of the incoming fermion or antifermion, q or \bar{q} . The cross section is maximal when the outgoing lepton or antilepton goes in the direction of the incoming quark or antiquark. As a result, for the $q\bar{q}' \rightarrow l\nu_l$ process, a $u\bar{d} \rightarrow W^+$ produced with large positive y_W decays into a l^+ with smaller rapidity y_l , while a $d\bar{u} \rightarrow W^-$ decays preferentially into l^- with larger rapidity y_l .

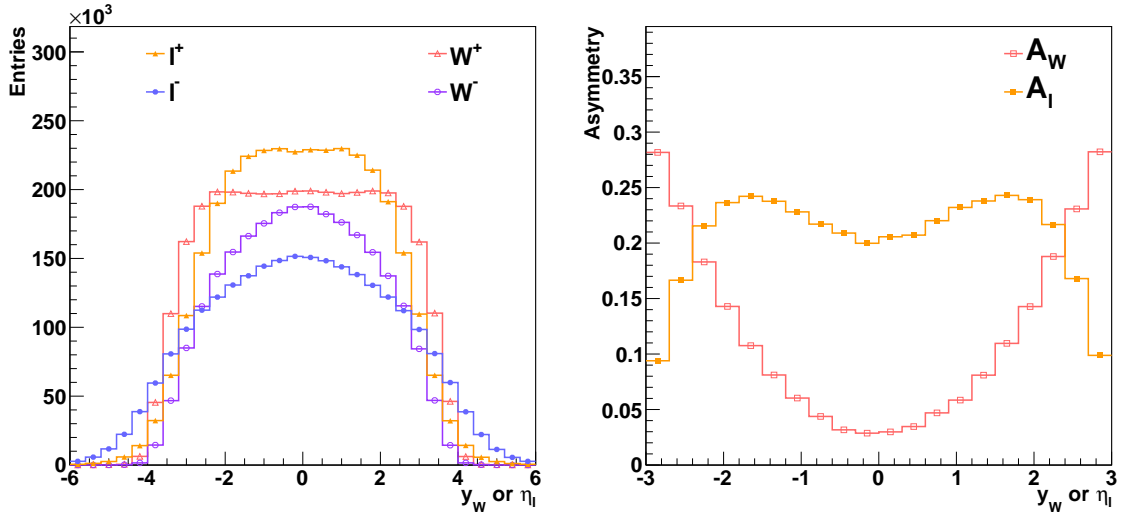


Figure 2.11: W boson rapidity and decay lepton pseudorapidity (left) and the corresponding W and decay lepton asymmetries (right). Prediction at NLO using MC@NLO with the CTEQ 6.6 PDF sets.

The rapidity distribution for the W boson and the pseudorapidity distribution for the decay lepton are compared in Figure 2.11 (left) for each charge, showing the impact of the angular dependence in the W decay. The y_W distributions for W^+ and W^- are symmetric about $y_W = 0$ and exhibit different shapes at large y_W . The drop in the W^+ distribution at larger y_W , around 3, is caused by a very low $x \bar{d}$ quark

scattering off a large x valence u quark.

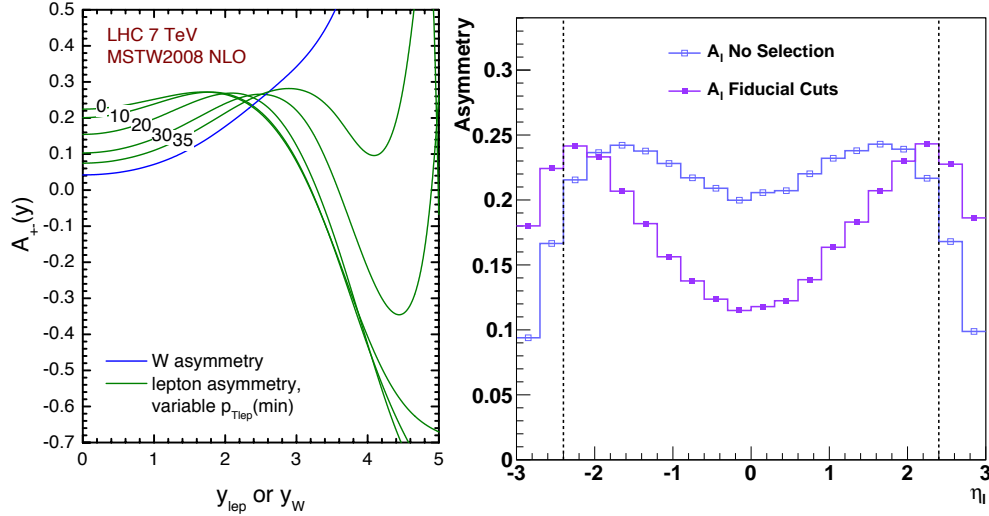


Figure 2.12: Comparison of W asymmetry and lepton asymmetry with a variety of p_T requirements on the lepton (left), from [34]. Comparison of the decay lepton asymmetry before and after applying fiducial requirements $p_T^l > 20$ GeV, $p_T^\nu > 25$ GeV and $m_T > 40$ GeV. The vertical lines at $|\eta_l| = 2.4$ indicate the boundaries of the geometrical acceptance of the ATLAS muon system (see Section 3.5).

The corresponding asymmetry distributions, shown in Figure 2.11 (right), indicate that while the W asymmetry is increasing in y , the decay lepton asymmetry increases in the central η region and then decreases at higher η . Despite the difference in shape, the W rapidity and the decay lepton pseudorapidity are correlated and the $V - A$ decay is known so the information about the incoming partons intervening in W production is also contained in the lepton asymmetry. The primary complication is that since the W decay introduces a further dependence, each value of η_l probes a range of y_W .

Finally, it may be noted that the asymmetry depends on the selection applied to the lepton, particularly the transverse momentum requirements used in experimental measurements. As the transverse momentum of the lepton is increased, the average angle between the W and the decay lepton decreases. As a result, the correlation between the y_W and the η_l is increased, and this is shown in Figure 2.12 (left) where the lepton asymmetries for increasing values of the lepton p_T requirement are increasingly closer to the asymmetry for the W . In addition, the lepton asymmetry before and after applying the analysis kinematic requirements: $p_T^\mu > 20$ GeV, $p_T^\nu > 25$ GeV and $m_T > 40$ GeV, are compared in Figure 2.12 (right).

2.2.3 Past W Asymmetry Measurements. An Overview of Tevatron Measurements

At the Tevatron $p\bar{p}$ collisions, there is no overall W^+ and W^- charge asymmetry. The W^+ bosons tend to be produced with a u quark from the proton and a \bar{d} quark from the antiproton. Since the u quark carries on average a larger fraction of the proton's momentum than the \bar{d} in the antiproton, due to the presence of an additional valence u quark, W^+ bosons are preferentially boosted in the proton direction. Similarly W^- bosons are preferentially boosted in the antiproton direction. The rapidity and asymmetry distributions for the W boson and the decay lepton in $p\bar{p}$ collisions are shown in Figure 2.13.

Measurements of the lepton charge asymmetry in $p\bar{p}$ collisions have been performed at the Tevatron by both the CDF [38, 39] and DØ [40, 37] collaborations, and the

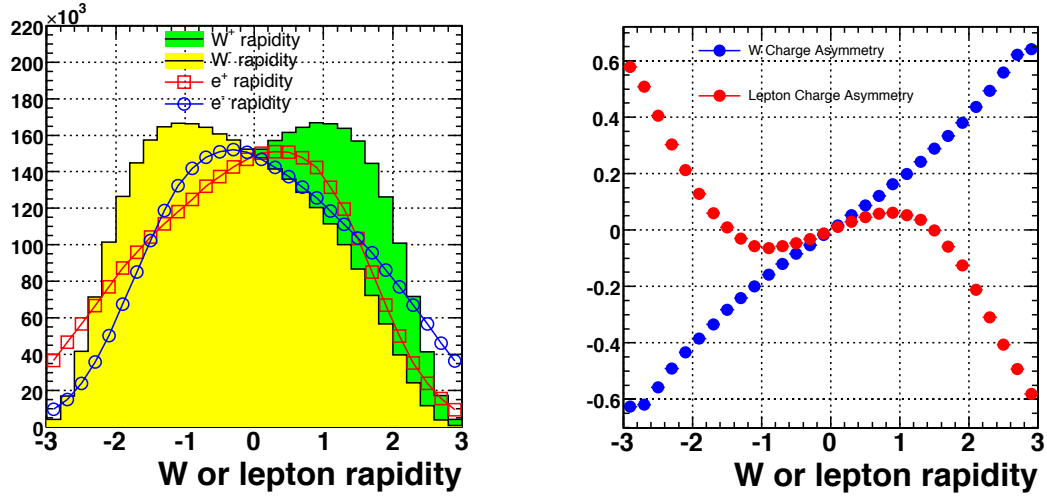


Figure 2.13: The W boson and the decay lepton rapidity distributions (left) and the charge asymmetry for W production and the decay lepton (right) in $p\bar{p}$ collisions, from [35].

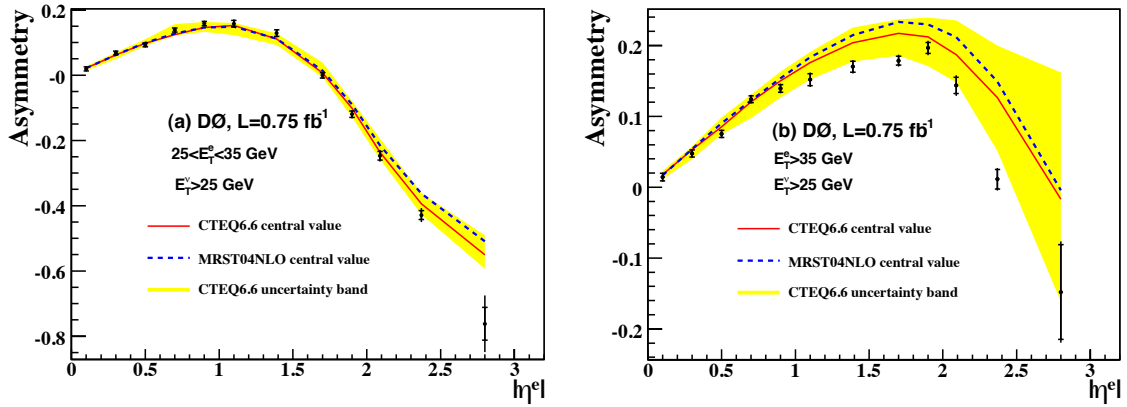


Figure 2.14: $D\bar{O}$ $W \rightarrow e\nu$ decay lepton charge asymmetry measurement in $|\eta|$ for two electron E_T ranges $25 < E_T < 35$ GeV (left) and $E_T > 35$ GeV (right) compared to theoretical predictions using RESBOS with NLO PDF sets CTEQ6.6 [15], including the PDF uncertainties, and MRST 2004 [36], from [37].

data have been included in global fits of parton distributions [17, 41]. A $W \rightarrow e\nu$ charge asymmetry result from the DØ collaboration in two bins of lepton p_T is shown in Figure 2.14. The two p_T regions probe different W rapidity regions, providing additional information about the x dependence. The result shows some disagreement with the QCD prediction at large lepton p_T . This has been confirmed in preliminary measurements performed by CDF⁴.

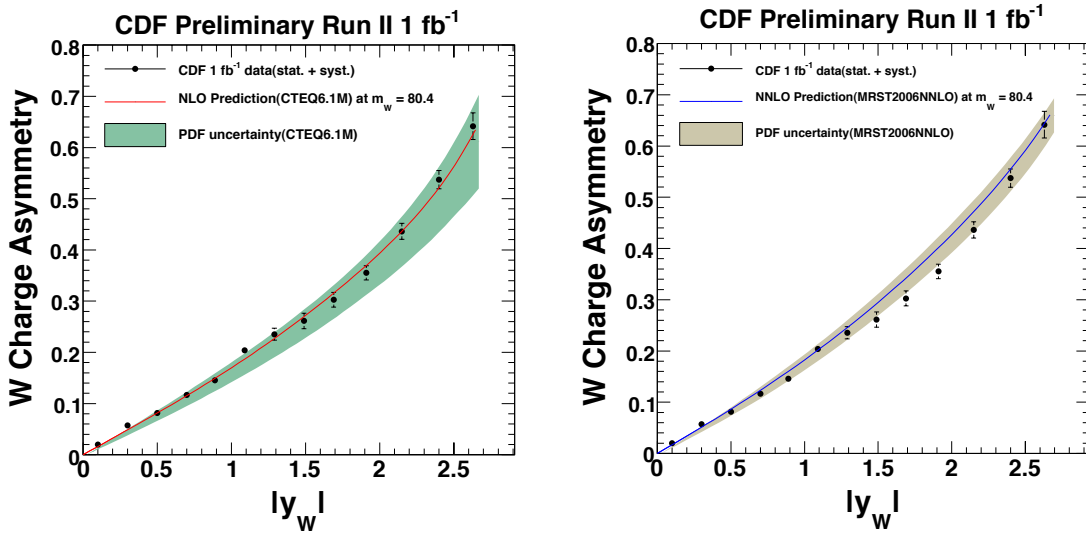


Figure 2.15: CDF W Asymmetry Measurement compared to predictions using RES-BOS [30] with PDF sets CTEQ6M [41] and MRST 2006 [42], from [35].

The CDF collaboration has also performed an asymmetry measurement where the W rapidity is estimated statistically, using kinematic constraints and an iterative weighting procedure based on the angular distribution of the $W \rightarrow e\nu$ decay [35, 43]. The result shows good agreement with theoretical predictions, as can be seen in Figure 2.15. The applicability of this method to the LHC has been investigated,

⁴From website <http://www-cdf.fnal.gov/physics/ewk/2009/WChargeAsym/>

indicating that this procedure is less capable of constraining PDFs than a lepton asymmetry measurement using the fiducial detector volume [44].

2.2.4 Kinematic Constraints from the Charge Asymmetry at the LHC

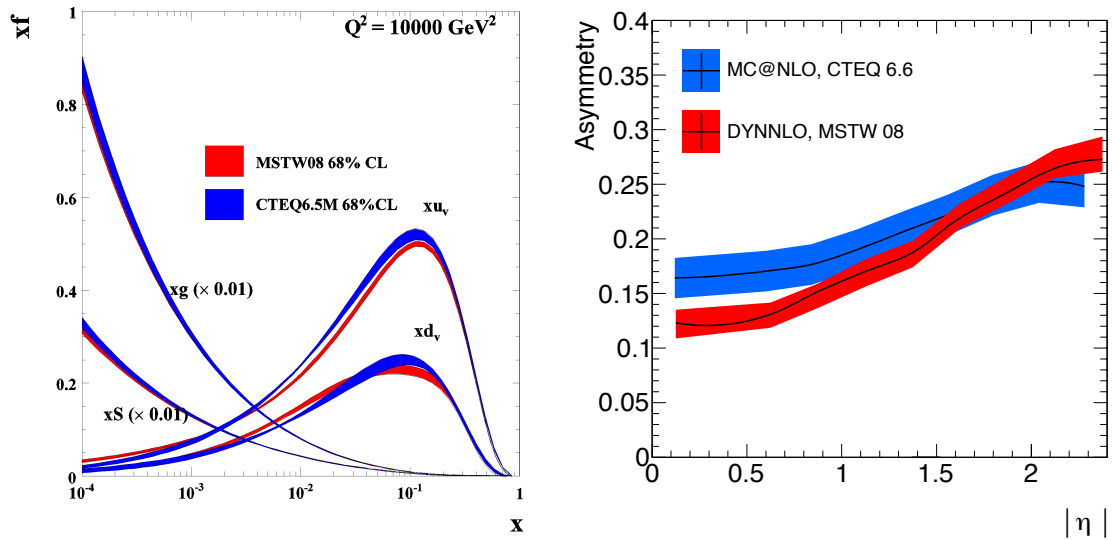


Figure 2.16: Comparison the valence, sea and gluon PDFs for CTEQ and MSTW. The error bands correspond to 68% C.L. PDF uncertainties (left, from [45]). Comparison of the asymmetry prediction for CTEQ 6.6 and MSTW 2008 showing the 90% C.L. PDF uncertainties (right, from [46]). The difference in valence PDFs shown in the central region of the left distribution explains the difference in the asymmetry between CTEQ and MSTW, shown in the right.

The main constraints on the ratio of u and d quark PDF distributions come from fixed target experiments and the lepton asymmetry from Tevatron measurements of $p\bar{p} \rightarrow W^\pm + X$, as can be seen in Table 2.1. The x range constrained by these data is $x \gtrsim 0.05$. At the LHC, at center-of-mass energy of $\sqrt{s} = 7 \text{ TeV}$, Equation 2.10

indicates that at $y = 0$ the partons are symmetric, with $x \sim 0.011$, and at increasing rapidities the parton configurations are increasingly asymmetric. For $y = 1.5$, $x_{\max} \sim 0.05$ and $x_{\min} \sim 0.003$, and for $y = 3$, $x_{\max} \sim 0.2$ and $x_{\min} \sim 0.0006$. As a result, the kinematic range of the LHC is not completely constrained by past measurements, so LHC predictions based on fixed target and Tevatron data rely on phenomenological extrapolations in x . This gives rise to differences in the predictions for different PDF sets, as can be seen in Figure 2.16, where the CTEQ [15] and MSTW [17] show disagreements even taking into account their uncertainty bands (see also [47]). The difference in the valence quark distributions at small x (central region of the left plot in Figure 2.16) accounts for the difference in the asymmetry predictions in the low η region, shown in Figure 2.16 (right). A measurement of the lepton charge asymmetry from W decays at the LHC can provide constraints in the parton momentum fraction range $10^{-3} \lesssim x \lesssim 10^{-1}$, helping resolve differences between the PDFs, and contributing in general to improve PDF descriptions.

Chapter 3

The LHC and the ATLAS Detector

The Large Hadron Collider (LHC) [48] is the largest hadronic accelerator built to date. It is located at CERN, on the Swiss-French border near Geneva, Switzerland, in a tunnel at a depth of 50 – 175 m underground with a circumference of about 27 km. The accelerator provides two counter-rotating beams of protons or heavy ions, colliding at four points on the circumference. The center-of-mass energy of the LHC has been $\sqrt{s} = 7$ TeV starting in 2010, half the nominal value of 14 TeV. Four detectors have been built surrounding each collision point, where ATLAS [49, 50, 51] is a general-purpose detector located at the point closest to the CERN Meyrin site. This chapter reviews the basic parameters of the LHC and presents the ATLAS detector, including a summary of the geometry and technologies used in its main sub-detectors: inner tracker, calorimeters and muon spectrometer.

3.1 The Large Hadron Collider

The LHC is an accelerator for hadrons of the same charge built in the LEP tunnel. The magnet system uses superconducting NbTi coils cooled to 1.9 K in order for the dipole to generate a maximum magnetic field of 8.33 T. The overall design is based on a two-in-one dipole magnet, shown in Figure 3.1, where the same magnet provides magnetic fields in opposite directions in order to bend the two counter-rotating beams of positively-charged particles. The resulting design choice is economical and compact, allowing the accelerator to fit in the preexisting tunnel. The machine is comprised of 9593 magnets, of which 1232 are main dipoles for bending the beam, and the remaining, including 392 quadrupoles and other superconducting and non-superconducting magnets, perform tasks such as beam corrections and focusing.

The LHC is part of the CERN accelerator complex (see Figure 3.2), where the protons go through different accelerators at increasingly higher energies that inject them into the next accelerator in the sequence. The protons are accelerated by the LINAC2, the PSB, the PS and the SPS accelerators prior to injection into the LHC. In particular, the SPS injects proton bunches in opposite directions at 450 GeV. In the 2010 runs, the protons in the LHC reached an energy per beam of $E_p = 3.5$ TeV. Once the desired configuration for collisions at the LHC is reached, the stable beam condition is declared and data-taking by the experiments proceeds.

Proton injection from the SPS is performed in bunches, corresponding to 1.15×10^{11} protons in an RF bucket. Prior to injection, bunches in the PSB (see Figure 3.2) are split into patterns of 72 bunches separated by 12 empty buckets, forming bunch trains.

LHC DIPOLE : STANDARD CROSS-SECTION

CERN AC/DI/MM - HE107 - 30 04 1999

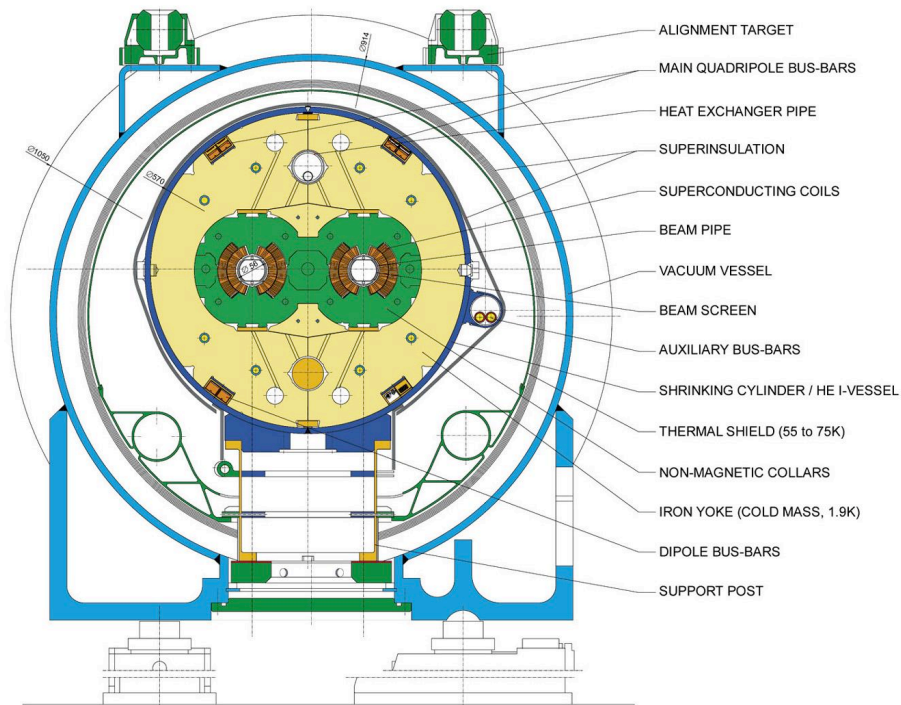


Figure 3.1: Diagram of superconducting LHC dipole magnet placed throughout the LHC ring showing its major components. The two proton beams move in opposite directions through the two aperture beam-pipes, from [52].

In the design configuration, bunches filled with protons in bunch trains are separated by 25 ns, while in 2010 the spacing was 75 ns. The large number of protons in colliding bunches gives rise to multiple collisions per bunch crossing, called in time pileup. In addition, the spacing between the bunches is shorter than the response time of the detectors, so additional collisions from different bunches are recorded simultaneously, referred to as out of time pileup. In nominal running conditions, about 20 inelastic collisions are expected to accompany each high energy event. In the low-luminosity running conditions of 2010, the average number of interactions per event was 2.2, with a maximum of 3.78, mostly arising from in time pileup. The instantaneous

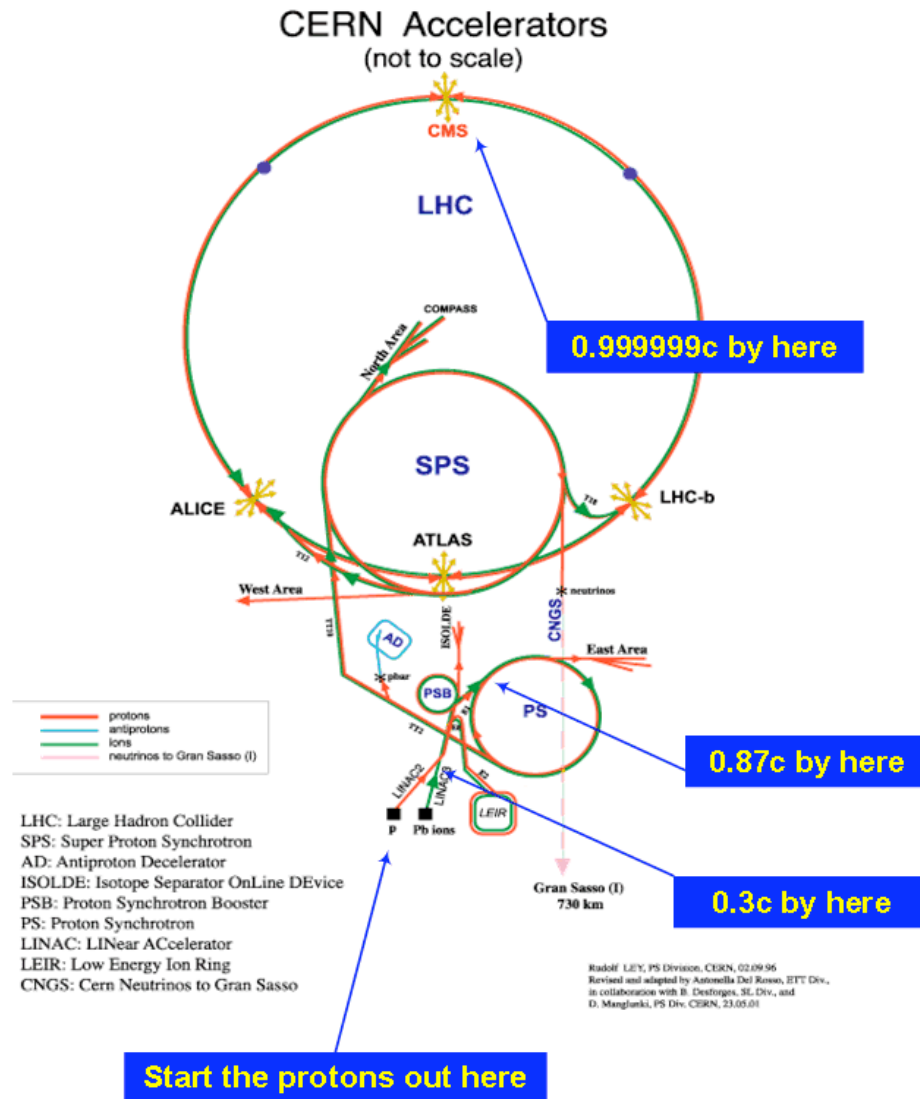


Figure 3.2: CERN Accelerator Complex, from [53]. The protons are first injected at the start of the LINAC2, where they are accelerated to 50 MeV, they are then injected into the PSB where they are accelerated to 1.4 GeV, then into the PS where they are accelerated to 26 GeV, then into the SPS where they are accelerated to 450 GeV and finally into the LHC where they are accelerated to 3.5 TeV (half the nominal beam energy of 7 TeV).

luminosity \mathcal{L} is the proportionality factor between the event yield rate and the cross section $dN/dt = \mathcal{L}\sigma$, and it is defined in its simplest form as

$$\mathcal{L} = \frac{N_p^2 k_b f}{4\pi\sigma_x\sigma_y}, \quad (3.1)$$

where N_p is the number of protons per bunch, k_b the number of bunches, f the revolution frequency, and σ_x and σ_y characterize the transverse beam profiles in the horizontal and vertical directions respectively.

In practice, the single particle transverse motion is modulated by an amplitude function β and the beam optics are configured such that the beams are focused at the interaction point (IP) in order to maximize the likelihood of collisions. The value of the amplitude at the IP is called β^* . Another important parameter to characterize beam performance is the emittance ϵ , corresponding to the space and momentum phase space occupied by the particles in the beam. A low emittance is desirable since it implies that the particles are confined to a small region in space and have a small range of momenta. In terms of the emittance and amplitude functions, the instantaneous luminosity may be rewritten as

$$\mathcal{L} = \frac{N_p^2 k_b f}{4\epsilon_n \beta^*} F, \quad (3.2)$$

where the factor F accounts for the impact of the crossing angle and other characteristics of the beam configuration. In order to achieve high luminosity, the beam should collide bunches with large numbers of particles with low emittance at high frequency in a region where the amplitude is as low as possible.

The total number of events for a process X produced with a cross section σ_X for an integrated luminosity L corresponding to a time period spanning t_0 to t_f is given by

$$N = \sigma_X L \quad \text{where} \quad L = \int_{t_0}^{t_f} \mathcal{L} dt. \quad (3.3)$$

The integrated luminosity as a function of time for the pp collisions at center-of-mass energy of 7 TeV is shown in Figure 3.3. The maximum luminosity delivered in one fill was 6.3 pb^{-1} , the maximum in a single day was 5.98 pb^{-1} and the maximum in a period of 7 days was 24.6 pb^{-1} .

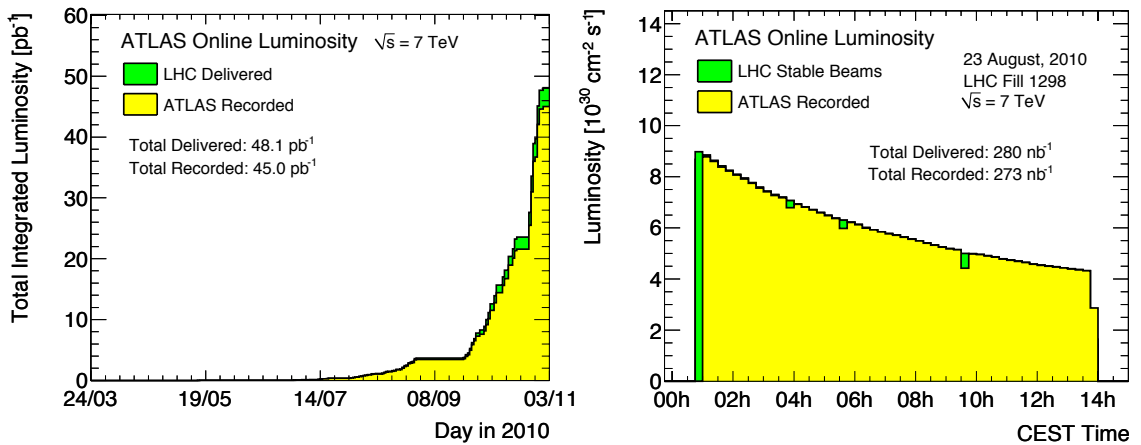


Figure 3.3: Total integrated luminosity from online measurements as a function of the day (left) delivered by the LHC (green) and recorded by ATLAS (yellow) during stable beams for pp collisions at $\sqrt{s} = 7 \text{ TeV}$. Instantaneous luminosity profile (right) as measured online for an LHC fill on August 23rd, 2010, comparing the luminosity delivered during stable beam conditions (green) and recorded with the entire detector available (yellow).

The luminosity is determined [54] from counting rates measured by the specialized luminosity detectors, calibrated with Van-der-Meer scans, where one beam is swept across the other beam and the collision rate is measured as a function of the beam

displacement. The systematic uncertainty of the luminosity measurement is estimated to be 11%, dominated by the uncertainty in the beam current of 10%. The luminosity delivered by the LHC and recorded by ATLAS during the stable beam period is compared in Figure 3.3. The ATLAS data-taking efficiency is 93.7%, where the inefficiencies result from the time taken to turn on and off the high voltage of the sensitive detectors, primarily the silicon tracking and muon detectors, and deadtime or problems with individual sub-detectors that prevented data-taking from proceeding (about 4.4%).

The instantaneous luminosity for an LHC fill from August 23rd 2010 is also shown in Figure 3.3. The luminosity lifetime¹ was around 15 – 20 hours. The luminosity drop is caused by a decrease in the beam intensity, where protons are lost in the collisions and on collimators (intensity lifetime about 90 hours) and an increase in the beam emittance. In 2010, the longest time in stable beams condition for one fill was 30.3 hours, for one day was 22.8 hours (94.9%) and for a period of 7 days was 69.9 hours (41.6%). The fastest turnaround to stable beams was 3.66 hours.

In 2010, the main goal of the LHC was to gain experience operating the machine, particularly in terms of injecting, ramping, squeezing and establishing stable beams. The machine initial commissioning period was finalized in February, allowing for beam injection at 450 GeV and recommissioning of the mechanisms for machine protection. The beam energy was then ramped up culminating in the first collisions at center-of-mass energy of 7 TeV on March 30th. In April, the optics were improved, allowing

¹The luminosity lifetime is defined as the time for the instantaneous luminosity to decrease by $1/e$.

Parameter	Design (10^{34})	2010 Runs
Beam Energy [TeV]	7	3.5
β^* [m]	0.55, 10, 0.55, 10	3.5, 3.5, 3.5, 3.5
Emittance ϵ_n [μm]	3.75	2.0 – 3.5
Transverse beam size at IP [μm]	16.7	~ 60
Number of protons	1.15×10^{11}	1.2×10^{11}
Number of bunches per beam	2808	368
Bunch spacing [ns]	25	75
Stored Energy [MJ]	360	28
Peak Instantaneous Luminosity [$\text{cm}^{-2}\text{s}^{-1}$]	10^{34}	2×10^{32}
Mean interactions per crossing	23	0 – 2.2

Table 3.1: LHC parameters for the nominal design and for the pp runs in 2010.

for “squeezing” of the beams in the transverse direction, until June, when operation with nominal bunch intensities was commissioned. There was an extended running period from August until September, when the bunch trains were commissioned in order to run at higher luminosity. For the remaining pp collision period extending to the end of October, the performance was ramped up and data was accumulated in the detectors for analysis. Many records were achieved in the 2010 LHC operation, particularly the peak stable luminosity delivered $2.07 \times 10^{32} \text{ cm}^{-2}\text{s}^{-1}$ exceeded the goal for 2010 by a factor of 2. The LHC parameters for the design energy and luminosity and for the 2010 runs are compared in Table 3.1.

3.2 The ATLAS Detector

The ATLAS (A Toroidal LHC ApparatuS) detector at the LHC was designed and built for general physics studies of high energy collisions, including measurements of SM parameters, confirmation or exclusion of the Higgs boson and searches for physics

signatures corresponding to phenomena beyond the SM (BSM). ATLAS is intended to provide a good quality measurement of high- p_T objects including electrons e , photons γ , muons μ , jets, b -quark jets and missing transverse energy E_T^{miss} .

An overview of the ATLAS detector and its sub-systems is shown in Figure 3.4. The detector is comprised of an inner tracking system (inner detector, or ID), surrounded by a superconducting solenoid providing a 2T magnetic field, electromagnetic and hadronic calorimeters and a muon spectrometer (MS). ATLAS also includes forward detectors whose main goal is to measure the luminosity: LUCID (LUminosity measurement using Cherenkov Integrating Detector) and ALPHA (Absolute LUminosity For ATLAS). The ID consists of pixel and silicon microstrip (SCT) detectors, surrounded by a transition radiation tracker (TRT). It provides precision transverse momentum (p_T) measurements of charged particles up to $|\eta| < 2.5$. The calorimeters are hermetic up to $|\eta| < 4.9$ and are designed to capture the showers of high energy electrons, photons and hadrons. The electromagnetic calorimeter is a lead liquid-argon (LAr) detector in the barrel and the endcap, while in the forward region copper LAr technology is used. Hadron calorimetry is based on two different detector technologies, with scintillator tiles or LAr as the active media, and with either steel, copper, or tungsten as the absorber material. The MS with coverage up to $|\eta| < 2.7$ is based on three large superconducting toroids, and a system of three stations of chambers for fast trigger and precision tracking measurements. Finally, the ATLAS detector includes a trigger and data acquisition system that collects the most interesting events. The data recorded is distributed world-wide using the LHC Computing Grid for processing and analysis.

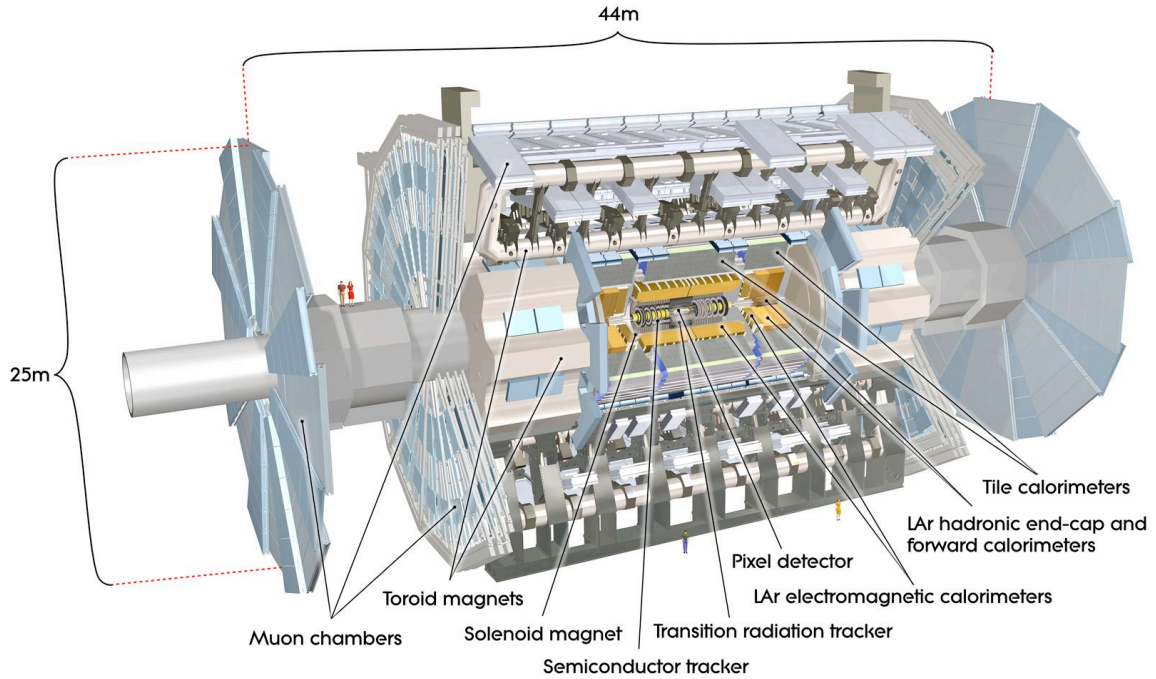


Figure 3.4: Overview of the ATLAS detector, including its main sub-systems, from [52].

The overall design choices for ATLAS, including its size, are derived from beam constraints, such as collisions energies and luminosity rates, and the expected physics reach. The harsh LHC collision environment and the operational lifetime of about ten years imposes strict requirements on the detector technologies that should be fast, radiation-hard and experience low rates of aging. Pileup interactions present additional challenges, requiring high granularity in order to reduce the impact of ambiguities that may arise in the overlap between interesting and minimum bias events. The amount of material in the calorimeters is driven by the need to contain 1 TeV electrons (about 30 radiation lengths X_0) and 1 TeV pions (about 11 absorption lengths λ) and the dimensions of the muon system are imposed by the desire to

measure 1 TeV muons, requiring several Tm of bending power. The choice of the magnet system, made up of two components: the solenoid surrounding the ID and the toroid for the MS, gives ATLAS its overall characteristic form.

The main performance goals for each sub-detector, as constrained by Higgs and hypothesized BSM signatures are listed in Table 3.2. The inner tracker should reconstruct the trajectory of charged particles with high efficiency and good momentum resolution in order to observe collision vertices, as well as secondary vertices associated with heavy quark decays. It is also crucial for electron, muon and tau identification. The calorimeters are designed to provide very good identification and a high resolution measurement of electrons and photons, important for example to observe a Higgs boson at low mass decaying to two photons². The calorimeters should additionally measure jets and missing transverse energy accurately, which is a requirement for any analyses, such as searches for supersymmetric particles decaying into stable non-interacting particles. The muon detectors are intended to provide reliable identification and good resolution for momenta ranging from a few GeV up to 1 TeV, in order to allow for the observation of new particles, such as heavy gauge bosons W' and Z' , with masses in the TeV range and decaying to muons. The detector is designed to be capable of identifying very rare event signatures, in some cases corresponding to 14 orders of magnitude below the total pp cross section. As a result, stringent requirements on the trigger are imposed to provide high efficiency for physics processes of interest while rejecting backgrounds.

²The predominant decay mode for the Higgs in the mass range $m_H \lesssim 2m_Z$ is to hadrons, corresponding to a signal that suffers from large QCD backgrounds.

Detector Component	Design Resolution	η Coverage	
		Measurement	Trigger
Tracking	$\sigma_{p_T}/p_T = 0.05\% \oplus 1\%$	2.5	
EM Calorimetry	$\sigma_E/E = 10\%/\sqrt{E} \oplus 0.7\%$	3.2	2.5
Hadronic Calorimetry			
Barrel and Endcap	$\sigma_E/E = 50\%/\sqrt{E} \oplus 3\%$	3.2	3.2
Forward	$\sigma_E/E = 100\%/\sqrt{E} \oplus 10\%$	3.1 – 4.9	3.1 – 4.9
Muon Spectrometer	$\sigma_{p_T}/p_T = 10\%$ at $p_T = 1$ TeV	2.7	2.4

Table 3.2: ATLAS performance goals. The units for E and p_T are GeV, from [51].

Inner Tracker			Calorimeters				Muon Detectors				
Pixel	SCT	TRT	EM	LAr	HAD	FW	Tile	MDT	RPC	CSC	TGC
99.0	99.9	100	90.5	96.6	97.8	94.3	99.9	99.8	96.2	99.8	

Table 3.3: Relative detector uptime and good quality data delivered during stable beams, weighted by the luminosity. The percentages correspond to the 2010 pp collision runs at $\sqrt{s} = 7$ TeV between March 30th and October 31st. The inefficiencies in the calorimeters can be largely recovered in future data reprocessings.

The ATLAS installation campaign finalized in 2008 and the detector has been recording data ever since. The large datasets obtained have been invaluable in order to exercise the detector operation, including the trigger and data-acquisition chain, as well as to calibrate and align the sub-detectors. In particular, the data-taking and detector commissioning efforts in 2008 and 2009 using cosmic rays have allowed for a highly successful collision data-taking experience in 2010. The high efficiency maintained by all sub-detectors during stable beam collisions can be seen in Table 3.3.

3.2.1 Coordinate System

The origin of the ATLAS coordinate system is defined as the nominal IP, located in the geometrical center of the detector. The beam direction defines the z -axis, the x -axis points to the center of the LHC ring and the y axis points towards the surface, as a right-handed coordinate system. The detector is symmetric in positive and negative z , called sides A and C respectively. The azimuthal angle ϕ is measured in the $x - y$ plane around the beam axis, and the polar angle θ corresponds to the angle from the beam axis. The pseudorapidity is defined from θ as $\eta = -\ln(\tan \theta/2)$. In the case of objects with large mass, the rapidity is used $y = 1/2 \ln[(E + p_z)/(E - p_z)]$. The distance ΔR in the $\eta - \phi$ angle space is defined as $\Delta R = \sqrt{\Delta\eta^2 + \Delta\phi^2}$. Finally, it may be noted that the transverse momentum p_T , the transverse energy E_T and the missing transverse energy E_T^{miss} are defined in the transverse $x - y$ plane.

3.3 Inner Detector

The inner detector (shown in Figure 3.5) is comprised of high-resolution semiconductor pixel and strip detectors (SCT) in the inner part, covering the region $|\eta| < 2.5$, and straw-tube tracking detectors (TRT) in the outer part, covering the region $|\eta| < 2.0$. The 2 T magnetic field is provided by a superconducting solenoid magnet extending over a length of 5.3 m with a diameter of 2.5 m. The ID performs momentum and vertex measurements for charged particles.

The active tracking detector elements record the position of charged particles traversing it, and this information is used to reconstruct the particle's trajectory

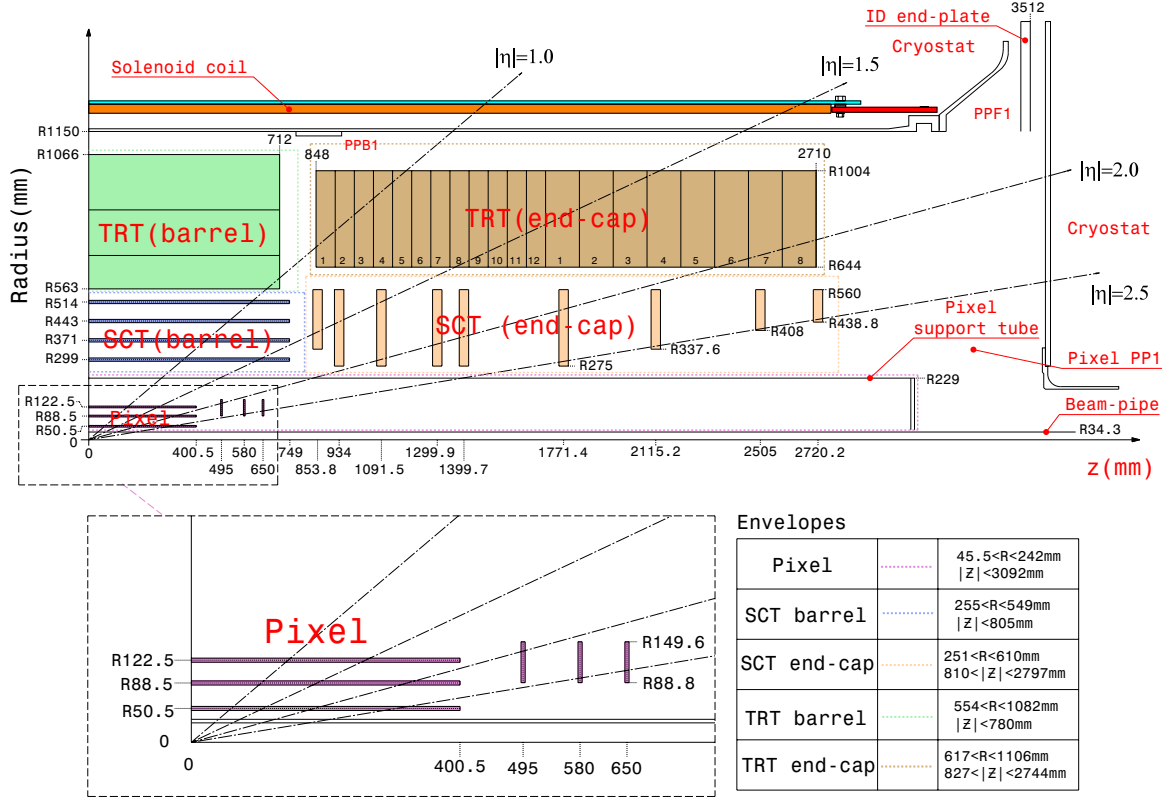


Figure 3.5: Schematic layout of the ATLAS inner tracker dimensions showing the pixels, the silicon strip tracker and the transition radiation tracker composed of straw tubes, from [51].

as a track. The charged particles bend in the presence of the magnetic field, and the radius of curvature determined by the tracking is used to derive the transverse momentum of the particle using the relation

$$p_T[\text{GeV}] = 0.3 \times B[\text{T}] \times R[\text{m}] \quad (3.4)$$

where B is the magnetic field and R the bending radius. The hit efficiency for the trackers is very high, about 99% in the silicon detectors, and typically about 3 pixel, 4 SCT and about 36 TRT measurements are provided per track. The limitations arise from the constraints imposed by the detector coverage and disabled detector modules.

3.3.1 Pixel Detector

The pixel modules are arranged around the beam axis in three concentric cylinders for the barrel region (at radii of 50.5, 88.5, and 122.5 mm) and in three disks (at $|z|$ positions of 495, 580 and 650 mm) for each endcap, providing coverage in the range $|\eta| < 2.5$. The pixels are the highest granularity sub-system and the innermost pixel layer is mounted on the beampipe in order to provide the best possible vertex resolution. Given the large radiation doses, it may be noted that the innermost layer is expected to survive five years at most, after which it is expected to be replaced in a detector upgrade campaign. The pixels are doped silicon detectors to which a bias voltage is applied. When a charged particle traverses the semiconductor, it creates sufficient electron-hole pairs to travel to the surface and produce a measurable signal.

The pixel detector is segmented in $R - \phi$ and z with size in $R - \phi \times z$ of $50 \times 400 \mu\text{m}^2$. Given the fine segmentation of the pixel modules, a traversing particle results in a signal in multiple contiguous pixels, forming “clusters”. Each track originating in the IP typically traverses three layers. The intrinsic spatial resolution is $10 \mu\text{m}$ ($R - \phi$) and $115 \mu\text{m}$ (z) in the barrel and $10 \mu\text{m}$ ($R - \phi$) and $115 \mu\text{m}$ (R) in the disks. The alignment constraints are $10 \mu\text{m}$ in R , $20 \mu\text{m}$ (barrel) or $100 \mu\text{m}$ (endcap) in z and $7 \mu\text{m}$ in $R - \phi$. The pixel detector has approximately 80.4 million readout channels, corresponding to close to 90% of the total number of ATLAS channels.

3.3.2 Semiconductor Tracker

The silicon strip tracker surrounding the pixel detector is arranged in four concentric cylinders for the barrel (at radii of 299, 371, 443, and 514 mm) and in six endcap disks on both sides of the IP (at $|z|$ positions of 890, 1091, 1350, 1771, 2115 and 2608 mm), also providing coverage in the range $|\eta| < 2.5$. The basic unit is a silicon strip with a mean pitch of $80 \mu\text{m}$, placed parallel to the beam in the barrel and radially in the endcap, thus providing a precision measurement in $R - \phi$. The barrel cylinders and the first, third and sixth endcap disks include “stereo-strips”, where a second module is attached to the first one at an angle of 40 mrad. These improve the resolution in the non-precision coordinate. A charged particle track typically traverses eight strip sensors corresponding to four space points. The intrinsic resolutions per module are $17 \mu\text{m}$ ($R - \phi$) and $580 \mu\text{m}$ (z) for the barrel and $17 \mu\text{m}$ ($R - \phi$) and $580 \mu\text{m}$ (R) for the endcap disks. The alignment constrains the position of the strips to be known to $100 \mu\text{m}$ in R , $50 \mu\text{m}$ (barrel) or $200 \mu\text{m}$ (endcap) in z , and $12 \mu\text{m}$ in $R - \phi$. The total number of readout channels in the SCT is approximately 6.3 million, of which about 0.97% were disabled in the 2010 pp collision runs.

3.3.3 Transition Radiation Tracker

The TRT surrounding the SCT is comprised of 4 mm diameter straw tubes that provide about 36 hits per track with coverage in the range $|\eta| < 2.0$. The tubes are placed parallel to the beam in the barrel region ($|\eta| < 1.0$) and radially in wheels in the endcap region ($0.8 < |\eta| < 2.0$), providing a measurement in $R - \phi$ with an intrinsic precision of $130 \mu\text{m}$ per tube. The alignment tolerance is $30 \mu\text{m}$. The tubes are filled

with a gaseous mixture of carbon dioxide and xenon and operate in a similar manner to the drift tubes used in the MS (see Section 3.5.2). Charged particles traversing the TRT also produce transition radiation that is used to distinguish between electrons and pions³. The total number of TRT readout channels is approximately 351,000.

3.4 Calorimeters

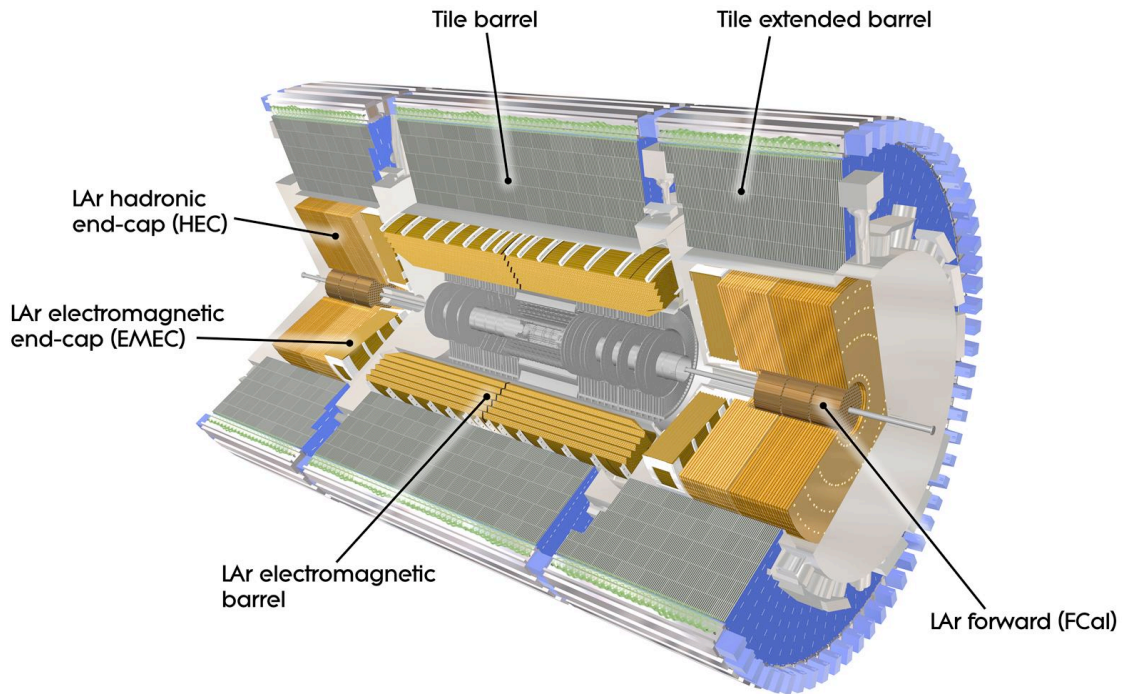


Figure 3.6: Overview of the ATLAS calorimeter system showing the electromagnetic calorimeter and the hadronic calorimeter, from [52].

³The TRT straws are surrounded with polypropylene fibers. Charged particles traversing into this material emit transition radiation (TR) photons with a probability proportional to the Lorentz factor $\gamma = E/m$. Electrons typically have larger γ than other particles such as pions and so the detection of TR photons is used for electron identification.

The ATLAS calorimeter system (shown in Figure 3.6) is comprised of multiple technologies that provide electromagnetic and hadronic energy measurements. The electromagnetic (EM) calorimeter is a liquid-argon (LAr) sampling calorimeter with high granularity covering the range $|\eta| < 3.2$. The calorimeter has over 22 radiation lengths (X_0) in the barrel and over 24 X_0 in the end-caps, allowing it to contain the showers of electrons and photons up to about 1 TeV and about 2/3 of most hadronic showers. The hadronic calorimeter comprises a scintillator-tile calorimeter with lead absorbers covering the central range $|\eta| < 1.7$ and LAr calorimeters with lead, copper or tungsten absorbers covering the endcap range $1.5 < |\eta| < 3.2$ (hadronic endcap calorimeter or HEC) and forward region which extends the coverage up to $|\eta| = 4.9$ (forward calorimeter or FCal). The depth of the hadronic calorimeters is about 9.7 interaction lengths (λ) of active calorimeter in the barrel and about 10λ in the endcaps, providing good resolution for high-energy jets. The presence of additional passive material (indicated by the last layer in Figure 3.7), increasing the thickness to over 11λ , greatly reduces punch-through to the MS, with levels below those from prompt and decay muons. The thickness and large η -coverage of the calorimeters provide a good measurement of the E_T^{miss} , which is important for many physics signatures including the measurement of W bosons.

In 2009 and 2010, the major challenges experienced by the LAr calorimeter have been the failure of the on-detector laser transmitters (OTXs) that transmit the signal from the calorimeter front-end electronics for a single cell to the data acquisition system. This impacts the readout data only and not the trigger that is issued using a separate readout system. In the case of the tile calorimeter some low voltage

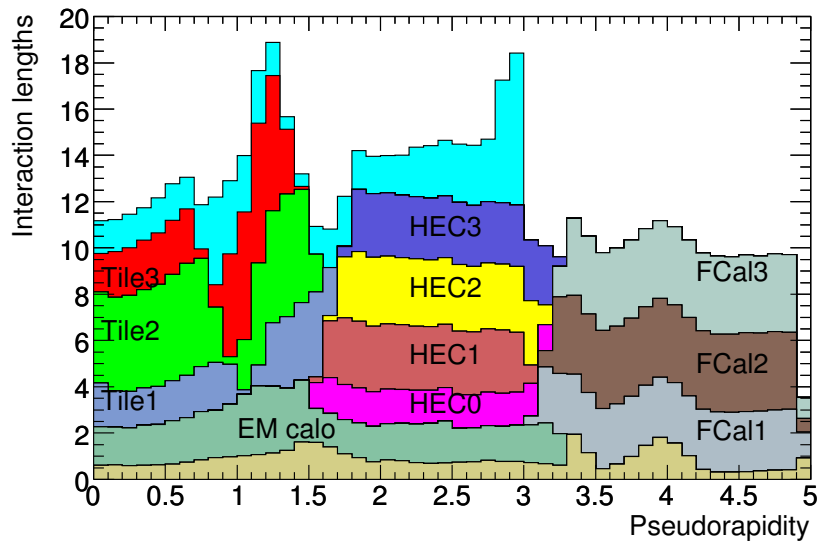


Figure 3.7: Cumulative amount of material as a function of $|\eta|$ in units of interaction length starting with the material in front of the electromagnetic calorimeters (light brown), in the electromagnetic calorimeters themselves, in each hadronic compartment, and the total amount at the end of the active calorimetry up to the first active layer of the muon spectrometer (for the range $|\eta| < 3.0$), from [51].

power supplies used for the front-end electronics failed, resulting in a loss of readout capability. Since most of the energy is deposited in the EM calorimeter, the impact of the few failed modules is relatively small. The overall availability was 90.5% for the LAr EM calorimeter, 96.6% for the LAr hadronic calorimeter, 97.8% for the LAr forward calorimeter and 94.3% for the tile calorimeter, as indicated in Table 3.3. In future data processings the trigger measurement can replace the energy deposit information from missing readout channels in order to recover the loss in coverage.

3.4.1 Electromagnetic Calorimeter

The EM calorimeter is a LAr detector with lead absorber plates in an accordion geometry that provides uninterrupted ϕ coverage. As particles traverse the calorime-

ter they ionize the LAr and the charge deposits are collected in the presence of an electric field by kapton electrodes mounted on the accordion plates. The calorimeter is divided into three regions: a barrel section covering the range $|\eta| < 1.475$ and an endcap and forward section on each side covering the ranges $1.375 < |\eta| < 3.2$ and $3.1 < |\eta| < 4.9$ respectively. The choice of LAr as the active detector medium is given by its intrinsic properties of linear behavior, stable response over time and radiation hardness. In order to maintain the argon in liquid state, it is cooled to about 87 K, so the calorimeters are located in cryostats composed of two concentric aluminium vessels, an inner cold vessel and an outer warm vessel. The barrel and endcap/forward calorimeters are enclosed in separate cryostats to allow access to the inner detector and space for services. Scintillators are installed in the region between the cryostats, but the range $1.37 < |\eta| < 1.52$ remains poorly instrumented, making the precise measurement of electrons and photons difficult. In order to minimize the amount of inactive material present, the solenoid magnet and the barrel EM calorimeter share the same vacuum vessel isolating the cryostat.

The thickness of the lead absorber plates is optimized for energy resolution performance, resulting in thicknesses of 1.53 mm for the range $|\eta| < 0.8$ and 1.13 mm for the range $|\eta| > 0.8$ in the case of the barrel, and 1.7 mm for the range $|\eta| < 2.5$ and 2.2 mm for the range $2.5 < |\eta| < 3.2$ for the endcap. In addition, the calorimeter is segmented in depth, with three sections for the range $|\eta| < 2.5$ and two sections in the rest of the endcap, where each section has increasingly coarser segmentation in $\eta - \phi$. Finally, it may be noted that there is significant material before the calorimeter, in the inner detector itself, corresponding to a thickness of about $1 - 4 X_0$, and in the

cryostat. A LAr presampler layer of 1.1 or 0.5 cm thickness in the barrel and endcap regions covering the range $|\eta| < 1.8$, is used to provide an additional shower sampling inside the cryostat, where significant energy is lost in the material before reaching the EM calorimeter.

3.4.2 Hadronic Calorimeter

Tile calorimeter

The hadronic calorimeter, surrounding the EM calorimeter, covers the range $|\eta| < 1.7$ and is comprised of scintillating tiles alternating with steel absorbers. As the shower traverses the tiles, scintillation light is produced and the light signal from the two sides of the tiles is collected by wavelength shifting optical fibers⁴ that transport it to photomultiplier tubes. The tile calorimeter is divided into a barrel region covering the range $|\eta| < 1.0$ and two endcaps covering the range $0.8 < |\eta| < 1.7$. The thickness of the rectangular scintillating tiles is 3 mm thick, oriented parallel to the beam and divided into 64 modules in ϕ , and the surrounding absorber is 4 – 5 mm thick. In the radial direction, the tile calorimeter, extending in radius from 2.28 m to 4.25 m, is segmented into three regions with about 1.5, 4.1 and 1.8 λ each for the barrel region and 1.5, 2.6, and 3.3 λ for the endcap region, with a total depth of 9.7 λ at $\eta = 0$. A steel yoke surrounding the tile calorimeter provides a support structure and the return for the solenoid field. The tile calorimeter is calibrated with Cesium sources installed throughout the active volume and with test laser pulses.

⁴Ionising particles traversing the tiles induce the production of ultraviolet scintillation light in the polystyrene material. The light is converted to the visible range with fluors that shift the wavelength so that it can be read out by optical fibers.

LAr hadronic end-cap calorimeter

The hadronic endcap calorimeter covers the range $1.5 < |\eta| < 3.2$ and is comprised of two wheels per side within the same cryostat as the endcap EM calorimeter. In order to increase the material coverage, the HEC overlaps with the tile calorimeter in the region $1.5 < |\eta| < 1.7$ and with the forward calorimeter in the range $3.1 < |\eta| < 3.2$. The front and back wheels made up of 24 copper plates of 25 mm thickness for the front wheel and 16 plates of 50 mm thickness for the wheel further away, with LAr as the active medium filling the 8.5 mm gaps between the plates. Each wheel is divided into 32 wedge sections in ϕ and in two sections in depth, providing 4 independently read out segments in total.

LAr forward calorimeter

The forward calorimeter covers the range $3.1 < |\eta| < 4.9$ and is comprised of one EM and two hadronic components, enclosed in the endcap cryostats. The active material is LAr and the absorber is copper for the first EM module and tungsten for the two subsequent hadronic modules. The modules are made up of copper or tungsten plates held together in a matrix by regularly spaced rods inside tubes of the same material that are placed parallel to the beam. The gaps between the rods and tubes, of size 0.269, 0.376 and 0.508 mm in each of the sections, are filled with LAr and the ionization signal is readout from the rods. Overall, the FCal has about 10λ of depth.

3.5 Muon Spectrometer

The muon spectrometer (MS) [55, 51, 56] is designed to provide a precise stand-alone measurement of the muon momentum and a momentum-selective trigger down to a few GeV. The air-core toroid magnet system, comprised of a barrel and two endcap magnets, provides a field integral in the range 2 – 8 Tm for the detector region $|\eta| < 2.7$. The superconducting coils comprising the toroid are arranged in eight-fold symmetry around the calorimeters. The field integral at two azimuthal angles as a function of $|\eta|$ is shown in Figure 3.8. The magnetic field provides good field integral up to $\eta \sim 2.6$ and poor coverage in the range $\eta \sim 1.4–1.6$, corresponding to the transition region between the barrel and endcap fields, where the fields largely cancel each other out.

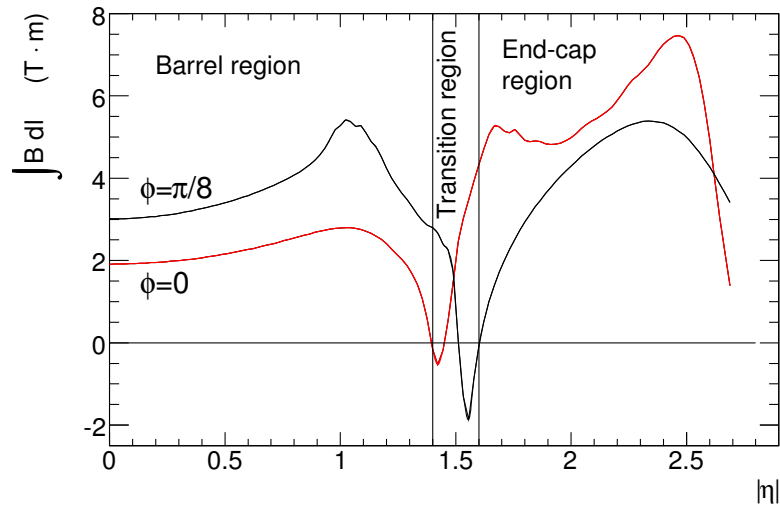


Figure 3.8: Field integral for the toroidal magnets as a function of absolute pseudorapidity $|\eta|$ for one octant of the toroid, corresponding to azimuthal angles $\phi = 0$ (red) and $\phi = \pi/8$ (black), from [51].

3.5.1 Chamber Layout

The layout of the MS, including an $x-y$ view of the barrel region and an $R-z$ view of a quadrant is shown in Figure 3.9. The muons typically traverse three chamber stations positioned along their trajectory from the IP. The momentum is determined from the sagitta of the track curvature as the particle bends in the magnetic field. Monitored Drift Tube (MDT) chambers cover most of the acceptance, where the wires are positioned parallel to the magnetic field, in order to provide a measurement in the precision or bending coordinate (z in the barrel and R in the endcap). In the region $|\eta| > 2.0$, the precision measurement in the innermost layer is provided by Cathode Strip Chambers (CSC) that have higher rate capability and improved time resolution.

In the barrel region, the three chamber layers form coaxial cylinders, while in the endcap region they form disks centered along the beam axis. The three stations are called “Inner”, “Middle” and “Outer”, with their increasing distance from the IP. For the barrel these are referred to as BI (radius $R \sim 5$ m), BM ($R \sim 7.5$ m) and BO ($R \sim 10$ m) and for the endcap as EI ($|z| \sim 7.4$ m), EM ($|z| \sim 14$ m) and EO ($|z| \sim 21.5$ m). The MS is divided into 16 sectors in the $x-y$ or ϕ plane, with 8 “large” sectors (odd numbers) and 8 “small” sectors (even numbers) that alternate the coverage in ϕ , as can be seen in Figure 3.9.

The input to the first level of muon trigger (see Section 3.6.2), based on the selection of muons pointing to the IP with p_T above a programmable threshold, is provided by fast tracking detectors. The trigger technologies have good time resolution for

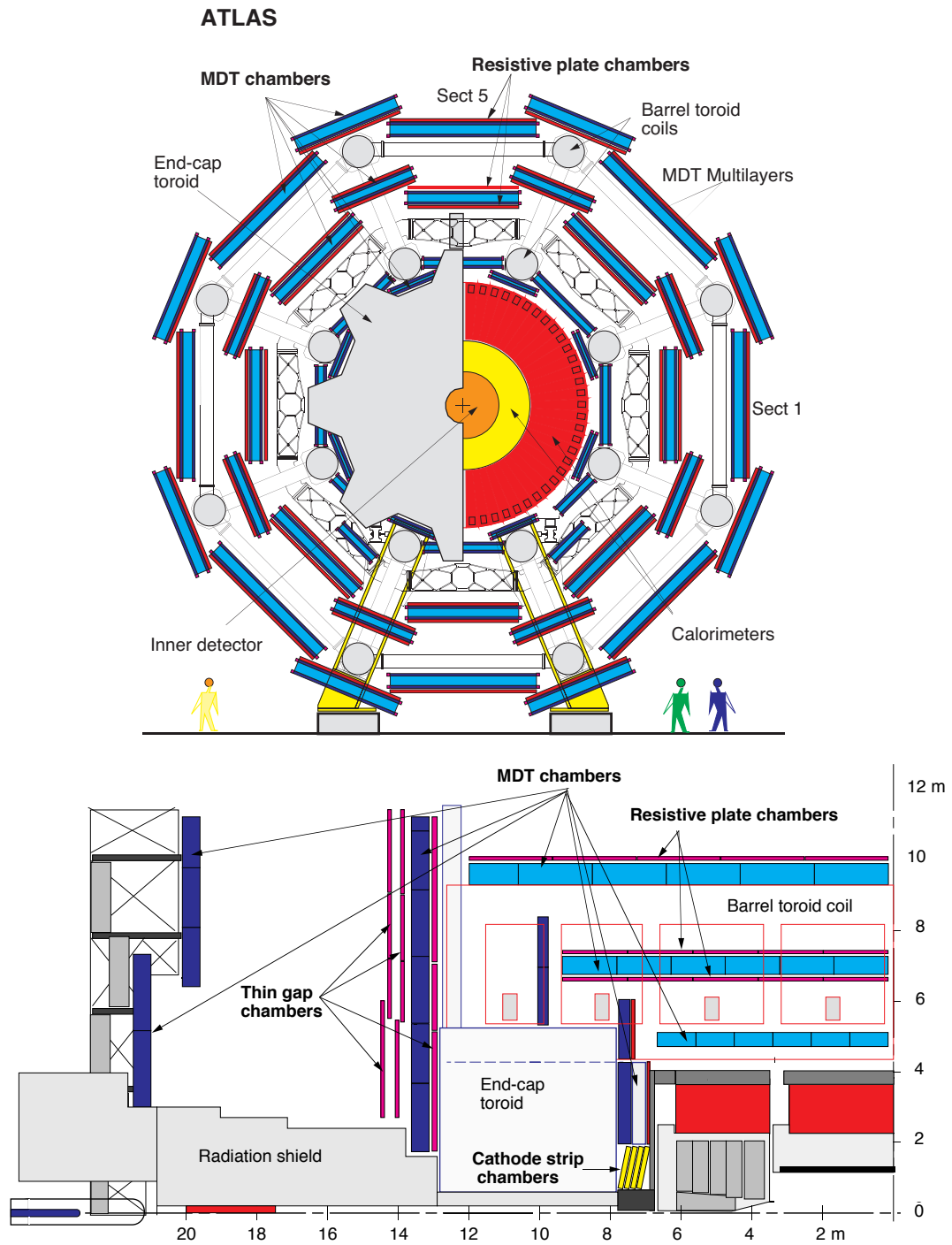


Figure 3.9: Overview of the ATLAS muon spectrometer system, from [55].

bunch-crossing identification and also provide measurement of the non-precision ϕ coordinate, along the MDT wire, with a resolution of 1 cm. Resistive Plate Chambers (RPC) cover the barrel region ($|\eta| < 1.05$) and Thin Gap Chambers (TGC) cover the endcap region ($1.05 < |\eta| < 2.4$ for the trigger and $1.05 < |\eta| < 2.7$ for the readout). Two RPC chambers surround each MDT BM chamber, providing the low- p_T trigger, while a third chamber, mechanically attached to the MDT BO chamber, provides additional information for the high- p_T threshold triggers. In the case of the TGCs, seven detector layers arranged in order from the IP into one triplet and two doublets surround the MDT EM layer, providing the high- p_T and low- p_T threshold triggers. Another layer of TGC chambers is located next to the MDT EI layer to provide an additional measurement of the non-precision or second coordinate, but is not used in the trigger.

3.5.2 Monitored Drift Tubes

A typical MDT chamber, composed of two multilayers (ML) of three or four layers of tubes, is shown schematically in Figure 3.10. The chambers are rectangular in the barrel region and trapezoidal in the endcaps. The dimensions vary depending on the position, in order to maximize coverage. All drift tubes, made of an aluminum encasing, are 30 mm in diameter, with a gold-plated tungsten anode wire of 50 μm in diameter set at a voltage of 3080 V running along the center. The tubes are filled with a gaseous mixture of argon (93%), carbon dioxide CO_2 (7%) and a trace of water vapor held at a pressure of 3 bar. The 1,150 MDT chambers (656 in the barrel and 494 in the endcap) comprise 354,000 tubes and cover an area of 5,500 m^2 . It may

be noted that in 2010, all chambers were operational except for some EE chambers, since 10 out of 62 have been installed to date.

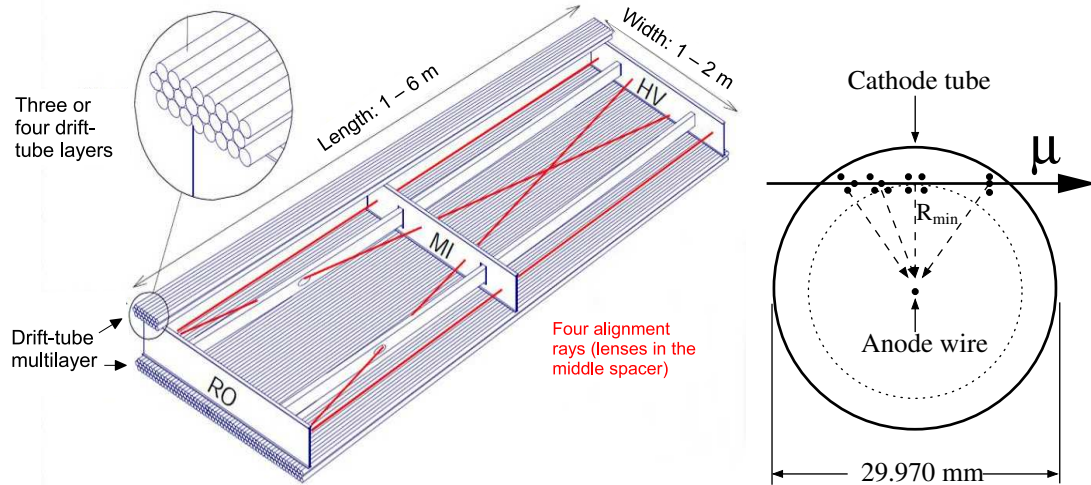


Figure 3.10: Mechanical structure of a MDT chamber (left). Three spacer bars connected by longitudinal beams form an aluminium space frame, carrying 2 multi-layers of 3 or 4 drift tube layers. Four optical alignment rays, two parallel and two diagonal, allow for monitoring of the internal geometry of the chamber. RO and HV designate the location of the readout electronics and high voltage supplies, respectively. A cross section of an MDT tube (right), shows the process of electron-ion pair formation. The drift circle is indicated by the dashed circle. From [51].

The operating principle of the drift tube, where a traversing muon ionizes the gas mixture, is shown in Figure 3.10. The electrons drift to the center and create an avalanche in the high-field region close to the wire, resulting in a measurable signal. Each track creates a sequence of pulses corresponding to the charge deposits along the particle trajectory. However, the electronics are configured to measure the time at which the first electrons arrive at the wire, the drift time, corresponding to the closest cluster. The operating gas was selected mainly because of its good aging properties, but poses the disadvantages of a large drift time, about 700 ns, and a

non-linear behavior in the space-drift time relation. The drift velocity for the MDT configuration is about $20.7 \mu\text{m}/\text{ns}$ on average and exhibits a strong dependence on the radius. The drift time is translated into a distance corresponding approximately to the point of closest approach of the muon to the wire, the drift radius.

A drift time spectrum for tubes in an MDT chamber, corresponding to the output provided by the MDT electronics (see Section 3.5.6), and a radius-to-drift time relation, $r - t$ relation, for an MDT chamber, are shown in Figure 3.11. The spatial resolution of the MDT tube is limited by the knowledge of the start time t_0 , corresponding to when a muon track traverses the wire of the tube and the $r - t$ relation. The t_0 depends on the time of flight, the trigger timing and the cable lengths, while the $r - t$ relation depends on parameters such as the temperature, the pressure, the magnetic field and the hit rate in the tube. The calibration of these parameters is performed continuously.

The average spatial single tube resolution is about $80 \mu\text{m}$, whereas at the chamber level the best achievable resolution is about $40 \mu\text{m}$ and about $35 \mu\text{m}$ for chambers with six and eight layers of tubes respectively. The performance goal of the MS is to measure the curvature of muons up to 1 TeV with a precision better than 10%. This requires the alignment of the chambers to be known within about $30 \mu\text{m}$. An optical alignment system that continuously monitors the positions and deformations of the MDT chambers is therefore used. The system is comprised of about 12,000 optical sources and cameras, including an in-plane system made up of four optical alignment rays (see Figure 3.10) to monitor chamber deformations and optical lines to monitor

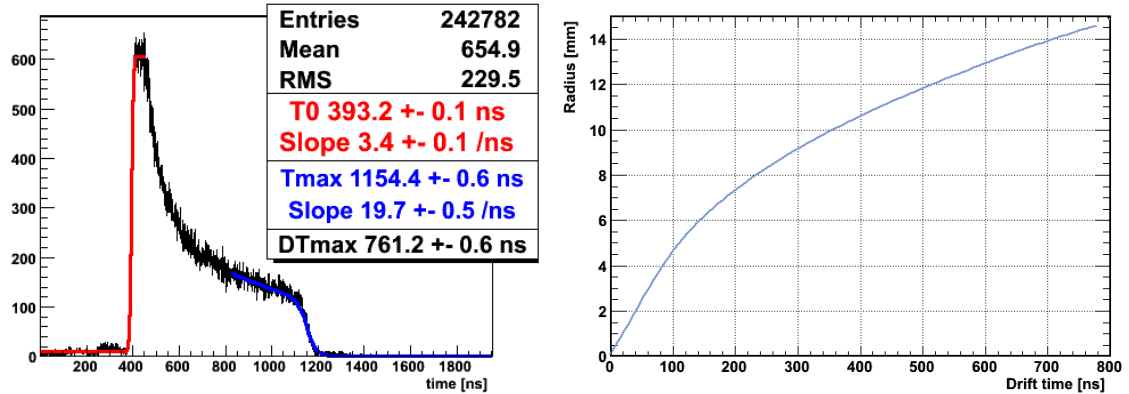


Figure 3.11: Example of chamber-level time spectra (left) from collision muon events. The shape is formed from muons from many events traversing multiple tubes in the chamber. The rise of the time spectrum corresponds to the initial time t_0 and the width to the fact that muons can pass through a tube at either a large or small distance from the wire. Example of an $r - t$ relation (right) derived from a gas monitoring chamber for a particular date and modified according to the temperature, pressure and magnetic field of the specific chamber. From [57].

the projective alignments between chambers.

3.5.3 Cathode Strip Chambers

The CSC chambers are multiwire proportional chambers based on a cathode strip read out. When the muon traverses the chamber, electron-ion pairs are created in the gas, and a signal is measured from the charge induced in the strips. The charge information from adjacent strips is interpolated, combining them into a signal that provides a spatial resolution of about $50 \mu\text{m}$ in the radial coordinate and about 5 mm in ϕ . The technology allows for fast signal readout, with a time resolution of 7 ns. The CSC chambers have 30,700 readout channels.

3.5.4 Resistive Plate Chambers

An RPC chamber is composed of two plates of resistive material (plastic laminate), placed 2 mm apart and filled with a mixture of $C_2H_2F_4$ /Iso- C_4H_{10} / SF_6 gas in the proportions (94.7/5/0.3)%. A muon traversing the plates experiences an average electric field of 4.8 kV/mm in the 2010 operating conditions, creating an avalanche that is read out by two metallic strips mounted on the resistive plates. Two layers of strips are placed orthogonally, providing a measurement in both the z and ϕ coordinates, with a spatial resolution of about 10 mm. The time resolution is 1.5 ns, allowing for good bunch-identification. It may be noted that in the range $|\eta| < 1.05$, the geometrical coverage of the RPC chambers in $\eta - \phi$ is about 80% due to spatial constraints in the middle chamber layer, particularly from gaps for services and support structures of the toroid magnets, and the “feet” at the base of the detector. The total number of RPC channels is 359,000.

3.5.5 Thin Gap Chambers

The design of the TGC chambers is driven by a need for a finer granularity compared to that afforded by the RPC chambers, in order to withstand higher rates and to achieve the same p_T resolution as in the barrel⁵. A TGC chamber is also a multi-wire proportional chamber comprised of anode wire planes, cathode planes and strip planes held together by honeycomb support structures. The chamber is filled with a highly-quenching gas mixture of CO_2 and n- C_5H_{12} (n-pentane). The anode-cathode

⁵The muon momentum corresponding to a particular p_T increases strongly with η . Even though the magnetic field is stronger in the forward region, it is insufficient to compensate for the momentum dependence in η .

distance is smaller than the distance between adjacent anode wires and the electrodes are held at a potential of 3.1 kV, ensuring fast signal generation. The anode wires are placed parallel to the MDT tubes, while the cathode strips are arranged radially providing a ϕ measurement. The geometrical coverage of the trigger in the endcaps is about 99%. The spatial resolution of the TGCs is 2 – 6 mm in R and 3 – 7 mm in ϕ (depending on R) and the timing resolution is 4 ns. The total number of TGC channels is 318,000.

3.5.6 Overview of MDT Readout Electronics

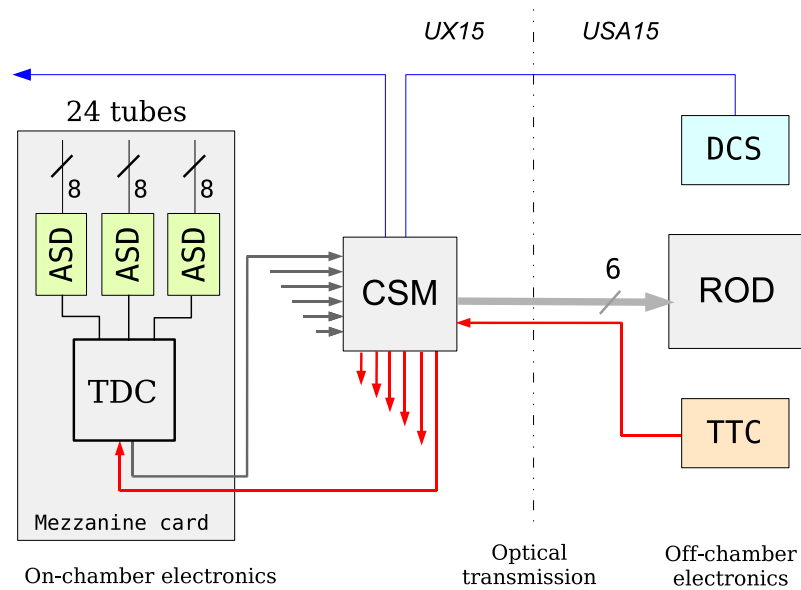


Figure 3.12: The MDT readout electronics scheme, from [51].

The MDT readout electronics scheme is shown in Figure 3.12 (see [58] for details). The raw signal from 24 drift tubes is routed to the mezzanine cards where it is

amplified and discriminated by Amplifier/Shaper/Discriminator (ASD) chips, and then digitized by a Time-to-Digital Converter (TDC) chip. Time measurements, measured in units of the Timing, Trigger and Control (TTC) clock of 40.08 MHz, are stored for the leading and trailing edges of the incoming signals, along with tube identification information, in a buffer memory. Each MDT chamber is comprised of up to 18 mezzanine cards, depending on its size, and these are readout through the Chamber Service Module (CSM), which is configured via the detector control system (DCS). The CSM is connected via two optical fibers to the TTC distribution box and the MDT Readout Driver (MROD), as shown in Figure 3.12. The data-taking sequence follows a level-1 trigger, whose accept signal is sent by the TTC to the CSM, which in turn routes it to the mezzanine cards. The data are sent to the MROD, a VME module located in the USA15 service cavern. The main goal of the MROD is to assemble the data of up to 6 CSMs and send it to the Readout Buffers (ROB). The remaining sequence, part of the central ATLAS data acquisition system, is described in Section 3.6.

3.6 Trigger and Data Acquisition

The Trigger and Data Acquisition (TDAQ) systems are designed to record approximately 200 Hz of the LHC's design 40 MHz bunch-crossing rate. An overview of the TDAQ system is shown in Figure 3.13. The trigger system has three levels: the first level (L1) is based on limited hardware information from the calorimeters and the MS, while the second (L2) and third (EF) levels (collectively called the High Level Trigger or HLT) are based on software and use increasing amounts of information from the

full detector. The trigger checks each bunch-crossing for certain programmed conditions (triggers), and at each subsequent level refines the decision of the previous level by applying progressively more selective criteria. The L1 trigger provides a decision in $< 2.5 \mu\text{s}$, reducing the output rate to $< 75 \text{ kHz}$. Upon a L1 trigger accept, the data acquisition system receives the data from each sub-detector and stores it in buffers. The data acquisition system moves data for processing and additionally allows for the configuration, control and monitoring of the hardware and software units that provide the data-taking functionality. After the final trigger decision is made, the data is written out to disk at a nominal rate of about 200 Hz with an event size of 1.3 Mbyte . In pp collision running in 2010, the output rate was about 300 Hz , exceeding the nominal rate.

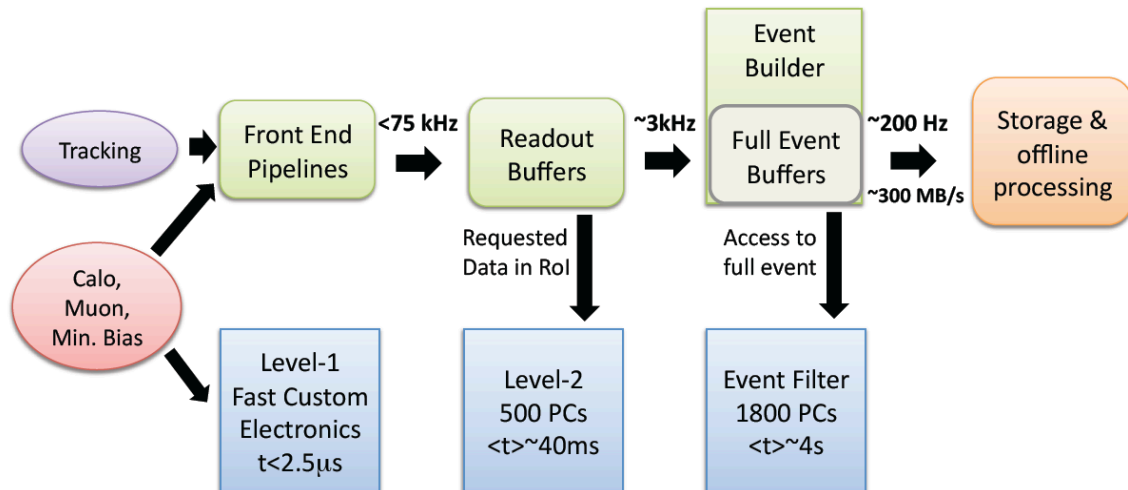


Figure 3.13: Overview of the TDAQ system showing the nominal parameters.

3.6.1 Trigger System Overview

The triggers apply criteria designed to identify physics signatures such as high- p_T electrons, photons, muons, taus, jets (including heavy flavor jets), missing transverse energy E_T^{miss} and large summed energy $\sum E_T$. The L1 trigger is based on information from a subset of the detectors. The muon trigger uses trigger chamber information from the barrel and endcap regions of the MS. The calorimeter triggers use coarse information from all calorimeter components. The L1 muon and calorimeter triggers are processed by the Central Trigger Processor (CTP) that additionally implements a trigger “menu” that includes combinations of trigger selections. The trigger menu is reconfigured over time in order to optimize the use of the available bandwidth as the luminosity and background conditions change.

Data from events satisfying the L1 trigger are transferred to the data acquisition system for further processing. The L1 defines at least one Region-of-Interest (RoI) corresponding to a region of the detector in $\eta - \phi$ where the trigger has identified interesting features (e.g. a high- p_T muon candidate). The full granularity and precision detector information associated with the RoI is used by the L2 to further refine the selection (about 2% of data), reducing the rate to about 3.5 kHz, with an average event processing time of about 40 ms. Finally, the EF uses the same procedures as for offline analysis to reduce the final rate to about 200 Hz, with an average event processing time of about 4 s.

In the 2010 runs, the LHC peak instantaneous luminosity increased from $10^{27} \text{ cm}^{-2}\text{s}^{-1}$ to $2 \times 10^{32} \text{ cm}^{-2}\text{s}^{-1}$. In the first phase of the pp collisions in 2010, when the instanta-

neous luminosity was low ($\mathcal{L} \sim 10^{27} \text{ cm}^{-2}\text{s}^{-1}$), triggers on inelastic collisions provided by the Minimum Bias Trigger Scintillators⁶ were used. Specialized commissioning trigger menus were deployed, recording events passing the L1 and minimum bias triggers. This data served to commission the HLT, allowing for checks of the correct functionality of the algorithms. As luminosity increased and trigger output rates approached the limits imposed by offline processing, the HLT started actively rejecting events from the highest rate L1 triggers ($\mathcal{L} \sim 1.2 \times 10^{29} \text{ cm}^{-2}\text{s}^{-1}$). For the remaining period of running ($10^{30} \text{ cm}^{-2}\text{s}^{-1}$ – $10^{32} \text{ cm}^{-2}\text{s}^{-1}$), the trigger menu implemented moved away from commissioning and was more oriented towards physics. The allocated bandwidth for the different trigger types for three different instantaneous luminosities are listed in Table 3.4, showing a progressive decrease in the bandwidth for the commissioning and minimum bias triggers and an increase in the lepton triggers.

Trigger Signature	Luminosity [$\text{cm}^{-2}\text{s}^{-1}$]	10^{30}	10^{31}	10^{32}
		Rate [Hz]	Rate [Hz]	Rate [Hz]
Minimum bias		20	10	10
Electron/Photon		30	45	50
Muon		30	30	50
Tau		20	20	15
Jet and forward jet		25	25	20
b -jet		10	15	10
B -physics		15	15	10
$E_{\text{T}}^{\text{miss}}$ and $\sum E_{\text{T}}$		15	15	10
Calibration triggers		30	13	13

Table 3.4: Guidelines for bandwidth allocation for various trigger groups normalized to about 200 Hz EF output rate at three luminosity points.

⁶The Minimum Bias Trigger Scintillators (MBTS) consist of two scintillator wheels mounted in front of the EM endcap calorimeters. Triggers on inelastic events are issued based on requirements for MBTS counters above threshold.

3.6.2 Muon Trigger

The L1 muon trigger is provided by a hardware-based system that selects muon candidates and identifies the corresponding bunch-crossing by processing information from the fast muon trigger detectors: RPCs in the barrel ($|\eta| < 1.05$) and TGCs in the endcap ($1.05 < |\eta| < 2.4$). The main requirement imposed is a p_T threshold that ranges from 6 to 40 GeV. The architecture allows for up to 6 thresholds to be defined, separated into 3 low- p_T thresholds with p_T range 4 – 10 GeV and 3 high- p_T thresholds with $p_T > 10$ GeV.

A schematic overview of the muon L1 trigger is shown in Figure 3.14. The RPCs and TGCs use a coincidence condition in η and ϕ in two or three trigger chambers⁷, depending on the p_T of the track. The trigger logic starts with a hit in the “pivot” plane (RPC2 or TGC3) and searches for hits in the low- p_T plane (RPC1 or TGC2) in a defined “trigger road” associated to the same bunch-crossing. A trigger road is essentially an $\eta - \phi$ region that contains the trajectories of muons traveling from the IP with p_T above a particular threshold.

If a corresponding hit coincidence is found, based on hits in at least three out of the four trigger detector layers in η and ϕ , a low- p_T trigger is issued. The logic then searches for additional hit coincidences in the third high- p_T plane (RPC3 or TGC1), checking for at least one additional hit in the case of the RPC and one ϕ hit and two out of three η hits for the TGC. If the coincidence requirements are satisfied,

⁷All RPC chambers (RPC1, RPC2 and RPC3) are comprised of two detector layers, providing up to four measurements in η and ϕ . This is also the case of TGC2 and TGC3 (doublets). The chambers in TGC1 provide up to two measurements in ϕ and three in η (triplet).

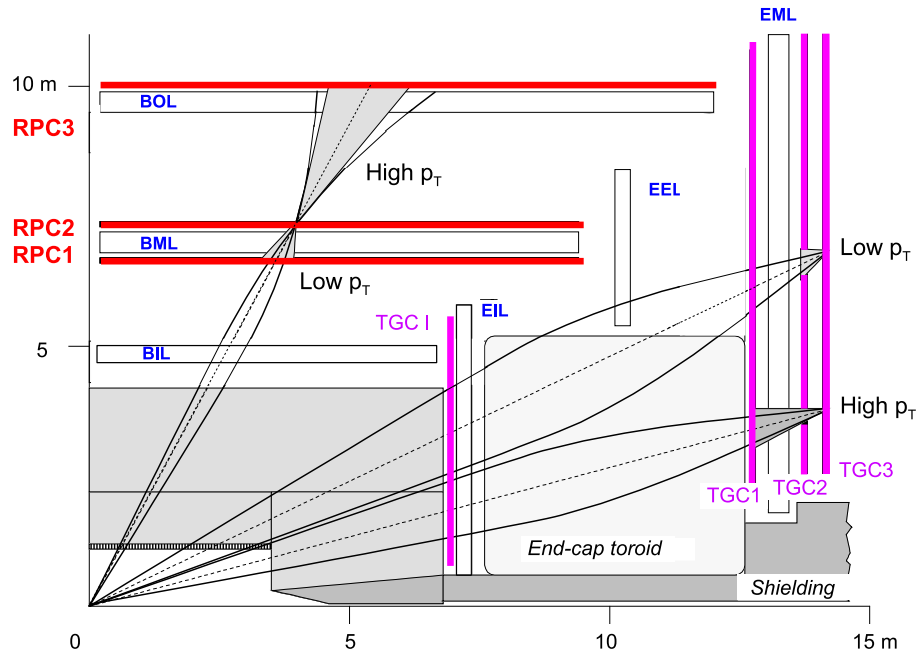


Figure 3.14: Overview of the ATLAS muon trigger system. The triggering schemes for high- p_T and low- p_T tracks are indicated, from [51].

a high- p_T trigger is issued. The coincidences in η and ϕ are issued separately, and combined to produce the final RPC or TGC trigger result. Overlaps between the RPC and TGC triggers are subsequently addressed in additional trigger logic in the CTP.

The L1 muon trigger was commissioned with muons from cosmic rays, though the first muons from collisions have been particularly important to validate the trigger roads and the timing. In the first 2010 collision runs, special commissioning trigger configurations were implemented, imposing the loosest possible geometrical requirements ($\eta \times \phi \sim 0.1 \times 0.1$) in order to maximize the acceptance. These datasets served to validate the p_T thresholds.

In addition, the timing, dependent on the signal delays from the muon time-of-flight, the signal propagation in the detector and electronics, and the overall trigger latency, was aligned to ensure the identification of the correct bunch-crossing. The timing of the TGCs is performed with calibration pulses. However, in the case of the RPCs, the timing relies on data, requiring a relatively large sample of collision muons. As a result, in the early stages of data-taking, CTP configurations allowing for up to three bunch crossings to be considered in the muon trigger were used, in order to avoid data-losses. By the end of September 2010, both systems were successfully timed-in to within one bunch crossing for both high- p_T and low- p_T triggers.

3.6.3 Data Acquisition

The data acquisition system works together with the trigger and is tasked with the movement of data from the detector to mass storage. When a L1 trigger accept is issued, the data from the front-end pipelines are transferred to the Read Out Drivers (ROD). The RODs, which are specific to each sub-detector, gather the data from several front-end streams, buffering and multiplexing it, formatting it to conform to the general ATLAS format, and subsequently sending it to the Readout Buffers (ROB). Subsets of the data, associated with the RoIs, are requested by the L2 trigger and sent to a L2 processing farm. The events accepted by the L2 are sent to the Event Builder and subsequently the EF decision is made. If an event is accepted, it is transmitted for permanent storage at the CERN computer center.

Chapter 4

Muon Reconstruction and Performance Studies with Cosmic Rays

Cosmic ray data collected in ATLAS during 2008 and 2009 served to commission the various sub-detectors in terms of operation, readout and trigger, as well as the general data acquisition and detector control systems. The installation of the muon spectrometer detector was finalized during this period with coverages of over 90% for all technologies, particularly over 99% for the MDTs and up to 95% for the RPC in Spring 2009. The large samples acquired, with many millions of events, allowed for a characterization of the spectrometer performance and served as excellent preparation for collision data-taking.

As described in [59], detailed studies of the detector coverage and efficiency, calibration and relative timing of the trigger chambers and MDTs, alignment, data quality, track reconstruction and resolution have been performed. The efficiency and resolution at the level of the detector unit for MDTs, TGCs and RPCs was found to agree with previous measurements from muon testbeams. In addition, the data acquired with magnetic field, provided the first opportunity to study the efficiency and resolution of tracks traversing multiple detector elements in their final configuration.

This chapter briefly introduces the track reconstruction algorithms in the muon spectrometer and describes the performance studies with cosmic ray data in the context of a measurement of the muon charge ratio. The relative detector acceptance and muon reconstruction efficiency are measured for positive and negative tracks in order to correct for a large charge bias introduced by the detector configuration. In addition, the performance of the muon reconstruction of cosmic rays is studied, measuring the momentum scale and resolution, and assessing the impact on the momentum dependent charge ratio. The results presented here are in agreement with past measurements of the charge ratio in cosmic rays by other experiments [60] over a wide range of muon momenta and extend these results in the intermediate-momentum region. This measurement was part of the effort to commission the muon spectrometer in order to maximize its capabilities prior to the availability of collisions.

4.1 Muon Reconstruction Overview

The goal of the muon reconstruction is to identify muons and measure their properties with high precision, particularly the position and momentum, for a wide range of momenta from a few GeV to a TeV. Tracks are defined in terms of five parameters typically at the perigee, i.e. the point of closest approach of the track to the z -axis. These parameters are the transverse d_0 and longitudinal z_0 coordinates, the polar θ_0 and azimuthal ϕ_0 angles and the inverse momentum signed by the charge of the track q/p . Two different packages are available to perform the MS track reconstruction, MOORE [61] and Muonboy [62]. The general strategy of the two algorithms is to reconstruct the trajectories at the chamber level, forming straight line segments, since over short distances the bending effects are small. Segments from at least two chambers are combined and refit into a full track at the spectrometer level. The fitting accounts for bending in the magnetic field and multiple scattering due to the presence of material.

The MOORE algorithm constructs roads of hits using a Hough transform in the bending and non-bending planes. Straight line segments are formed from at least three hits on MDT chambers in the precision coordinate and trigger hits are associated with the segments for non-precision coordinate information. Segment patterns are then formed using another Hough transform, and a track is then fit to the hits (at least six MDT hits). The Muonboy algorithm is conceptually similar, though differs in the details. The algorithm first identifies Regions of Activity (ROA) based on the information provided by the RPC and TGC measurements and segments are recon-

structed in the ROA. Track candidates are subsequently formed from combinations of segments from different stations and finally a global fit is performed.

4.2 Muon Charge Ratio in Cosmic Rays

Cosmic rays incident at the Earth's atmosphere undergo atomic collisions and produce showers of secondary particles that propagate down to the Earth's surface. The interaction products include significant amounts of charged pions and kaons that decay into muons, which are the dominant charged particles at ground level. The mean energy of cosmic muons at the Earth's surface is about 4 GeV. Muons can further penetrate through rock, reaching significant depths underground. Multiple measurements of cosmic muons have been performed on the ground at different altitudes and in the atmosphere from airplanes and balloons [60]. Models of cosmic ray interaction in the atmosphere have been developed to interpret experimental data. These studies aim to characterize the energy spectrum and composition of the primary flux of cosmic rays and to understand important processes for particle and astro-particle physics such as the production of atmospheric neutrinos at high energy.

The charge and momentum spectra of the muons reaching the Earth's surface are determined by the production mechanism for charged mesons in the collisions in the atmosphere. Since both cosmic rays and air include more positively charged particles, positive meson production is favored. The excess of positive muons from the showers is directly related to the ratio of positive to negative mesons produced [63]. Since the charged pion is longer lived than the kaon, it is more likely to have hadronic

interactions, losing energy, and so the decay muons tend to have lower momenta. Therefore the higher momentum spectrum probes more of the kaon component of the primary shower. In addition, the showers produce more positive than negative kaons, compared to the case of positive and negative pions, since the K^+ has more production modes than the K^- . The strange quark in the kaon is pair-produced and in the case of K^+ an associated lambda can be produced, which is not the case for K^- . As a result, the observed charge ratio is expected to rise as a function of muon momenta, as seen in this and previous results.

The muon charge ratio, defined as the ratio of positive to negative muons R^μ at the Earth's surface, has been extensively studied in the past by a variety of experiments [64, 65, 66, 67]. A recent measurement from the L3 collaboration reveals a flat value for the sea-level charge asymmetry at 1.285 with an accuracy of about 10% in the range 20 – 500 GeV [67]. At lower momenta, geomagnetic and solar effects play a significant role ($\sim 10\%$). The measured charge asymmetry drops to the 1.1 range at 1 GeV. A summary of available results ranging up to the 1 TeV scale can be found in [60] and for older summaries see [68, 69]. Some measurements of cosmic muons have been conducted underground, such as those performed with the L3 detector, which require a calculation of the energy loss through the Earth [60]. The muon flux decreases with depth as the energy threshold increases. The rate of cosmic muons in the ATLAS cavern is a few Hz/m², depending strongly on the location. The measurement of the muon charge ratio serves to study properties of cosmic rays, such as its primary mass composition, and has implications for neutrino physics, providing information of phenomena like the atmospheric neutrino anomaly.

4.2.1 Analysis Techniques and Measurement Outline

The muon spectrometer was designed for collisions and the cosmic ray data present important differences. In particular, tracks do not point to the interaction point, they traverse the top half of the detector in the “wrong” direction and they are not in time with the clock. The standard ATLAS event reconstruction has been adapted to reconstruct cosmic ray events with improved resolution and higher efficiency. Two major challenges associated with the studies presented here are the fact that the muon spectrometer acceptance is asymmetric for the two muon charges and that the detector was being commissioned. In addition, there was also a lack of appropriate Monte Carlo simulation, covering the full acceptance of the spectrometer, that accounts for the correct response of the muon chambers to cosmic rays and estimates the impact of the decay and energy loss of muons traversing the rock above the detector cavern as well as the shafts connecting the underground area to the surface. To address these challenges, a variety of data-driven techniques are introduced for this measurement, in order to estimate the acceptance and efficiencies for cosmic ray muons.

The measured charge ratio is given by

$$R_m^\mu = \frac{N_m^+}{N_m^-}, \quad (4.1)$$

where N_m^\pm are the measured number of positive and negative muon tracks respectively, and the measured ratio can be related to the true charge ratio as

$$R_m^\mu = \frac{N_m^+}{N_m^-} = \frac{N_t^+ \times A^+ \times T_{\text{eff}}^+ \times R_{\text{eff}}^+ \times S_{\text{eff}}^+}{N_t^- \times A^- \times T_{\text{eff}}^- \times R_{\text{eff}}^- \times S_{\text{eff}}^-}, \quad (4.2)$$

where $A^\pm, T_{\text{eff}}^\pm, R_{\text{eff}}^\pm, S_{\text{eff}}^\pm$ are the acceptance, trigger efficiency, tracking reconstruction efficiency, and selection efficiency of positive and negative muon tracks respectively.

Rearranging the equation and solving for the true muon track ratio yields

$$R_t^\mu = \frac{N_t^+}{N_t^-} = \frac{N_m^+ \times A^- \times T_{\text{eff}}^- \times R_{\text{eff}}^- \times S_{\text{eff}}^-}{N_m^- \times A^+ \times T_{\text{eff}}^+ \times R_{\text{eff}}^+ \times S_{\text{eff}}^+}. \quad (4.3)$$

In order to measure the charge ratio, the selection and tracking reconstruction efficiencies are measured using data-driven techniques and corrected for positive and negative tracks separately. The acceptance and muon trigger efficiency for positive and negative tracks are not calculated directly. Instead the charge-asymmetric nature of the spectrometer acceptance and trigger are corrected, bringing the terms A^-/A^+ and $T_{\text{eff}}^-/T_{\text{eff}}^+$ in the previous equation to unity. Finally the momentum is corrected to the surface for energy loss in the rock above the ATLAS cavern.

4.3 Dataset and Reconstruction Configuration

The data sample used for these studies is comprised of about five million events from a run in June 2009. All events were collected with the ATLAS magnets on. This analysis is restricted to the barrel region of the spectrometer where muons are triggered by the RPC chambers. As expected from pp collisions, the trigger is designed to detect and measure the momentum of particles originating in the interaction point (IP), at precise times coinciding with the accelerator collisions marked by the LHC clock. Hence in order to trigger on cosmics, these runs included a special trigger configuration that loosened muon-pointing requirements and accepted particles arriving at random times. The trigger rate provided by the RPC was around a few hundred Hz, limited by the recording capabilities given by the event size. The TGC chambers were typically operating at very low gain during this period of cosmic ray runs. More

details of detector operating conditions and data quality considerations can be found in [59].

The MOORE track reconstruction program [61] was used to reconstruct stand-alone muon spectrometer tracks. Since cosmic ray muons do not originate in the interaction point, changes have been introduced into the standard MOORE algorithm. The tracks are assumed to originate from outside the detector volume, typically from above, and are allowed to traverse the full detector. In addition, the algorithm allows for more flexibility in spatial configurations, with loosened pointing requirements in the pattern finding, both at the hit and segment levels. The cleanup and track quality cuts were also released, and modifications were implemented to the logic in case of missing non-precision coordinate hits. While the MOORE algorithm allows for track-finding even in the absence of trigger hits, the issue of missing hits in the non-precision component poses problems for the reconstruction of cosmic ray muons where there are no constraints for this coordinate, otherwise given by the passage through the IP. As a result, the presence of ϕ -hits is a requirement for the analysis, see Section 4.4.

The calibration and reconstruction configurations use as many of the standard procedures as possible. In the case of the muon spectrometer calibrations, the data processing used the MDT drift parameters and chamber positions provided by the MDT calibration group. The data recorded from the MDT and trigger chambers, as well as those from the Detector Control System (DCS), were copied to dedicated calibration centers in Michigan, Munich and Rome, where the calibration parameters were subsequently derived. These were then loaded into the ATLAS COOL database

and used in the offline data reprocessing. Alignment constants from the optical system and survey information were included. These corrections modify the detector geometry according to the fit results from the optical system, providing alignment for chambers within each chamber layer (station) as well as between stations. Particularly at these early stages, misalignments constitute a major source of uncertainty for the momentum measurement, especially for high momentum muons.

Moreover, the calibration precision of MDT drift parameters, produced using the calibration center procedure for the global commissioning cosmic runs, suffers from significant limitations. The main difficulty is the determination of the MDT hit zero-time t_0 , corresponding to hits on the tube wire, in the case of cosmic ray muons. Timing issues stem from the 25 ns jitter due to the random arrival of particles compared to the LHC clock, and also from the wide range in time-of-flight as the muons travel from different locations. In addition, rapid changes in run conditions and limited statistics for a given configuration imply that in practice only one t_0 calibration per chamber could be determined reliably. In order to help overcome these limitations, a t_0 fitter, based on a free global timing parameter, has been introduced into the segment reconstruction. This has been shown to significantly improve tracking performance [59, 70]. The major limitation of the t_0 fitter is that it can only be used in cases where a segment with at least four MDT hits has already been found, so calibrations are still critical for the initial segment-finding as well as for segments with three MDT hits.

The final dataset used for this measurement was repeatedly processed in order use more accurate $r - t$ and t_0 calibrations for the drift tubes, and better alignment constants. The reconstruction was also improved with regard to the treatment of the track hit uncertainties. The tracks are first fit with enlarged uncertainties in order to compensate for possible misalignments, using a fixed hit error of 2 mm. The track is then refit with twice the nominal uncertainties.

4.4 Event Selection Criteria

A set of quality cuts are applied to yield a sample of high-quality muon tracks with well-defined geometric characteristics. Most cosmic muons arrive through the shafts connecting the surface to the underground cavern located over the sides of muon-spectrometer barrel. Due to an abundance of acceptance effects, the sample is simplified by requiring muons to traverse the top half of the MS barrel, crossing all three stations, Inner, Middle and Outer, with a minimum number of MDT hits per layer $\geq 4, 3, 3$ respectively. The MDT hit multiplicities per station are shown in Figure 4.1. Tracks traversing the three stations of the barrel typically have more than twenty MDT hits and are of higher quality. In addition, these trajectories have a sufficient field integral to provide good momentum measurement as well as reliable charge determination.

In addition, tracks are required to have ϕ -hits in at least two different RPC layers. The multiplicity of RPC layers on a track is shown in Figure 4.2, indicating agreement between the two charges. Good constraint in the ϕ coordinate is important because of

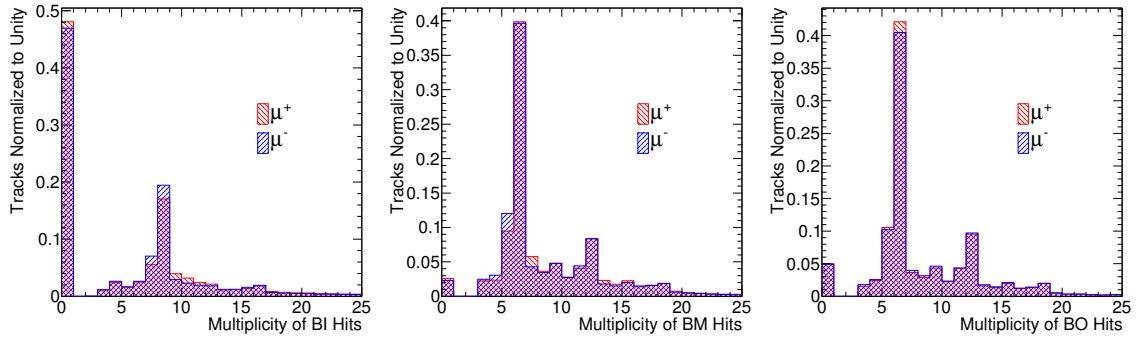


Figure 4.1: The number of MDT hits assigned to positive and negative muon track candidates in the Inner (left), Middle (center), and Outer (right) barrel stations.

the large variations in the magnetic field that affect both the momentum and charge determination. Due to the limited knowledge of alignment across ϕ -sectors, tracks are required to be contained within the same ϕ -sector.

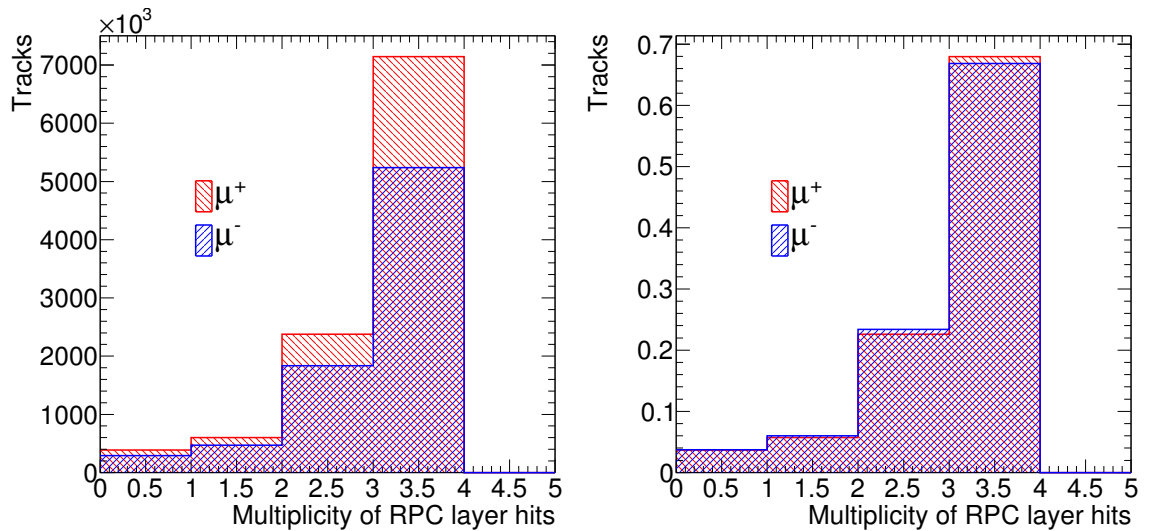


Figure 4.2: The number of RPC ϕ -layers crossed by positive and negative muon track candidates. The distributions are normalized to unity in the right plot.

The distribution of the χ^2/NDF , shown in Figure 4.3, is peaked below one due to the use of enlarged hit uncertainties in the tracking. Tracks that were very poorly

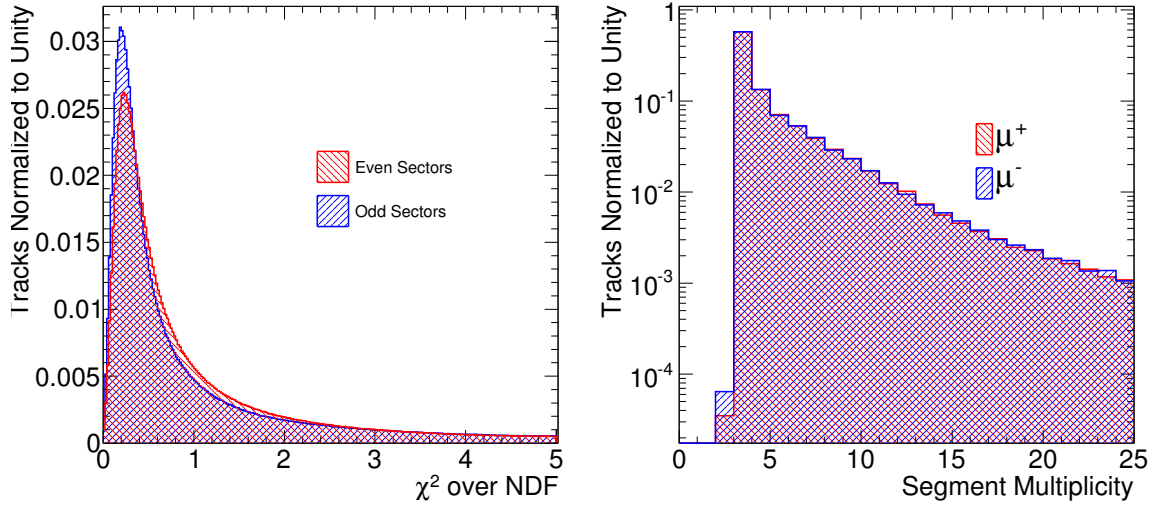


Figure 4.3: The track χ^2 per degree of freedom at left, before applying any requirements. The right distribution shows the number of muon segments in the same sector as the candidate track.

reconstructed were removed by requiring $\chi^2/\text{NDF} \leq 10$. The number of segments in the same sector as the candidate track is shown in Figure 4.3, and the requirement ≤ 10 was applied to reject shower events. Finally, the sample was restricted to tracks with a momentum above 10 GeV, in order to ensure the trajectory traverses the entire detector. The cutflow is reported in Table 4.1. The criteria that have the most significant impact on the sample size are the geometrical selection and the transverse momentum requirements. The dataset used corresponds to 5,075,823 events, of which 6.85% fulfill all the selection criteria; 3.32% yield a positive muon track and 3.53% a negative one.

Selection criterion	Efficiency (Global) [%]	
	μ^+	μ^-
$\chi^2/\text{NDF} < 10$	99.7 (99.7)	99.6 (99.6)
3-station track	49.8 (49.7)	50.5 (50.3)
Track in top detector	53.6 (26.6)	54.6 (27.5)
All hits in same sector	32.4 (8.62)	33.1 (9.08)
4/3/3 BI/BM/BO MDT hits	99.0 (8.54)	99.0 (8.99)
≥ 2 RPC ϕ -layers	95.4 (8.15)	95.2 (8.56)
$p \geq 10$ GeV	43.8 (3.57)	44.4 (3.80)
≤ 10 segments in sector with track	93.1 (3.32)	93.0 (3.53)

Table 4.1: Efficiency of the selection requirements showing the relative and absolute values in parenthesis.

4.5 Acceptance Correction

The acceptance for positive and negative tracks depends strongly on the position in the detector. The majority of cosmic ray muons enter the cavern through the two main shafts at the edges of the detector. The rate of muons arriving in the central region, between the shafts, is reduced due to the presence of 60 m of rock above the detector. The toroidal field is right-handed with respect to the positive z axis. Therefore, the positive muons entering the larger shaft ($z > 0$) bend into the detector, whereas negatively charged muons are bent out of the acceptance, as shown in Figure 4.4. In the smaller shaft, the opposite effect occurs. As a result, the different regions of the detector are populated differently by muons of each charge and differences in the size and position of the shafts introduces an overall charge bias in muon detection.

Since a realistic Monte Carlo simulation of cosmic ray events was not available, a new method is devised to select events where the acceptance of positive and negative

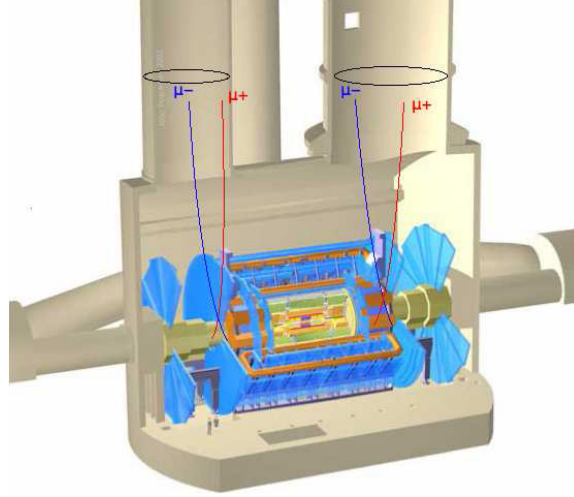


Figure 4.4: The diagram shows the shafts through which most cosmic ray muons enter the ATLAS detector cavern (modified from [52]). The toroidal field is right-handed with respect to the positive z axis. Positive muons that enter the larger shaft, on the right side, bend into the detector, whereas negatively charged muons entering this same shaft, tend to bend out of the acceptance. The opposite effect occurs in the smaller shaft, on the left side of the diagram. The difference in size of the shafts, and hence in the muon flux through them, impacts the overall charge composition of the sample.

tracks are identical and hence cancel in the ratio. In the Mirror Track method, tracks are extrapolated [71] backwards to a plane above the detector at $y = 13$ m, where the magnetic field is negligible¹. A new track, the mirror track, is defined at this surface, with the same parameters and covariance matrix as the original one, but of opposite charge. The mirror track is then extrapolated through the simulated detector volume to determine which active detector units are crossed. The track model is made more realistic by including detector and tracking inefficiencies (Sections 4.7 and 4.6). If the track fails to be in the geometric acceptance of the detector and satisfy the

¹Models of the B-field in the ATLAS cavern show that the expected field at the $y = 13$ m plane is below $20 \mathcal{G}$ and is set to zero in reconstruction algorithms.

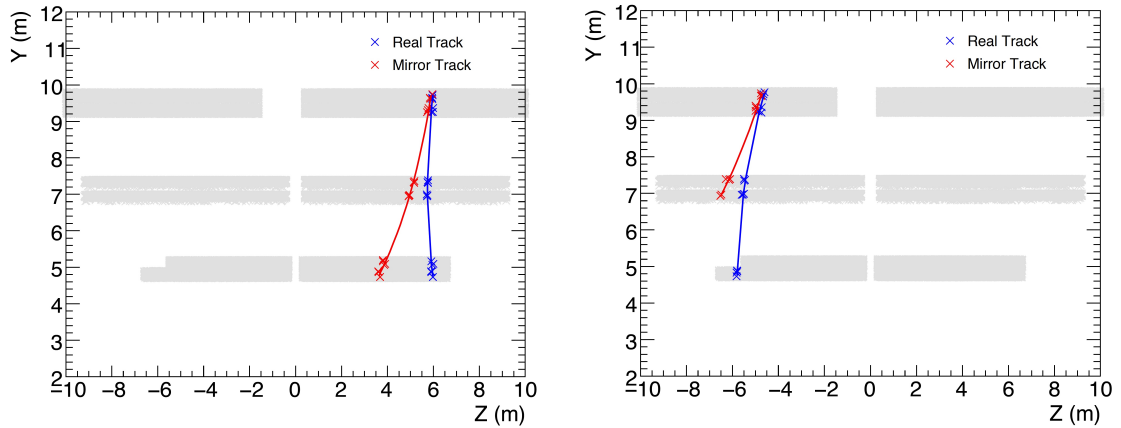


Figure 4.5: An example of the mirror track correction: in the event display at left, both the real (blue) and the mirror (red) tracks are contained within the geometrical acceptance of the MS. In the event display at right, the mirror track (red) falls outside the geometric acceptance. Hence the real track (blue) is also rejected and charge biases caused by the acceptance are thus corrected.

selection criteria, as shown in Figure 4.5, it is discarded from the sample. This method by construction ensures tracks of the two charges satisfy identical selections, thus cancelling acceptance biases.

4.5.1 Mirror Track Validation

The mirror track method was validated by extrapolating mirror tracks without inverting their charge and comparing this model, called shadow track, to the original one. This study commissioned and validated the extrapolator code [71], which is widely used in ATLAS software. Shadow tracks can be described as purely geometric trajectories across the detector. The model differs from a real track in that it is based on a simplified geometric description, it only uses one readout unit (such as an MDT tube) per active layer and the material interactions modify the momentum of the track only and not its direction.

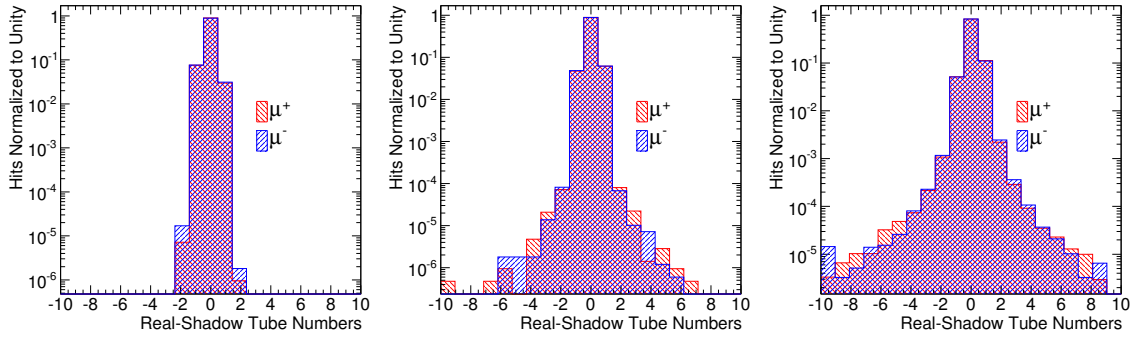


Figure 4.6: Differences between the number of the readout channel crossed by a real track and its shadow track, at each MDT layer, BO (left), BM (center) and BI (right). The distribution is progressively wider since these correspond to increasingly larger extrapolations.

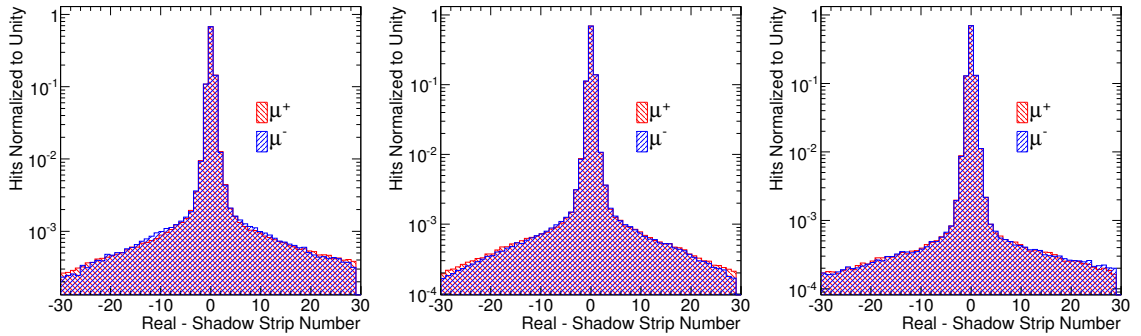


Figure 4.7: Differences between the readout channel number crossed by a real track and its shadow track, at each RPC layer. From left to right, the ϕ -channel-number difference in the three RPC stations, ordered by their distance from the IP: RPC1, RPC2 and RPC3.

Despite these differences, studies of the spatial proximity of real and shadow tracks indicate that there is good agreement between them. The difference between the MDT tube number crossed by the shadow track and the real tube number hit is shown in Figure 4.6. The shadow tracks are within one tube from the real track modeled for almost 100% of the tracks in the BO and BM stations and 98.8% in the BI stations. The corresponding distributions for RPC ϕ -hits are shown in Figure 4.7. The fraction of hits within one RPC strip number is 96.2%, 97.2%, and 95.1%, in the three RPC stations, ordered by their distance from the IP: RPC1, RPC2 and RPC3, respectively. These studies indicate that the extrapolated track accurately models the trajectories of real ones and hence mirror tracks can be used to study acceptance effects.

The distance between real tracks and their mirror counterparts shows that the difference between the real track and the mirror track decreases with increasing momentum, as expected due to the bending in the magnetic field (see Figure 4.8). A large proportion, about 94%, of mirror-real track pairs are contained in the same BM chamber, as shown in Figure 4.9. Since trigger chambers are installed only in BM and BO stations, this implies that the impact of trigger efficiencies is small, as discussed in Section 4.6.

4.6 Muon Trigger Efficiency

The trigger can cause charge biases due to pointing requirements in the pattern-finding and uneven hardware performance. For cosmic data-taking, the loosest possi-

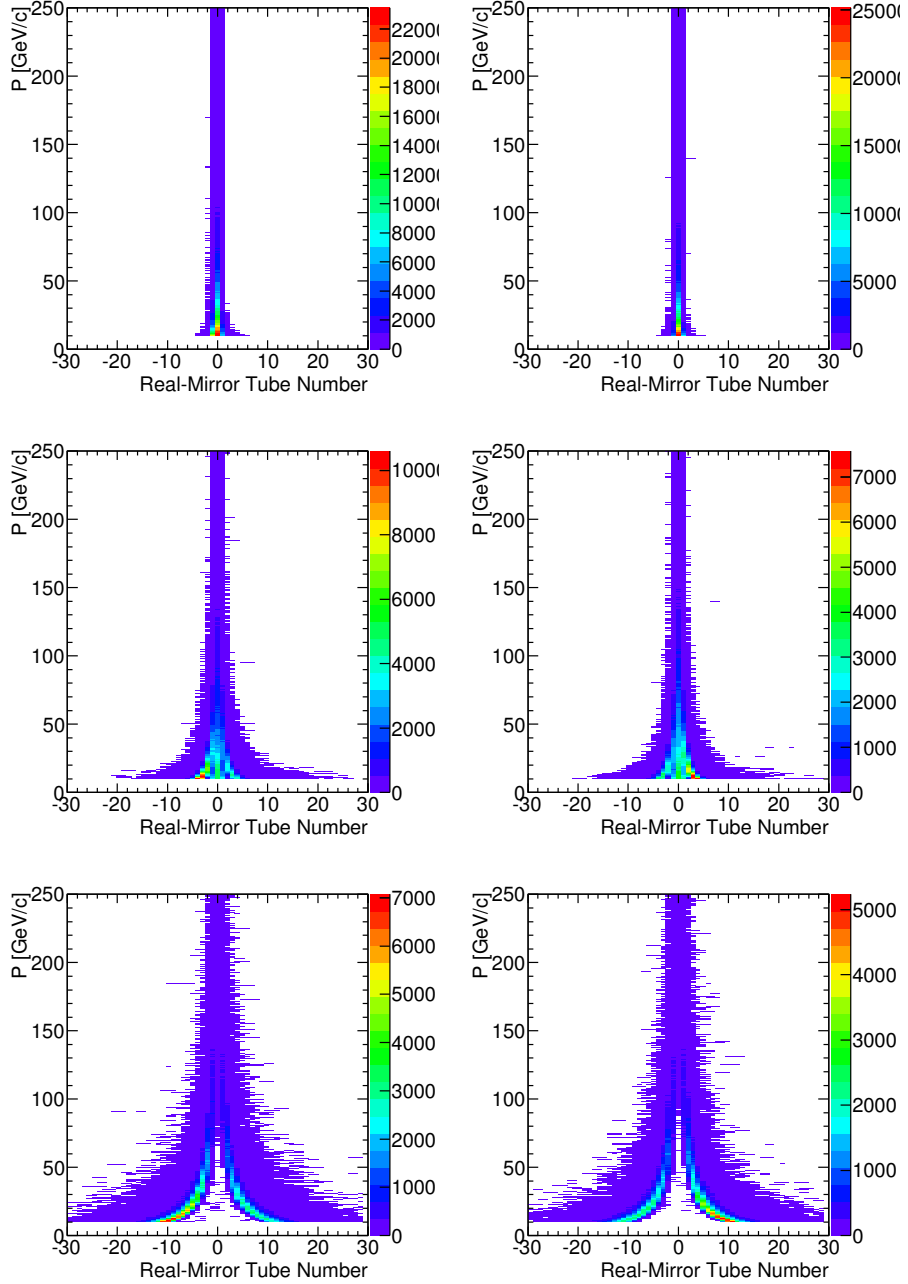


Figure 4.8: Differences between the tube number crossed by a real track and its mirror at different MDT stations as a function of the track momentum for positive (left) and negative (right) tracks in the BO (upper), BM (center) and BI (lower) stations.

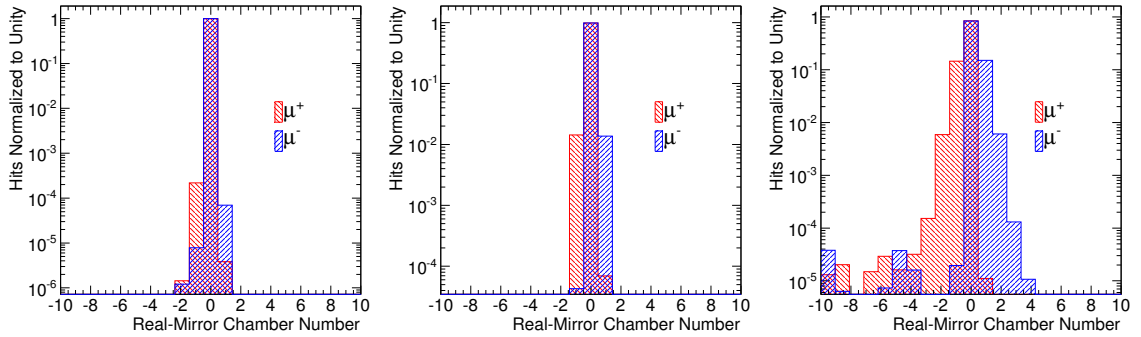


Figure 4.9: Differences between the chamber number crossed by a real track and its mirror track for different MDT stations. The chamber index runs along η . From left to right, the chamber-number difference in BO, BM and BI stations.

ble trigger configuration is used. It looks for hits in the two innermost RPC stations, RPC1 and RPC2, within the same trigger tower, the basic trigger unit defining a projective region in $\eta - \phi$. Selecting events with trigger hits in the same trigger tower maintains an implicit pointing requirement for muon candidates.

The RPC trigger coverage was not uniform throughout the detector. This is mainly caused by hardware inefficiencies due to lowered voltage thresholds, temperature sensitivity or trigger tower timing. Some ϕ -sectors were not issuing triggers and single RPC panel efficiencies varied in the range 80 – 100% (see Section 4.7). This has impact on the overall trigger efficiency for that region. The multiplicity of triggers as a function of η and RPC ϕ -sector is shown in Figure 4.10. While some differences can be explained by the dependence of the rate of cosmic ray muons on their position in the detector (such as the large concentration of muons under the shafts), other variations are due to hardware inefficiencies. A clear example of this is the lack of triggers in two ϕ -sectors, as shown in the lower section of Figure 4.10 (phi strips $\lesssim 200$).

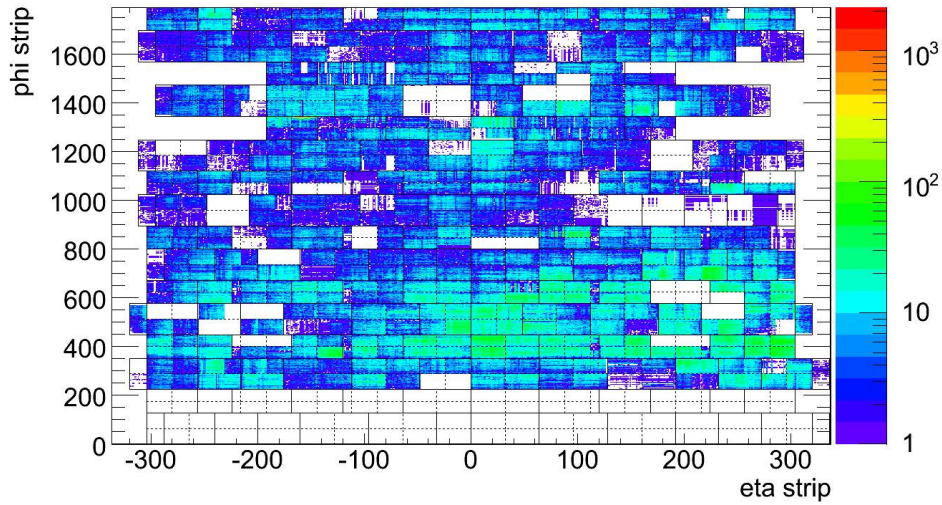


Figure 4.10: RPC low- p_T trigger coverage for the run used in the analysis. Each entry corresponds to an η and ϕ -strip issuing a low- p_T trigger. The superimposed solid and dashed lines define the boundaries of the RPC readout units, from [72].

In order to correct for charge biases introduced by the RPC trigger, a detailed simulation of the trigger logic of the hardware components was developed. The algorithm maps the projective trigger towers defined by the trigger cabling and imposes requirements on the hit pattern in each tower. The simulation was made more realistic by including the impact of hardware inefficiencies using a map of RPC panel efficiencies. These hardware efficiencies are applied to the RPC hits in an event, removing hits with a probability corresponding to the inefficiency of the chamber where the hit is located. An inefficient trigger is thus simulated by checking the trigger logic requirement on the remaining subset of hits. Charge biases introduced by the trigger were corrected for by checking the RPC trigger requirement offline for the selected track and imposing the same requirement on the mirror track.

4.7 Detector Efficiencies

The mirror track method requires mirror tracks to behave as much like real tracks as possible. In particular, the quantities used in the selection of candidates should be correctly modeled in the mirror track. This section presents efficiency measurements for finding and assigning MDT and RPC hits to a track, which are used as correction factors for mirror tracks.

The MDT single tube efficiency has been measured in cosmic rays by reconstructing the segments in a chamber where one layer of tubes is removed from the fits. The tube crossed by the segment in the excluded layer is checked for the corresponding hit, providing a measure of the hardware efficiency². A measure of the tracking efficiency is given by the fraction of hits within a distance from the segment less than $n = 3, 5, 10$ times the uncertainty, where the error used is a combination of the tube resolution and the track extrapolation uncertainty. The MDT hardware and tracking efficiencies as a function of the hit radius are shown in Figure 4.11. The efficiency is high for all radii, though a small decrease in efficiency occurs close to the edge of the tube, due mainly to δ -electrons [59]. The average tube hardware efficiency is 99.8% and the average tracking efficiency is 94.6%, 96.3% and 97.2% for the requirements $n = 3, 5, 10$ respectively. The figure also shows an example of the efficiency per tube in a multilayer. This is high and uniform given the statistical uncertainty associated with the efficiency measurements. Disconnected tubes contribute to the uncertainty, although these correspond to about 0.2% of the MDT channels.

²The MDT hardware efficiency is that with which the chamber electronics records a hit in the tube when a charged particle traverses it.

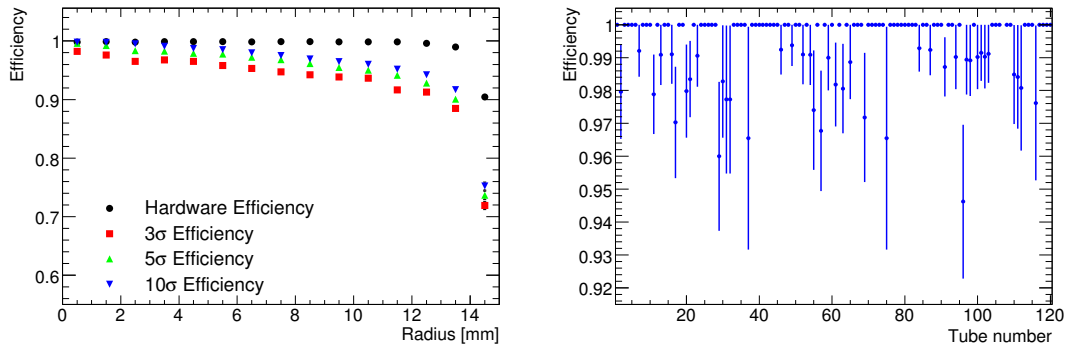


Figure 4.11: MDT hit finding efficiency as a function of the hit radius (left) corresponding to the fraction of hits found within 3, 5 and 10 standard deviations of the distribution of hit residuals from a fit track [59]. MDT Hardware hit efficiency distribution (right) for the tubes of chamber BML4C05, multilayer 1.

The efficiency situation differs in the case of RPCs since these chambers suffer from more hardware instability and were not fully commissioned at the time of this analysis. A trigger bias in the middle station is removed by imposing the trigger requirement of a three out of four hit coincidence, and checking the fourth layer. The distribution of efficiencies per panel is shown in Figure 4.12, with a peak at around 93%. The MDT and RPC hardware efficiencies are applied to the channels crossed by the mirror tracks in the sample.

4.8 Muon Reconstruction Efficiency

The efficiency for finding tracks is a source of charge bias in the charge ratio measurement. Features such as a preference for IP-pointing configurations at different stages of the track reconstruction lead to a larger population of positively charged muons reconstructed under the large shaft compared to negatively charged muons which bend away from the IP. This section presents a method to study charge biases

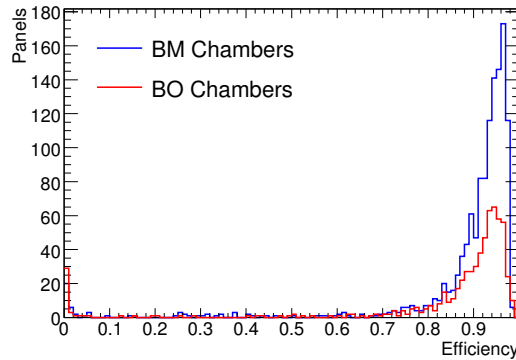


Figure 4.12: Distribution of RPC hit efficiencies. Each entry represents an individual RPC panel, from [72].

in the tracking by measuring the track-finding efficiency separately for positive and negative tracks. A correction is then applied as a function of the z position and θ of the track.

Since cosmic rays can traverse the full detector, a single muon may be reconstructed as two tracks in the top and bottom halves of the detector. Events are selected with a track in the bottom half, pointing to hits in the top half. The extrapolator is used to determine the expected muon trajectory in the top half, accounting for energy loss and the presence of the magnetic field. If the extrapolation succeeds in traversing the three stations (BI, BM and BO) in the same top ϕ -sector, the algorithm searches for raw MDT hits in the vicinity of the extrapolator. The raw hit search region is defined per MDT layer as the range of tubes within 3σ of the extrapolated position³. The distributions of tube layers crossed by the extrapolated track versus the number of raw MDT hits in the hit search region for the BI, BM and BO stations are shown in Figure 4.13. The large excess at zero is due to the loose requirements on the bottom

³The error considered is the extrapolator local error in the precision coordinate.

track and the geometry of the MS, since sometimes no top track is expected. The extrapolation to the top of the detector points to the trajectory of a real muon, with at least three hits in each of the three stations around the extrapolator, in about 45% of cases.

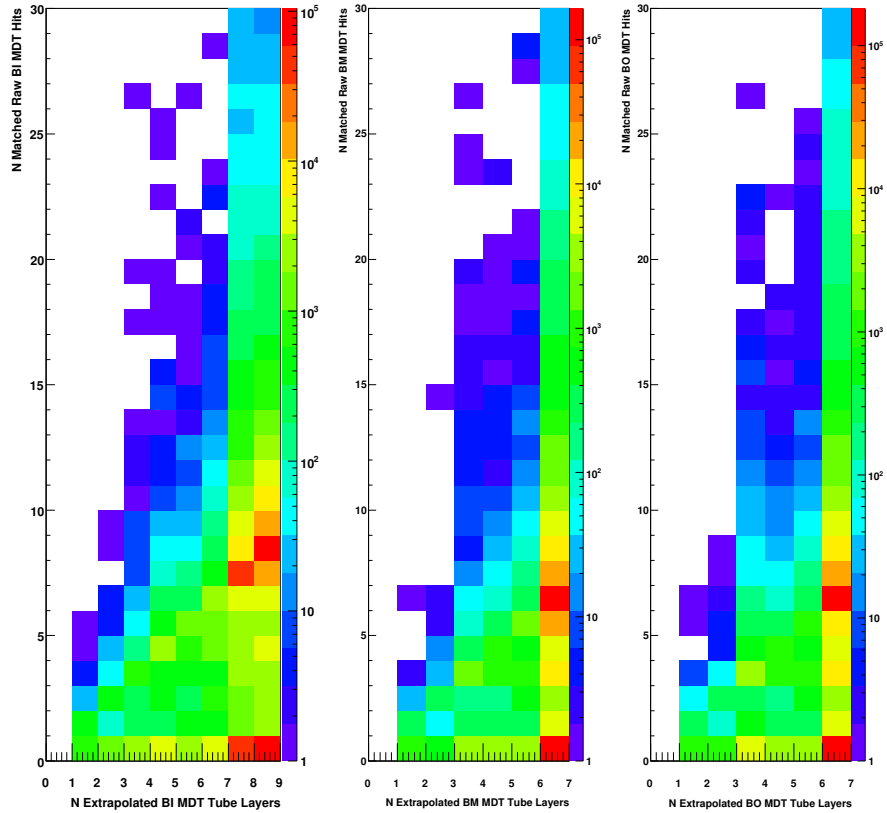


Figure 4.13: A comparison of the number of tube layers crossed by the extrapolator and the number of raw MDT hits in the proximity of the channel hit by the extrapolated track for the BI (left), BM (center) and BO (right) stations. The two axes are asymmetric because the extrapolator provides the number of tube layers traversed (at most 8, 6 and 6 layers for the BI, BM and BO stations respectively) while for real tracks the number of hits can be different from one per layer.

If at least three raw MDT hits are found in each of the three stations (BI, BM and BO), the raw hit combination is considered to correspond to a real muon. This is

the minimum requirement on the number of hits in a layer imposed by the tracking algorithm since segments can only be fit with at least three MDT hits. A raw hit combination is associated to a track by comparing the raw hits to the hits associated on track. The number of raw MDT hits found in the hit search region versus the number of those hits associated to a muon track for the BI, BM and BO stations is shown in Figure 4.14. As expected from the high MDT hit efficiency, a muon traversing a chamber provides a signature of about a hit per layer (see Figure 4.13) and all these hits are typically associated to the track (see Figure 4.14), yielding about eight, six and six hits for the BI, BM and BO stations respectively. A hit combination is matched if there are at least three hits per layer in common between the raw MDT hits in the combination and the track. The track finding efficiency is defined as the frequency with which the hit combinations are matched to a track and is measured to be $(96.5 \pm 0.1)\%$ overall.

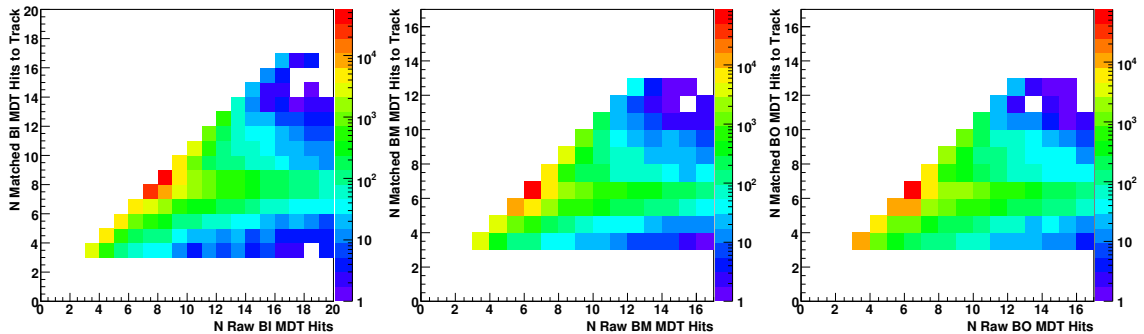


Figure 4.14: A comparison of the number of raw MDT hits found in the proximity of the extrapolated track path and the number of hits associated with a muon track for the BI (left), BM (center) and BO (right) stations.

The efficiency is measured for both positive and negative tracks as a function of the incident angle θ and the z position at the point of entry to the detector, as shown in Figure 4.15. This is found to depend weakly on these variables, although exhibits a slightly higher efficiency for positive tracks originating from the larger shaft, as expected from low momentum tracks bent towards the detector center. The measured tracking inefficiencies are applied to the mirror track in order to correct for charge biases introduced by the tracking.

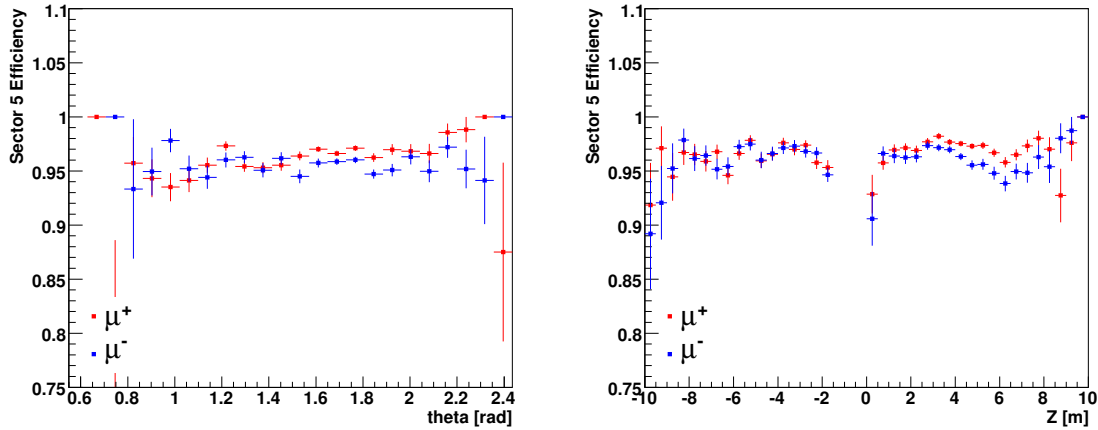


Figure 4.15: Tracking efficiency calculated using raw MDT hit combinations matched to MOORE tracks for positive and negative tracks in Sector 5. The θ (left) and z (right) dependence shows slightly higher efficiency for positive tracks from the large shaft ($\theta > \pi/2$ and $\sim 3 \geq Z \geq 8$ m).

4.9 Selected Muon Sample

The efficiencies described in the previous sections complete the modeling of mirror tracks, ensuring that they are a good representation of real tracks traversing the detector with the same parameters but opposite charge. Biases due to the geometric

acceptance are corrected for by requiring that the mirror track satisfies the requirements of at least 4, 3, 3 hits in the BI, BM and BO chambers respectively, contained in a single ϕ -sector, and at least 2 RPC ϕ -hits. In addition, the mirror track should satisfy the track-finding efficiency expectation and both the mirror and shadow tracks should confirm the RPC trigger simulation in order to remove tracking and trigger biases. As a result, if the original track had been of opposite charge, it would have been equally likely to be a part of the data sample. The z coordinate for muon tracks before and after applying the selection criteria is shown in Figure 4.16. The agreement in the shapes for the two charges after the corrections indicates that the geometrical charge dependencies are greatly reduced by the selection. The charge ratio measured inside the ATLAS cavern is shown in Figure 4.17, indicating that the analysis requirements do address the geometrical dependence of the various sources of charge bias introduced by the different size and position of the cavern shafts.

4.10 Surface-Cavern Energy Correction

The momentum is measured in the ATLAS detector cavern about 70 m underground. Hence the muon energy requires correction for energy losses in the rock above the detector. Based on the geometry of the cavern shafts, a parametrization of the energy loss in terms of the muon z and incident angle θ has been developed. The muon path length in rock and in air is estimated using a simplified material description of the cavern, shown in Figure 4.18.

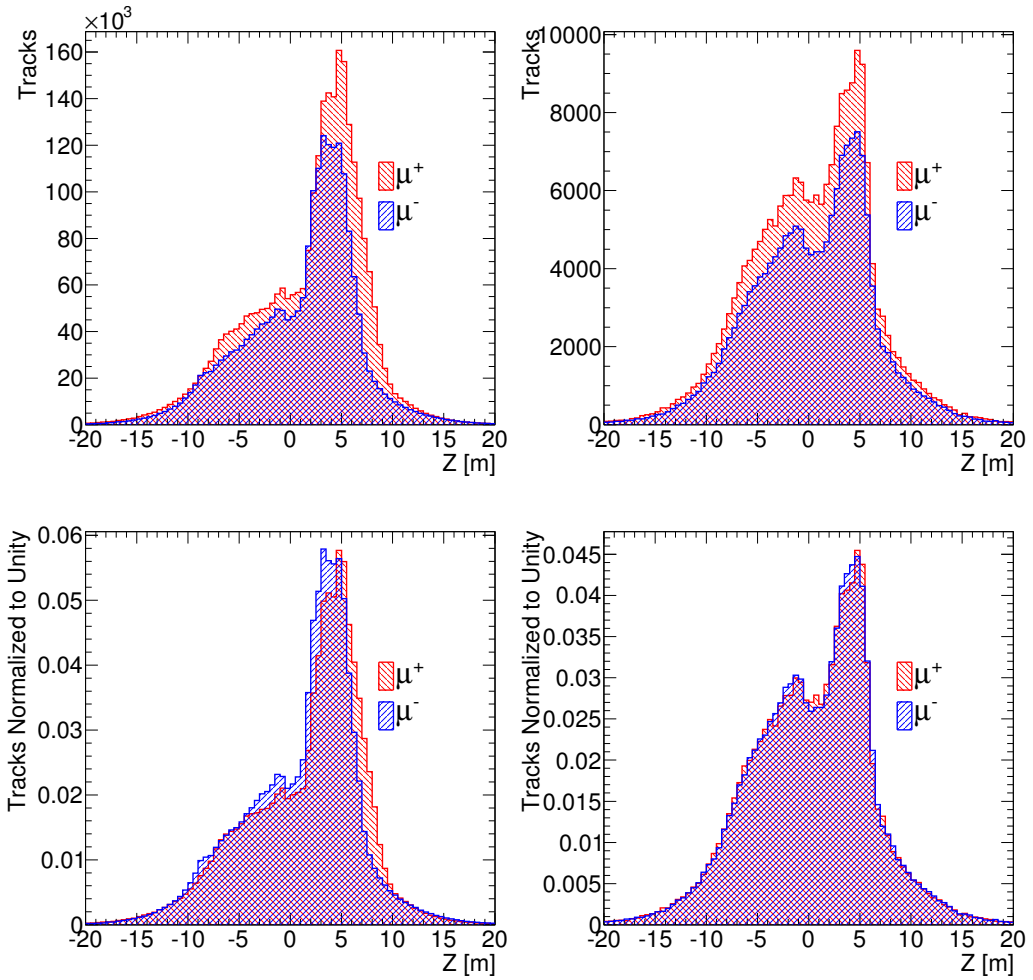


Figure 4.16: Distribution of z of all reconstructed muons (left) and after selection cuts, mirror track correction, and trigger confirmation on shadow and mirror tracks (right). In the bottom row, the distributions are normalized to unity.

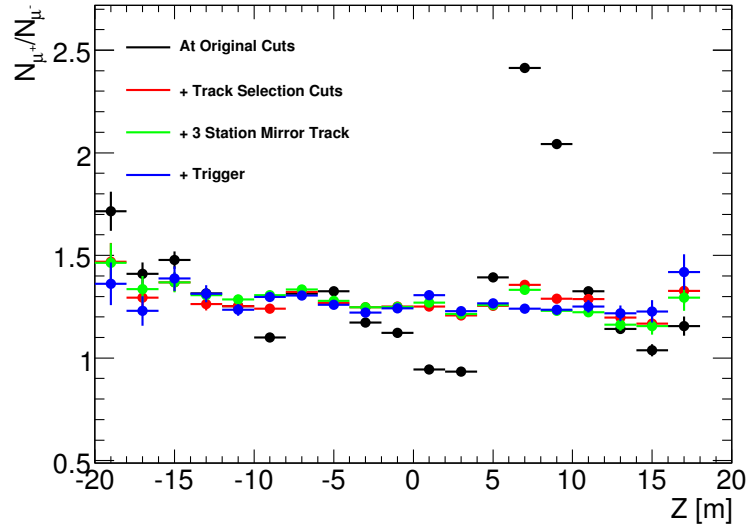


Figure 4.17: Charge ratio in cosmic muons as a function of the muon z measured at the BO layer. The charge bias introduced by the differences in size and position of the ATLAS cavern is eliminated by each level of the corrections described in the text.

The shafts are modeled as square wells. The length of the sides is given by the corresponding shaft diameter. The following surfaces are defined

- Earth surface

- $y = 72.6$ m, for any x and z

- ATLAS ceiling

- $y = 15$ m, for any x and z

- PX14 shaft

- $x = \pm 9$ m, for $15 < y < 72.6$ m and $|z - 13.5| < 9$ m

- $z = 13.5 \pm 9$ m, for $15 < y < 72.6$ m and $|x| < 9$ m

- PX16 shaft

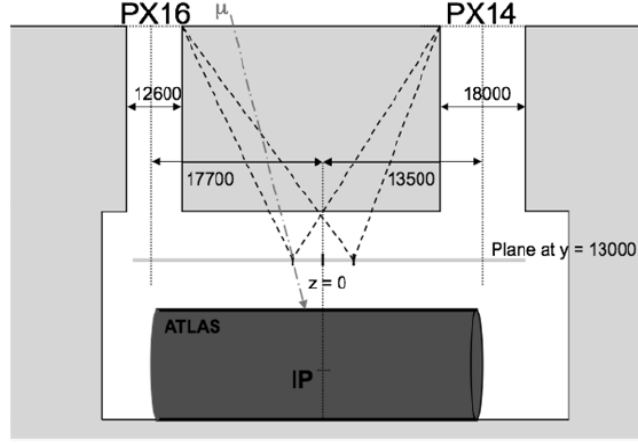


Figure 4.18: A sketch of the ATLAS cavern used to model the path in rock traversed by a muon from the surface to the MS.

- $x = \pm 6.3$ m, for $15 < y < 72.6$ m and $|z + 17.7| < 6.3$ m
- $z = -17.7 \pm 6.3$ m, for $15 < y < 72.6$ m and $|x| < 6.3$ m.

Each track is represented by the parametric equations

$$\begin{cases} x = x_0 + t \sin \theta_0 \cos \phi_0, \\ y = y_0 + t \sin \theta_0 \sin \phi_0, \\ z = z_0 + t \cos \theta_0, \end{cases} \quad (4.4)$$

where x_0, y_0, z_0 correspond to the position of the track at the $y = 13$ m plane. The parameters θ_0 and ϕ_0 correspond to the angular direction of the track at the same point on the plane. The intersections between the parametric track and the surfaces define the transitions between the rock and air.

Using the path of each muon traversing the rock, defined by the intersection points, the average energy loss may be expressed in terms of ionization and radiative processes

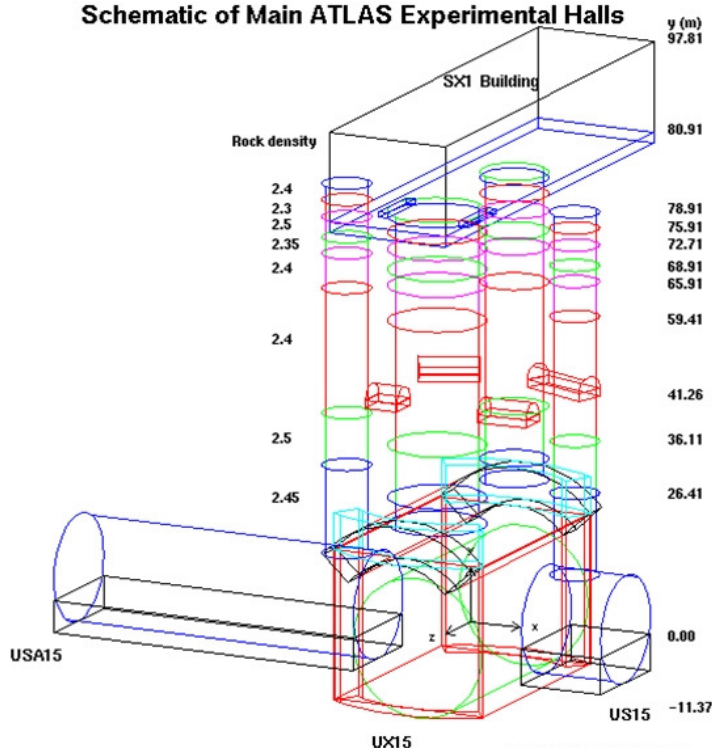


Figure 4.19: A profile of the rock layers located above the ATLAS cavern shown with their respective densities in g/cm^3 .

as

$$E_{\text{surface}} - E_{\text{ATLAS}} = \epsilon \cdot (e^{bL} - 1) , \quad (4.5)$$

where $\epsilon = 500 \text{ GeV}$ and $b = 2.5 \cdot 10^5 \text{ g}/\text{cm}^2$ [63]. The average rock density above the ATLAS cavern is $\rho = 2.42 \text{ g}/\text{cm}^3$, exhibiting some variation with depth, as shown in Figure 4.19. The distribution of momentum energy loss corrections is shown in Figure 4.20. The energy correction for an approximately vertical muon traversing about 70 m of rock shows a peak at about 30 GeV. The momentum corrections as a function of z and ϕ , and z and θ are shown in Figure 4.21. The size of the correction depends strongly on the position and angle of the track, since muons coming from the shafts tend to lose significantly less energy than those traversing mostly rock. The

lightest colored regions in Figure 4.21 correspond to the span of track parameters for muons arriving through the shafts. The darkest regions, at very large and very small angles, correspond to muon trajectories that traverse large amounts of rock surrounding the cavern and receive a correspondingly larger energy loss correction. Finally, the muon momentum distribution is compared in Figure 4.22 before and after applying the surface-cavern momentum correction. The peak is shifted to higher momenta after applying the correction though still exhibits a sharply falling tail. The final corrected sample shown is used for measuring the charge ratio.

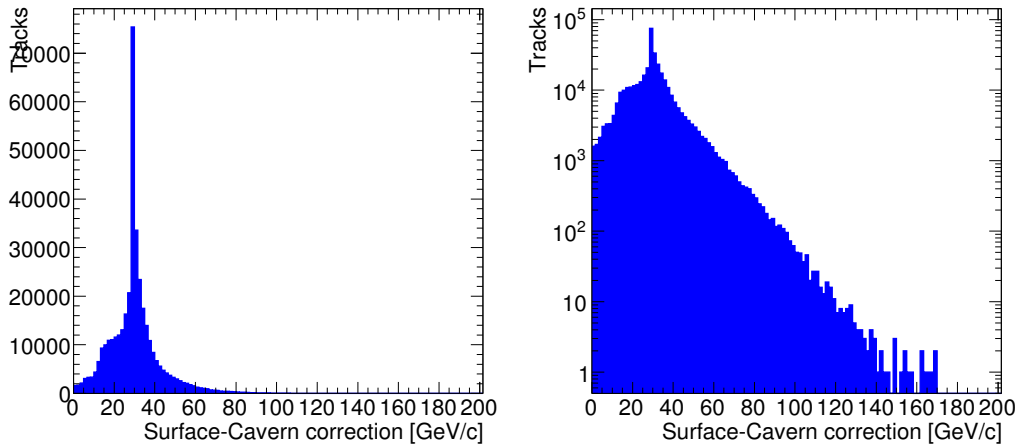


Figure 4.20: Surface-to-cavern momentum corrections in linear (left) and logarithmic scales (right). The peak at $\simeq 30$ GeV corresponds to the vertical muons traversing about 70 m of rock.

4.11 Uncertainty Estimation

The main sources of systematic uncertainty on the charge ratio measurement relate to the uncertainty on the momentum scale and resolution, and energy loss correction from the detector cavern to the surface. The uncertainties associated with the accep-

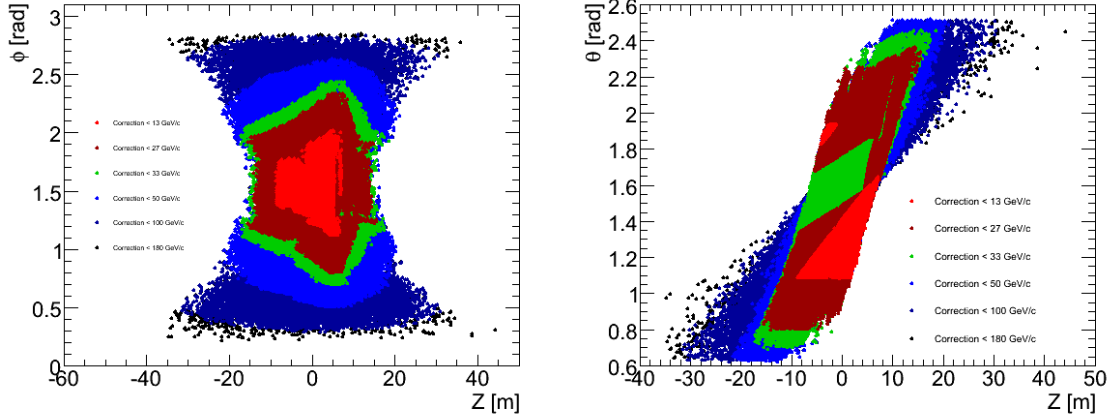


Figure 4.21: Surface-to-cavern momentum corrections as a function of various track parameters at the $y = 13 \text{ m}$ plane: z vs. ϕ (left) and x vs. θ (right), for different ranges of the energy loss correction (shown in different colors).

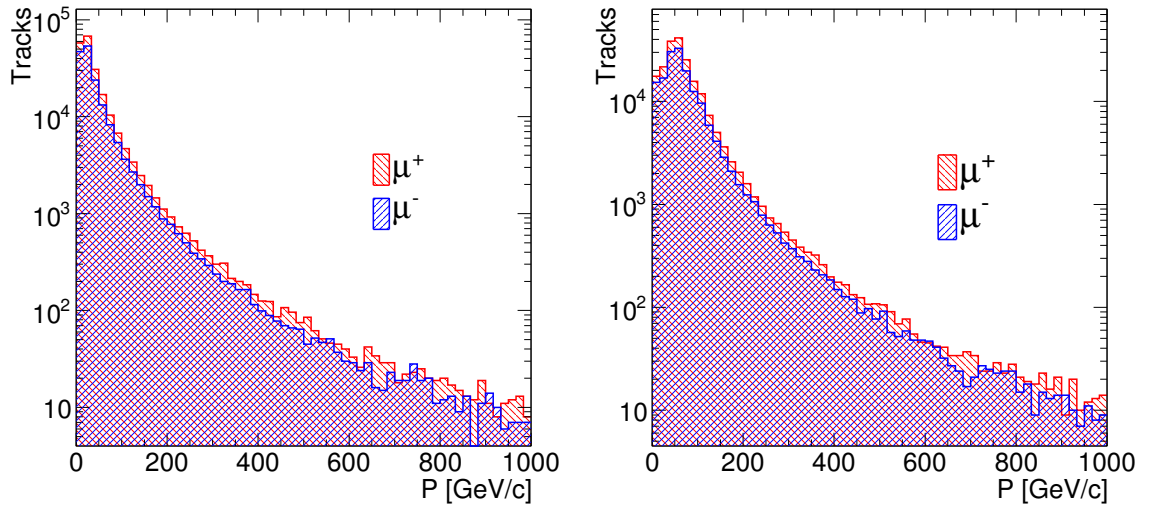


Figure 4.22: Distribution of the momentum of muons before (left) and after (right) applying the correction for the momentum loss in the path between the ATLAS cavern and the surface. The distribution on the right side corresponds to the sample used in the final charge ratio measurement.

tance and event selection, as well as tracking efficiency corrections, are calculated by varying the correction parameters within their uncertainties. These are found to be relatively small. The systematic uncertainties are summarized in Table 4.2.

Effect [10^{-2}]	Momentum Bins [GeV]						
	10	40	70	100	200	350	600
Track eff. $+\sigma$	0.516	0.515	0.692	0.777	0.797	0.857	0.894
Track eff. $-\sigma$	-0.512	-0.511	-0.685	-0.768	-0.787	-0.847	-0.882
Allow sector crossers \dagger	0.699	0.690	0.015	0.751	0.235	0.954	2.459
No trigger confirmation \dagger	0.361	0.527	0.340	0.136	0.280	0.460	0.512
MDT I/M/O hits $+$ \dagger	0.311	0.206	0.641	0.298	0.582	3.923	0.993
MDT I/M/O hits $-$ \dagger	-0.561	-0.032	-0.189	-0.149	-0.023	-3.923	-0.128
Segment / Sector $+$ \dagger	0.507	0.324	0.354	0.884	1.542	0.525	1.889
Segment / Sector $-$ \dagger	-0.119	-0.296	-0.157	-0.884	-1.542	-1.990	-4.037
Curvature resolution	0.127	0.171	0.430	0.431	1.184	2.947	6.462
Curvature scale	5.487	0.515	0.462	0.615	1.279	3.712	3.817
Rock density $+$	0.405	0.844	0.206	0.097	0.569	1.109	0.884
Rock density $-$	-0.374	-0.584	-0.458	-0.124	-0.569	-1.109	-0.884
Cavern size $+$	1.421	1.640	0.342	0.209	0.935	1.695	0.038
Cavern size $-$	-0.624	-2.051	-0.342	-0.530	-0.935	-1.695	-0.542

Table 4.2: The contributions of different sources of systematic error on the charge ratio in momentum bins. The lines marked by \dagger are not included in the estimate of the total systematic uncertainty, since these are cross-checks of the stability of the measurement.

4.11.1 Momentum Scale and Resolution, Charge Misidentification and Bin Migration

Scale and resolution effects result in the migration of candidates from one momentum bin to another and, in some cases, the wrong charge assignment. In order to estimate this effect, the scale and resolution uncertainty has been studied in data for positive and negative muons separately. Some muons traverse the full detector

and are reconstructed as two separate tracks in the spectrometer. The two redundant curvature measurements in the top and bottom halves of the detector were compared. The selection criteria for the analysis (see Section 4.4) was applied to both tracks in the pair, except for the momentum requirement, which was lowered to $p \geq 2$ GeV in order to allow for muons below the momentum requirement to migrate into the sample. Events with only one track in the top and one in the bottom were used. These correspond to the majority of events with a track in the two halves, as shown in Figure 4.23.

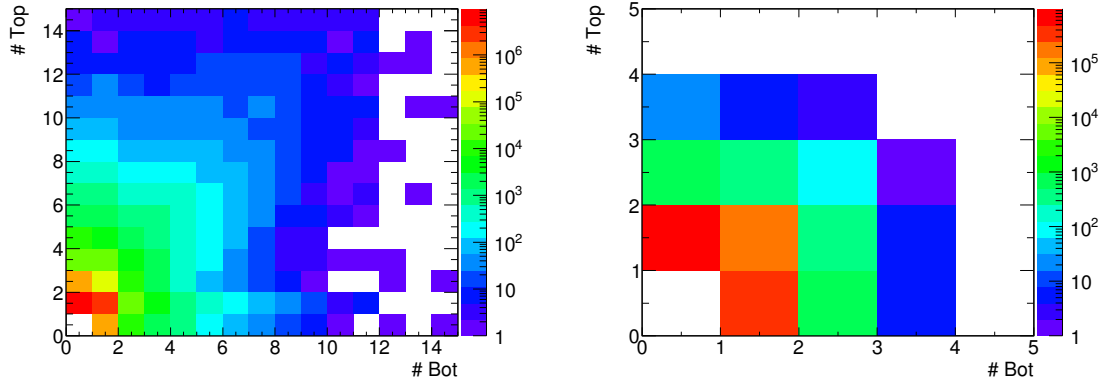


Figure 4.23: Comparison of the multiplicity of top and bottom muons before and after applying the analysis selection criteria are shown at left and right respectively.

The difference in curvature between top and bottom tracks $\delta c = 1/p_{\text{top}} - 1/p_{\text{bottom}}$ is shown in Figure 4.24 and Figure 4.25 for positive and negative tracks in ten momentum ranges $[0, 10]$ GeV, $(10, 15]$ GeV, $(15, 20]$ GeV, $(20, 35]$ GeV, $(35, 50]$ GeV, $(50, 75]$ GeV, $(75, 100]$ GeV, $(100, 200]$ GeV, $(200, 300]$ GeV, $(300, 1000]$ GeV. The distributions are fit to a double Gaussian where the means of the two Gaussians are independent in order to describe the asymmetric tails associated with the Landau tail

from energy loss fluctuations in the calorimeter. The mean of the narrower Gaussian in each fit serves as an estimate of the curvature scale, while the width, divided by $\sqrt{2}$, provides a measure of the curvature resolution. The fit results as a function of the momentum of the top track are shown in Figure 4.26.

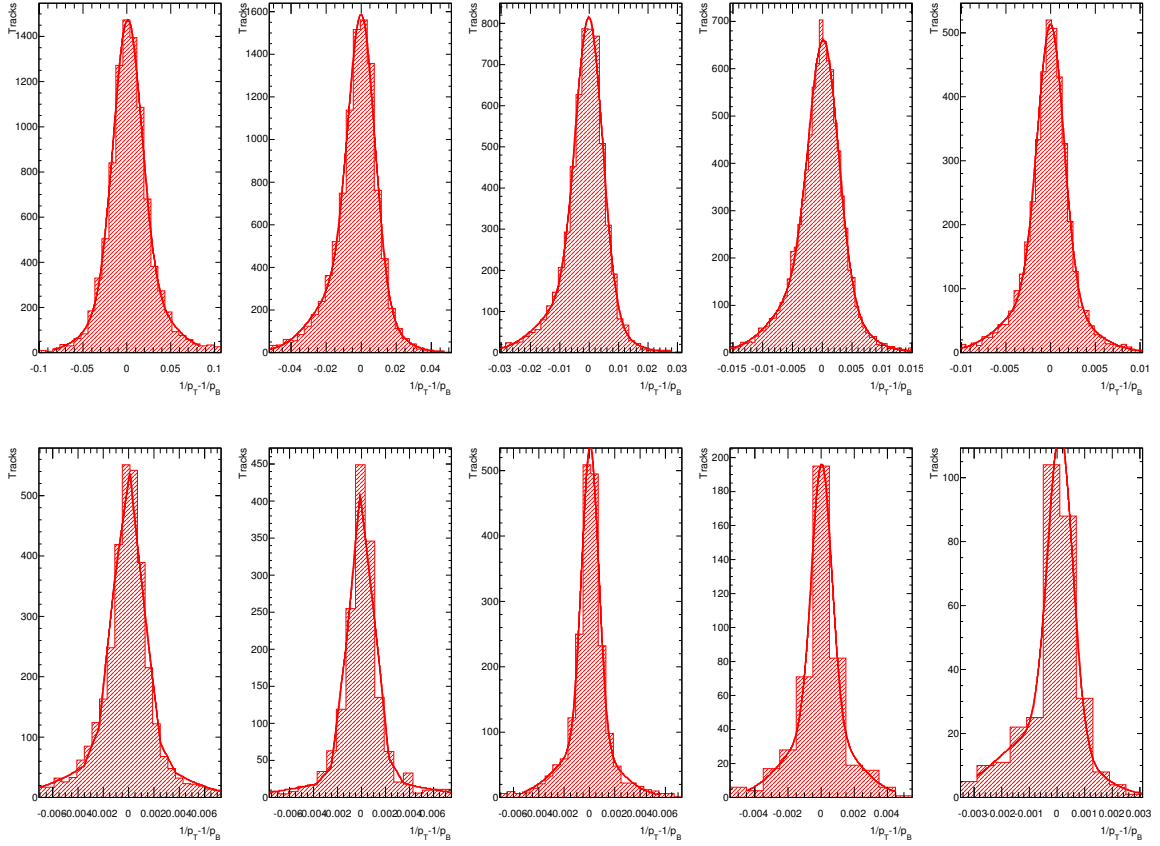


Figure 4.24: Distribution of $1/p_{\text{top}} - 1/p_{\text{bottom}}$ in bins of p_{top} , for positive muons, increasing in momentum from upper-left to lower-right. Each histogram is fit with two Gaussian functions.

The momentum dependence of the curvature scale is fit with the function $\mathcal{S}(p) = s_0 + s_1/p$ and the curvature resolution with $\mathcal{R}(p) = k_0 \oplus k_1/p$, where the two terms are added in quadrature. The coefficients k_0 and k_1 represent the contributions from

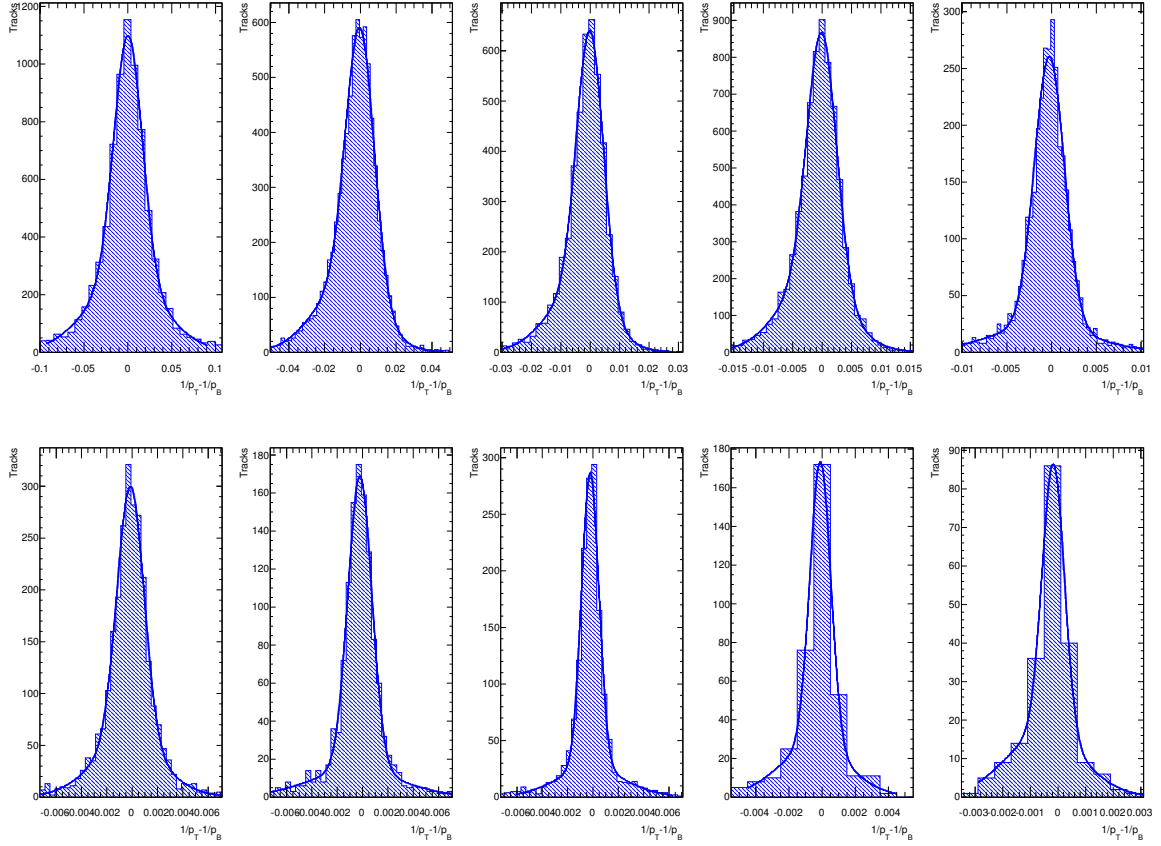


Figure 4.25: Distribution of $1/p_{\text{top}} - 1/p_{\text{bottom}}$ in bins of p_{top} , for negative muons, increasing in momentum from upper-left to lower-right. Each histogram is fit with two Gaussian functions.

intrinsic resolution and multiple scattering respectively. The curvature scale and resolution function fit results are shown in Table 4.3. These results are in general agreement with those described in [59].

The impact on the charge ratio is estimated using pseudo-experiments where the curvature of each track used in the measurement is shifted by the scale uncertainty and Gaussian-smearred by the resolution uncertainty. The distributions of charge ratios from 5,000 pseudo-samples are fit with a Gaussian whose width provides an estimate

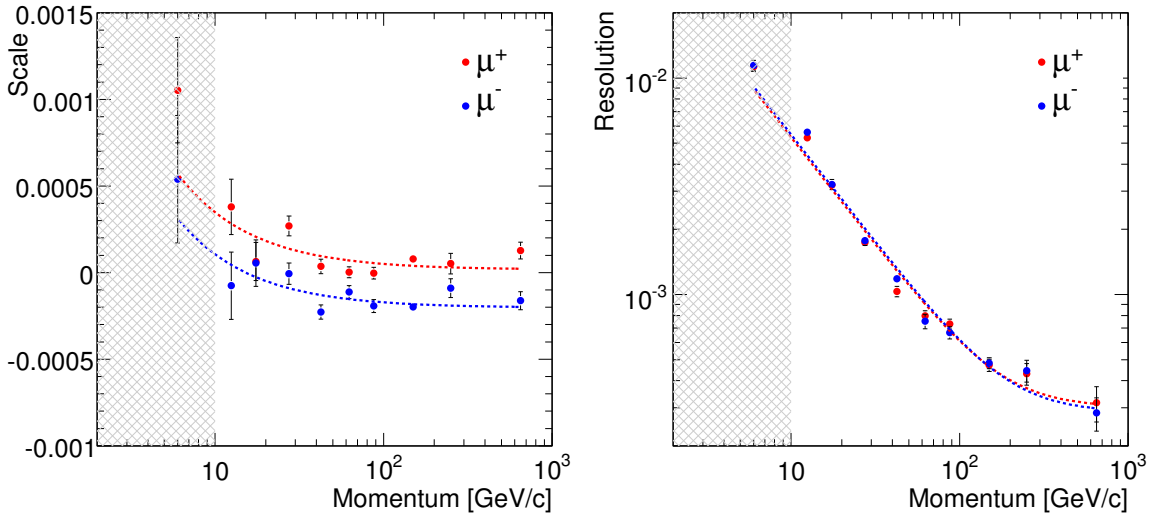


Figure 4.26: Curvature scale (left) and resolution (right), as a function of the muon candidate momentum measured in the top MS, for positive (red) and negative muons (blue). The region removed by the momentum requirement used in the analysis corresponds to the shaded area.

the momentum resolution uncertainty, while the difference between the mean of the fit Gaussian and the default ratio estimates the momentum scale uncertainty. The corresponding uncertainty ranges from under 1% up to 6%, constituting the dominant source of uncertainty in the highest momentum range, as indicated in Table 4.2.

Parameter		μ^+	μ^-
Multiple Scattering	[%]	5.32 ± 0.10	5.49 ± 0.12
Intrinsic Resolution	$[10^{-4} \text{ GeV}^{-1}]$	3.01 ± 0.30	2.86 ± 0.30
Scale s_0	[%]	0.33 ± 0.10	0.31 ± 0.11
Scale s_1	$[10^{-4} \text{ GeV}^{-1}]$	0.17 ± 0.19	-2.03 ± 0.21

Table 4.3: Resolution and scale fit results for positive and negative muons. The parameters are in good agreement between these samples, except for the curvature scale, which exhibits a moment-independent offset of about $2 \cdot 10^{-4} \text{ GeV}^{-1}$.

4.11.2 Surface-Cavern Correction

The systematic uncertainty due to the energy loss correction to the surface is estimated by varying the parameters used in the calculation. The main contributors to the uncertainties are the average rock density and the dimensions of the cavern. The nominal charge ratio compared to that obtained by replacing the average rock density above ATLAS with the maximum and minimum densities, using the values listed in Figure 4.19, and from varying the size of all the lengths such as the cavern depth and shaft size by $\pm 10\%$, are shown in Figure 4.27. The combined differences from all the effects considered, ranging from less than 0.5% to 1.6% and listed in Table 4.2, is used as the systematic uncertainty.

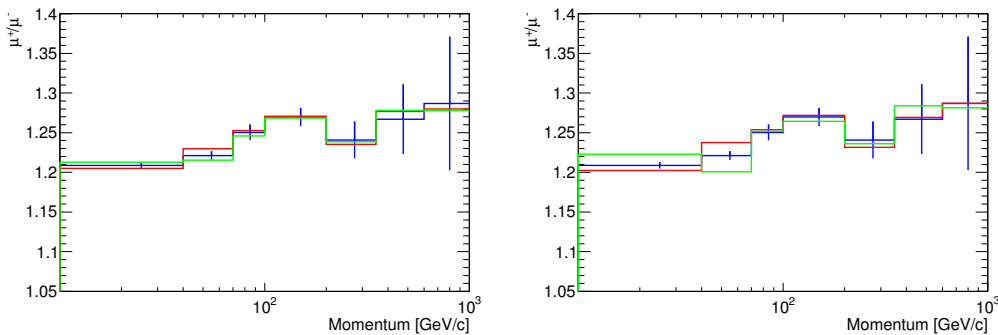


Figure 4.27: Systematic uncertainties evaluated for the surface-cavern momentum correction. Comparison of the ratio calculated with the average rock density above ATLAS (blue) with its maximum (red) and minimum (green) values at left. All lengths used to describe the ATLAS cavern are modified by +10% (red) and -10% (green) with respect to the default (blue) at right.

4.11.3 Tracking Efficiency

The tracking efficiency templates were varied within their uncertainties and the corresponding impact on the charge ratio is shown in Figure 4.28. Half the variation

in each bin serves as an estimate of the systematic uncertainty, contributing approximately 0.6% to the total error. The resulting absolute uncertainties are shown in Table 4.2.

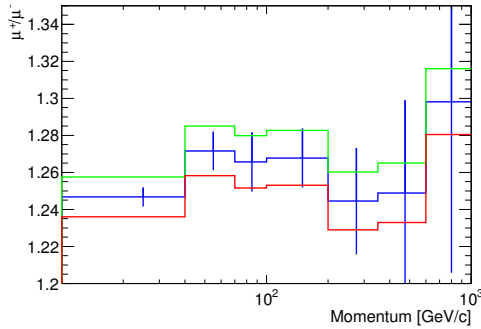


Figure 4.28: The default charge ratio (blue) is compared to that obtained by varying the tracking efficiency by $+1\sigma$ (green) and -1σ (red).

4.11.4 Selection Criteria

The selection criteria and acceptance corrections are checked for robustness by varying a range of selection criteria: trigger confirmation, low segment multiplicity, ϕ -sector crossing and MDT hit requirements. The impact of the selection criteria on the asymmetry is small, as shown in Figure 4.29 and in Table 4.2. These serve as tests for the robustness and are not included in the global systematic uncertainty.

4.12 Results

The charge asymmetry in cosmic muons in ATLAS is measured to be

$$\frac{\mu^+}{\mu^-}(p_{\text{surface}} > 40 \text{ GeV}) = 1.235 \pm 0.004 \text{ (stat.)} \pm 0.017 \text{ (syst.)}, \quad (4.6)$$

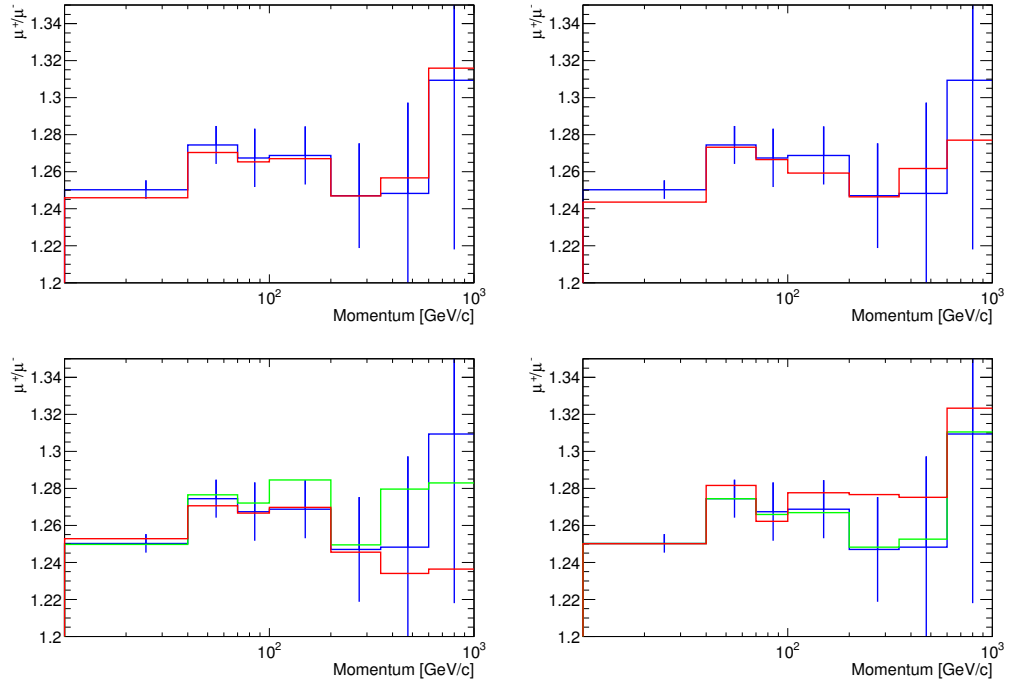


Figure 4.29: Comparison of the muon charge ratio with (blue) and without (red) the offline trigger confirmation applied to mirror and shadow tracks (upper left). Similarly for the requirement that real and mirror tracks are fully contained within one ϕ -sector (upper right). Impact of the removal of the segment per sector requirement (lower left) for < 5 segments (green), < 10 segments (blue) and when no requirement is applied (red). Impact of varying the number of MDT hits (lower right) in BI, BM, BO stations: 1, 1, 1 (green), 4, 5, 5 (blue), 7, 5, 5 (red).

and its momentum dependence is shown in Figure 4.30. The charge ratio for momenta measured in the ATLAS cavern, before the correction for the energy loss between the surface and the cavern, is

$$\frac{\mu^+}{\mu^-}(p_{\text{cavern}} > 10 \text{ GeV}) = 1.252 \pm 0.004 \text{ (stat.)}. \quad (4.7)$$

The difference between these two results is due to the inclusion of muons with momenta in the range 2 – 10 GeV in the measurement at the surface due to bin migrations. These muons do not affect the momentum-dependent ratio result in the most important bins where $p > 100$ GeV.

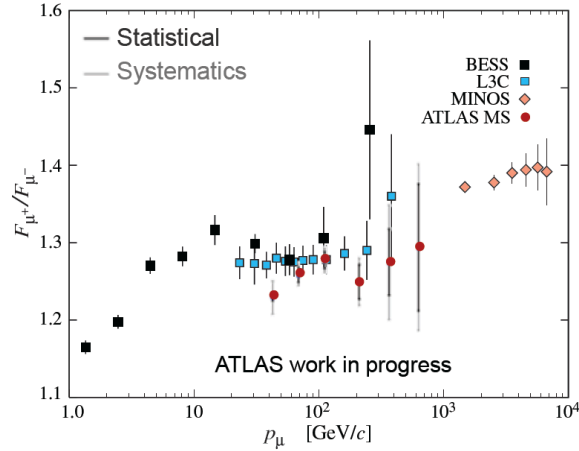


Figure 4.30: The charge ratio in cosmic ray muons measured in the ATLAS detector is shown as a function of the momentum corrected for energy loss as it passes from the Earth’s surface to the ATLAS cavern. The result of this analysis is comparable to previous measurements of cosmic charge asymmetry, taken from [60].

4.13 Conclusions

This chapter presents an analysis of the muon charge ratio $R^\mu = N_{\mu^+}/N_{\mu^-}$ in cosmic-ray data using the ATLAS MS. The measurement of the ratio as a function of momentum includes the range between 400 GeV and 1 TeV, unexplored in previous measurements. For momenta above 10 GeV, the overall measurement is 1.235 ± 0.004 (stat.) ± 0.025 (syst.), consistent with previous results. The large cosmic-ray sample acquired by the detector in 2009 provided an opportunity for detailed studies of the muon spectrometer performance ahead of high-energy collisions. Special attention is paid to the understanding of the detector acceptance for different muon charges, the muon tracking resolution and the momentum scale, and some of these techniques have been used in the early collision data period, when muon tracks with transverse momenta above 10 GeV were scarce. This sample still provides the most detailed information for muons in the momentum range 0.5 – 1 TeV.

Chapter 5

$W \rightarrow \mu\nu$ Event Selection and First Asymmetry Measurement

This chapter describes the first W charge asymmetry measurement in the muon decay channel performed in ATLAS with a dataset corresponding to about 310 nb^{-1} of integrated luminosity. It includes a description of the criteria used to select $W \rightarrow \mu\nu$ candidate events and the measurement of the W inclusive production cross section. These first W measurements were published at the end of 2010 [1] and established the bases for the differential W charge asymmetry measurement described in Chapter 6.

W bosons are expected to be produced abundantly at the LHC, so the startup of the pp collisions at $\sqrt{s} = 7 \text{ TeV}$ presents an opportunity to study their production at a new energy scale. The well known properties of the W boson, in conjunction with the Z boson, provide important constraints on the detector performance, including an understanding of the energy and momentum scale and resolution, and

lepton identification and trigger efficiencies. The first step is the identification of W and Z events at the LHC. An observation was performed in ATLAS using 40 candidate $W \rightarrow \mu\nu$ events from a dataset corresponding to an integrated luminosity¹ of 6.4 nb^{-1} , collected over a seven week period from March to May 2010 [73]. An event display of one of the first $W \rightarrow \mu\nu$ candidate events is shown in Figure 5.1. A preliminary measurement of the W production cross section and charge asymmetry was performed [74] in the Summer of 2010, culminating in the published results that are described in this chapter.

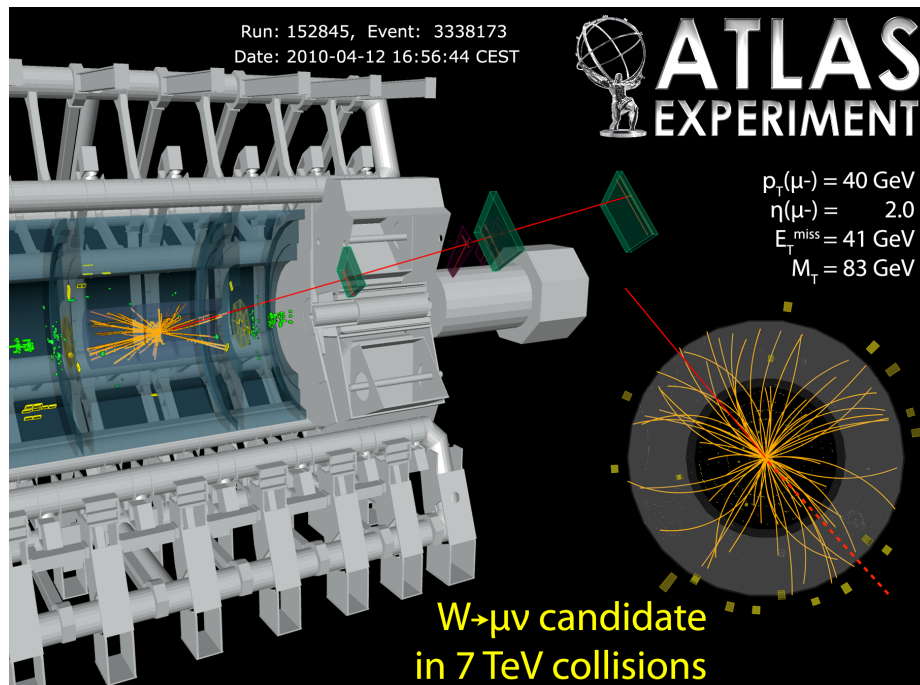


Figure 5.1: Event display of one of the first $W \rightarrow \mu\nu$ candidate events recorded in ATLAS from April 12, 2010. A negatively charged muon with $p_T = 40 \text{ GeV}$ is reconstructed in the MS endcap at $\eta = 1.1$.

¹The uncertainty on the luminosity determination for this analysis is of the order of 20%.

5.1 Event and Object Reconstruction

5.1.1 Inner Detector Tracking

The reconstruction algorithms in the ID allow for the formation of tracks associated with charged particles and vertices. Track reconstruction provides measurements of the parameters of charged particles traversing the tracker ($|\eta| < 2.5$ for the pixel and SCT and $|\eta| < 2.0$ for the TRT). The pattern recognition algorithm [75] searches for prompt tracks, originating in the interaction region. It starts with the silicon detectors, namely the pixel and the SCT, benefitting from the high granularity of these detectors. The silicon hits are clustered and converted into three-dimensional space points, as described in Section 3.3. Track seeds are formed from combinations of three space points in three distinct layers, and extended to the remaining layers. Good track candidates with transverse momenta above 100 MeV are refit. Track candidates are extended into the TRT, associating hits in a road around the track path and finally refit into a track. If the track fit with the associated TRT hits improves the fit result, a global ID track is formed. If not, the silicon component alone is used in the fit and the TRT extension is maintained in association with the track.

Since this tracking algorithm requires multiple silicon hits in the formation of track seeds, it is inefficient for the reconstruction of tracks from secondary interactions such as long-lived hadron decays. Therefore another step in the algorithm starts with track segments in the TRT that have not previously been associated with a track. The track segments are extended into the silicon tracker forming a road in $r - \phi$.

Previously unassigned silicon space points are added to the track candidate until finally the tracks are refit. This second step recovers tracks with momenta above 300 MeV, see [76] for general information on the ID tracking performance.

5.1.2 Primary Vertex Reconstruction

The reconstruction of primary vertices (PV) in the interaction region serves to identify a collision event. In particular, the requirement for at least three ID tracks being associated with a vertex in the luminous region rejects non-collision backgrounds such as beam halo and cosmic rays. The primary vertex reconstruction algorithm [77] forms vertex candidates by associating tracks and then fits for the vertex position. The tracks associated with the vertex are also refit using the reconstructed interaction point as constraint. Tracks with transverse momentum of at least 150 MeV and with hits in the silicon detector compatible with an origin in the interaction region² are selected. A vertex seed is established at the maximum of the z coordinate distribution of the tracks defined with respect to the center of the beam spot. An adaptive multi-vertex fitter algorithm is used to fit all the tracks iteratively. Tracks considered outliers in a vertex fit are used to form another vertex candidate. As a result, multiple vertices are simultaneously fitted until no tracks or vertices remain.

Studies of the properties and performance of the primary vertex reconstruction indicate [78, 79, 76] that the luminous region was well centered in ATLAS during 2010 runs. It was within a few hundred microns in x and y , about 1 mm in z from

²The interaction region is determined from a fit to the primary vertex distribution where vertices are reconstructed without the luminous region constraint.

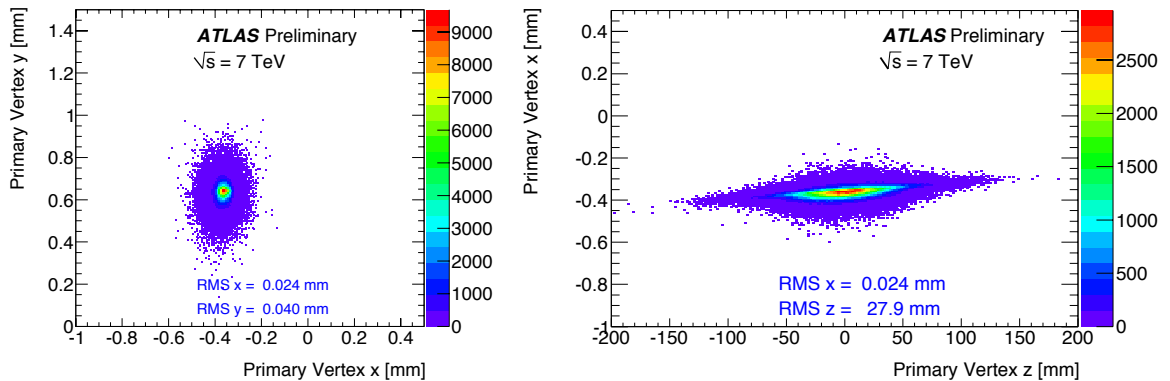


Figure 5.2: Two-dimensional distribution of reconstructed primary vertices in 7 TeV data, in the x-y plane (left) and in the z-x plane (right), from [78].

the nominal position, and with about a 20 mm width in z , see Figure 5.2, stable to within about 1 mm. The efficiency in finding a primary vertex with at least three tracks is close to 100%, with a fake rate of about 1%. Finally, the position resolution is about $15 \mu\text{m}$ and $50 \mu\text{m}$ perpendicular and along the beam directions respectively. The vertex with the highest sum- p_T^2 of tracks serves as the primary one.

5.1.3 Combined Muon Reconstruction

The combined tracking of muons reconstructs the trajectory of particles in both the ID and the MS. This improves the measurement of the track parameters provided by each component alone. At low momentum, Coulomb scattering in the material upstream of the MS degrades the momentum resolution. For muons in the p_T -range less than about 100 GeV in the barrel and about 20 GeV in the endcap, the ID provides better p_T measurement relative to the MS. The combination of the ID and MS for these momentum ranges is still important in order to reject fakes. The ID and MS tracks are reconstructed separately and their combination is carried out by

dedicated algorithms: MuID for the MOORE tracks and STACO for the Muonboy tracks.

The main difference between the MuID and STACO algorithms is that the former performs a full track refit, accounting for material and magnetic field effects, while the latter uses a statistical combination to merge the ID and MS track parameters into combined parameters given by

$$T = (C_{MS}T_{MS} + C_{ID}T_{ID})/(C_{MS} + C_{ID}) \quad (5.1)$$

where T is the combined track vector of five track parameters expressed at the perigee, $T_{ID/MS}$ are the corresponding ID and MS track parameters and $C_{ID/MS}$ are the covariance matrices for the ID and MS components respectively. A combination is successful if it is below a match χ^2 requirement. If more than one combination is allowed, the one with the lowest χ^2 is kept and the procedure repeated until all possible combinations are found. The studies presented in this dissertation use the STACO combined tracks with a match $\chi^2 < 200$ requirement.

5.1.4 Alignment Status of the ID and MS Trackers

The ID and MS trackers have been assembled following precise configurations but accuracy of the knowledge of the position of the various detector elements is less than the intrinsic resolution due for example to limitations in the assembly of the detectors, mechanical stress, sagging and temperature gradients. The detector alignment attempts to correct for differences between the nominal geometry and the actual spatial configuration, in order to provide the most accurate measurement of the position

of the individual hits used for track reconstruction. The initial alignment of the detector in preparation for first collisions was based on hardware information: from sources such as surveys and dedicated optical alignment systems, and also included alignment corrections derived from tracks, mainly from cosmic ray runs.

For the ID, the alignment goal is a knowledge of the position and orientation of the detector modules with an uncertainty in the position of about $10 \mu\text{m}$. The alignment parameters used for first 7 TeV collisions were derived using tracks from cosmic ray data from 2008 and 2009, and collision data at 900 GeV from 2009 [80]. The procedure used calculates the best values for a range of alignment parameters with a χ^2 minimization algorithm using the track-hit residuals. The performance has been studied with the first collision data at 7 TeV and found to be of about $17 \mu\text{m}$ for the pixels in the barrel region. There are limitations to the initial alignment since the cosmic rays, entering from the shafts above, provide a highly uneven detector illumination. In particular, the sides of the barrel and the endcaps do not have alignment corrections at the same level of precision as the barrel top and bottom. The alignment of the ID has been much improved subsequently due to a large sample of tracks from 7 TeV collisions becoming available (see for example [81]).

The MS has also been aligned with information including data from cosmic ray runs and the optical alignment system [59]. This tracker has very good overall alignment, with most MDT chambers being aligned to within $100 \mu\text{m}$. However, there are a few regions that suffer from poorer alignment, due primarily to missing or degraded optical links. In addition, the position of the MS with respect to the ID is known at

the mm level. Estimates of the muon resolution for the different regions of the MS at the time of first collisions are shown in Table 5.1. Performance studies suggest that misalignments in the CSC region are worse than has been indicated, but this is not unexpected since the CSC chamber alignment was not validated with cosmic muons.

Region	Resolution
Barrel Large sectors	50 μm on sagitta
Barrel Small sectors	< 150 μm on sagitta
EndCap Small+Large	50 μm on sagitta
BEE	10 mm on translations
BIS8	20 mm on translations
EIL5	5 mm on translations
CSC Large+Small	200 – 400 μm on sagitta
EEL A-11, C-13	50 μm on sagitta
EEL A-13, C-15	150 – 200 μm on sagitta
EEL A-05, C-05	5 mm on translations
Barrel/EndCap	1 mm on translations
MS/ID	1 mm on translations

Table 5.1: Estimate of expected muon resolutions for different regions of the MS.

5.1.5 Missing Transverse Energy Reconstruction

Due to the presence of the neutrino, which is not measured by the detector, W bosons cannot be reconstructed directly. Instead, the neutrino transverse momentum is inferred from the energy imbalance in the transverse plane. The $E_{\text{T}}^{\text{miss}}$ can be calculated by adding the energy and momenta of all particles in the event: summing the energy depositions in the calorimeter and including the muon p_{T} . Energy depositions in calorimeter cells are combined into three-dimensional topological clusters [82]. Cells with energy levels significantly above the noise threshold³ $E > 4\sigma_{\text{noise}}$ seed the cluster-

³ σ_{noise} is the Gaussian width of the cell energy distribution in randomly triggered events

finding algorithm. Secondary neighboring cells with $E > 2\sigma_{\text{noise}}$ are then associated and finally all direct neighbors of the secondary cells are added. The baseline energy scale assumes that all processes are electromagnetic, so the cluster energy is corrected for hadronic response as well as energy losses due to dead material and out-of-cluster deposits [83].

The missing transverse energy is calculated from the sum of all the topological cluster energy components $E_{x,y}$. Since muons typically do not deposit a significant fraction of their energy in the calorimeter, the momentum measurement of all muons in the event, both isolated and non-isolated in the range $|\eta| < 2.7$, is included in the $E_{\text{T}}^{\text{miss}}$ calculation. The resulting definition is

$$E_{x,y}^{\text{miss}}|_{\mu} = -\sum_i E_{x,y}^i - \sum_j^{\text{isolated}} p_{x,y}^j - \sum_k^{\text{non-isolated}} p_{x,y}^k. \quad (5.2)$$

For isolated muons, the combined p_{T} measurement is used and a correction is made for the energy deposited by the muon in the calorimeter. In the case of non-isolated muons, defined as muons within $\Delta R \leq 0.3$ of a jet in the event, and for muons beyond the coverage of the ID ($2.5 < |\eta| < 2.7$), the MS standalone p_{T} measurement is used⁴. The $E_{\text{T}}^{\text{miss}}$ performance has been studied in the early data [84]. Its measurement is limited by the coverage of the detectors (including holes and cracks), as well as the presence of dead or noisy regions inside them. In the case of the muons, limited coverage up to $|\eta| < 2.7$ and the presence of gaps in the central MS region, imply that some muons escape detection and contribute to the missing transverse energy.

⁴In the case of non-isolated muons, if the MS standalone p_{T} and combined p_{T} measurements are very different from each other, the combined measurement is used and a parametrization for the expected energy loss in the calorimeter serves to correct the calorimeter contribution.

5.2 Data and Simulated Monte-Carlo Samples

The dataset used was collected from March to July 2010. After applying basic beam, detector and data-quality requirements, the total integrated luminosity was 316 nb^{-1} , with an uncertainty of 11% [54]. The trigger used is based on the L1 information alone, with a p_T threshold of 6 GeV, corresponding to the single muon trigger with the lowest p_T threshold available, providing a total of 5.1×10^6 events.

The main backgrounds to $W \rightarrow \mu\nu$ arise from:

- $W \rightarrow \tau\nu$, particularly where the tau decays leptonically $\tau \rightarrow \mu\nu\nu$.
- $Z \rightarrow \mu\mu$ where one of the muons is outside the detector acceptance range, generating E_T^{miss} .
- $Z \rightarrow \tau\tau$ where at least one of the tau decays leptonically $\tau \rightarrow \mu\nu\nu$, constituting a smaller additional background.
- $t\bar{t}$ with a leptonic decay also contributes a smaller background due to the lower production cross section.
- Jet production via QCD processes, mainly from semi-leptonic decays of heavy quarks and decays in flight.

The Monte Carlo (MC) signal and background processes used for comparison with the data, the estimation of some backgrounds and the acceptance calculation are listed in Table 5.2. The signal and background samples (except $t\bar{t}$) have been generated with PYTHIA 6.421 [85] using the MRST 2007 LO* [86] PDF set. The $t\bar{t}$ sample

was generated with a POWHEG-HVQ v1.01 patch 4 [87] using the CTEQ 6.6M [15] PDF set for the NLO matrix element calculations and the CTEQ 6L1 set for the parton showering and underlying event performed through the POWHEG interface to PYTHIA. Photons radiated from charged leptons were treated using PHOTOS v2.15.4 [88] and the tau decays are simulated with TAUOLA v1.0.2 [89]. The underlying and pileup events were simulated following the prescription of the ATLAS MC09 tune [90]. The samples generated were passed through the GEANT4 [91] simulation of the ATLAS detector [92], reconstructed and analysed with the same analysis chain as the data. The cross section predictions for W and Z were calculated to next-to-next-to-leading-order (NNLO) using FEWZ [30] with the MSTW 2008 [17] PDF set. The $t\bar{t}$ cross section was calculated at NLO (plus next-to-next-to-leading-log, NNLL) with POWHEG [93].

The simulated samples were generated with an average of two minimum bias collisions overlaid on top of the hard-scattering event. Events in the MC samples are weighted so that the distribution of the number of inelastic collisions per bunch crossing matches that in data. During this analysis period, the data had approximately one additional interaction per event.

5.3 Event Selection

The selection of candidate events includes the selection of a collision-like event, high- p_T muon requirements and W event selection. The criteria are summarized in Table 5.3. Collision candidates are selected with a PV with at least three tracks,

Physics process	Generator	$\sigma \cdot \text{BR}$ [nb]	
$W \rightarrow l\nu$ ($l = \mu, \tau$)	PYTHIA 6.4.21 [85]	10.46 ± 0.52	NNLO [30]
$W^+ \rightarrow l^+\nu$		6.16 ± 0.31	NNLO [30]
$W^- \rightarrow l^-\bar{\nu}$		4.30 ± 0.21	NNLO [30]
$Z/\gamma^* \rightarrow ll, m_{ll} > 60 \text{ GeV}$	PYTHIA 6.4.21 [85]	0.99 ± 0.05	NNLO [30]
$t\bar{t}$	POWHEG-HVQ v1.01 patch 4 [87]	0.16 ± 0.01	NLO+NNLL [93]
Dijet (μ channel, $\hat{p}_T > 8\text{GeV}, p_T^\mu > 8\text{GeV}$)	PYTHIA 6.4.21 [85]	10.6×10^6	LO [85]

Table 5.2: Signal and background MC samples used in the W asymmetry analysis and the production cross section times the corresponding branching ratio (BR). The variable \hat{p}_T is the average p_T of the two outgoing partons involved in the hard-scattering process, before modifications from initial and final-state radiation and from the underlying event.

consistent with the beam spot position. In addition, the PV is required to be within 15 cm of the geometrical center of the detector in z . These requirements remove non-collision backgrounds from cosmic rays and beam halo. They would mimic $W \rightarrow \mu\nu$ if half the track is lost. The requirement is highly efficient for collision events since the width of the PV distribution in z was 6.2 cm.

Studies of minimum bias events in the first collision data occasionally found localized very high-energy deposits in the calorimeter, associated with noise spikes or cosmic rays [94]. These rare events can impact the E_T^{miss} measurement and hence are removed from the analysis sample. The requirements applied, referred to as “cleaning cuts”, reject 0.004% of $W \rightarrow l\nu$ events in simulation. In addition, the muon is required to be consistent with the PV, requiring $|z_0 - z_{vtx}| < 10 \text{ mm}$, where z_0 is the position of the track extrapolated to the beam line.

Collision event selection	
Primary vertex	$N_{vtx} \geq 1$ with $N_{tracks} \geq 3$ $ z_{vtx} < 150$ mm
Jet cleaning	cleaning cuts
Trigger	L1_MU6
High- p_T event selection	
Muon selection	combined tracks $p_T > 20$ GeV, $ \eta < 2.4$
Muon quality	$p_T^{MS} > 10$ GeV $ p_T^{MS} - p_T^{ID} < 15$ GeV $ z_0 - z_{vtx} < 10$ mm
$W \rightarrow \mu\nu$ event selection	
ID isolation	$\sum p_T^{ID} / p_T < 0.2$
Missing transverse energy	$E_T^{\text{miss}} > 25$ GeV
Transverse Mass	$m_T > 40$ GeV

Table 5.3: Event selection used for W candidates.

The high- p_T muon selection criteria are devised from detailed performance studies [95, 96]. The analysis uses only combined muons, since these provide the best momentum resolution and the lowest fake rate, particularly against muons from pion and kaon decays. The range $|\eta| < 2.4$ is limited by the geometrical coverage of the muon trigger chambers. Muons are selected with a transverse momentum $p_T > 20$ GeV, although muons in the $15 < p_T < 20$ GeV range are used as a control sample for estimation of the QCD background (see Section 5.4.2).

In order to reject backgrounds from decays in flight, the MS component has a large transverse momentum $p_T^{MS} > 10$ GeV requirement. Track reconstruction mismatches in the ID and MS are rejected based on the difference between the p_T for the ID and MS components, where the MS component is corrected for the energy loss in material before the spectrometer, with the requirement $|p_T^{ID} - p_T^{MS}| < 15$ GeV. These

mismatches arise from particle decays, particularly charged pions and kaons, where the momentum of the meson in the ID and the decay muon in the MS is very different due to the emission of a neutrino.

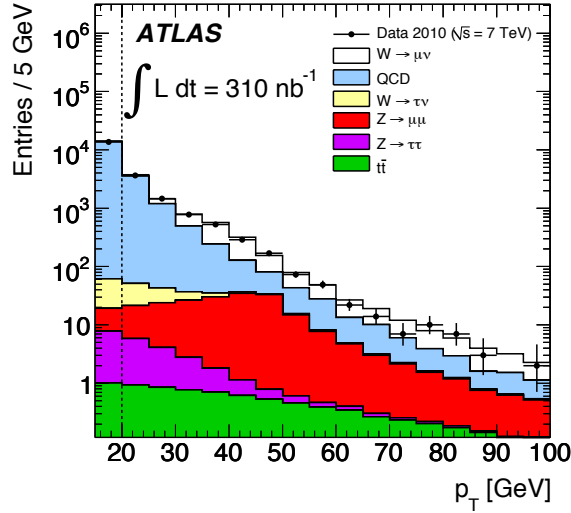


Figure 5.3: Muon p_T distribution to compare data and MC simulation shows contributions from signal and background processes. The vertical line corresponds to the selection requirement used in the W candidate selection. The sample in the range $15 < p_T < 20$ GeV is primarily QCD background and serves as a control sample for this background estimate.

The muon p_T distribution after applying the high- p_T muon selection criteria is shown in Figure 5.3. At this stage the sample is dominated by the QCD background, so further requirements are applied to increase the signal fraction. The distribution of a track-based isolation parameter, defined as the sum of inner detector tracks in a cone of size $\Delta R < 0.4$ around the muon track divided by the muon p_T , is shown in Figure 5.4 (left). A requirement removing the sample in the tail of this isolation variable is effective in enhancing the signal-to-background ratio. Background muons are often produced within a jet of particles, corresponding to large values of

the isolation variable, while muons from W bosons tend to be produced away from hadronic activity. The requirement used in the analysis is $\sum p_T^{ID}/p_T < 0.2$ rejects over 84% of the expected QCD background, while maintaining $(98.4 \pm 1.0)\%$ of signal events.

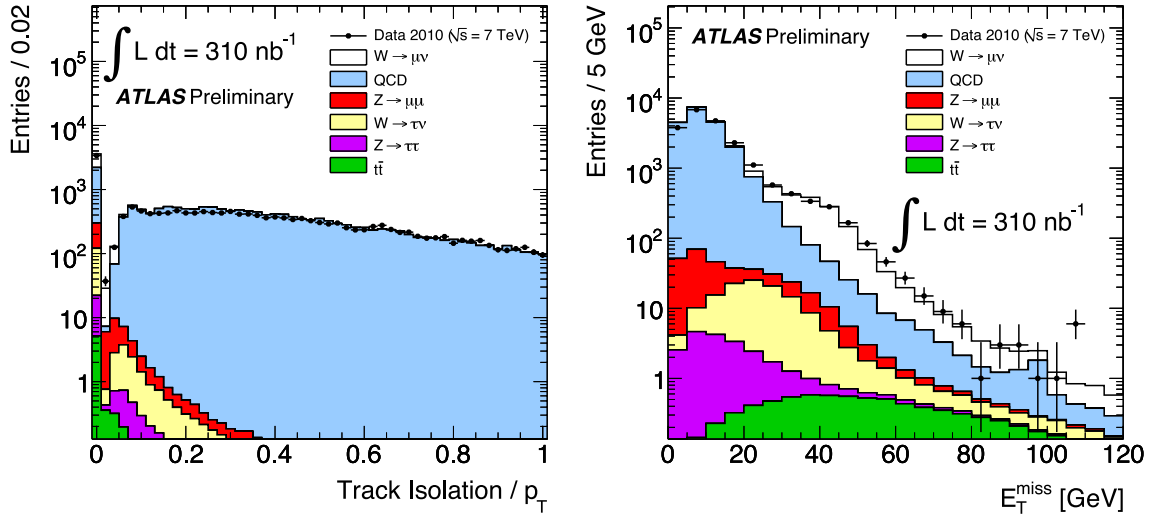


Figure 5.4: Muon isolation (left) and E_T^{miss} (right) for events with a muon passing the quality selection criteria with $p_T > 15$ GeV (high- p_T event selection). The sample is dominated by QCD background and requirements for isolation of $\sum p_T^{ID}/p_T < 0.2$ and the $E_T^{\text{miss}} > 25$ GeV serve to reject it.

The E_T^{miss} distribution in events satisfying the high- p_T muon selection criteria is also shown in Figure 5.4 (right). Signal events populate the large E_T^{miss} region due to the escaping neutrino in the W decay, while backgrounds are mainly in the lower E_T^{miss} range. A requirement for the missing transverse energy is applied in the candidate selection, $E_T^{\text{miss}} > 25$ GeV, further rejecting backgrounds. The transverse mass distribution of the muon- E_T^{miss} distribution is defined in terms of the azimuthal angle

between the muon and the E_T^{miss} , $\Delta\phi$, as

$$m_T = \sqrt{2p_T E_T^{\text{miss}}(1 - \cos \Delta\phi)}. \quad (5.3)$$

The m_T distribution before and after applying the E_T^{miss} requirement is shown in Figure 5.5. The MC simulation reproduces well the behavior of the data. Final W candidates are selected with $m_T > 40$ GeV, yielding a total of 1181 candidates. A candidate event display is shown in Figure 5.1, where the event includes a muon with $p_T = 40$ GeV, $E_T^{\text{miss}} = 41$ GeV and $m_T = 83$ GeV, consistent with a W decay.

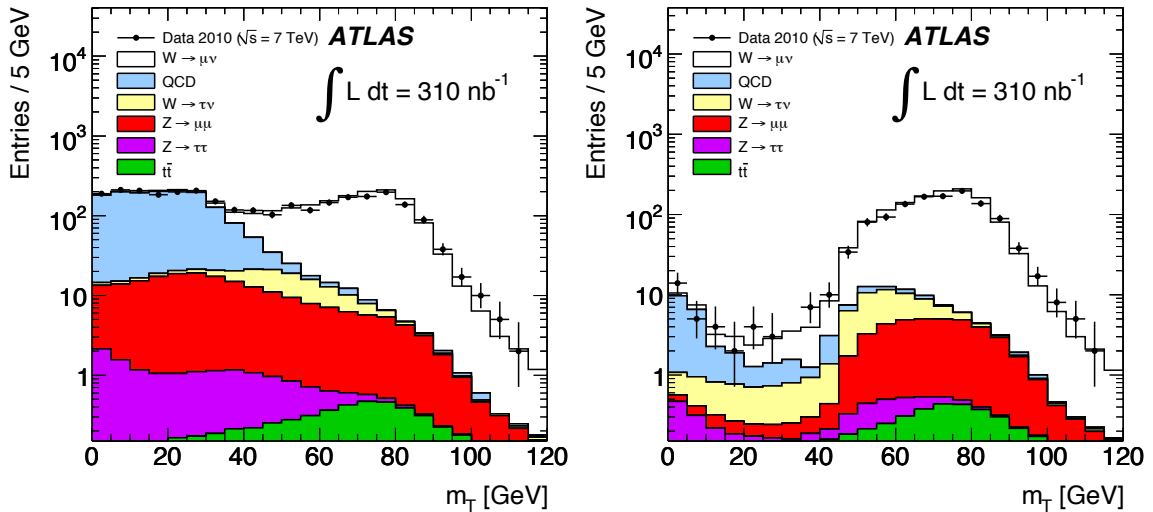


Figure 5.5: Transverse mass distribution of the muon- E_T^{miss} system before and after applying the E_T^{miss} requirement (at left and right respectively), comparing data and MC simulation for the signal and backgrounds.

5.4 Background Estimation

The backgrounds to $W \rightarrow \mu\nu$ arise primarily from processes involving real W and Z bosons, and from QCD events. The estimate of the background contribution from

l	Observed candidates	Background (EW+ $t\bar{t}$)	Background (QCD)	Signal Yield $N - B$
μ^+	710	$42.5 \pm 0.2 \pm 2.9$	$12.0 \pm 3.0 \pm 4.6$	$655.5 \pm 26.6 \pm 6.2$
μ^-	471	$35.1 \pm 0.2 \pm 2.4$	$10.9 \pm 2.4 \pm 4.1$	$425.0 \pm 21.7 \pm 5.4$
μ^\pm	1181	$77.6 \pm 0.3 \pm 5.4$	$22.8 \pm 4.6 \pm 8.7$	$1080.6 \pm 34.4 \pm 11.2$

Table 5.4: The number of observed candidate events, electroweak and $t\bar{t}$, and QCD background estimates, and signal yield. The statistical and systematic uncertainties are shown separately. The 11% uncertainty on the luminosity, applicable to the EW and $t\bar{t}$ backgrounds, is not included.

electroweak (EW) and top sources is derived from MC, while a data-driven estimate is used for the QCD background. Contamination from cosmic rays is estimated to be small, though is also included in the analysis. The number of observed candidate events, background estimations for the EW and $t\bar{t}$, and QCD backgrounds and the corresponding signal yield are summarized in Table 5.4.

5.4.1 Electroweak and $t\bar{t}$ Backgrounds

One category of $W \rightarrow \mu\nu$ backgrounds includes high- p_T muons due to the presence of a real W or Z boson. The background processes considered are: $W \rightarrow \tau\nu$, $Z \rightarrow \mu\mu$, $Z \rightarrow \tau\tau$, and $t\bar{t}$. In the case of $W \rightarrow \tau\nu$ and $Z \rightarrow \tau\tau$, the muon is produced by a τ lepton decay. The expected backgrounds are estimated from MC, scaled by the NNLO or NLO+NNLL cross sections and normalized to the integrated luminosity of the data sample. The predictions are scaled by trigger and reconstruction efficiency corrections (Sections 5.5 and 5.6).

5.4.2 QCD Background

The QCD background to $W \rightarrow \mu\nu$ decays comes primarily from b and c quark decays, with smaller contributions from decays in flight and fakes. Contributions from these background sources are estimated using a data-driven method due to the large uncertainty in the dijet cross section and the difficulties in simulating hadron decays faking muons.

The background expectation is estimated using the “matrix” method whereby the sample of events that pass the full W selection criteria, except for the isolation requirement, is compared before and after its application. This distinguishes a loose from a tight sample that can be defined in terms of a QCD and non-QCD component. Mathematically, let N_{loose} be the number of events in data satisfying all requirements except for the isolation, and N_{tight} the number of events after the relative track-isolation requirement is also imposed. Let $\epsilon_{\text{non-QCD}}$ and ϵ_{QCD} denote the relative isolation efficiencies for non-QCD events (signal, electroweak and $t\bar{t}$ sources) and for the QCD background respectively, then

$$\begin{aligned} N_{\text{loose}} &= N_{\text{non-QCD}} + N_{\text{QCD}} \\ N_{\text{tight}} &= \epsilon_{\text{non-QCD}} N_{\text{non-QCD}} + \epsilon_{\text{QCD}} N_{\text{QCD}} \end{aligned} \quad (5.4)$$

yielding

$$N_{\text{QCD}} = \frac{N_{\text{loose}} \epsilon_{\text{non-QCD}} - N_{\text{tight}}}{\epsilon_{\text{non-QCD}} - \epsilon_{\text{QCD}}}. \quad (5.5)$$

The muon isolation efficiency for non-QCD events is measured in data with dimuon events from the $Z \rightarrow \mu\mu$ sample, yielding 0.993 ± 0.010 . The efficiency for QCD events

is estimated in a control sample of low p_T muons ($15 < p_T < 20$ GeV) extrapolated to the high- p_T signal region using the simulated multijet sample. Since samples obtained before and after isolation can be defined in terms of a QCD and non-QCD component, the expected number of QCD events after the isolation (tight) requirement in the signal region ($\epsilon_{\text{QCD}}N_{\text{QCD}}$) can thus be determined. The resulting background prediction is 21.1 ± 4.5 (stat) ± 8.7 (syst), where the dominant source of systematic uncertainty arises from the uncertainty in the isolation efficiency for QCD events.

A cross check of the QCD background estimate has been performed by comparing control samples in the E_T^{miss} and lepton isolation plane [47]. The four separate regions defined in terms of the E_T^{miss} and lepton isolation variables are shown in Figure 5.6. The number of QCD background events in the signal region, high E_T^{miss} and low isolation, is given by the number of non-isolated events in the high E_T^{miss} region scaled by the isolation efficiency factor at low E_T^{miss} . The estimate subtracts contributions from the signal and EW and $t\bar{t}$ backgrounds, and accounts for the correlation between the E_T^{miss} and lepton isolation using simulation. The resulting prediction is 13.5 ± 0.9 (stat) ± 12.7 (syst). Another cross check is performed by comparing the non-isolated muons in simulation and data, indicating that the MC over-estimates the rate by a factor of 1.6. The E_T^{miss} distribution in data and simulation after reversing the isolation requirement are shown in Figure 5.6. Applying this scale factor to the estimate provided by the dijet simulated sample yields a prediction of 9.7 ± 0.4 . The resulting predictions are all consistent with each other.

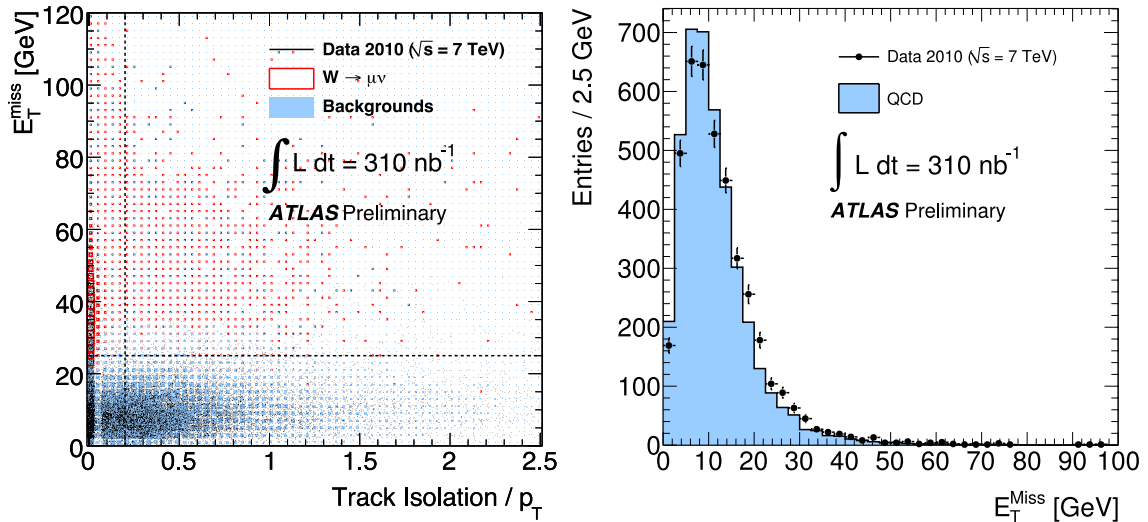


Figure 5.6: Comparison of the E_T^{miss} and muon track isolation variable in events passing the high- p_T lepton requirement (left). The horizontal and vertical lines correspond to the values used to define the signal region. The E_T^{miss} distribution in data and simulation after reversing the muon isolation requirement (right).

5.4.3 Cosmic Ray Background

Another source of background arises from cosmic ray muons that overlap a minimum bias collision event. This background contribution has been estimated using a sample of muons in non-collision bunches where the W selection criteria is applied. This yields an estimate of 1.7 ± 0.8 events.

5.5 Muon Reconstruction Efficiency

The muon reconstruction efficiency for a combined muon relative to an inner detector track was measured using data and compared to simulation by two approaches. The first method, called the MS hit technique, measures the efficiency to reconstruct an isolated combined track relative to an ID track matched to hits in the muon spec-

trometer. The method is based on the techniques developed for cosmic rays, described in Section 4.8. Collision events are selected with a high quality isolated ID track. The ATLAS extrapolator tool [71] is used to extend the trajectory of the ID track into the MS and raw hits are checked in the vicinity of the extrapolated path. If multiple tube layers in at least two MDT stations have raw hits, the ID track is tagged as a muon. The efficiency is defined as the fraction of tagged ID tracks that are matched to a combined track.

The main difficulty with applying this efficiency measurement to the W sample is that the tagged ID track sample is contaminated by decays in flight. These are more likely to fail the combined track reconstruction requirements, lowering the efficiency and introducing bias. The background contribution from decays in flight has been estimated from fitting the MDT hit residual distribution in data to simulation templates. A MC sample of W s is used for the prompt muons and a single pion sample for the decays in flight. The background contamination and efficiency calculation correction is determined from the fit and the result is shown in Figure 5.7 (left). The resulting efficiency is 0.994 ± 0.006 (stat) ± 0.024 (syst), compared to 0.986 in simulation. This measurement has a small statistical uncertainty due to the large sample size, but suffers from a large systematic uncertainty due to contamination from decays in flight. This method was particularly important early on when there was little statistics from dimuon events associated with the Z resonance.

The second method is based on dimuon events associated with the Z boson resonance. The advantage of this method compared to the MS hit technique is that the

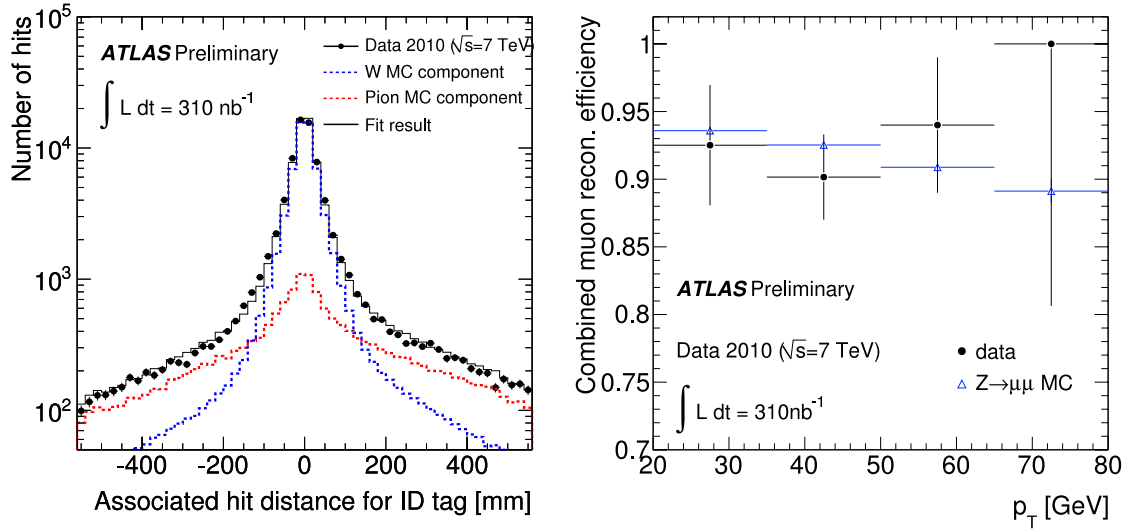


Figure 5.7: Results of fitting hit residual distributions in data to prompt muon and decay in flight samples (left). This technique serves to subtract the background contamination in the sample used in the MS hit method to measure the reconstruction efficiency in data. The combined muon efficiency measurements using an alternative method based on Z events in data and simulation is also shown (right, from [96]).

Z signature provides a very pure sample of events with well-identified muons in the relevant p_T range. However, since Z bosons are produced at a rate about ten times lower than W s, this efficiency measurement is statistically limited. The efficiency is determined using the “tag-and-probe” method, where events are selected by requiring one good muon to satisfy strict selection criteria, the “tag”, and another ID track to satisfy loose selection criteria, the “probe”. To reduce the impact of backgrounds, both the tag and the probe are required to match the signature of a Z boson decay, i.e. the pair is required to have opposite charge and an invariant mass within 10 GeV of the Z mass, 91 GeV. The efficiency, defined as the fraction of combined isolated muons matched to the ID track,

$$\epsilon = \frac{N_{probes}^{matched}}{N_{probes}}, \quad (5.6)$$

is 0.933 ± 0.022 (stat) ± 0.013 (syst) compared to 0.924 in simulation. Results of the efficiency measurement, comparing data and simulation, are shown in Figure 5.7 (right). The main systematic uncertainty arises from the background contamination, which is small for the Z signature.

The efficiency measurement is lower using the second method due to the geometrical acceptance of the MS. This is not included in the first method which explicitly requires MS hits. The two efficiency measurements show good agreement between data and simulation. The total uncertainties are about 2.5% in both cases. The reconstruction efficiency measurements are described in more detail in [97]. These results were used to assign a systematic uncertainty on the W measurements.

5.6 Trigger Efficiency

The trigger efficiency is measured in data relative to reconstructed muons using a sample of high- p_T muons selected with an independent jet trigger. Tracks satisfying the muon selection criteria for the analysis are extrapolated to the trigger chamber planes and the efficiency is defined as the fraction of cases when the associated trigger hits are found. The ratio of the trigger efficiency in data and in simulation is 0.929 ± 0.010 (stat) ± 0.015 (syst). This discrepancy is due to the differences in the configuration used to acquire data, and to hardware inefficiencies not included in simulation. The systematic uncertainty is determined by changing the criteria used to associate trigger signals to the track, stability checks of the plateau region above 20 GeV and comparisons between the two different muon reconstruction algorithms.

The trigger efficiency as a function of p_T for the barrel and endcap regions is shown in Figure 5.8. From these efficiencies, a per-muon scale factor SF quantifying the difference between the efficiency measured in data and MC is defined as

$$\text{SF} = \frac{\epsilon(\text{Data})}{\epsilon(\text{MC})}. \quad (5.7)$$

The SF based on the ratio of the trigger efficiency in data and simulation is applied to the simulation, in order to improve the modeling of the observed data.

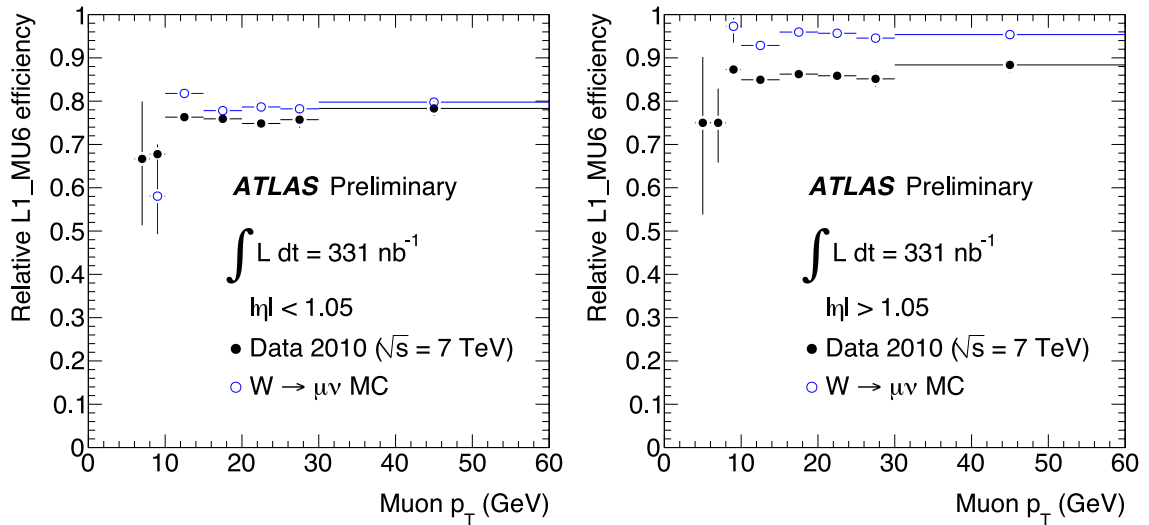


Figure 5.8: Measurement of the trigger efficiency relative to combined muons as a function of p_T for the barrel (left) and the endcap (right) regions, from [96]. The data measurement is compared to the predictions from simulation.

5.7 Muon Momentum Scale and Resolution

The muon momentum scale and resolution differs in data and simulation due to effects such as residual detector misalignment and imperfections in the description of the inert material and the magnetic field map. They have been estimated from

fits to the invariant mass distribution of dimuon candidate events consistent with the Z resonance. The fit function used is a Breit-Wigner convoluted with a Gaussian function. The momentum scale and resolution are varied in simulation until the fit result agrees with that observed with data. The result of fitting the Z lineshape compared to simulation for the peak position and width is shown in Figure 5.9. The mean momentum scale is within $\pm 1\%$ of the nominal value in simulation, while the width is $(4 \pm 2)\%$ in the barrel and $(7 \pm 3)\%$ in the endcap regions. A systematic uncertainty on the acceptance due to the momentum scale and resolution is assigned using these results.

5.8 The W Cross Section Measurement

The cross section is calculated from the equation

$$\sigma_W \cdot BR(W \rightarrow \mu\nu) = \frac{N - B}{A_W \cdot C_W \cdot L} \quad (5.8)$$

where N is the number of W candidate events that pass the selection criteria, B is the number of expected background events and L is the integrated luminosity for the dataset used. The $A_W \cdot C_W$ term corresponds to the fraction of signal events expected to pass the full selection criteria. The acceptance calculation is factorized into two parts: A_W and C_W , where A_W is extracted from generation-level quantities alone, while C_W depends also on reconstructed quantities.

The A_W factor denotes the acceptance for W s, computed from MC simulation and defined as the fraction of generated events that satisfy the kinematic selection requirements of the analysis $p_T^\mu > 20$ GeV, $|\eta| < 2.4$, $p_T^\nu > 25$ GeV and $m_T > 40$ GeV

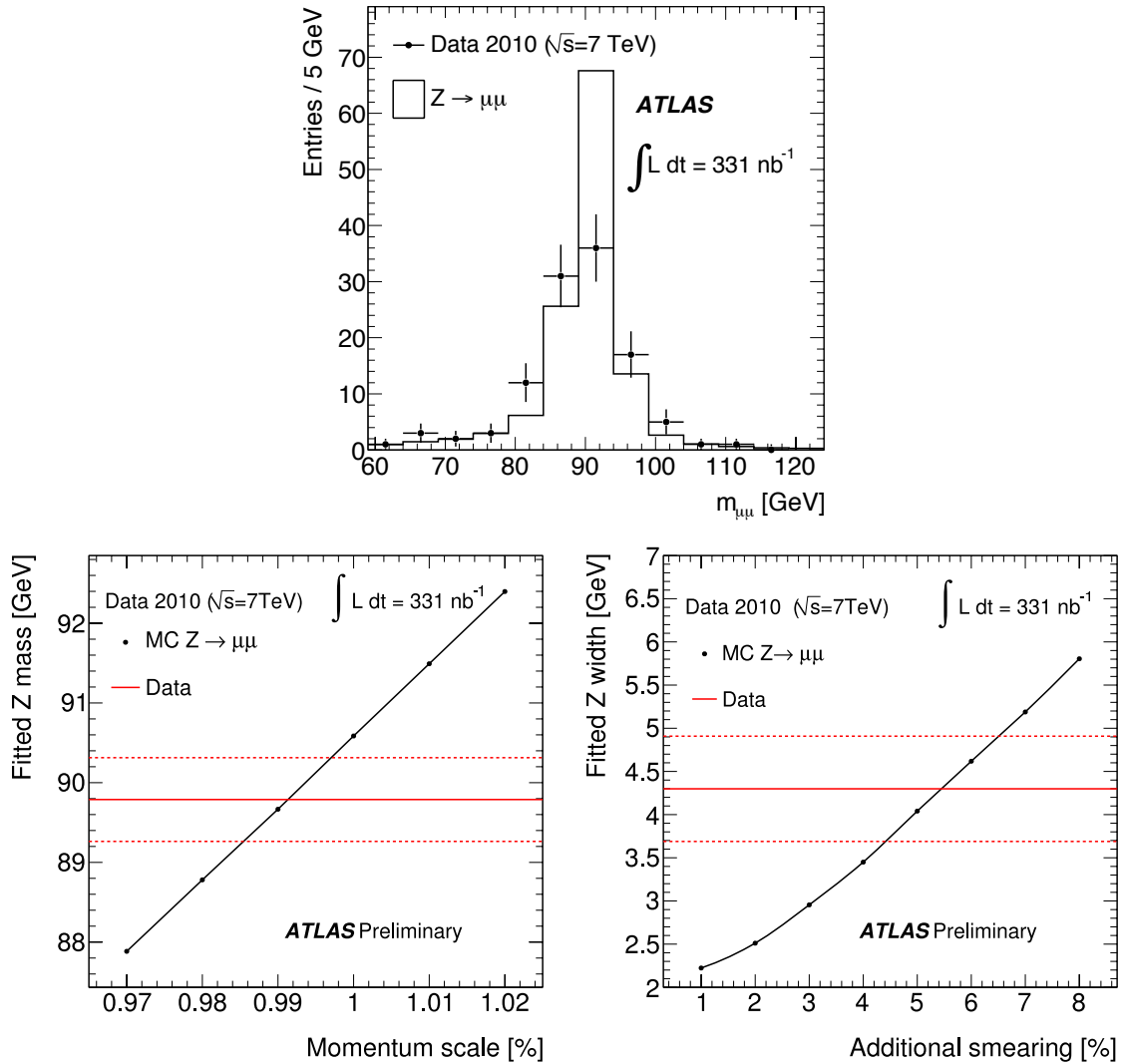


Figure 5.9: A comparison of the dimuon invariant mass for Z candidate events (top) shows differences between data and simulation. The muon momentum scale (lower left) and resolution (lower right) are determined by fitting the peak position and width in data and comparing this to simulation. The red lines show the fit peak position and the statistical uncertainty band. The black points correspond to the fit peak position for different values of input scale (left) and resolution smearing (right). The intersection of the curves provides the best estimate of the scale and resolution parameters. From [96].

(fiducial acceptance). The central value for the acceptance factor A_W is determined from the simulated signal event sample generated with PYTHIA using the MRST LO* PDF set. The factors for W^+ , W^- and total W are listed in Table 5.5. The systematic uncertainty of the acceptance calculation is dominated by the PDF uncertainty and the impact of higher order contributions. The uncertainty is derived from the PDF error set of CTEQ 6.6 evaluated using MC@NLO, from comparisons of different PDF set predictions: MRST LO*, CTEQ 6.6 and HERAPDF 1.0, and from a comparison of LO and NLO calculations based on PYTHIA and MC@NLO with the same CTEQ 6.6 PDF set. The resulting uncertainty estimate is 3%.

The C_W factor denotes the ratio between the total number of reconstructed events passing the full selection and the generated events satisfying the kinematic selection requirements of the fiducial acceptance above. The central value of the correction factor C_W is also determined from the simulated $W \rightarrow \mu\nu$ event sample. The factor is defined as

$$C_W = \frac{N_{\text{sel}}^{\text{MC}}}{N_{\text{gen, fid}}^{\text{MC}}} \times \frac{\epsilon_{\text{trig}}^{\text{data}}}{\epsilon_{\text{trig}}^{\text{MC}}} \times \frac{\epsilon_{\text{rec}}^{\text{data}}}{\epsilon_{\text{rec}}^{\text{MC}}}, \quad (5.9)$$

where $N_{\text{sel}}^{\text{MC}}$ and $N_{\text{gen, fid}}^{\text{MC}}$ are the number of W MC candidates selected after reconstruction and generated in the fiducial volume respectively. The ratio of trigger efficiencies in data and MC correct for differences between data and MC simulation, as described in Section 5.6, and no factor is applied for the reconstruction efficiency $\epsilon_{\text{rec}}^{\text{data}}/\epsilon_{\text{rec}}^{\text{MC}} = 1$ in this iteration of the analysis (see Section 6.3.2). The C_W factors for W^+ , W^- and total W are shown in Table 5.5.

	C_W	A_W
W^+	0.765 ± 0.031	0.484 ± 0.015
W^-	0.748 ± 0.030	0.475 ± 0.014
W	0.758 ± 0.030	0.480 ± 0.014

Table 5.5: The correction factors C_W and the acceptance factors A_W for W^+ , W^- and the total W with their corresponding systematic uncertainties.

Parameter	$\delta C_W / C_W$ [%]
Trigger efficiency	1.9
Reconstruction efficiency	2.5
Momentum scale	1.2
Momentum resolution	0.2
E_T^{miss} scale and resolution	2.0
Isolation efficiency	1.0
Theoretical uncertainty (PDFs)	0.3
Total uncertainty	4.0

Table 5.6: Summary of the contributions to the systematic uncertainty on C_W .

The uncertainties from the various efficiency and acceptance components of C_W are listed in Table 5.6. The dominant sources of uncertainty are from the reconstruction efficiency and the E_T^{miss} scale and resolution. The uncertainty from the E_T^{miss} scale and resolution is estimated from the uncertainty in the response of cells in topological clusters (1.5%) as well as the imperfect modelling of the overall E_T^{miss} response due to the presence of low energy hadrons, the underlying event and pile-up effects (1%), yielding a total uncertainty on C_W due to E_T^{miss} of 2%. Uncertainties from QED final-state radiation and other theoretical uncertainties on C_W , primarily from PDFs, contribute an uncertainty of 0.3% [88]. The total systematic uncertainty is 4%.

5.8.1 Cross Section Results

The fiducial cross sections, defined in terms of the C_W factor alone, where $A_W = 1$, are listed for W^+ , W^- and the total W in Table 5.7. These cross sections are dominated by the systematic uncertainties, particularly the luminosity 11% followed by the systematic uncertainties on C_W . The fiducial cross sections have small theoretical uncertainties, since these primarily impact the acceptance correction A_W . The fiducial cross sections serve as input to the charge asymmetry measurement described in Section 5.9.

	$\sigma_{W\mu^\pm}^{\text{fid}} \cdot \text{BR}(W \rightarrow \mu\nu)$ [nb]
W^+	2.77 ± 0.11 (stat) ± 0.12 (syst) ± 0.30 (lumi)
W^-	1.83 ± 0.09 (stat) ± 0.08 (syst) ± 0.20 (lumi)
W	2.77 ± 0.15 (stat) ± 0.20 (syst) ± 0.51 (lumi)

Table 5.7: The measured fiducial cross section times leptonic branching ratio for W^+ , W^- and total W production. The phase space requirements are $p_T^\mu > 20$ GeV, $|\eta| < 2.4$, $p_T^\nu > 25$ GeV, $m_T > 40$ GeV.

Applying the acceptance factors A_W for the phase space requirements yields the total cross sections, listed in Table 5.8. The cross section has also been measured in the electron final state. This measurement has been combined with the muon result, thus decreasing the uncertainty. In combination, all the contributions are assumed uncorrelated except for the uncertainty on the integrated luminosity, on the acceptance factor A_W and on the hadronic component of the E_T^{miss} measurement. The muon-only and combined measurements for W^+ , W^- and the total W are listed in Table 5.9. These results are compared to the electron measurement in Figure 5.10, showing that the two decay channels are in agreement. Theoretical predictions at

	$\sigma_W^{\text{fid.}} \cdot \text{BR}(W \rightarrow \mu\nu)$ [nb]
W^+	5.71 ± 0.23 (stat) ± 0.30 (syst) ± 0.63 (lumi)
W^-	3.86 ± 0.20 (stat) ± 0.20 (syst) ± 0.42 (lumi)
W	9.58 ± 0.30 (stat) ± 0.50 (syst) ± 1.05 (lumi)

Table 5.8: The total cross section times leptonic branching ratio for W^+ , W^- and W production measured in the muon final state.

	$\sigma_W \cdot \text{BR}(W \rightarrow l\nu)$ [nb]	$\sigma_W^{\text{NNLO}} \cdot \text{BR}(W \rightarrow l\nu)$ [nb]
W^+	$5,93 \pm 0.17$ (stat) ± 0.30 (syst) ± 0.65 (lumi)	6.16 ± 0.31
W^-	4.00 ± 0.15 (stat) ± 0.20 (syst) ± 0.44 (lumi)	4.30 ± 0.21
W	9.96 ± 0.23 (stat) ± 0.50 (syst) ± 1.10 (lumi)	10.46 ± 0.52

Table 5.9: The total cross section times leptonic branching ratio for W^+ , W^- and W production measured for the combination of the electron and muon final states. Theoretical predictions at NNLO pQCD are shown for comparison.

NNLO in pQCD obtained using ZWPROD [29] and FEWZ [30, 31] with the MSTW 2008 PDF set [17] are also shown in Table 5.9 for comparison. The theoretical uncertainties correspond to the PDF uncertainties at 90% C.L. as well as uncertainties from α_s and the renormalization μ_R and factorization μ_F scales. The measurements are in agreement with the theoretical predictions. A comparison of the combined ATLAS cross section results for W^+ , W^- and the total W with theoretical predictions as a function of center-of-mass energy (Figure 5.11) also shows good agreement.

5.9 The W Charge Asymmetry Measurement

The cross section results show the difference in the production rates for W^+ and W^- that gives rise to a non-zero charge asymmetry. The charge asymmetry variable

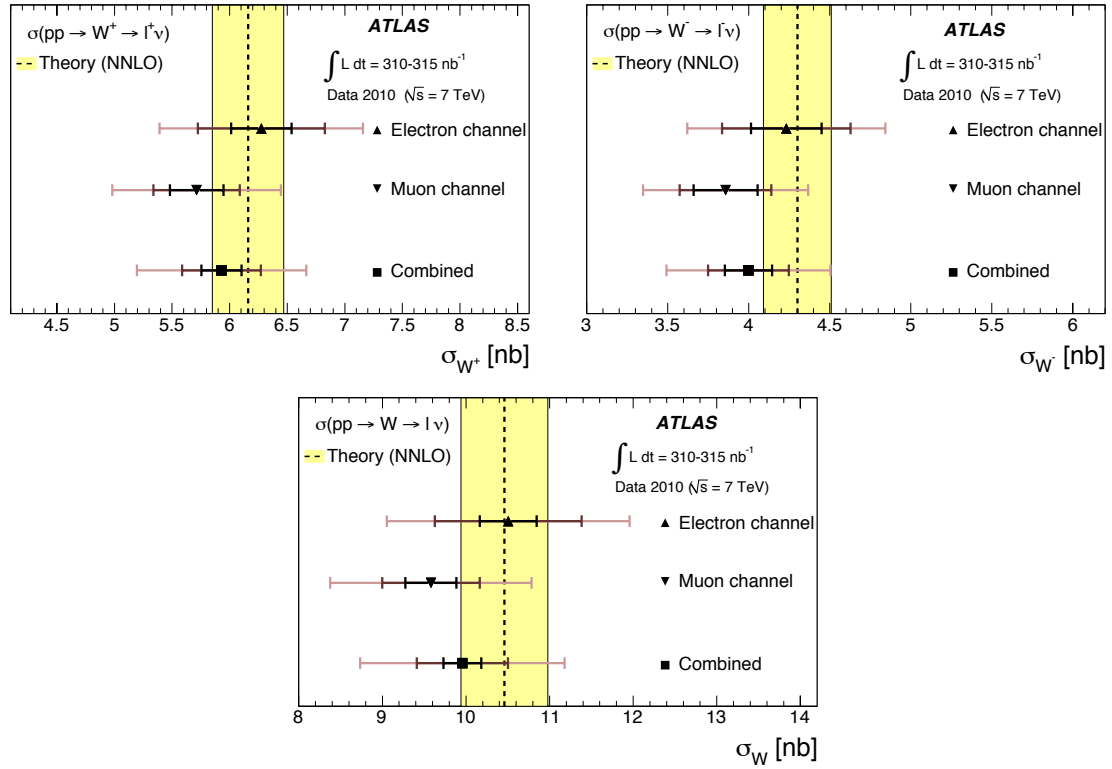


Figure 5.10: Measurements of the inclusive cross section $\sigma_W \cdot BR(W \rightarrow l\nu)$ for the electron and muon channels and their combination. The results for W^+ (upper left), W^- (upper right) and the total W (lower) are shown separately and compared to theoretical predictions at NNLO in pQCD. Uncertainties correspond to statistical, statistical plus systematic and total (statistical, systematic and luminosity) uncertainties, where these are added in quadrature. From [1].

is defined from the fiducial cross sections $\sigma_{Wl^\pm}^{\text{fid}}$ as

$$A_l = \frac{\sigma_{Wl^+}^{\text{fid}} - \sigma_{Wl^-}^{\text{fid}}}{\sigma_{Wl^+}^{\text{fid}} + \sigma_{Wl^-}^{\text{fid}}}, \quad \sigma_{Wl^\pm}^{\text{fid}} = \frac{N_{Wl^\pm}^{\text{obs}} - N_{Wl^\pm}^{\text{bkg}}}{L \times C_{Wl^\pm}}. \quad (5.10)$$

where $N_{Wl^\pm}^{\text{obs}}$ and $N_{Wl^\pm}^{\text{bkg}}$ are the number of selected candidate and expected background events respectively, and L is the integrated luminosity which cancels to first order in the asymmetry calculation. The C_{Wl^\pm} factors are defined as in Equation 5.9 separately for positive and negative charges, and include acceptance and efficiency corrections. In the asymmetry calculation A_l , the C_{Wl^\pm} factors and the data-MC corrections largely

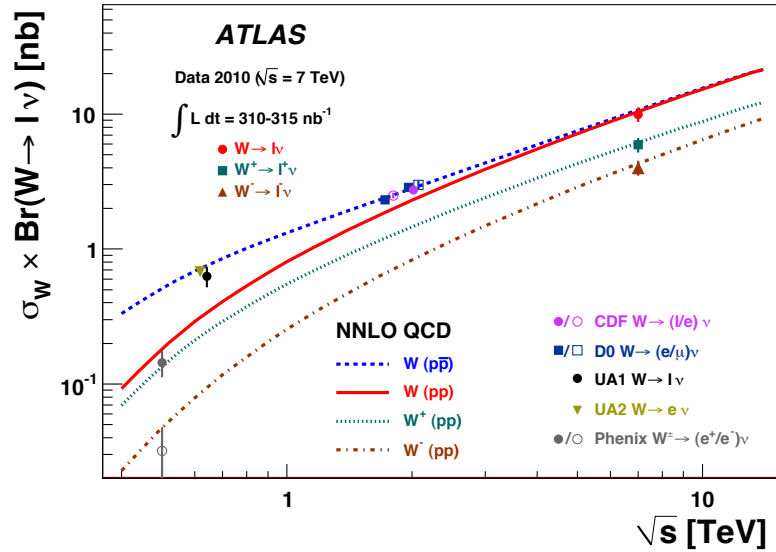


Figure 5.11: The W boson production cross section predictions at NNLO include curves for W^+ and W^- , in $p\bar{p}$ and pp collisions, as a function of the center-of-mass energy. Past measurements from the SppS, Tevatron and RIHC colliders, including the total experimental uncertainties, are also shown. The ATLAS results for the inclusive production cross section for W^+ , W^- and the total W are in agreement with the theoretical predictions. From [1].

cancel out, since the efficiencies for positive and negative muons are similar and effects such as charge mis-identification and bin migrations are small. As a result, this measurement is primarily concerned with understanding possible sources of bias between positive and negative muons that impact the acceptance and efficiency for W events. No attempt is made to extrapolate from the fiducial cross sections to the full phase space, since this relies on the theoretical modeling of W production that is affected by the PDF model used, thus introducing theoretical dependencies in the measurement.

The decay lepton pseudorapidity is correlated with the momentum fraction of the incoming partons, so the aim is to measure the asymmetry as a function of the muon

pseudorapidity. The choice of binning is driven by the statistics available for the signal events and the samples used for the calculations of efficiencies, backgrounds and systematic uncertainties. This first measurement of the charge asymmetry has been performed in two bins of lepton absolute pseudorapidity: $0 < |\eta| < 1.37$ and $1.52 < |\eta| < 2.4$, where the boundaries are chosen to overlap between the muon and electron channels. In particular, the crack between the barrel and endcap EM calorimeter is contained in one bin $1.37 < |\eta| < 1.52$, which is a region where electrons cannot be precisely measured. The upper boundary is set at $|\eta| < 2.4$, limited by the coverage of the muon trigger. All the results are presented as bin integrals. W candidates are selected and the expected background is subtracted per charge and bin in $|\eta|$. The muon η and p_T , and m_T distributions for positive and negative W candidates show reasonable agreement with expectations from simulation (Figure 5.12). The muon η spectrum is then corrected back to the fiducial volume, using charge separated C_W factors.

The main sources of systematic uncertainty on the asymmetry are the muon momentum scale and resolution (5.0%), the trigger efficiency uncertainty (2.7%) and the uncertainty on the QCD (0.8%) and EW and $t\bar{t}$ (0.5%) background estimates. The impact of the momentum scale and resolution is of particular concern since effects such as detector misalignments can affect the bending of tracks of opposite charge in opposite directions and introduce biases in the acceptance (see Section 6.5). The scale and resolution uncertainties on the asymmetry measurement are treated as anti-correlated in order to account for these types of effects.

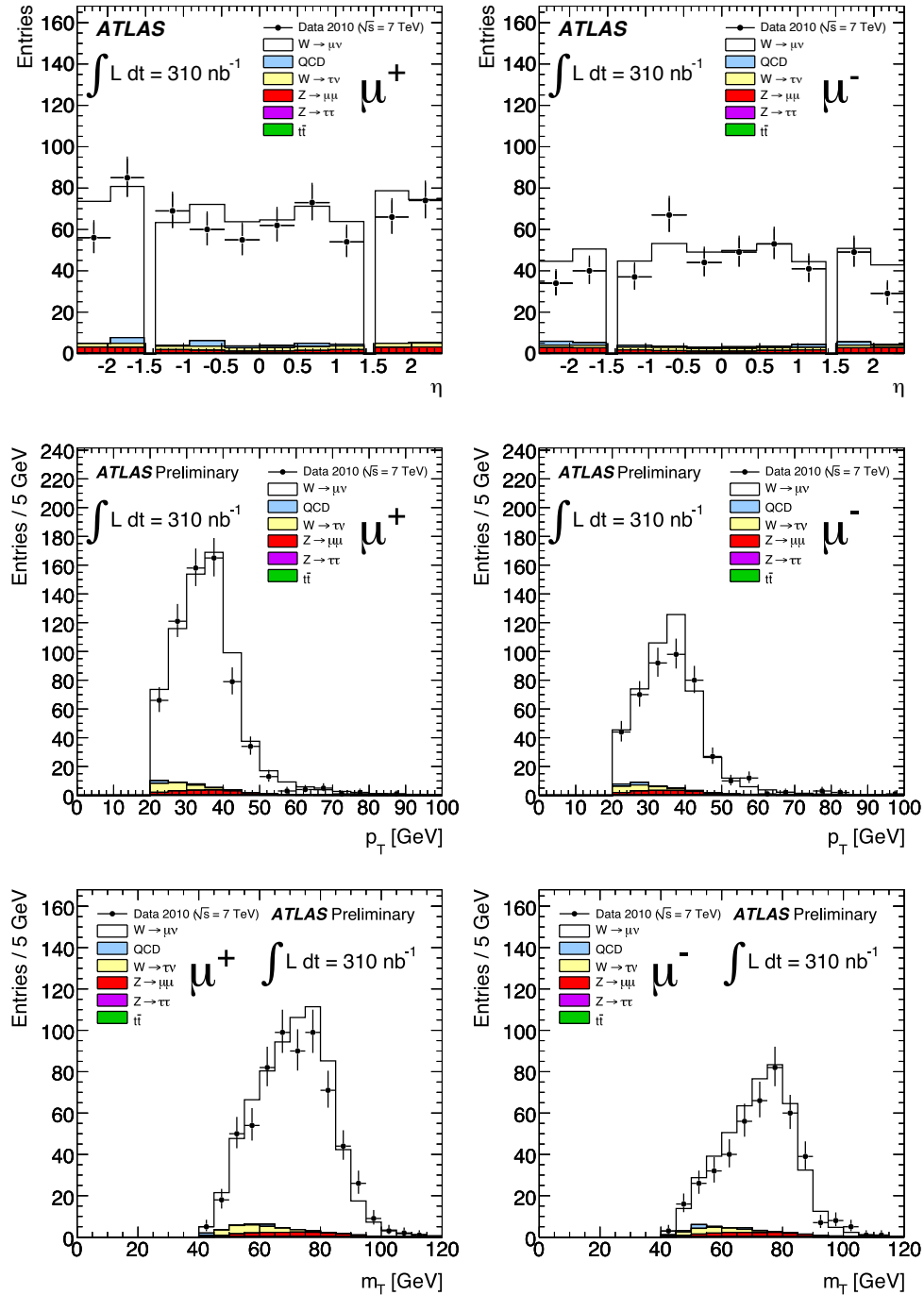


Figure 5.12: Pseudorapidity (upper), p_T (center) and m_T (lower) distributions for μ^+ (left) and μ^- (right) for candidates satisfying the W selection requirements. The data are compared to simulation showing the signal and various background components. The MC distributions are normalized to the integrated luminosity of the data.

The asymmetry values for the different $|\eta|$ bins and the integrated result for the muon channel, as well as the combination of the muon and electron channels are listed in Table 5.10. The measurements are limited by statistics, but they do confirm an asymmetry in the production of W^+ and W^- in pp collisions that increases with the decay muon pseudorapidity. This constitutes the first measurement of the W production asymmetry at the LHC center-of-mass energy of 7 TeV. The results for the asymmetry measurement in the muon channel and for the combination of channels are shown in Figure 5.13. The results are compared to predictions at NLO in pQCD using different PDF sets, showing agreement with all predictions. This measurement does not yet provide sufficient information to distinguish between the models nor serve as useful input to the PDF fits. An update of this measurement with a dataset a hundred times larger is the subject of the next chapter. However, it may be noted that the first measurements of the production properties of W bosons constitute crucial steps for the differential asymmetry measurement since they define the event selection and the methods for background estimates. The first asymmetry measurement established the feasibility of this procedure and provided the first study of the systematic uncertainties that are examined in further detail in the next iteration of the measurement.

$ \eta $ range	Muon A_μ	Combination A_l
0 – 1.37	$0.12 \pm 0.04 \pm 0.01$	$0.14 \pm 0.03 \pm 0.01$
1.52 – 2.4	$0.32 \pm 0.05 \pm 0.02$	$0.31 \pm 0.04 \pm 0.01$
0 – 1.37, 1.52 – 2.4	$0.19 \pm 0.03 \pm 0.01$	$0.20 \pm 0.02 \pm 0.01$

Table 5.10: The measured asymmetries for the barrel and endcap regions as well as integrated over the full pseudorapidity range, for the muon analysis and the combination of the muon and electron channels. The uncertainties are statistical and systematic.

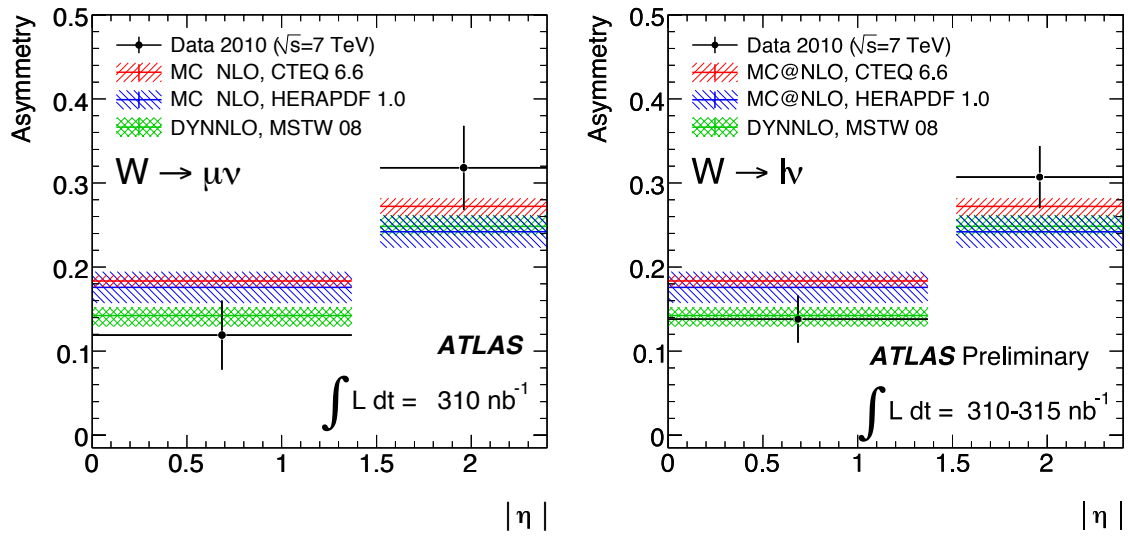


Figure 5.13: Lepton charge asymmetries for the muon channel (left) and the combination of the muon and electron channels (right). Various theoretical predictions are shown for comparison with their corresponding PDF uncertainties at 90% C.L.

Chapter 6

Differential W Charge Asymmetry Measurement

This chapter presents the differential measurement of the W charge asymmetry in the $W \rightarrow \mu\nu$ decay mode using the pp collision dataset recorded with the ATLAS detector from September 25th to October 29th, 2010. It provides details of the analysis accepted for publication in Phys. Lett. B [2]. The measurement is performed in 11 bins of the charged lepton absolute pseudorapidity $|\eta|$, listed in Table 6.1. The topics described in this chapter include the event selection applied to the data and MC samples, corrections to the MC in order to improve the agreement with data: scale factor corrections for the trigger and reconstruction efficiencies, event weights to correct for pileup of minimum bias events, and the muon momentum resolution and scale corrections affecting the selection of positive and negative W s. The background estimates for the EW and $t\bar{t}$, and QCD components are presented subsequently. Finally, calculations of the systematic uncertainties and the results of

the asymmetry measurement end the chapter.

Lepton $ \eta $ Bin Ranges
0.00, 0.21, 0.42, 0.63, 0.84, 1.05, 1.37, 1.52, 1.74, 1.95, 2.18, 2.40

Table 6.1: Ranges for the 11 bins in absolute lepton pseudorapidity used in the differential asymmetry measurement. Many corrections and systematic tests are performed using binning with signed η , by adding 11 mirror bins at negative η .

6.1 Data and Simulated Monte-Carlo Samples

The dataset¹ included in the measurement corresponds to an integrated luminosity of about 31.4 pb^{-1} with an 11% uncertainty [54]. This is about 100 times larger than the dataset used in the previous iteration of the analysis, presented in Section 5.2. The dataset is based on the available sample from pp collisions in 2010 satisfying the stable beam and detector and data-quality requirements for the full detector, including the inner tracker, the calorimeters and the muon spectrometer. The first 3.8 pb^{-1} of integrated luminosity satisfying these requirements are excluded in order to yield a sample that is additionally stable both from the point of view of the muon trigger and the reconstruction.

In particular, the main considerations driving the dataset choice are related to the trigger operation in the first data [98]. The rapidly increasing instantaneous luminosity in 2010 made it necessary to start using the HLT for the muon triggers by the end of the Summer. However, the trigger chain was not fully commissioned and

¹The data used in this analysis were processed using the ATLAS central production based on Athena release v15.6.13.2 and analyzed using the SM W/Z group D3PDs.

led to highly variable conditions at the start-up of the HLT-rejection period. One issue is the L1 trigger timing, since out of time L1 triggers do not seed the HLT and cause inefficiencies. Various timing adjustments were performed, particularly for the RPCs, impacting the trigger efficiency on one side of the detector especially. Due to the toroidal field in the MS (with bending in η) these regions create differences in the efficiency between positive and negative muons, which are not included in the simulation. In addition, the HLT was operated without alignment parameters in the first period of HLT-rejection. Since this analysis is based on the selection of positive and negative muons, which is sensitive to the alignment, the problematic trigger conditions provide further justification to remove this initial sample from the analysis dataset.

Run Ranges	Trigger	Integrated Luminosity [pb^{-1}]
165703 – 167576	EF_mu13_MG	15.83
167607 – 167776	EF_mu13_MG_tight	15.57

Table 6.2: Trigger paths and corresponding integrated luminosity in the two periods included in the dataset used for analysis.

Two trigger configurations are used in this dataset (see also Section 6.3), with the corresponding integrated luminosities shown in Table 6.2. The trigger requirement is based on the lowest available unrescaled trigger, adapted to the conditions of increasing instantaneous luminosity in the different periods of obtaining data. Finally, the simulated samples used in this analysis are identical to those used for the first W measurements, described in Section 5.2.

	Collision event selection
Primary vertex	$N_{vtx} \geq 1$ with $N_{tracks} \geq 3$ $ z_{vtx} < 200$ mm
Jet cleaning	cleaning cuts
Trigger	EF_mu13_MG or EF_mu13_MG_tight
	High- p_T event selection
Muon selection	combined track $p_T > 20$ GeV, $ \eta < 2.4$
Muon quality	$p_T^{MS} > 10$ GeV $ (p_T^{MS} - p_T^{ID})/p_T^{ID} < 0.5$ Silicon Hit requirement: $N_{pix} \geq 1$, $N_{SCT} \geq 6$ TRT Hit requirement: for $N_{TRT} = N_{TRT}^{hits} + N_{TRT}^{outliers}$ if $ \eta < 1.9$ then $N_{TRT}^{hits} > 5$ and $N_{TRT}^{outliers}/N_{TRT} < 0.9$ if $ \eta \geq 1.9$ and $N_{TRT}^{hits} > 5$ then $N_{TRT}^{outliers}/N_{TRT} < 0.9$
Muon-PV matching	$ z_0 - z_{vtx} < 10$ mm
	$W \rightarrow \mu\nu$ event selection
ID isolation	$\sum p_T^{ID}/p_T < 0.2$
Missing transverse energy	$E_T^{miss} > 25$ GeV
Transverse Mass	$m_T > 40$ GeV

Table 6.3: Full event selection applied to select W candidates. The selection is identical to that described in [1, 96] except for the trigger, the PV z_{vtx} cut and the muon quality cuts.

6.2 Event Selection

The event selection follows that described in Section 5.3 with some small modifications that will be described here. The final selection criteria are summarized in Table 6.3. The main differences are in the trigger, the PV z_{vtx} requirement and the muon quality criteria. The selection of the z_{vtx} of the PV has been loosened from $|z_{vtx}| < 150$ mm to $|z_{vtx}| < 200$ mm due to the larger width of the z_{vtx} distribution in this period, increasing the efficiency from about 98.7% to about 99.9%.

The main modifications to the muon quality criteria are a change from an absolute momentum difference variable $|p_T^{MS} - p_T^{ID}|$ to a relative one $|(p_T^{MS} - p_T^{ID})/p_T^{ID}|$ and

the inclusion of hit requirements to select high quality ID tracks. The use of a scaled momentum matching criteria instead of an absolute one improves the signal efficiency at high p_T , while still rejecting backgrounds from decays in flight of hadrons. The MS p_T measurement, the ID and MS matching variable and the TRT hit multiplicity are compared in data and signal MC in Figure 6.1. The presence of a population of muons characterized by low MS momentum ($p_T < 10$ GeV), low $(p_T^{\text{MS}} - p_T^{\text{ID}})/p_T^{\text{ID}}$ and poor ID tracks, often with no TRT hits on track, is visible in the data and not in the signal MC. This background sample is attributed to muons from π/K decays and is removed by the quality requirements. Tracks with highly inconsistent p_T measurements in the ID and MS arising from π/K decays are also typically associated with problematic regions in the detector and have large uncertainties in the measurement of their momentum, so they are also removed from the sample under analysis. Finally, the ID hit requirements improve the consistency of the analysis with the selection used for efficiency calculations and performance studies. More detailed studies on the efficiencies for these requirements can be found in [99]. Applying the full selection criteria to the analysis dataset yields 129,157 W candidates, of which 78,053 have a positively charged muon and 51,104 a negatively charged one.

6.3 Trigger and Reconstruction Efficiencies

The muon trigger and reconstruction efficiencies are calculated from data using dimuon events associated with the Z resonance. The use of a larger dataset relative to that of the previous measurements, described in Sections 5.5 and 5.6, implies the efficiencies can be calculated with smaller statistical uncertainties and finer binning.

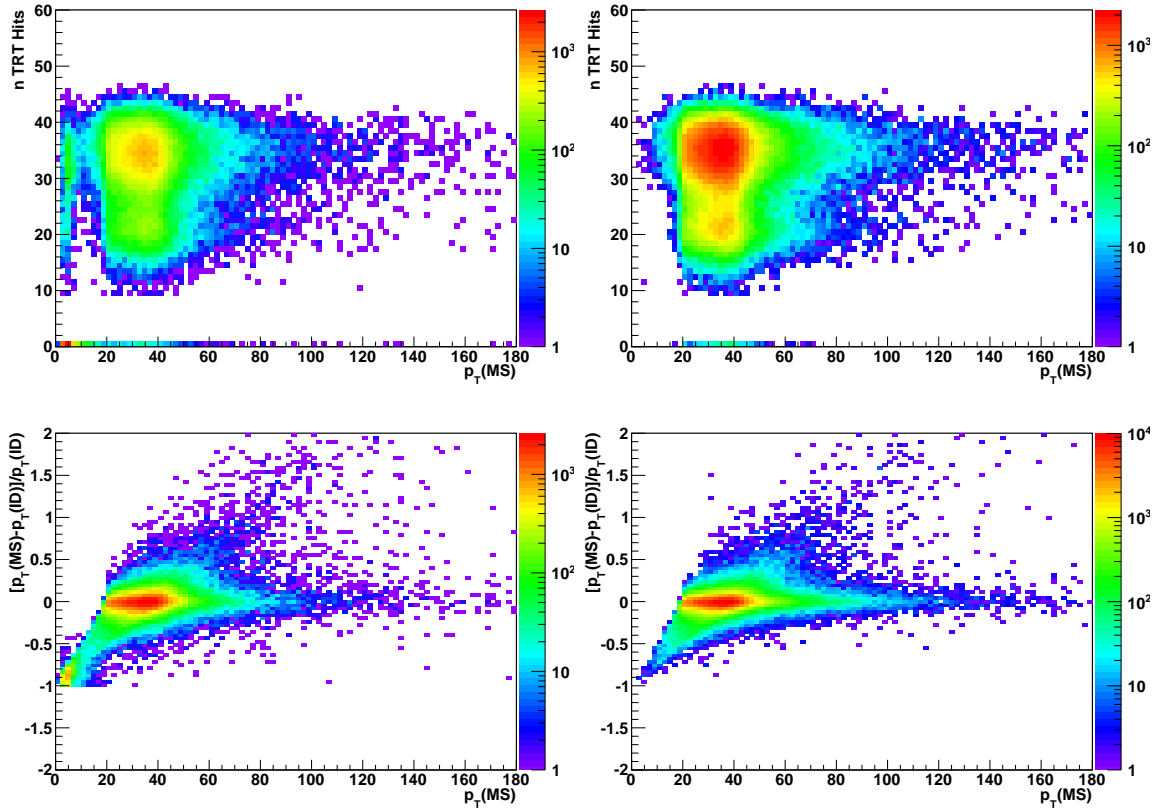


Figure 6.1: Distribution of the number of TRT hits on track compared to MS p_T (upper) for muons passing the W selection in data (left) and W Monte Carlo (right). Only tracks in the range $|\eta| < 1.9$ are included in these distributions, corresponding to the coverage of the TRT detector. The distribution in data includes a population at low MS p_T typically with no TRT hits associated to the track (plots are in log scale). These tracks are likely to come from π/K decays in flight. The lower distributions compare $[p_T^{MS} - p_T^{ID}]/p_T^{ID}$ and p_T^{MS} for data (left) and W MC (right). Tracks with inconsistent p_T measurements in the ID and MS are removed from the sample under analysis.

6.3.1 Trigger Efficiency

As mentioned in Section 6.2, two trigger chains are used to select events for the analysis dataset. For runs 165703 to 167576, `EF_mu13_MG` is used, while for runs 167607 to 167776, `EF_mu13_MG_tight` is used. These are the lowest momentum threshold muon triggers available that are unrescaled. The difference in the two chains is that the former is seeded by `L1_MU0` and the latter by `L1_MU10`. The trigger configuration with the `L1_MU0` seed for the EF trigger used is not present in the Monte Carlo simulation. As a result, events in MC are selected using the simulation of the `EF_mu10_MG` chain, which is seeded from `L1_MU10`². The EF chain used is based on the MuGirl algorithm that uses ID tracks and extrapolates them to the MS where it looks for spectrometer hits and then refits the full track. The algorithm is relatively loose in terms of MS requirements and independent from the offline track reconstruction algorithm, which is based on separate tracking in the ID and MS and the subsequent combination of the two. As a result, this algorithm is less sensitive to regions with poor MS measurement, due to misalignments for instance, and introduces a relatively small trigger bias. Scale factor corrections for the trigger efficiencies in data and MC are applied to correct for differences in the trigger configuration between the two.

Details of the implementation of the “tag-and-probe” method to calculate the muon trigger efficiency with respect to an offline muon and the corresponding uncertainty estimation can be found in [98]. In order to avoid trigger bias, all tags are required to have fired the event trigger. The event selection is performed in three steps: collision

²The `L1_MU10` configuration in data and MC is also different in the endcap, since it requires a 2-station coincidence in the data and a 3-station coincidence in simulation.

event selection, tag selection and probe selection. The beam and detector data quality requirements are applied and the event is also required to pass the trigger used in the corresponding data period. The full selection criteria for the trigger efficiency measurement are summarized in Table 6.4.

Event Selection	
Tags	≥ 1
Probes	≥ 1
Tag Selection	
ID hit requirement	PIX ≥ 1 , SCT ≥ 6 , and TRT requirement
Muon Quality	$p_T^{\text{MS}} > 10 \text{ GeV}$
	$ (p_T^{\text{MS}} - p_T^{\text{ID}})/p_T^{\text{ID}} < 0.5$
Kinematics	$p_T \geq 15 \text{ GeV} \ \& \ \eta \leq 2.4$
Isolation	$\sum p_T^{\text{ID}} / p_T < 0.2$
Trigger	EF_mu13_MG or EF_mu13_MG_tight
Probe Selection	
ID hit requirement	PIX ≥ 1 , SCT ≥ 6 , and TRT requirement
Muon Quality	$p_T^{\text{MS}} > 10 \text{ GeV}$
	$ (p_T^{\text{MS}} - p_T^{\text{ID}})/p_T^{\text{ID}} < 0.5$
Isolation	$\sum p_T^{\text{ID}} / p_T < 0.2$
Charge	$c_{\text{Tag}} \cdot c_{\text{Probe}} < 0$
Tag and probe matching	$d_0^\mu - d_0^{\text{probe}} < 2 \text{ mm}$ and $z_0^\mu - z_0^{\text{probe}} < 2 \text{ mm}$
Invariant mass	$ M_Z - M_{\text{TP}} < 15 \text{ GeV}$

Table 6.4: Selection criteria used in the trigger efficiency measurement using the Z “tag-and-probe” method.

The trigger efficiency turn-on curves in data for the two trigger chains, EF_mu13_MG and EF_mu13_MG_tight, are shown separately for the barrel and the endcap in Figure 6.2. The trigger efficiency in the endcap region is a few percent lower for the trigger chain based on L1_MU10 compared to that based on L1_MU0 due to the different trigger-logic configuration (see Section 3.6.2). The plateau efficiencies are consistent between the positive and negative charges, as can be seen in Figure 6.3. The scale

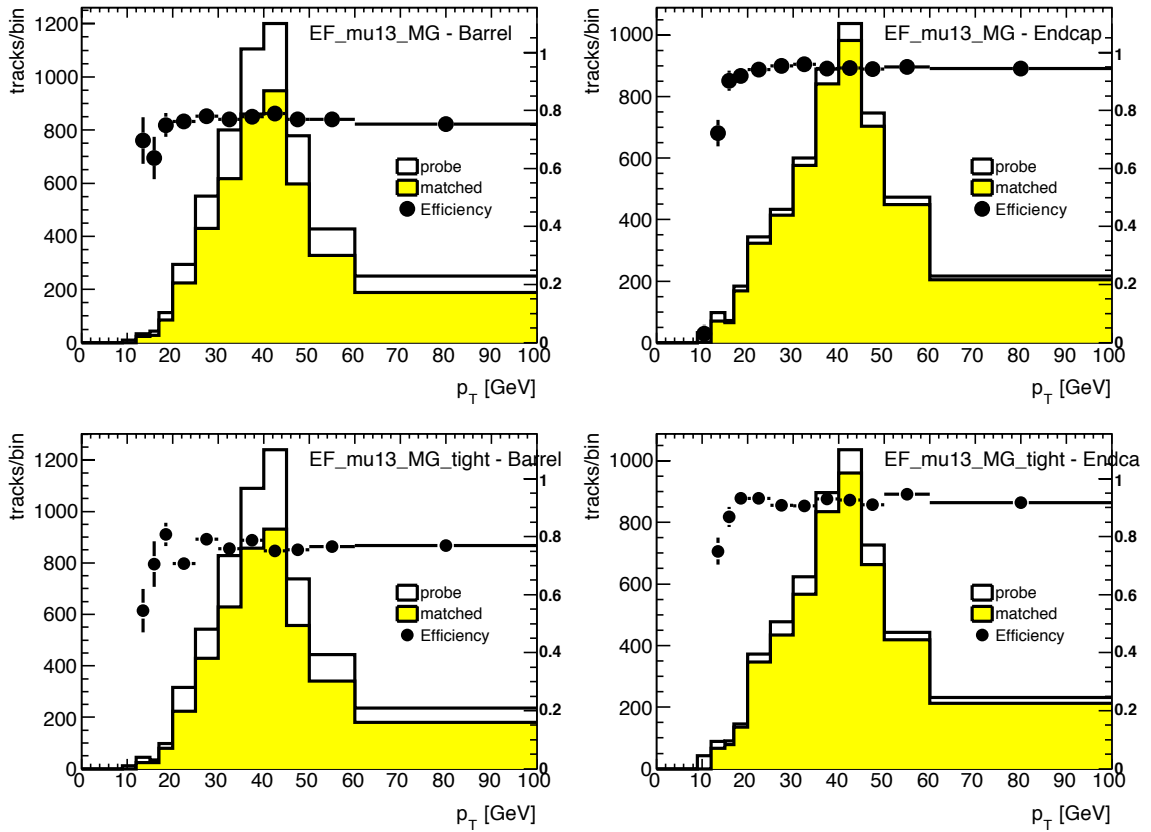


Figure 6.2: The efficiency of the 13 GeV threshold muon trigger in data as a function of muon p_T and the corresponding probe distributions entering the efficiency numerator (trigger-matched probes) and denominator (all probes). The upper distributions correspond to the EF_mu13_MG chain and the lower ones to the EF_mu13_MG_tight chain for barrel (left) and endcap (right), from [98].

factors comparing data and MC for the two trigger chains are shown in Figure 6.4, indicating that no significant bias exists between positive and negative charges for all pseudorapidity bins. Therefore the combined positive-negative SFs, that have smaller statistical uncertainties, are applied to the simulation and the SFs for the two chains are combined, weighted by the integrated luminosity for each period.

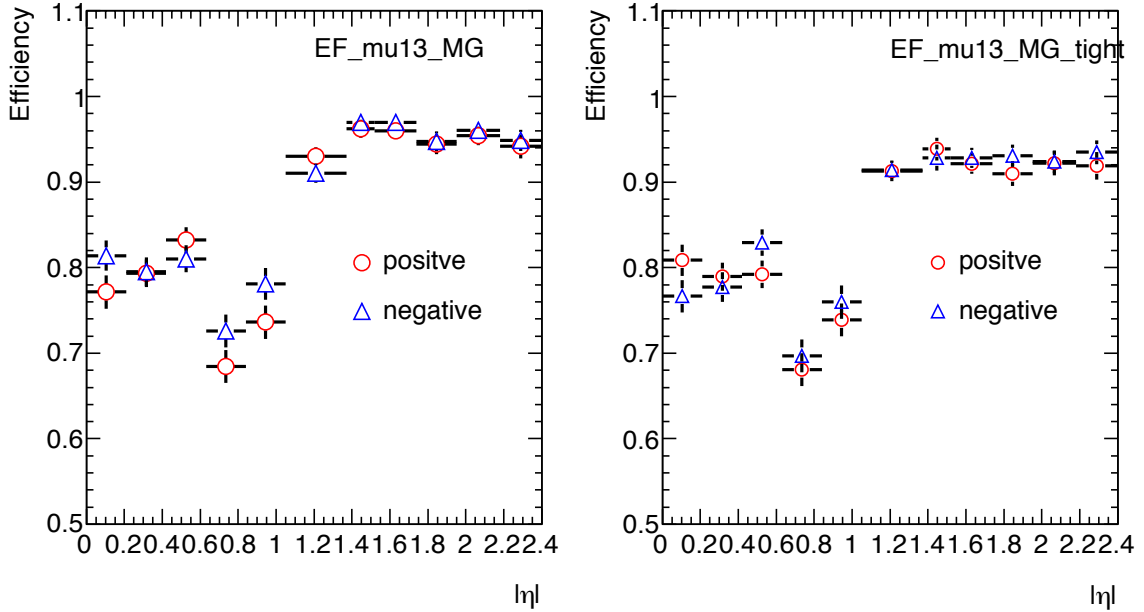


Figure 6.3: Trigger efficiency in data comparing positive and negative muons for EF_mu13_MG (left) and EF_mu13_MG_tight (right) as a function of muon $|\eta|$, from [98].

6.3.2 Reconstruction Efficiency

The muon reconstruction efficiency for combined muons satisfying the analysis selection criteria is also determined from Z decays using the “tag-and-probe” method, following the procedure described in Section 5.5. Unlike in the case of the trigger efficiency calculation, instead of requiring two reconstructed muons, events are selected with at least one muon as the tag, and at least one other charged particle track as the probe. The probe track is measured with the ID and is required to yield an invariant mass close to the Z mass when combined with the muon tag. This efficiency measurement probes the efficiency for finding a muon spectrometer track (including geometrical acceptance effects and MS track reconstruction inefficiencies) and for combining the MS and ID tracks. The efficiency for reconstructing muons

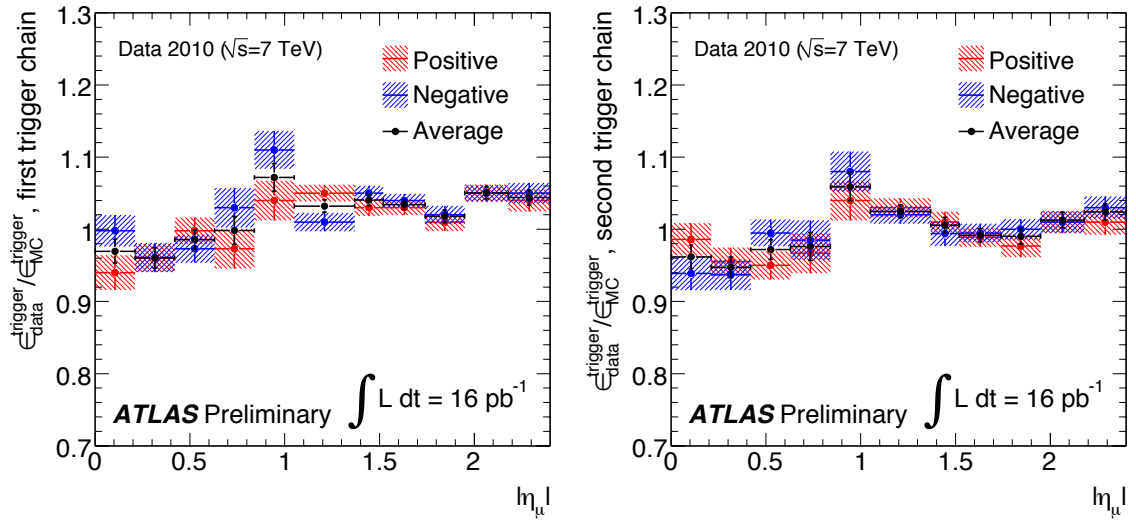


Figure 6.4: Trigger efficiency scale factors for EF_mu13_MG (left) and EF_mu13_MG_tight (right) in data over EF_mu10_MG in Z MC. The SFs for positive and negative muons, and their combination are shown, from [98]. The efficiencies for the two charges are consistent within their uncertainties.

in the ID in the p_T range above 20 GeV is about 99% as indicated by tag-and-probe results using an MS track as the probe.

The differences in this efficiency calculation compared to the one described in Section 5.5 arise from the use of a larger dataset in this case and a few modifications to the selection criteria, adapted to the specifics of this analysis. All the event selection requirements are summarized in Table 6.5. Requirements are imposed on the number of ID hits in order to reject possible fake tracks in the inner detector and the remaining criteria serve to ensure that the probe originates from a Z decay. A probe is considered to match a reconstructed muon if it is within a radius of $\Delta R < 0.05$ from a muon that satisfies the full muon selection criteria.

Event Selection	
Tags	≥ 1
Probes	≥ 1
Tag Selection	
ID hit requirement	PIX ≥ 1 , SCT ≥ 6 , and TRT hit requirement
Muon Quality	$p_T^{\text{MS}} > 10 \text{ GeV}$
	$ (p_T^{\text{MS}} - p_T^{\text{ID}}) / p_T^{\text{ID}} < 0.5$
Combined track kinematics	$p_T \geq 20 \text{ GeV} \ \& \ z_0 < 10 \text{ mm}$
Trigger	EF_mu13_MG or EF_mu13_MG_tight
Probe Selection	
ID track kinematics	$p_T \geq 20 \text{ GeV} \ \& \ \eta \leq 2.4$
Isolation	$\sum p_T^{\text{ID}} / p_T < 0.2$
ID hit requirement	PIX ≥ 1 , SCT ≥ 4 , Silicon ≥ 6
Charge	$c_{\text{Tag}} \cdot c_{\text{Probe}} < 0$
Tag and probe matching	$d_0^\mu - d_0^{\text{probe}} < 2 \text{ mm}$, $z_0^\mu - z_0^{\text{probe}} < 2 \text{ mm}$ and $\Delta\phi > 2$
Invariant mass	$ M_Z - M_{\text{TP}} < 10 \text{ GeV}$

Table 6.5: Full selection criteria used in the reconstruction efficiency measurement.

The reconstruction efficiency results are shown in Figure 6.5, including statistical and systematic uncertainties. The overall systematic uncertainty is about 0.4%, dominated by the background contribution. Details of the procedure used for the efficiency calculation, including the background subtraction procedure and the estimate of the systematic uncertainties are included in [100]. A comparison of the efficiency in data and MC shows some differences. As a result SFs corresponding to the ratio of the efficiency in data and MC, shown in the bottom of Figure 6.5, are applied as a correction to match the reconstruction efficiency in MC to that measured using data. It may be noted however that since the efficiencies separated by charge show no significant charge bias, the impact of this correction on the asymmetry result is small.

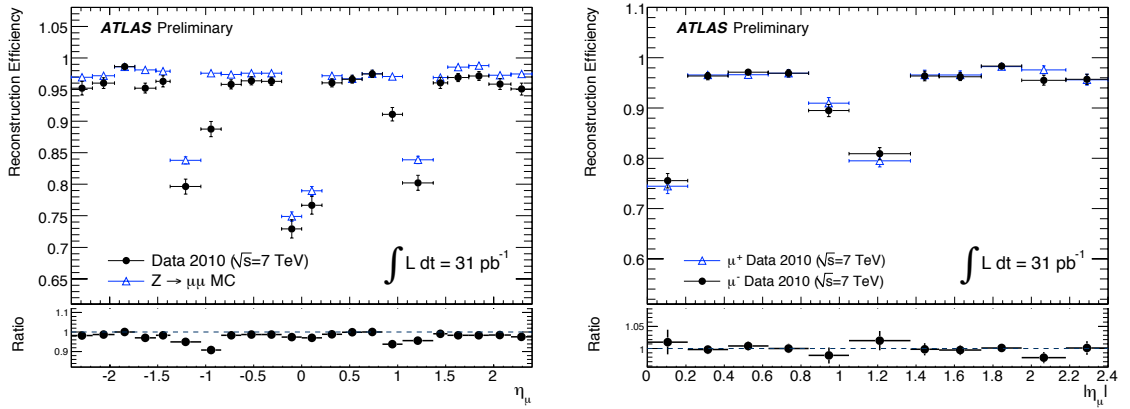


Figure 6.5: Reconstruction efficiency for combined muon tracks as measured from Z bosons using the “tag-and-probe” method where the probe is an ID track. The efficiency in η compares data and Monte Carlo (left) and the efficiency in data for positive and negative charges as a function of $|\eta|$ (right) shows agreement between the two charges. From [101].

6.3.3 Muon Isolation Efficiency

The efficiency of the isolation requirement is also estimated from Z bosons using the “tag-and-probe” method. In this case both the tag and the probe tracks are required to satisfy the full tag requirements used in the reconstruction efficiency measurement, except for the isolation criteria on the probe. The measurement of the efficiency is performed by testing the isolation requirement $\sum p_T^{\text{ID}}(\Delta R < 0.4) / p_T < 0.2$ on the probe track, after all other requirements are applied. The efficiency results are shown separately for positive and negative muons and compared to Z Monte Carlo in Figure 6.6, showing consistency between the charges. The isolation efficiency measurement is incorporated into the overall reconstruction efficiency correction and is also used for the QCD background estimation described in Section 6.6.

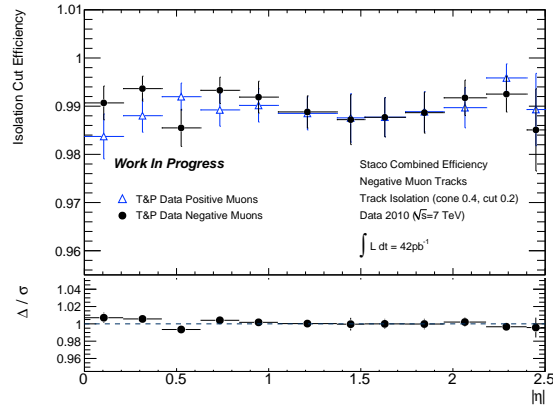


Figure 6.6: The isolation efficiency calculated using the Z “tag-and-probe” method shows agreement between positive and negative muon tracks. Note the sample of muons with $|\eta| > 2.4$ is not included in the analysis. From [101].

6.4 Pileup Simulation

Events can have multiple primary vertices as a consequence of pileup, i.e. multiple minimum bias interactions occurring in the same beam crossing. The Monte Carlo samples used, described in Section 5.2, include a simulation of pileup. An event-by-event weight is used to match the distribution of primary vertices in MC to that observed in data. The event weights are obtained by applying a selection to both the data and MC, and calculating the ratio of the distribution of the number of vertices in both. The event selection criteria applied includes the beam and detector data quality requirements, the trigger and the vertex requirements of at least one PV with ≥ 3 tracks in the range $|z_{vtx}| < 20$ cm. In addition, events are required to have at least one high transverse momentum muon satisfying the full muon selection requirements listed in Table 6.3. The distribution of the number of vertices in data and W MC satisfying this selection criteria and the corresponding event weights are listed in Table 6.6 and shown in Figure 6.7.

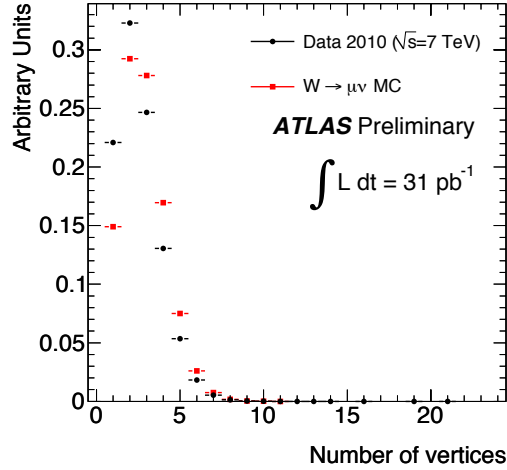


Figure 6.7: The distribution of the number of primary vertices in data and in W MC after applying the high- p_T muon selection. The ratio of these distributions is used to obtain event weights in order to correct the pileup simulation to match the data.

Vertices	0	1	2	3	4	5	6	7	8	9	≥ 10
Weight	1	1.48	1.10	0.89	0.77	0.71	0.70	0.70	0.79	0.92	0.87

Table 6.6: Event weights used to correct the number of vertices in simulation with pileup to the number of vertices in data. At least one primary vertex is required for the event selection.

6.5 Muon Momentum Scale and Resolution

The muon momentum scale and resolution affects the acceptance, particularly in the case of the muon p_T requirement, which is in a region where the spectrum is rising. It also impacts the E_T^{miss} and m_T requirements that depend on the muon measurement, as well as the isolation and muon quality criteria. The resolution of the muon transverse momentum is affected by a range of factors, including the amount of material traversed by the muon, the spatial resolution of the track hits and the internal alignment of the ID and MS detectors. Some effects, such as the knowledge

of the material and the magnetic field, impact the p_T measurement, but typically not in a charge dependent manner. Other effects, particularly misalignments, can result in charge dependent effects on the p_T , introducing bias in the acceptance of positive and negative muon events. An overview of the status of the alignment in the ID and MS trackers is presented in Section 5.1.4. This is a particular concern in the first data where there is limited knowledge of the detector alignment and not all types of distortions of the geometry of the ID and MS trackers are corrected. The MC is smeared and scaled using parameters derived from studies of muons in W and Z events in order to address these types of effects.

6.5.1 Muon Momentum Resolution

Since the momentum resolution is associated with detector effects such as misalignments, it has been studied as a function of η for the four main detector regions: the MS barrel region covering $|\eta| < 1.05$, the MS barrel-endcap transition region covering $1.05 < |\eta| < 1.7$, the endcap region covering $1.7 < |\eta| < 2.0$ and the forward region covering $2.0 < |\eta| < 2.4$. The resolution measurement is performed using the width of the dimuon invariant mass distribution in $Z \rightarrow \mu\mu$ decays, and from the comparison of the momentum measurements in the ID and MS in $Z \rightarrow \mu\mu$ and $W \rightarrow \mu\nu$ decays, as described in [102]. The measured resolution is worse than expected from simulation by 1–5%, with the maximum discrepancy reached in the high- η region of the detector. The discrepancy is attributed to residual misalignments in the ID and MS, imperfections in the description of the inert material in simulation and an imperfect mapping of the magnetic field, particularly in the MS transition region

where the field is not uniform. The distributions used for the resolution measurements have been combined into a fit using MC templates in order to derive the values of smearing parameters that yield the best agreement with data. In particular, the templates are varied using three smearing parameters and the χ^2 normalized to the number of degrees of freedom to the data is calculated. The values of the smearing parametrizations that minimize the χ^2 are listed in Table 6.7.

Parameter	Barrel	Transition	Endcap	Forward
	$ \eta < 1.05$	$1.05 < \eta < 1.7$	$1.7 < \eta < 2.0$	$2.0 < \eta < 2.4$
Δp_2^{ID}	0.000403	0.000913	0.001273	0.002667
Δp_1^{MS}	0.02619	0.067	0.0377	0.0407
Δp_2^{MS}	0.00018	0.00018	0.00018	0.0005

Table 6.7: Smearing parameters for ID and MS tracks used to improve the agreement between the data and MC, from [102].

The smearing parametrizations used to rescale the simulated muon p_T are separated for the ID and MS tracks, using parameters Δp_2^{ID} , Δp_1^{MS} and Δp_2^{MS} . The MS track transformation is given by

$$p_T(MS) \rightarrow p_T(MS) \times (1 \oplus f(0, 1) \times \Delta p_1^{MS} \oplus f(0, 1) \times \Delta p_2^{MS} \times p_T), \quad (6.1)$$

where $f(0, 1)$ is a normally distributed random number. Similarly, for the ID component

$$p_T(ID) \rightarrow p_T(ID) \times (1 \oplus f(0, 1) \times \Delta p_2^{ID} \times p_T) \quad (|\eta| < 1.9), \quad (6.2)$$

and

$$p_T(ID) \rightarrow p_T(ID) \times (1 \oplus f(0, 1) \times \Delta p_2^{ID} \times p_T / \tan^2 \theta) \quad (|\eta| > 1.9). \quad (6.3)$$

For the combined muon (CB), its resolution is given by the combination of the ID and MS resolutions, weighted more heavily by the better measurement of the two.

The combined resolution is thus applied based on a weighting of the corresponding ID and MS resolutions:

$$p_T(CB) \rightarrow p_T(CB) \times \left[1 + \frac{\Delta p_T(MS)/\sigma(MS) \oplus \Delta p_T(ID)/\sigma(ID)}{1/\sigma(MS) \oplus 1/\sigma(ID)} \right], \quad (6.4)$$

where Δp_T for MS or ID are the smearing corrections to the MS or ID p_T from above and $\sigma(MS)$, $\sigma(ID)$ the values for the expected resolution at that MS or ID p_T . More details of the fitting procedure and inputs used can be found in [102].

The fit results for the momentum smearings are used as corrections applied to the W MC in order to improve the agreement between data and simulation. The average smearings provided by the parametrizations in the W sample per region are approximately $(4.5 \pm 0.2)\%$ in the forward region, $(3.1 \pm 0.3)\%$ in the endcap, $(3.0 \pm 0.3)\%$ in the transition and $(1.4 \pm 0.1)\%$ in the barrel. The uncertainties on the resolution corrections for each detector region are estimated from the uncertainties on the smearing parameters provided in [102]. The W transverse mass distribution for positive and negative muons, before and after smearing is applied, are compared in Figure 6.8 and show an improvement in the agreement between data and MC with the smearing correction.

6.5.2 Muon Momentum Scale

If the accuracy of the scale of the muon momentum measurement differs for positive and negative muons, this can introduce a bias in the acceptance of positive with respect to negative muon events. Methods used to assess the muon p_T scale based on the mass scale of resonances like the Z peak, do not typically provide separate infor-

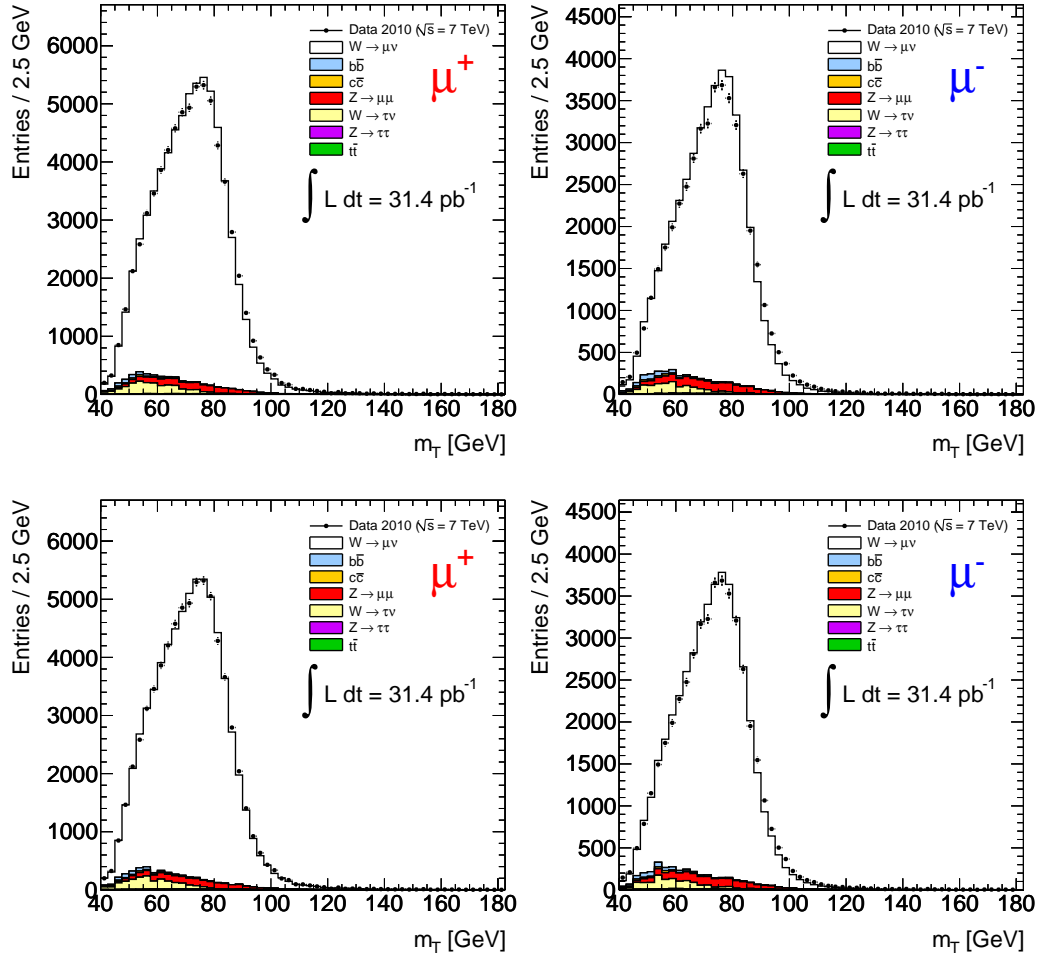


Figure 6.8: Comparison of transverse mass distribution for positive (left) and negative (right) muons before and after smearing (upper and lower figures respectively). Smearing improves the agreement between data and MC.

mation for positive and negative muons. A comparison of the curvatures of the ID and MS components of the combined track, as used in the studies of the momentum resolution, can yield information about the momentum scale for differently charged muons. A disadvantage of these comparison studies is that they do not provide a measurement of the absolute scale for a combined track. It may be noted that one difficulty when comparing the ID and MS components arises from the need to account for the uncertainties associated with each component relative to the combined measurement. The comparison is otherwise dominated by regions with poor measurement in the MS (for example the transition and BEE³ regions) or the ID (for example the forward region) and thus tends to over-estimate the uncertainty on the combined track.

A new approach has been used to examine the differences in the scale of the muon p_T measurement between data and simulation, based on a comparison of the curvature of muons from W candidates, in data and in templates derived from simulation. This method provides an estimate of the momentum scale in data relative to MC that can be derived separately for the two charges and with fine binning due to the large statistics available. In the new method, a binned likelihood fit for a momentum-scale correction that yields the best agreement between data and simulation is performed as a function of η , for positive and negative charges separately. The fitting procedure is based on building an MC template from signal and EW backgrounds, normalized to the cross sections, and applying all trigger and reconstruction scale factors. The

³The BEEs are MDT chambers mounted on the endcap toroids that suffer from significant misalignments, as indicated in Section 5.1.4.

template is then smeared with the resolution smearing parametrization described above (Section 6.5.1). Finally, the value of the scale parameter that minimizes the negative log likelihood function with respect to the data is derived. The parameter used is a p_T dependent scale parametrized by $C1$

$$p_T \rightarrow C1 \times p_T. \quad (6.5)$$

Only the curvature range $0.01 - 0.04 \text{ GeV}^{-1}$ is considered in the fit, since the QCD background, present at larger curvature, is not included in the template due to the low statistics of the QCD MC and the large uncertainties in its shape and normalization. Two example scale fits for positive muons in the region $1.05 < \eta < 1.7$ and negative muons in the region $-2.4 < \eta < 2.0$ are shown in Figure 6.9. In these example regions, the fit results indicate approximately 1% positive scale difference for negative muons and about 2% negative scale difference for positive muons. A limitation of this method is that it depends on the theoretical modeling of the distribution of the curvature of muons, including the choice of PDF set and higher order corrections. The theoretical uncertainties associated with the application of this method to the asymmetry analysis are presented in Section 6.7.4.

These studies do however provide an estimate of the impact of detector effects on the muon momentum scale, which are of particular concern since significant misalignments are known to be present in the reconstruction of the first data, as described in Section 5.1.4. It may be noted that some of the most problematic alignment modes are those associated with global systematic effects. In the case of the ID tracker, examples include curls and twists. In the case of the MS, examples include displace-

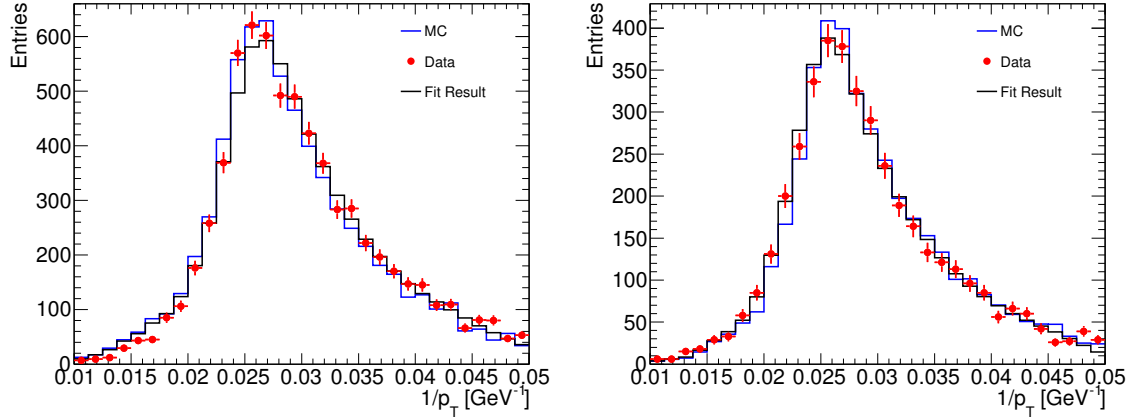


Figure 6.9: An example of the muon curvature $1/p_T$ fit for positive muons in the region $1.05 < \eta < 1.7$ (left) and negative muons in the region $-2.4 < \eta < -2.0$ (right).

ments in z of a chamber layer, such as the middle one relative to the inner and outer layers for the barrel, or of the middle wheel relative to the inner and outer ones in the endcap. These types of geometrical distortions introduce systematic charge biases in the momentum measurement. Some of these misalignment modes have not been addressed in the alignment corrections since the methods used in the derivation of the alignment parameters are not sensitive to them. For example, the χ^2 used for fitting alignment parameters, presented in Section 5.1.4, is invariant under some of these types of distortions.

In order to validate the curvature fitting method and understand the origin of detector effects and the impact from theoretical limitations, the scale for the ID and MS components contributing to the combined measurement are studied separately. The results of the fits for CB, ID and MS measurements as a function of η are shown in Figure 6.10. The ID, MS and CB fits yield consistent results, where the scales for the

CB track appear to be a combination of the ID and MS scales. In the large negative η region for example, the ID and MS scale charge differences are large but opposite, and hence the CB scale difference is much smaller. These fit results also show that the charge bias in the p_T scale differs for $\eta > 0$ and $\eta < 0$ which indicates the presence of detector effects that are dependent on the region of the detector. The ratio of the scales for $\eta > 0$ and $\eta < 0$ for the ID and MS tracks are shown in Figure 6.11. These ratios correspond to antisymmetric detector effects, since symmetric effects, including theoretical dependencies of the method, cancel. They also indicate that the scale effects are larger in the forward region $|\eta| \gtrsim 2$ of the ID and in the transition region $1.0 \lesssim |\eta| \lesssim 1.7$ of the MS. These correspond to the regions of the detector where the performance is known to be worse due to misalignments and limitations in the knowledge of the complex toroidal magnetic field map. Studies of the p_T scales for the ID in different ϕ regions, shown in Figure 6.12, also indicate the presence of significant misalignments in the endcaps. These results suggest that the origin of the charge bias in the CB muon p_T scale lies in a combination of detector effects from the ID and MS, including known sources such as misalignments and possibly the magnetic field modeling.

In order to test the validity of the momentum scale corrections, the W asymmetry measurement is performed with the ID and MS tracks separately. The measurement using the combined and the independent ID-only and MS-only muon momentum components are compared in Figure 6.13, before applying momentum scale corrections. The differences between the ID, MS and combined measurements of up to 11% in some regions indicate that the charge dependent detector effects in the ID and MS

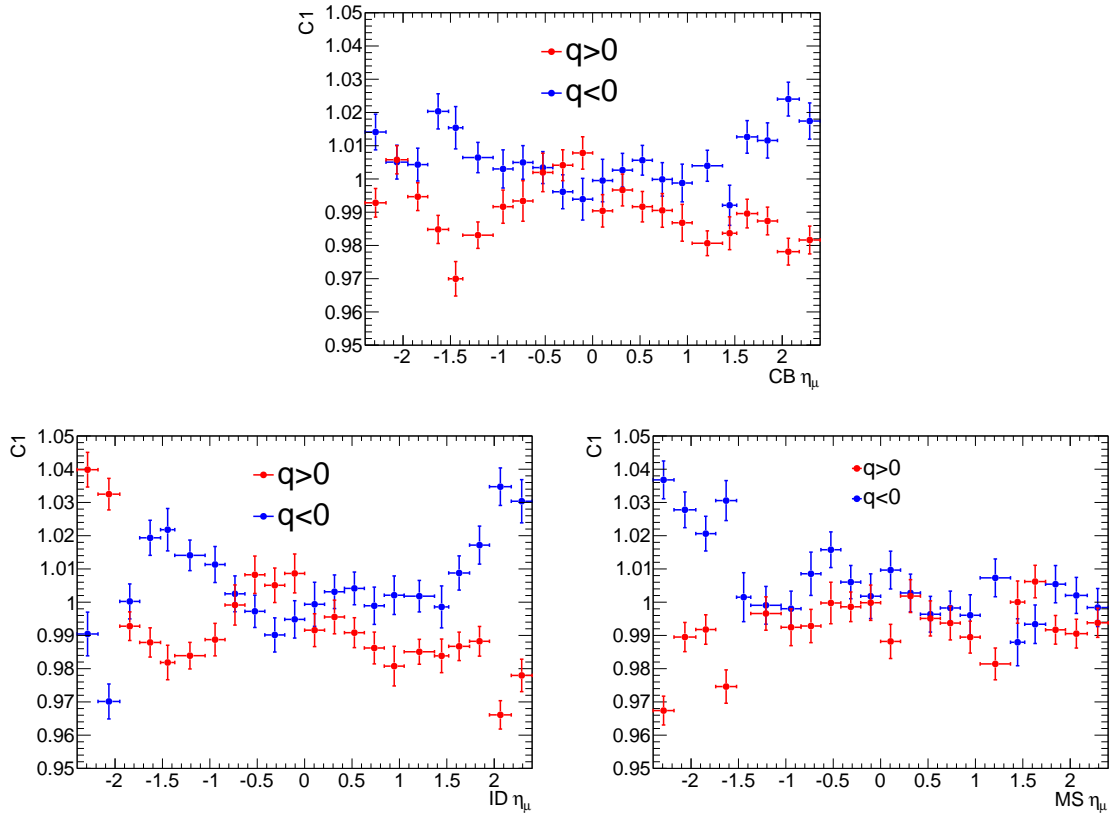


Figure 6.10: Fit results for scale parameters of the p_T measurement using the CB track (upper) and the ID (lower left) and MS (lower right) components.

trackers have a significant impact on the asymmetry. All corrections, including those for the momentum scale, are derived independently for the ID and MS and the results for the two corresponding corrected charge asymmetry distributions are shown in Figure 6.14. The good agreement of the independent asymmetry measurements after applying the momentum scale corrections show the method is working. It may be noted that the uncertainties in Figure 6.14 correspond to those associated with the momentum scale correction alone which are uncorrelated between the ID and MS measurements.

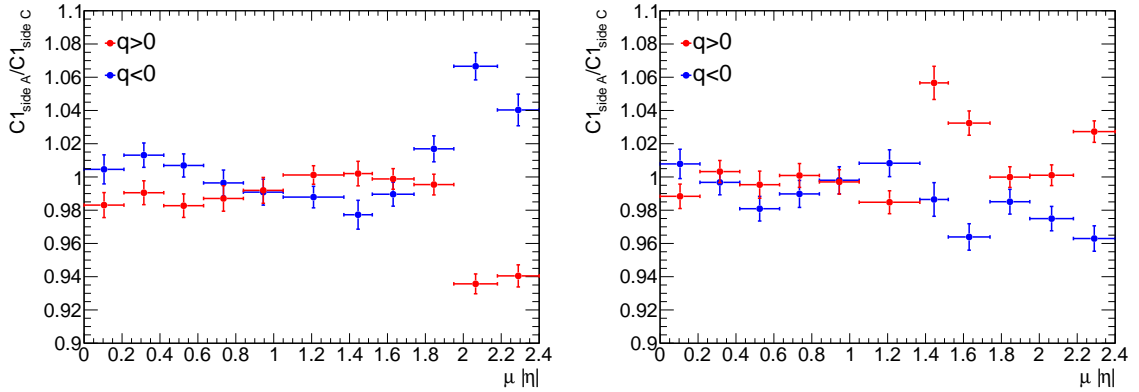


Figure 6.11: Ratio of scale fit results for $\eta > 0$ (detector side A) and $\eta < 0$ (detector side C) for positive and negative muons for ID (left) and MS (right) tracks, showing the impact of antisymmetric detector effects.

Since the p_T scale bias has a direct impact on the asymmetry, this effect is corrected for in each measurement bin, using the scale corrections shown in Figure 6.15. The measured biases in the combined muon p_T scale between the two charges are $< 1\%$, but they increase to about 3% in the transition and high- η regions. These scale corrections, together with the resolution smearings, are applied to the muon momenta in the simulated samples. The muon quality, isolation, E_T^{miss} and transverse mass variables are recalculated accordingly. The selection criteria are then applied to the updated variables and the asymmetry recomputed. The uncertainties on the scale parameters and the propagation of the error to the asymmetry measurement are described in Section 6.7.2. The overall p_T distribution for positive and negative muons from W candidate events (Figure 6.16) show reasonable agreement between data and MC.

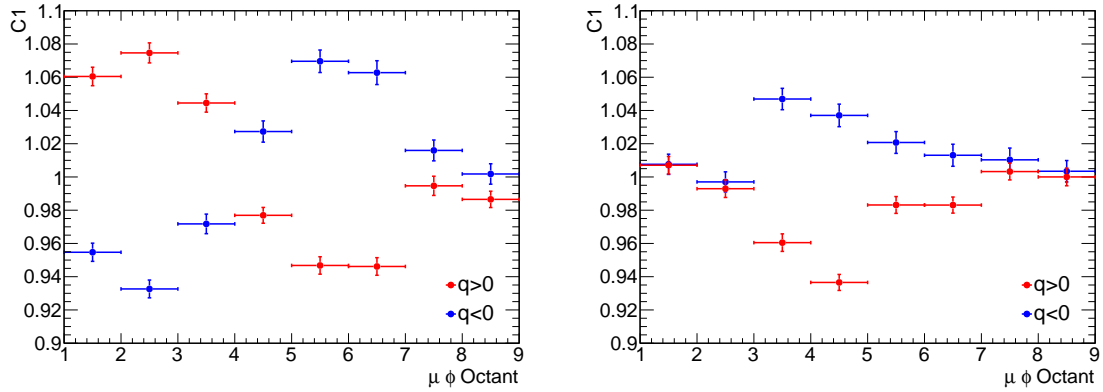


Figure 6.12: Scale fit results for positive and negative muons in the ID in eight ϕ regions for the endcap $|\eta| > 1.05$ for the $\eta < 0$ (left) and $\eta > 0$ (right). The octants are defined as ϕ regions of size $\pi/4$ ranging $[0, \pi]$ and $[-\pi, 0]$, i.e. starting at 0 and going counterclockwise in ϕ .

6.5.3 Charge Misidentification

Given the observed tracking performance, it is unlikely for a muon in the p_T range 15–50 GeV, to be reconstructed as a track of opposite charge. In order to quantify the possible impact of charge misidentification, the rate is estimated using the uncertainty of the curvature measurement to compute the likelihood that a track is reconstructed with opposite charge. Two error estimations on the curvature are considered. First, using the error provided by the tracking on the curvature parameter and assuming Gaussian errors, the probability that the curvature sign is opposite can be calculated. This estimate yields an average charge misidentification rate of order 10^{-6} for both positive and negative tracks, though a very small sample of poorly measured tracks (such as those with opposite ID and MS charge) have a probability reaching the percentage level. The second estimate is based on the assumption of a fixed error in resolution of 2% in the barrel and 5% in the endcap, for a muon of 15 GeV, and

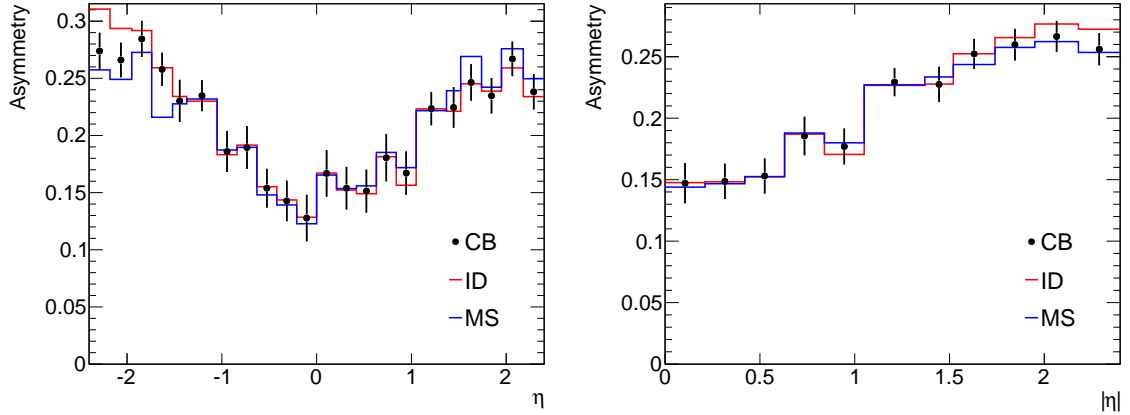


Figure 6.13: Comparison of asymmetry using the p_T measurement from the ID only, the MS only and the combined (CB) measurement in bins of η (left) and $|\eta|$ (right). Only statistical uncertainties for the CB measurement are shown.

computing the Gaussian probability. This estimate yields a misidentification rate of $< 10^{-4}$ for both positive and negative tracks. These estimates indicate that the overall misidentification rates are, at most, at the per-mille level with negligible impact on the asymmetry measurement, $< 0.01\%$.

6.6 Background Estimation

The estimate of the background contributions to W bosons from EW and $t\bar{t}$ sources is derived from MC while for QCD events a data-driven estimate is used, as described in Section 5.4. The contamination from cosmic rays is estimated to be less than a single event, as in Section 5.4.3, and is therefore neglected in this analysis. The total background estimations are summarized in Table 6.8 for positive and negative muon events in each pseudorapidity bin.

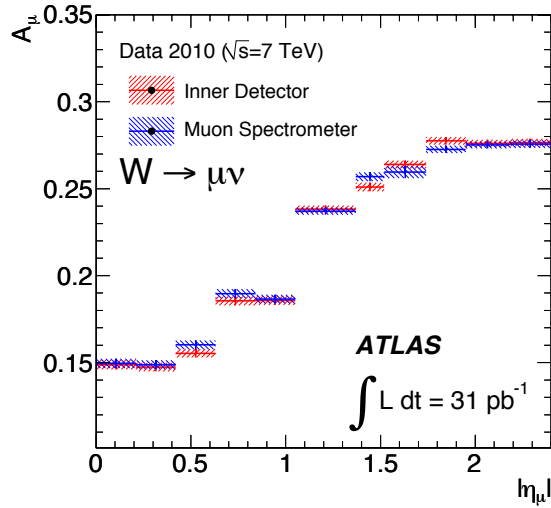


Figure 6.14: Comparison of asymmetry using the p_T measurement from the ID and MS only in bins of $|\eta|$ after applying independent corrections to them. The tracks crossing the BEE chambers are removed from the MS only measurement. The uncertainties correspond to those associated with the muon momentum scale correction, uncorrelated between the ID and MS measurements.

6.6.1 EW and $t\bar{t}$ Backgrounds

For the W , Z and top background sources, the processes considered are $W \rightarrow \tau\nu$, $Z \rightarrow \mu\mu$, $Z \rightarrow \tau\tau$, and $t\bar{t}$, as described in Section 5.4. In the case of $W \rightarrow \tau\nu$ and $Z \rightarrow \tau\tau$, the muon is produced by the leptonic decay of a τ lepton. The background estimates are based on the MC acceptance, scaled by the cross section for the corresponding process and normalized to the integrated luminosity. The predictions are scaled by the trigger and reconstruction efficiencies, described in Section 6.3, and corrected for pileup, described in Section 6.4. The muon momentum is smeared and scaled as described in Section 6.5. The predicted events for the various background sources are listed in Table 6.9, showing that the $W \rightarrow \tau\nu$ background differs for the two charges, as expected for W s, while other backgrounds, such as $Z \rightarrow \mu\mu$,

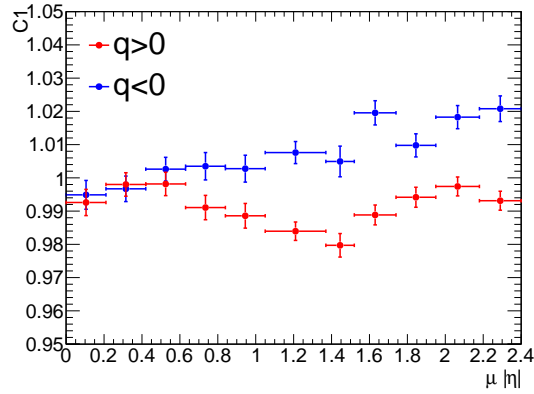


Figure 6.15: Scale fit of the muon curvature $1/p_T$ distribution for positive and negative muons in the measurement $|\eta|$ bins.

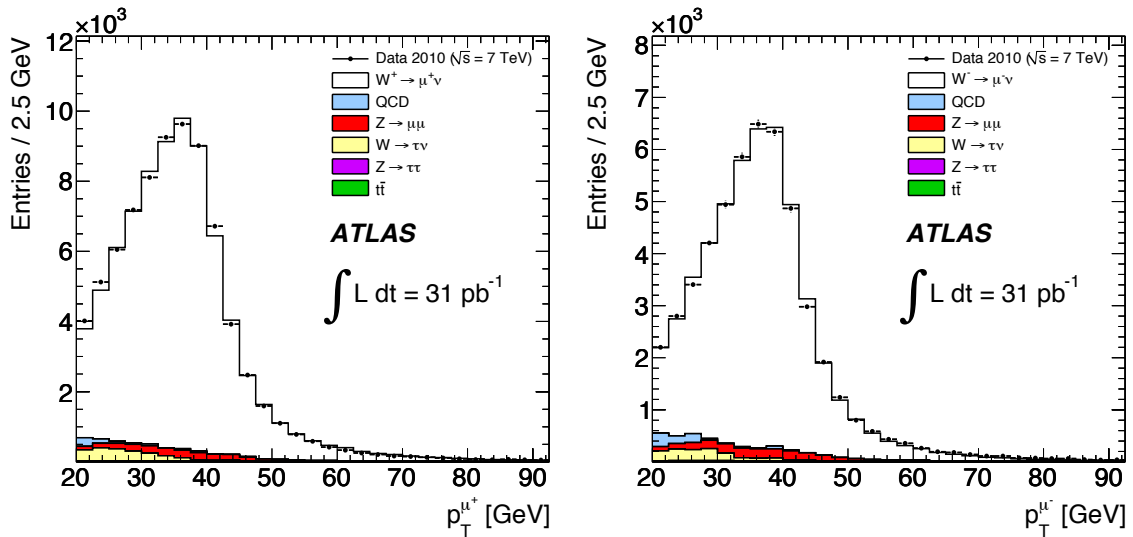


Figure 6.16: Comparison of muon p_T distributions for positive (left) and negative (right) muons after the final W selection and applying all corrections to the MC. The MC distributions are normalized to the total number of entries in data.

$ \eta_\mu $ Range	μ^+			μ^-		
	EW & top	QCD	Total	EW & top	QCD	Total
0.00 – 0.21	210 ± 35	61 ± 30	272 ± 51	179 ± 30	57 ± 28	236 ± 55
0.21 – 0.42	301 ± 47	83 ± 38	385 ± 70	248 ± 39	86 ± 39	334 ± 70
0.42 – 0.63	346 ± 52	134 ± 62	481 ± 88	263 ± 40	94 ± 42	357 ± 70
0.63 – 0.84	298 ± 46	69 ± 32	366 ± 76	272 ± 42	56 ± 27	329 ± 64
0.84 – 1.05	359 ± 54	36 ± 18	395 ± 63	292 ± 44	65 ± 30	358 ± 63
1.05 – 1.37	559 ± 77	67 ± 32	627 ± 93	502 ± 70	83 ± 37	585 ± 101
1.37 – 1.52	315 ± 45	48 ± 24	363 ± 57	282 ± 40	66 ± 31	348 ± 59
1.52 – 1.74	481 ± 66	61 ± 29	542 ± 89	442 ± 60	75 ± 35	518 ± 82
1.74 – 1.95	554 ± 75	51 ± 26	605 ± 114	396 ± 54	60 ± 29	456 ± 80
1.95 – 2.18	601 ± 81	45 ± 25	647 ± 100	481 ± 65	67 ± 33	548 ± 91
2.18 – 2.40	492 ± 66	42 ± 22	534 ± 81	427 ± 57	64 ± 34	492 ± 82

Table 6.8: Summary of expected number of EW and top, and QCD background events for positive and negative muons. All statistical and systematic uncertainties are included.

are charge symmetric. The systematic uncertainties on these background predictions include the uncertainties on the muon trigger and reconstruction efficiencies. An additional contribution associated with the theoretical uncertainties on the acceptance, comprised of PDF, 3%, and cross section uncertainties, 5% for $Z \rightarrow \mu\mu$, $W \rightarrow \tau\nu$ and $Z \rightarrow \tau\tau$, and 6% for $t\bar{t}$, are included.

6.6.2 QCD Background

The QCD background for W events is predominantly from heavy quarks decaying to muons. Applying the techniques used in the cross section analysis introduced in Section 5.4.2, the multijet background to $W \rightarrow \mu\nu$ is estimated using the “matrix” method. Following the same derivation, loose and tight muon samples are defined before $N_{\text{loose},i}^{+(-)}$ and after $N_{\text{tight},i}^{+(-)}$ applying the isolation requirement, where the indices

$ \eta $ Range	μ^+				
	$Z \rightarrow \mu\mu$	$W \rightarrow \tau\nu$	$Z \rightarrow \tau\tau$	$t\bar{t}$	Total
0.00 – 0.21	55 ± 4	125 ± 24	6 ± 1	25 ± 2	210 ± 26
0.21 – 0.42	83 ± 6	179 ± 30	7 ± 2	33 ± 2	301 ± 33
0.42 – 0.63	99 ± 7	205 ± 32	11 ± 2	31 ± 2	346 ± 36
0.63 – 0.84	108 ± 8	159 ± 28	6 ± 1	25 ± 2	298 ± 32
0.84 – 1.05	123 ± 8	208 ± 32	5 ± 1	22 ± 2	359 ± 37
1.05 – 1.37	261 ± 17	256 ± 36	13 ± 2	29 ± 2	559 ± 47
1.37 – 1.52	186 ± 12	110 ± 22	5 ± 1	14 ± 1	315 ± 28
1.52 – 1.74	292 ± 18	163 ± 28	8 ± 2	17 ± 1	481 ± 39
1.74 – 1.95	310 ± 19	223 ± 32	8 ± 2	13 ± 1	554 ± 44
1.95 – 2.18	367 ± 23	215 ± 31	9 ± 2	11 ± 1	601 ± 46
2.18 – 2.40	332 ± 21	145 ± 25	8 ± 2	7 ± 1	492 ± 38
$ \eta $ Range	μ^-				
	$Z \rightarrow \mu\mu$	$W \rightarrow \tau\nu$	$Z \rightarrow \tau\tau$	$t\bar{t}$	Total
0.00 – 0.21	57 ± 4	94 ± 21	4 ± 1	24 ± 2	179 ± 23
0.21 – 0.42	76 ± 5	132 ± 25	9 ± 2	31 ± 2	248 ± 28
0.42 – 0.63	101 ± 7	120 ± 23	11 ± 2	31 ± 2	263 ± 27
0.63 – 0.84	96 ± 7	144 ± 26	7 ± 2	26 ± 2	272 ± 29
0.84 – 1.05	119 ± 8	143 ± 26	6 ± 1	24 ± 2	292 ± 30
1.05 – 1.37	255 ± 16	202 ± 32	14 ± 2	30 ± 2	502 ± 42
1.37 – 1.52	176 ± 11	86 ± 18	6 ± 1	15 ± 1	282 ± 25
1.52 – 1.74	277 ± 17	138 ± 25	10 ± 2	17 ± 1	442 ± 36
1.74 – 1.95	277 ± 17	99 ± 21	7 ± 1	13 ± 1	396 ± 31
1.95 – 2.18	333 ± 21	128 ± 24	10 ± 2	10 ± 1	481 ± 37
2.18 – 2.40	321 ± 20	91 ± 19	8 ± 2	7 ± 1	427 ± 32

Table 6.9: Expected number of EW background events for positive and negative muons shown separately for $W \rightarrow \tau\nu$, $Z \rightarrow \mu\mu$, $Z \rightarrow \tau\tau$ and $t\bar{t}$, and the total. All systematic uncertainties are included, except for the luminosity uncertainty of 11% throughout. The number of predicted events is normalized to 31 pb^{-1} .

indicate the corresponding charge and the $|\eta|$ bin i . Equation 5.4 then becomes

$$\begin{aligned} N_{\text{loose},i}^{+(-)} &= N_{\text{non-QCD},i}^{+(-)} + N_{\text{QCD},i}^{+(-)} \\ N_{\text{tight},i}^{+(-)} &= \epsilon_{\text{non-QCD},i}^{+(-)} N_{\text{non-QCD},i}^{+(-)} + \epsilon_{\text{QCD},i}^{+(-)} N_{\text{QCD},i}^{+(-)} \end{aligned} \quad (6.6)$$

yielding, as in Equation 5.5, the solution

$$N_{\text{QCD},i}^{+(-)} = \frac{N_{\text{loose},i}^{+(-)} \epsilon_{\text{non-QCD},i}^{+(-)} - N_{\text{tight},i}^{+(-)}}{\epsilon_{\text{non-QCD},i}^{+(-)} - \epsilon_{\text{QCD},i}^{+(-)}} \quad (6.7)$$

where $\epsilon_{\text{non-QCD},i}^{+(-)}$ and $\epsilon_{\text{QCD},i}^{+(-)}$ refer to the relative isolation efficiencies for non-QCD events (signal and EW and top backgrounds) and for the QCD background respectively. The expected QCD background in the signal region is given by $N_{\text{QCD-tight},i}^{+(-)} = \epsilon_{\text{QCD},i}^{+(-)} N_{\text{QCD},i}^{+(-)}$.

The isolation efficiency for QCD muons ϵ_{QCD} is estimated using a control sample of muons with $15 < p_{\text{T}} < 20$ GeV in events with $E_{\text{T}}^{\text{miss}} < 25$ GeV, which are predominantly from multijet events. However, the prompt muon component is subtracted using an iterative procedure that uses the signal $W \rightarrow \mu\nu$ and background $W \rightarrow \tau\nu$, $Z \rightarrow \mu\mu$, $Z \rightarrow \tau\tau$ and $t\bar{t}$ MC predictions. The iterations converge rapidly since the estimate is stable after the third iteration, with negligible impact on the QCD background estimate. The efficiency calculated from the control region in data is corrected, using the ratio in jet MC of the isolation efficiency in the control and signal ($p_{\text{T}} > 20$ GeV and $E_{\text{T}}^{\text{miss}} > 25$ GeV) regions. The main difference between the efficiency calculation described here, and the one presented in Section 5.4.2, is that the correlation between muon p_{T} and $E_{\text{T}}^{\text{miss}}$ in QCD events is explicitly accounted for. In particular, the correction of the efficiency in $E_{\text{T}}^{\text{miss}}$ reduces the efficiency dependence

on p_T . Finally, the isolation efficiency for non-QCD muons $\epsilon_{\text{non-QCD}}$ is calculated using $Z \rightarrow \mu\mu$ events, as described in Section 6.3.3. All the efficiencies are derived per charge and $|\eta|$ bin.

The statistical uncertainty on the expected number of QCD events satisfying the full event selection criteria $N_{\text{QCD-tight},i}^{+(-)} = \epsilon_{\text{QCD},i}^{+(-)} N_{\text{QCD},i}^{+(-)}$ is given by

$$\frac{\delta N_{\text{QCD-tight},i}^{+(-)}}{N_{\text{QCD-tight},i}^{+(-)}} = \frac{1}{\sqrt{N_{\text{loose},i}^{+(-)}}} \oplus \frac{\delta \epsilon_{\text{non-QCD},i}^{+(-)} \left(\alpha_i^{+(-)} - \epsilon_{\text{QCD},i}^{+(-)} \right)}{\left(\epsilon_{\text{non-QCD},i}^{+(-)} - \alpha_i^{+(-)} \right) \left(\epsilon_{\text{non-QCD},i}^{+(-)} - \epsilon_{\text{QCD},i}^{+(-)} \right)} \oplus \frac{\delta \alpha_i^{+(-)}}{\left(\epsilon_{\text{non-QCD},i}^{+(-)} - \alpha_i^{+(-)} \right)} \oplus \frac{\delta \epsilon_{\text{QCD},i}^{+(-)} \epsilon_{\text{non-QCD},i}^{+(-)}}{\epsilon_{\text{QCD},i}^{+(-)} \left(\epsilon_{\text{non-QCD},i}^{+(-)} - \epsilon_{\text{QCD},i}^{+(-)} \right)} \quad (6.8)$$

where $\alpha_i^{+(-)} = N_{\text{tight},i}^{+(-)} / N_{\text{loose},i}^{+(-)}$ is the overall isolation efficiency in data.

The systematic uncertainty on the isolation efficiencies is comprised of the sum in quadrature of various contributions derived per charge and pseudorapidity bin. These include the uncertainty on the QCD isolation efficiency estimate in the control region, derived from the difference in the isolation efficiencies in data and MC in the control sample. The uncertainty on the correction of the efficiency to the signal region is determined using two semi-control samples based on reversing one of the requirements $15 < p_T < 20$ GeV but with $E_T^{\text{miss}} > 25$ GeV, and $p_T > 20$ GeV maintaining $E_T^{\text{miss}} < 25$ GeV. These two regions include a significant QCD contribution, but once the non-QCD contribution is subtracted, the predictions for the isolation efficiency in data and MC show reasonable agreement. The difference in the efficiency prediction in the non-QCD subtracted data sample and the QCD MC is used as an estimate of the systematic uncertainty on the efficiency correction. The extrapola-

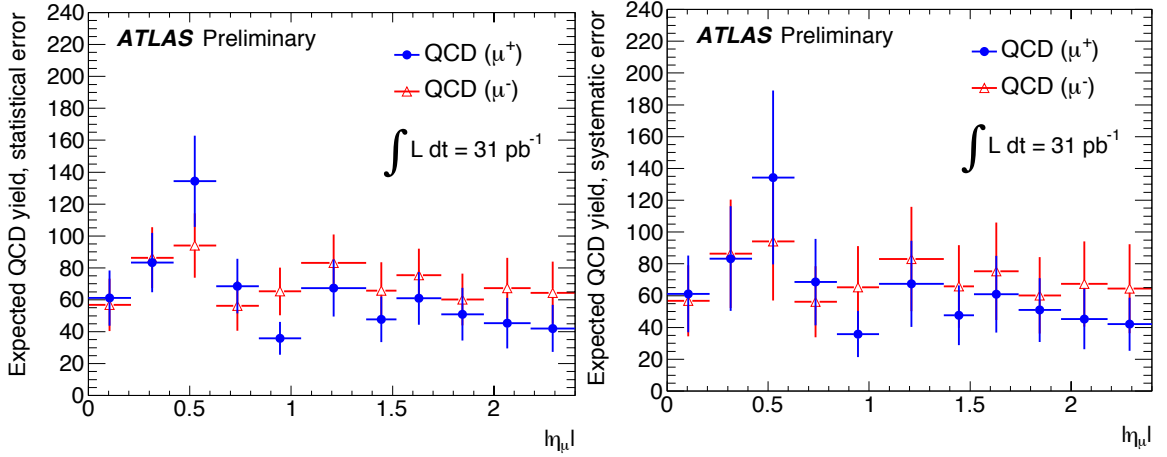


Figure 6.17: The QCD prediction for positive and negative charged muons is shown separately, with the statistical (left) and only systematic (right) uncertainties.

tion in muon p_T yields uncertainties of 17% and 3% for positive and negative muons respectively, and the extrapolation in E_T^{miss} differences of 22% and 20% for positive and negative charges. An overall uncertainty of 39%, applied to both charges, is used as a conservative estimate of this systematic uncertainty contribution.

The QCD background estimate $N_{\text{QCD-tight},i}^{+(-)}$ can thus be determined, using the derived isolation efficiencies $\epsilon_{\text{QCD},i}$ and $\epsilon_{\text{non-QCD},i}$, and the fraction of events in the tight-loose samples $\alpha_i^{+(-)}$, yielding the predictions shown in Figure 6.17. The overall prediction is 697 ± 58 (stat) ± 279 (syst) for events with a positive muon and 775 ± 58 (stat) ± 310 (syst) for events with a negative muon. The systematic uncertainties are treated as fully correlated between the charges.

In order to check the stability of the QCD prediction, the isolation efficiency for QCD events is also estimated from the semi-control sample $15 < p_T < 20$ GeV and $E_T^{\text{miss}} > 25$ GeV, where the prompt muon contribution is subtracted using the iterative

procedure as before. The extrapolation to the signal region $p_T > 20$ GeV and $E_T^{\text{miss}} > 25$ GeV is performed using the jet MC. The full range of the extrapolation is taken as an estimate of the systematic uncertainty on the efficiency prediction. Since the efficiency is obtained from a control sample enriched in non-QCD contributions, the efficiency is larger and more strongly dependent on the prompt muon subtraction procedure. The resulting predictions, yielding overall expectations of 969 ± 109 (stat) and 957 ± 102 (stat) for positive and negative charges respectively, are in agreement with the baseline prediction.

6.7 Uncertainty Estimation

All uncertainties on the asymmetry are calculated per pseudorapidity bin accounting for the correlations between the bins and the charges. The statistical uncertainty is uncorrelated between the bins and for an asymmetry of the form $A = (a-b)/(a+b)$ is given by

$$\frac{\delta A}{A} = \frac{2ab}{a^2 - b^2} \left(\frac{\delta a}{a} \oplus \frac{\delta b}{b} \right) = \frac{1 - A^2}{2A} \left(\frac{\delta a}{a} \oplus \frac{\delta b}{b} \right) \quad (6.9)$$

where δa and δb are the uncertainties on a and b respectively and \oplus indicates the sum in quadrature. The uncertainty on the number of selected candidate events in data N is given by Poisson statistics \sqrt{N} . The propagation of systematic uncertainties on C_W that are of statistical origin is performed using pseudo-experiments, while those of systematic origin are estimated by performing variations of the corresponding parameter and calculating the impact on the asymmetry. This second type of systematic

$ \eta $ Range	Trigger Efficiency	Reco. Efficiency	p_T Scale and Reso.	QCD Norm.	EW and $t\bar{t}$ Norm.	Theoretical Modeling
0.00 – 0.21	0.011	0.010	0.003	0.003	< 0.001	0.007
0.21 – 0.42	0.010	0.004	0.003	0.003	< 0.001	0.005
0.42 – 0.63	0.009	0.004	0.003	0.003	< 0.001	0.006
0.63 – 0.84	0.012	0.004	0.003	0.002	0.001	0.007
0.84 – 1.05	0.013	0.006	0.003	0.003	0.001	0.008
1.05 – 1.37	0.006	0.007	0.002	0.002	0.001	0.006
1.37 – 1.52	0.006	0.005	0.002	0.003	0.002	0.005
1.52 – 1.74	0.005	0.004	0.002	0.003	0.002	0.007
1.74 – 1.95	0.006	0.003	0.002	0.002	0.001	0.006
1.95 – 2.18	0.006	0.004	0.002	0.003	0.002	0.009
2.18 – 2.40	0.007	0.005	0.002	0.003	0.002	0.007

Table 6.10: Absolute systematic uncertainties on the W charge asymmetry from different sources as a function of absolute muon pseudorapidity.

uncertainties is given by

$$\frac{\delta A}{A} = \frac{1 - A^2}{2A} \left(\frac{\delta a}{a} \pm \frac{\delta b}{b} \right) \quad (6.10)$$

where uncertainties that are fully correlated between the two charges subtract and those that are anti-correlated add. The dominant sources of systematic uncertainty arise from the muon trigger and reconstruction efficiencies, the impact of the momentum scale and resolution, the theoretical uncertainties and the background estimations. A summary of all the systematic uncertainties considered in $|\eta|$ bins is shown in Table 6.10 and a graphical comparison with the statistical uncertainties can be found in Figure 6.18. The statistical uncertainty is 6 – 8% in the barrel and 3 – 4% in the endcap while the total systematic uncertainty is 8 – 11% in the barrel and 4 – 5% in the endcap.

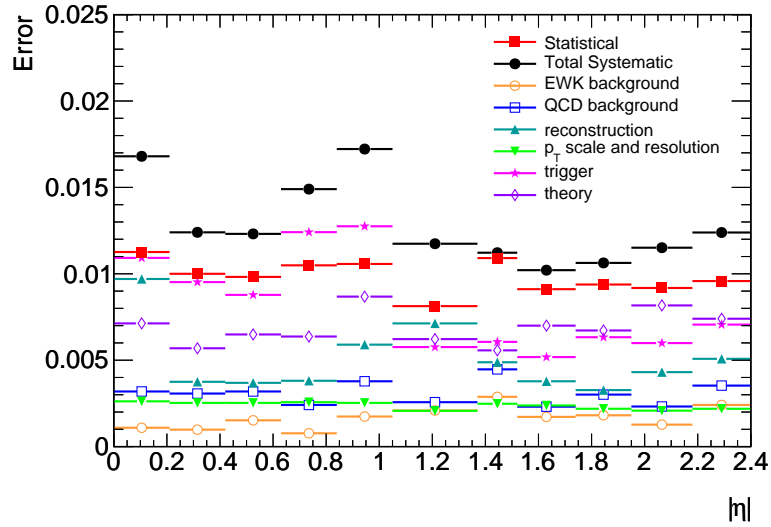


Figure 6.18: Absolute uncertainties on the differential W lepton charge asymmetry measurement as a function of absolute muon pseudorapidity showing the various contributions to the systematic uncertainty and the statistical uncertainty.

6.7.1 Impact of the Trigger and Reconstruction Efficiencies

The uncertainty on the trigger and reconstruction efficiencies is mainly due to the statistical uncertainty associated with the availability of $Z \rightarrow \mu\mu$ events. The trigger and reconstruction efficiencies show no significant charge bias, so the average value for the efficiency scale factors, which have smaller statistical errors, are used, as discussed in Section 6.3. The systematic uncertainties on the efficiencies are determined from studies of the impact of the selection criteria and background contamination, both providing a smaller contribution and exhibiting no significant charge bias. Since the dominant source of uncertainty is statistical and this is independent for each bin, the binned uncertainties are propagated in an uncorrelated way to an overall uncertainty on the asymmetry. These systematic uncertainties are evaluated by repeating the asymmetry analysis 5,000 times, where a different random Gaussian smearing is

added to the trigger and reconstruction scale factors independently each time for each pseudorapidity bin. These pseudo-experiments provide a set of 5,000 asymmetry measurements per η bin that are fit with a Gaussian and its width is used to estimate the corresponding systematic uncertainty.

The trigger efficiency is lower in the barrel region $|\eta| < 1.05$, at about 80%, compared to the endcap trigger efficiency, which is over 90%, due to a reduced geometrical acceptance. This results in a larger statistical uncertainty of the scale factors and consequently a larger uncertainty on the asymmetry. The trigger systematic uncertainty is dominant in the barrel pseudorapidity bins, 6 – 7% for $|\eta| < 1.05$ and 2 – 3% for $|\eta| > 1.05$. The uncertainties associated with the reconstruction efficiencies are largest for $|\eta|$ about 0, with approximately 7%, and the MS barrel-endcap transition region around $|\eta|$ around 1.05, with about 3% uncertainty. This is also due primarily to the impact of geometrical acceptance effects associated with reduced chamber coverage and regions with poor momentum measurements. In the remaining regions, the uncertainty is 1 – 2%.

6.7.2 Impact of the Muon Momentum Scale and Resolution

The main contribution to the uncertainty in the muon momentum scale and resolution is due to the limited statistics of the samples used in the fitting procedures to measure the differences between data and MC in various pseudorapidity regions, as described in Section 6.5. The systematic error arising from the momentum scale and resolution uncertainties is derived from the variation in the asymmetry associated with a shift of the muon p_T scale and increased resolution relative to MC expecta-

tions. The impact of the momentum scale and resolution is assessed for the muon p_T , muon quality, isolation, E_T^{miss} and m_T requirements.

For the statistical uncertainties on the scale corrections derived in Section 6.5, the uncertainty on the asymmetry is calculated by repeating the asymmetry measurement 1,000 times, using a p_T scale smeared by a Gaussian whose width is given by the statistical uncertainty on the scale each time. The statistical uncertainty on the scale parameter $C1$, from Equation 6.5, for each charge and pseudorapidity bin is about 0.4%. These pseudo-experiments result in a set of asymmetry measurements that are fit with a Gaussian and the width is used to estimate the systematic uncertainty. This uncertainty propagation is performed independently in each $|\eta|$ bin.

An additional uncertainty arises from bias in the template shapes used to derive the corrections. The overall impact of this uncertainty is determined by shifting parameters affecting the shapes of the templates, such as the resolution described in Section 6.5.1, within the uncertainties and recalculating the asymmetry. In order to assess the impact of possible bias introduced by the fitting procedure itself, toy Monte Carlo studies are performed to compare the input scale parameter $C1$, from Equation 6.5, to the fit value. The results are shown in Figure 6.19. For the case where the resolution in the template and the fit distribution are the same (left figure), the fit result corresponds to the true value of the scale parameter, as indicated by the diagonal line. However, if the resolution smearing differs between the template and the fit distribution (corresponding to the case where the resolution is different in data and MC after the smearing correction, from Section 6.5.1, is applied), the scale

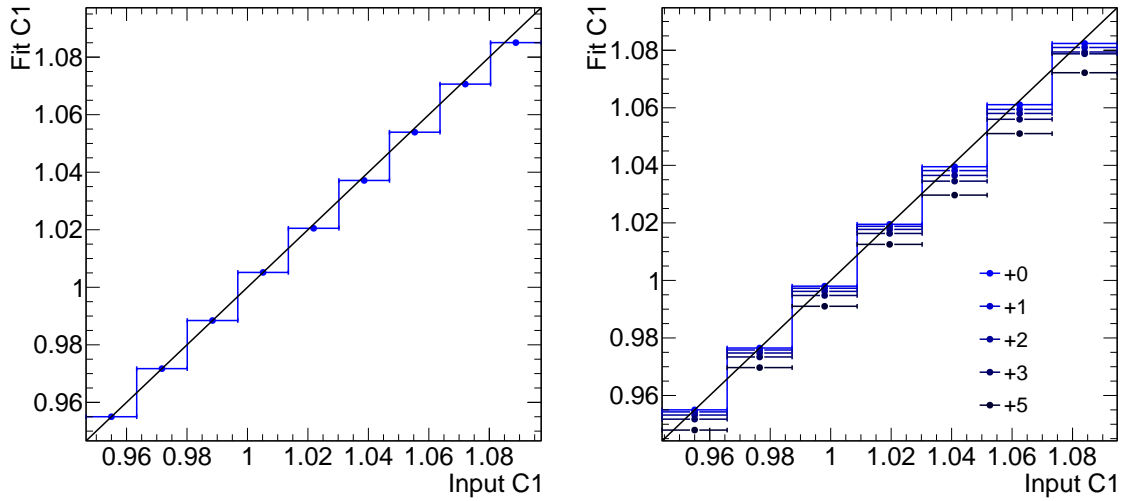


Figure 6.19: Toy Monte Carlo study of input scale parameter $C1$ and fit result. The left distribution shows the result when the resolution smearing in the template is identical to the fit distribution, corresponding to the scenario where the resolution in data and MC after the smearing corrections are applied is the same. The right distribution shows the bias introduced by an additional smearing of 1 – 5% of the fit distribution compared to the template. This corresponds to the case where the resolution in data is different from the MC corrected for resolution effects.

fit can yield a biased result. This is shown in the distribution on the right, where increasing the smearing in the fit distribution relative to the template results in a shifted value compared to the true input parameter. It may be noted that the same effect is observed, in the opposite direction, if the template is oversmeared relative to the fit distribution. The effect is a factor of about 0.1 times the difference in smearing between the template and the fit distribution (for example, a 3% smearing difference yields about a 0.3% shift in scale).

The impact of the resolution on the scale fits contributes to the uncertainty particularly because the smearings are derived for only four detector regions, as described in Section 6.5.2, but the scale fits are performed in the finer measurement bins. This

can give rise to differences in the resolution in data and MC, where in some cases the MC is undersmeared compared to the data while in other cases it is oversmeared. A systematic uncertainty is assigned to account for possible differences in resolutions in data and MC by investigating the impact of a 1σ resolution bias on the scale fits. The parameters are varied in opposite directions for the two charges in order to account for possible charge bias. The average effects are small, about 0.1% in the barrel, endcap and forward regions and 0.2% in the transition region.

Another source of uncertainty arises from the modeling of the background contributions in the templates, particularly the QCD background which has large uncertainty. A template for the QCD background prediction is derived from the integrated MC sample and included in the overall template for each η bin where the normalization is given by the QCD background estimate in each bin, plus 1σ of the uncertainty. This serves as an estimate of the maximum expected impact and the positive and negative charges are treated as fully correlated, since the QCD background affects the same side of the distribution (low- p_T tail) for both. The scale factors obtained with and without the QCD component of the template differ by $< 1\%$, indicating negligible impact on the asymmetry.

The resulting uncertainty on the asymmetry is in the range $1 - 2\%$ and shows weak dependence on the muon pseudorapidity. Finally, the redundant measurements in the ID and MS components of the combined muon result in a charge misidentification rate, for the p_T range considered, of less than 10^{-4} , with negligible impact on the asymmetry.

6.7.3 Impact of Backgrounds

The main source of uncertainty on the QCD background prediction comes from the uncertainty in the isolation efficiency for QCD events, as described in Section 6.6.2. The main contributor is from modeling the extrapolation in muon p_T and E_T^{miss} of the efficiency in a QCD control region to the signal region, yielding a 39% uncertainty in the efficiency. The other main sources of uncertainty include the statistical uncertainty of the background prediction and the isolation efficiency for the non-QCD component. As previously, the statistical uncertainty is derived using 5,000 pseudo-experiments where the background predictions are varied on a bin-by-bin basis within their uncertainties, and are treated as uncorrelated between the two charges. The uncertainties on the asymmetry associated with systematic effects on the isolation efficiencies are determined from variations of the background predictions in a correlated manner between the charges, since these components to the QCD background estimate show no significant charge bias. The corresponding uncertainty on the asymmetry is in the range 1–3%, with little dependence on muon pseudorapidity.

In the case of the electroweak and $t\bar{t}$ backgrounds, the theoretical and luminosity uncertainties on the predictions, described in Section 6.6.1, are treated as fully correlated across samples, except for the uncertainty from the W/Z and $t\bar{t}$ cross sections that are treated as uncorrelated. The resulting impact on the asymmetry measurement is small, under 1% across all bins.

6.7.4 Impact of Theoretical Modeling

Studies of the theoretical uncertainties on the C_W acceptance factors used in the W inclusive cross section measurement indicate that the impact of PDFs, after applying the kinematic and selection cuts, is small, typically below 0.3% [103]. For this analysis the $W \rightarrow \mu\nu$ simulation is used for the derivation of the fiducial acceptance factors $C_{W\mu^\pm}$, defined in Equation 5.9, for the estimation of the muon momentum scale and in the estimation of some backgrounds (see Section 6.6.2). The impact of theoretical modeling on the analysis is derived by comparing the default PYTHIA sample based on the MRST LO* PDF set and a sample generated with MC@NLO using the CTEQ 6.6 NLO PDF set. PYTHIA provides a leading-log calculation for W production and is expected to give reasonably accurate prediction for the low p_T^W region, while MC@NLO [104] includes higher-order matrix elements and is thus expected to be more reliable for the high W transverse momentum regime. Therefore a systematic uncertainty associated with the theoretical modeling is derived from the differences between the two MC calculations. A comparison of the PYTHIA and MC@NLO predictions show differences in the muon p_T distribution of about 2% for positive muons and -1% for negative muons, as shown in Figure 6.20. The underlying truth distributions in PYTHIA are rescaled by those derived with MC@NLO and the full analysis is performed to include a recalculation of the fiducial acceptance factors with the corresponding momentum scale corrections and updated background predictions. Variations of about 3% are observed on the asymmetry. This serves as an estimate of the theoretical impact of the choice of MC.

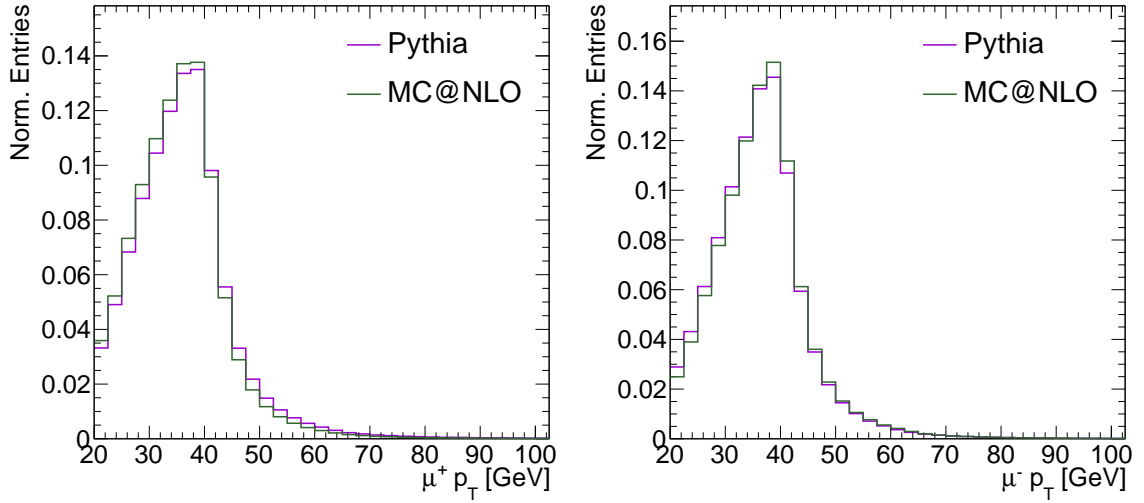


Figure 6.20: Truth p_T distributions comparing PYTHIA and MC@NLO for positive (left) and negative (right) muon charges.

6.8 Results

The η distribution for positive and negative muons after the full event selection, comparing data and Monte Carlo expectations is shown in Figure 6.21. The acceptance features of the muon system due to effects such as chamber coverage and the different acceptance for positive and negative muons introduced by the toroidal field in the barrel-endcap MS transition region are described by the MC. The candidate events and total expected background contribution per bin in $|\eta|$ for positive and negative muons are provided in Table 6.11. The $C_{W\mu^\pm}$ correction factors, corresponding to the ratio of reconstructed over generated events in the $W \rightarrow \mu\nu$ simulated sample that satisfy all the kinematic requirements of the event selection: $p_T^\mu > 20$ GeV, $p_T^\nu > 25$ GeV and $m_T > 40$ GeV, are also listed. These factors include the trigger and muon reconstruction scale factors used to correct differences between data and MC. The $C_{W\mu^\pm}$ factors are smaller in the lower $|\eta|$ bins. This is due primarily to

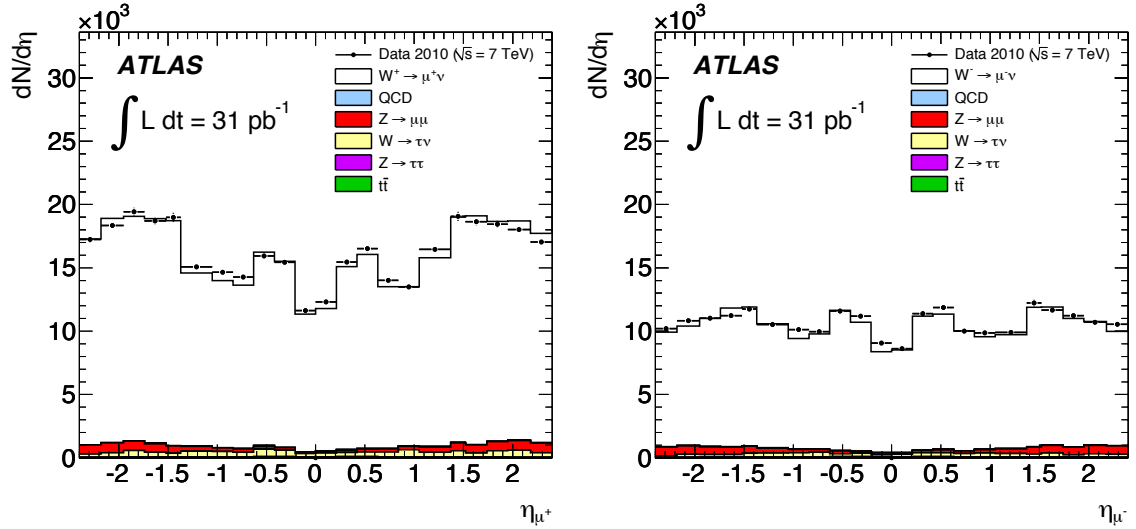


Figure 6.21: Pseudorapidity distribution of W candidate muons for positive (left) and negative (right) muons. The Monte Carlo is normalized to the number of entries in data and trigger and reconstruction efficiency scale factors are applied.

geometrical acceptance effects from chamber coverage. The differences between the positive and negative charges are small, 2% at most.

The asymmetry is calculated from the fiducial cross section in each $|\eta|$ bin, as shown in Equation 5.10. The expected background is subtracted from the number of candidate events in each bin. The result is then unweighted by dividing by the corresponding $C_{W\mu^\pm}$ factor, as defined in Equation 5.9. The normalized differential fiducial cross sections for positive and negative charges as a function of $|\eta|$ are shown in Figure 6.22 (left). The distributions exhibit the characteristic drop in the negative cross section with increasing $|\eta|$ and a much flatter distribution for the positive charge⁴. The results at various stages of the asymmetry calculation are shown in Figure 6.22 (right), comparing the asymmetry distribution in $|\eta|$ for all candidates to the

⁴As a shape comparison, see for example Figure 2.11.

$ \eta $ Range	μ^+			μ^-		
	N	B	$C_{W\mu^+}$	N	B	$C_{W\mu^-}$
0.00 – 0.21	5028	272 ± 51	0.594 ± 0.005	3711	236 ± 55	0.584 ± 0.004
0.21 – 0.42	6486	385 ± 70	0.779 ± 0.009	4736	334 ± 70	0.759 ± 0.008
0.42 – 0.63	6818	481 ± 88	0.808 ± 0.009	4923	357 ± 70	0.800 ± 0.009
0.63 – 0.84	5939	366 ± 76	0.686 ± 0.008	4194	329 ± 64	0.691 ± 0.008
0.84 – 1.05	5909	395 ± 63	0.672 ± 0.007	4195	358 ± 63	0.681 ± 0.008
1.05 – 1.37	10086	627 ± 93	0.735 ± 0.007	6531	585 ± 101	0.752 ± 0.007
1.37 – 1.52	5708	363 ± 57	0.905 ± 0.009	3595	348 ± 59	0.914 ± 0.009
1.52 – 1.74	8218	542 ± 89	0.905 ± 0.008	5035	518 ± 82	0.925 ± 0.008
1.74 – 1.95	7956	605 ± 114	0.896 ± 0.009	4671	456 ± 80	0.898 ± 0.008
1.95 – 2.18	8364	647 ± 100	0.903 ± 0.009	4952	548 ± 91	0.910 ± 0.009
2.18 – 2.40	7541	534 ± 81	0.881 ± 0.010	4561	492 ± 82	0.896 ± 0.010

Table 6.11: Summary of observed number of events, expected background and correction factor $C_{W\mu^\pm}$ for positive and negative muons in bins of $|\eta|$. The uncertainties of the background estimates include all systematic sources, even the uncertainty due to the luminosity, used in the normalization of the electroweak and $t\bar{t}$ components. The uncertainties of the $C_{W\mu^\pm}$ factors include the statistical uncertainty from the MC sample and trigger and reconstruction scale factors.

result following background subtraction, and the result after $C_{W\mu^\pm}$ correction. These distributions agree within the statistical uncertainty, indicating that background subtraction and $C_{W\mu^\pm}$ corrections have a small impact on the asymmetry measurement.

The measured differential muon charge asymmetry in 11 bins of muon $|\eta|$ is shown in Table 6.12 and Figure 6.23. The full statistical and systematic uncertainties are included and contribute comparable amounts to the total uncertainty. Expectations from W predictions at NLO obtained using MC@NLO [104] with three different PDF sets: CTEQ 6.6 [41], HERA 1.0 [20] and MSTW 2008 [17], are also shown for comparison. The uncertainties of the predictions are derived from the PDF uncertainties by adding in quadrature the deviations in the predictions derived with each of the

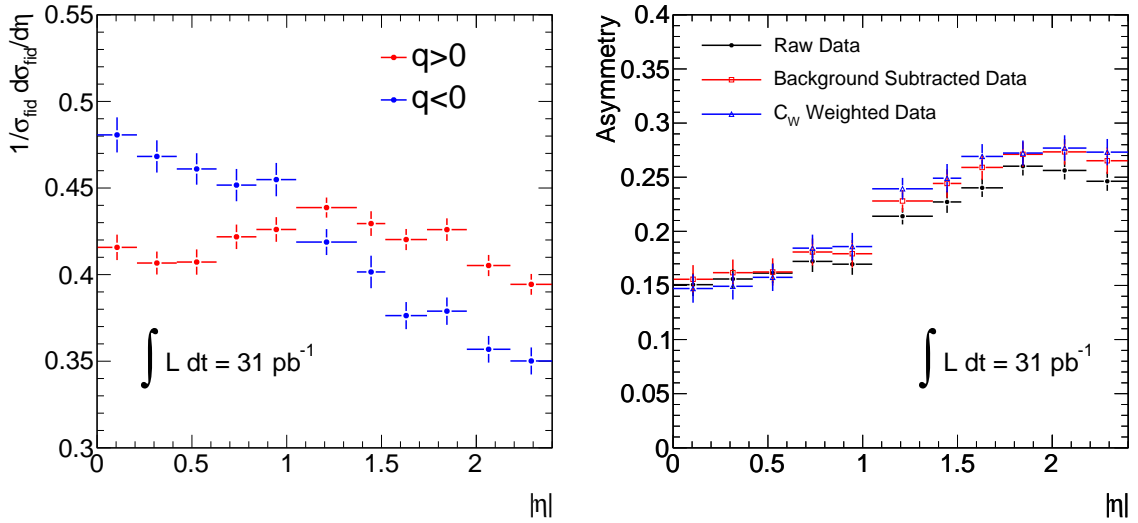


Figure 6.22: Normalized fiducial cross section for positive and negative charges as a function of $|\eta|$ (left). Only statistical uncertainties are included. Muon charge asymmetry in $|\eta|$ bins (right) for raw candidates, following background subtraction and after weighting by the corresponding $C_{W\mu^\pm}$ factor.

PDF error sets from the nominal prediction [105] and are quoted for the 90% C.L. bands. These PDF uncertainties include experimental uncertainties, as well as model and parametrization uncertainties. In addition, the prediction based on the HERA 1.0 [20] PDF set also includes the uncertainty in α_s , providing a smaller contribution to the uncertainty. The predictions are calculated with the kinematic selection criteria applied to the truth particles. The asymmetry measurement performed with ATLAS and the predictions follow the same global trend for the range probed, increasing in $|\eta|$. The measurement does not clearly favor the prediction derived with any particular PDF set.

$ \eta_\mu $ Range	Data	MSTW 2008	CTEQ 6.6	HERA 1.0
0.00 – 0.21	$0.147 \pm 0.011 \pm 0.017$	$0.142^{+0.006}_{-0.014}$	$0.164^{+0.006}_{-0.007}$	0.163 ± 0.007
0.21 – 0.42	$0.149 \pm 0.010 \pm 0.012$	$0.147^{+0.007}_{-0.014}$	$0.168^{+0.006}_{-0.007}$	0.167 ± 0.007
0.42 – 0.63	$0.157 \pm 0.010 \pm 0.012$	$0.151^{+0.007}_{-0.013}$	$0.173^{+0.006}_{-0.007}$	0.169 ± 0.007
0.63 – 0.84	$0.184 \pm 0.010 \pm 0.015$	$0.163^{+0.008}_{-0.012}$	$0.186^{+0.007}_{-0.008}$	$0.179^{+0.008}_{-0.007}$
0.84 – 1.05	$0.186 \pm 0.011 \pm 0.017$	$0.176^{+0.009}_{-0.012}$	$0.198^{+0.007}_{-0.008}$	0.188 ± 0.008
1.05 – 1.37	$0.239 \pm 0.008 \pm 0.011$	0.197 ± 0.010	$0.219^{+0.008}_{-0.010}$	$0.203^{+0.009}_{-0.008}$
1.37 – 1.52	$0.249 \pm 0.011 \pm 0.010$	$0.215^{+0.011}_{-0.010}$	$0.237^{+0.009}_{-0.010}$	0.214 ± 0.009
1.52 – 1.74	$0.269 \pm 0.009 \pm 0.010$	$0.230^{+0.012}_{-0.010}$	$0.251^{+0.009}_{-0.011}$	0.224 ± 0.009
1.74 – 1.95	$0.272 \pm 0.009 \pm 0.010$	$0.251^{+0.013}_{-0.009}$	$0.270^{+0.010}_{-0.011}$	$0.239^{+0.010}_{-0.009}$
1.95 – 2.18	$0.277 \pm 0.009 \pm 0.012$	$0.266^{+0.014}_{-0.010}$	$0.284^{+0.010}_{-0.011}$	$0.251^{+0.009}_{-0.010}$
2.18 – 2.40	$0.273 \pm 0.010 \pm 0.012$	$0.272^{+0.015}_{-0.011}$	$0.288^{+0.009}_{-0.010}$	$0.255^{+0.009}_{-0.010}$

Table 6.12: The muon charge asymmetry from W -boson decays in bins of absolute pseudorapidity. The data measurements are listed with statistical and systematic uncertainties respectively. Predicted asymmetries obtained with MC@NLO using the MSTW 2008, CTEQ 6.6, and HERA 1.0 PDF sets are shown for comparison.

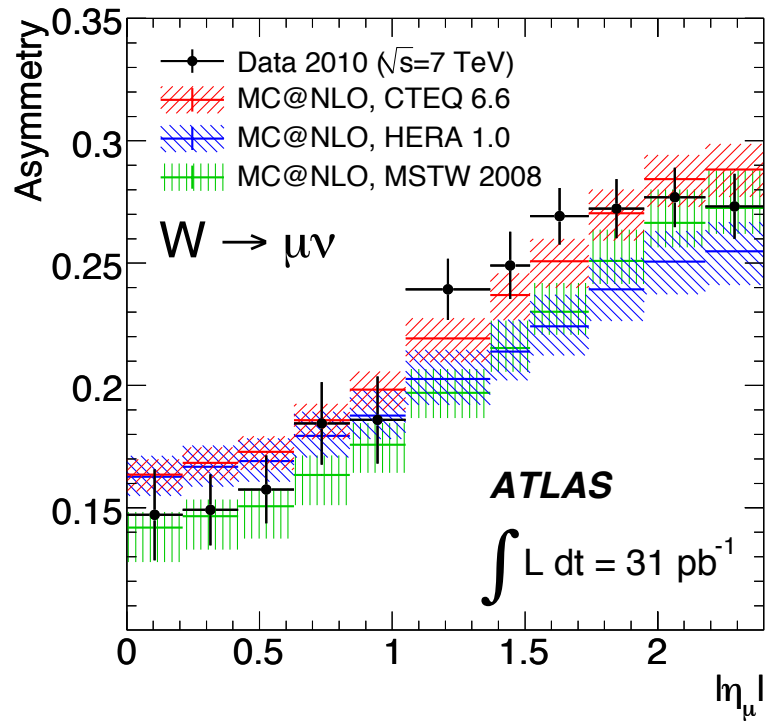


Figure 6.23: The measurement of the W charge asymmetry in the $W \rightarrow \mu\nu$ decay mode in 11 bins of absolute muon pseudorapidity. The kinematic requirements are $p_T^\mu > 20$ GeV, $p_T^\nu > 25$ GeV and $m_T > 40$ GeV. The measurement, shown with statistical and systematic uncertainties, is compared to predictions using MC@NLO with different PDF sets.

Chapter 7

Conclusions

This thesis presents a measurement of the W charge asymmetry in the $W \rightarrow \mu\nu$ decay mode in pp collisions at $\sqrt{s} = 7$ TeV using the ATLAS detector. An asymmetry measurement at the LHC is sensitive to the proton PDFs, particularly the valence quarks. The final result, shown in Figure 6.23, is compatible with theoretical predictions using the MC@NLO generator with three different PDF sets. However, the predictions derived with the various PDF sets are not fully consistent among themselves, differing within their uncertainty bands. This is due to the different predictions for the valence quark distributions, which are not well constrained kinematically for $x \lesssim 0.05$ by past measurements [17], as discussed in Section 2.2.4. The measurement favors some predictions over others. A χ^2 -comparison using the measurement uncertainty and the central value of the PDF predictions yields values per degrees of freedom of 9.16/11 for the CTEQ 6.6 PDF set, 35.81/11 for the HERA 1.0 PDF set and 27.31/11 for the MSTW 2008 PDF set. The asymmetry results from the LHC, such as the one presented here, and the corresponding one performed

by CMS [106], can serve as input to the PDF sets, bringing the predictions closer together and contributing to a reduction of the PDF uncertainties.

Preliminary studies of the impact of the ATLAS asymmetry measurement on the PDFs [45] have been performed using the HERA 1.5 PDF set [20, 107], which is based on the full combined dataset from HERA¹. The agreement between the data and the prediction improves with the inclusion of the data in the fit, yielding a χ^2/NDF of 16/11. The effect on the valence u and d quark, sea quark and gluon distributions is shown in Figure 7.1. The result of the fit after including the additional data (blue line) is normalized to the original prediction and compared to the relative errors on the prediction (lower distributions in each subfigure). The central values of the HERA PDF predictions are altered significantly by the inclusion of the new data in the fit. The ATLAS measurement pulls the fit outside the uncertainty bands, particularly in the case of the valence u distribution. The pull of the data is not unexpected given the difference between the prediction and the measurement shown in the asymmetry result comparison in Figure 6.23.

The HERA data constrains the valence quark distributions in the kinematic region² of large x and large Q^2 , which is different from the kinematic region of the LHC that is more sensitive to lower x . Therefore an inclusion of additional data in the HERA PDF fits, such as Tevatron measurements of the W charge asymmetry and the Z

¹The HERA 1.5 PDFs include the full combined HERA dataset, which is larger than the one used in the HERA 1.0 PDFs. The HERA 1.0 set is used for the prediction shown previously in Figure 6.23.

²HERA data constrains the valence quark distributions in charged current events, where the proton and the lepton exchange a W .

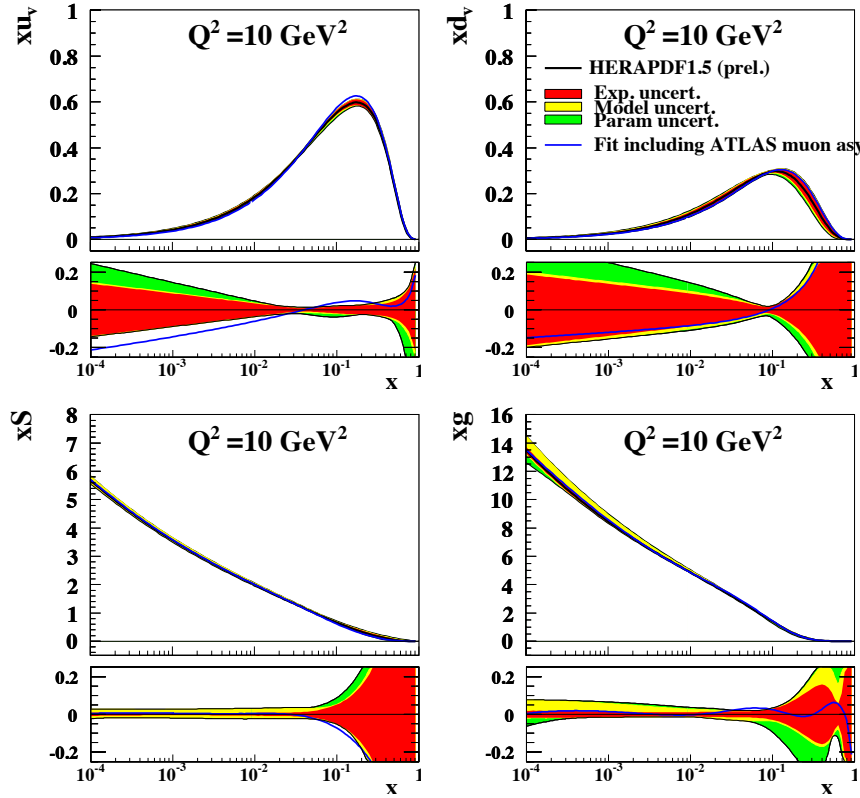


Figure 7.1: Comparison of the valence u (upper left) and d (upper right) quark, sea quark (lower left) and gluon (lower right) PDF predictions from the HERA 1.5 PDF set before and after the inclusion of the ATLAS asymmetry measurement, from [45].

rapidity, can improve the reliability of the predictions. The impact of the inclusion of both Tevatron data and the ATLAS asymmetry measurement on the HERA PDF fit is shown in Figure 7.2. The resulting χ^2/NDF are 27/28 for the CDF y_Z , 14.4/13 for the CDF W asymmetry and 14.2/11 for the ATLAS asymmetry measurements. This corresponds to an improvement in the χ^2 with the addition of all three datasets, since the inclusion of the CDF y_Z and W asymmetry measurements alone yields χ^2/NDF values of 27/28 and 19/13 respectively. The fit results also indicate that the addition of the ATLAS asymmetry measurement, on top of the Tevatron data, has a small impact in terms of reducing the uncertainties, as indicated by a comparison of

the distributions in the left and right columns in Figure 7.3. It may be noted that the inclusion of the charge asymmetry measurement impacts all flavors, particularly since these are related by the sum rules which are used as constraints in the fit. For example, the gluon distribution uncertainty in Figure 7.3 is reduced with the inclusion of the new data.

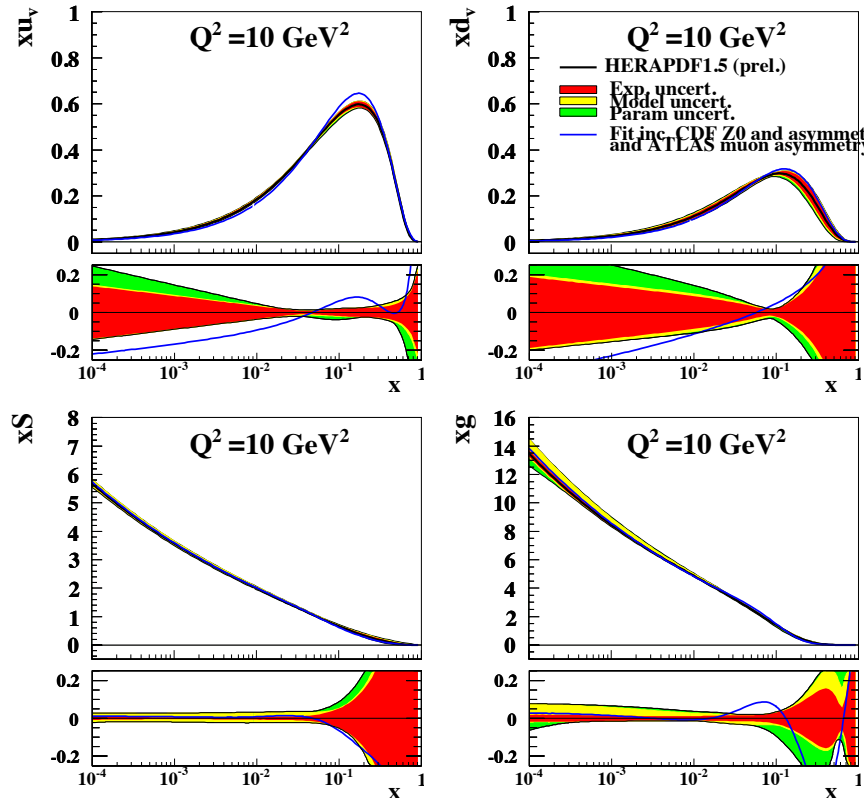


Figure 7.2: Comparison of the valence u (upper left) and d (upper right) quark, sea quark (lower left) and gluon (lower right) PDF predictions from the HERA 1.5 PDF set before and after the inclusion of the ATLAS asymmetry measurement and CDF W asymmetry and y_Z measurements. These studies are from [45].

The NNPDF collaboration has also performed preliminary studies of the impact of the ATLAS asymmetry measurement on the NNPDF2.1 set [110]. The ATLAS measurement is compared to the prediction using this PDF set in Figure 7.4 (left).

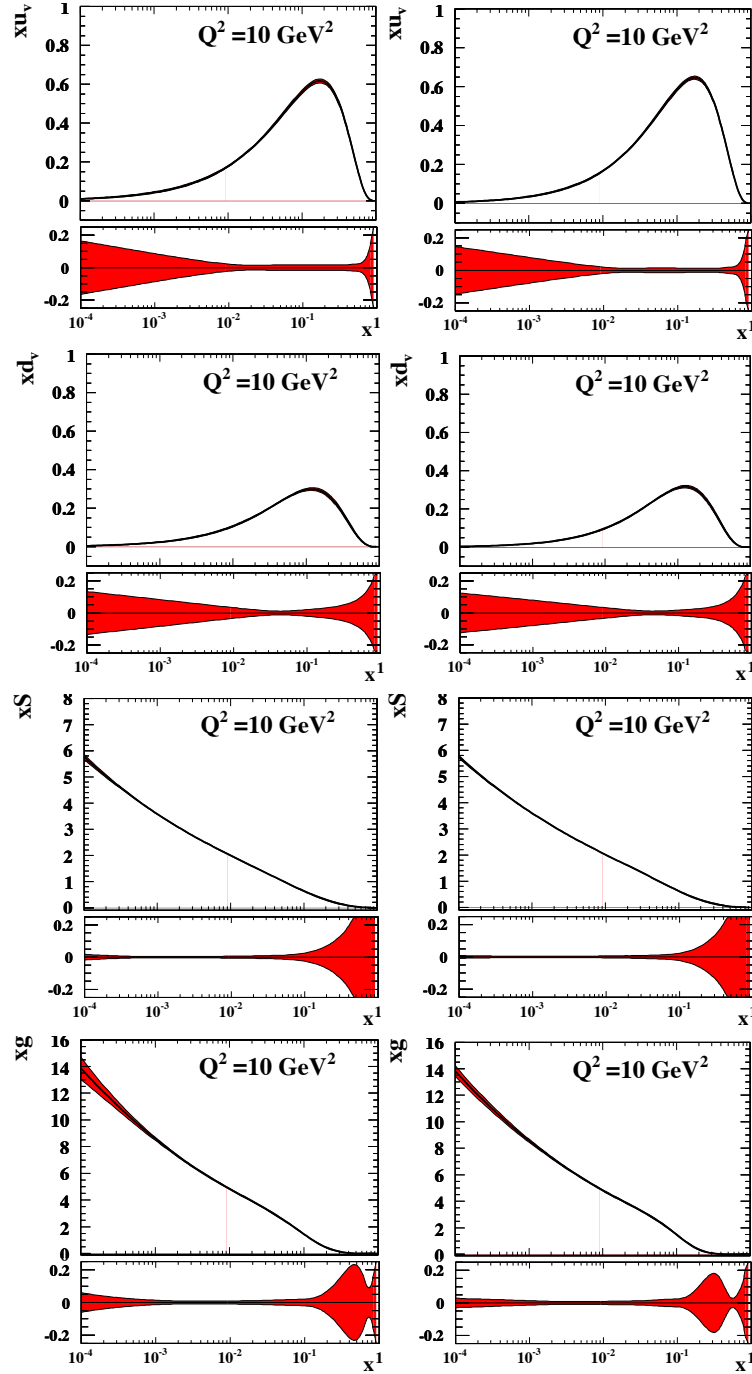


Figure 7.3: PDF predictions and uncertainties from the HERA 1.5 PDF set, including Tevatron measurements of W asymmetry and y_Z from CDF, before (left) and after (right) the inclusion of the ATLAS asymmetry measurement. The rows from top to bottom correspond to the PDF predictions for valence u and d quarks, sea quarks and gluons. From [45].

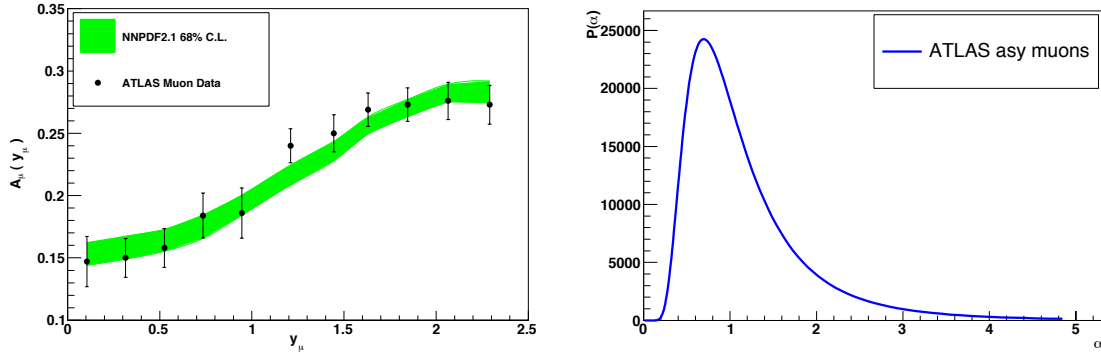


Figure 7.4: Comparison of the ATLAS asymmetry measurement to the NNPDF2.1 prediction (left). The agreement is quantified by a method based on the calculation of the χ^2 to the data, following the procedure described in [108]. A probability function $P(\alpha)$ is derived by rescaling the uncertainties associated with the ATLAS measurement with a parameter α , shown at right. The peak value close to 1 indicates the ATLAS measurement is compatible with the rest of the data included in the NNPDF2.1 set. These studies are from [109].

The NNPDF set is a global PDF, including a wider range of experimental inputs (see Figure 2.5) compared to the HERA PDF set. In addition, the use of a neural network rather than a parametrization, as done by the CTEQ, MSTW and HERA PDF fitting groups, has some advantages. These include a reduction in the theoretical bias associated with the choice of a parametrization and an improved treatment of the uncertainties. The NNPDF group provides a method to assess the impact of incorporating new data into the NNPDF fit using a technique that reweights the PDFs based on the calculation of the χ^2 to the dataset [108]. The errors in the data are rescaled using a parameter α and the corresponding probability distribution $P(\alpha)$ as a function of the parameter determined. This distribution for the ATLAS asymmetry measurement is shown in Figure 7.4 (right). The peak value close to unity indicates the ATLAS measurement is compatible with the rest of the data included in the NNPDF2.1 PDF set. The impact on the PDF predictions is studied using

this reweighting technique, and a comparison of the u , d and s quark PDF uncertainties before and after the inclusion of the measurement is shown in Figure 7.5. These studies indicate that the ATLAS asymmetry measurement imposes moderate constraints on the NNPDF2.1 PDF set since it agrees well with its predictions. However it reduces the uncertainties by approximately 15 – 20% for the u , d and s quark PDFs in the region $10^{-3} \lesssim x \lesssim 10^{-2}$. The charge asymmetry measurement the first experimental result from ATLAS that starts to constrain the PDFs at the LHC.

The differential measurement of the W charge asymmetry presented here is limited by the statistics available for the W signal sample and the samples used for the calculations of efficiencies, backgrounds and systematic uncertainties. The analysis is based on a dataset corresponding to an integrated luminosity of 31 pb^{-1} with $\sim 130,000$ W events and a sample of Z s approximately ten times smaller. The inclusion of the pp collision dataset from 2011, expected to reach about 1 fb^{-1} of integrated luminosity, can significantly reduce the uncertainty of the asymmetry measurement. An indication of the uncertainties that can be expected from a comparable measurement performed with a 1 fb^{-1} dataset is shown in Figure 7.6. Here the uncertainties that are predominantly of statistical origin are scaled to those corresponding to a 1 fb^{-1} dataset, while the other uncertainties remain unchanged. A total systematic uncertainty on the asymmetry of 5 – 3% and about a 1% statistical uncertainty can be reasonably attained with 1 fb^{-1} of data. It may be noted that the sources of uncertainty dominated by systematic sources are also likely to improve with the larger dataset.

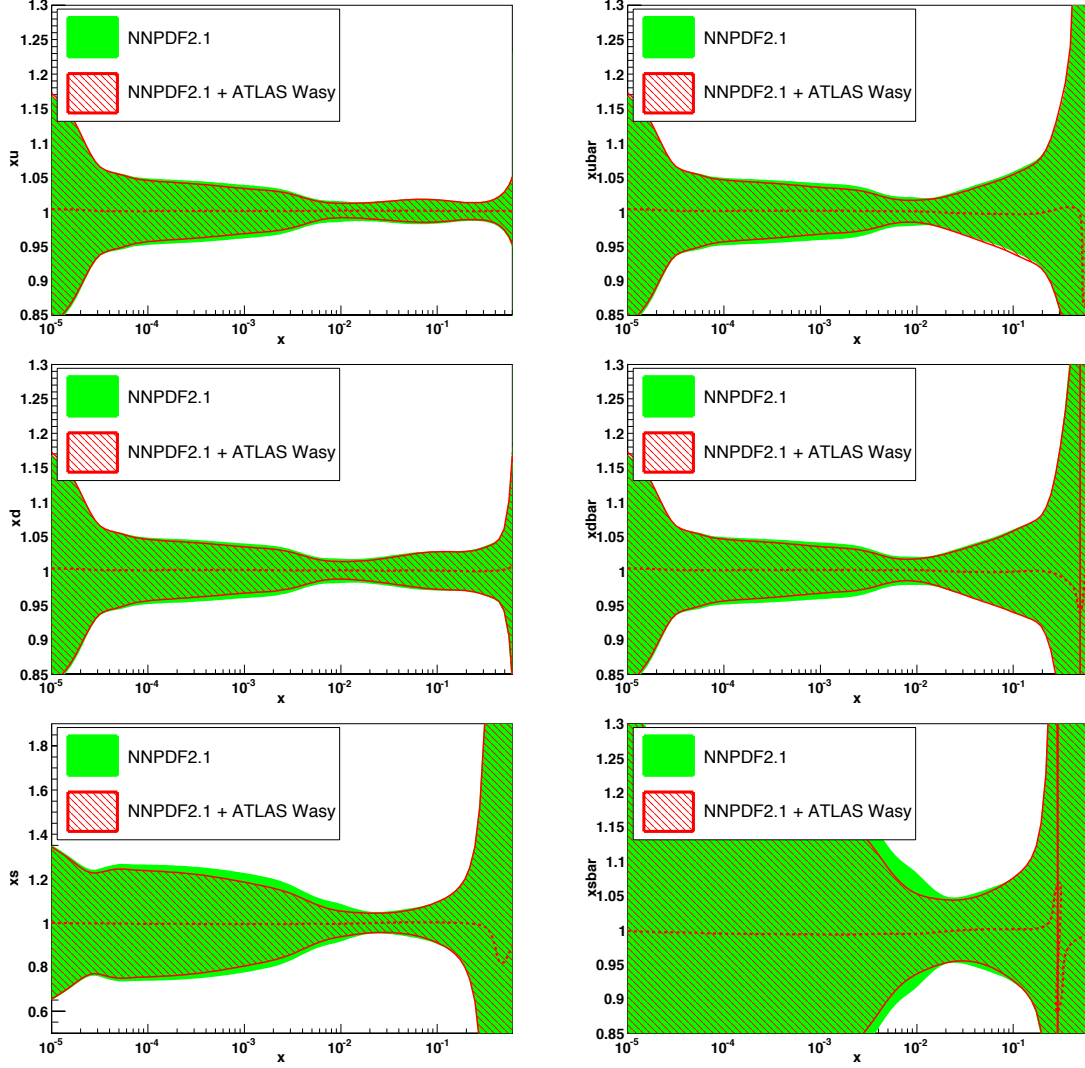


Figure 7.5: Comparison between the NNPDF2.1 [110] PDF uncertainties with and without the ATLAS asymmetry measurement for u (top), d (center) and s (bottom) quark (left) and antiquark (right) PDFs at $Q^2 = m_W^2 \text{ GeV}^2$. The curves are shown as ratios with respect to the central NNPDF2.1 result, from [109].

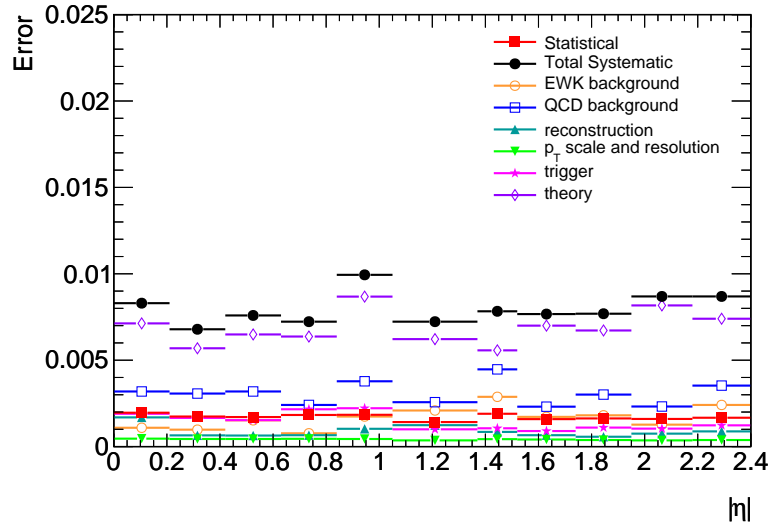


Figure 7.6: Estimated absolute uncertainties for an identical differential W lepton charge asymmetry measurement performed with a dataset of 1 fb^{-1} . The various contributions to the uncertainty of statistical origin are scaled to the increased sample size, as can be seen by comparison with Figure 6.18.

The main impact of using a larger sample of W and Z events is a reduction in the uncertainties in the muon trigger and reconstruction efficiency measurements and an improved understanding of the muon momentum resolution and scale. More accurate muon calibrations and alignment corrections will also have a favorable impact on a future asymmetry measurement. The expected dominant source of uncertainty is from the theoretical modeling of the acceptance and the momentum scale and resolution. The acceptance corrections can be improved by using for example higher order MC predictions. Finally, a measurement of the asymmetry in the $W \rightarrow e\nu$ channel would provide an additional valuable cross check of the $W \rightarrow \mu\nu$ measurement. A combined measurement in the two W decay modes would result in a measurement with reduced uncertainties that can provide further constraints on the PDF predictions.

Bibliography

- [1] The ATLAS Collaboration. Measurement of the $W \rightarrow l\nu$ and $Z/\gamma^* \rightarrow ll$ production cross sections in proton-proton collisions at $\sqrt{s} = 7$ TeV with the ATLAS detector. *JHEP*, 12:060, 2010.
- [2] The ATLAS Collaboration. Measurement of the Muon Charge Asymmetry from W Bosons Produced in pp Collisions at $\sqrt{s} = 7$ TeV with the ATLAS detector. arXiv:1103.2929 [hep-ex].
- [3] R. K. Ellis, W. J. Stirling, and B. R. Webber. *QCD and Collider Physics*. Camb. Monogr. Part. Phys. Nucl. Phys. Cosmol., 1996.
- [4] S. Bethke. The 2009 World Average of $\alpha_s(M_Z)$. *Eur. Phys. J.*, C64:689–703, 2009.
- [5] M. Gell-Mann. A Schematic Model of Baryons and Mesons. *Phys. Lett.*, 8:214–215, 1964.
- [6] E. D. Bloom et al. High-Energy Inelastic ep Scattering at 6-Degrees and 10-Degrees. *Phys. Rev. Lett.*, 23:930–934, 1969.
- [7] M. Breidenbach et al. Observed Behavior of Highly Inelastic electron-Proton Scattering. *Phys. Rev. Lett.*, 23:935–939, 1969.
- [8] J. D. Bjorken. Asymptotic Sum Rules at Infinite Momentum. *Phys. Rev.*, 179:1547–1553, 1969.
- [9] Richard P. Feynman. Very High-Energy Collisions of Hadrons. *Phys. Rev. Lett.*, 23:1415–1417, 1969.
- [10] J. D. Bjorken and E. A. Paschos. Inelastic Electron Proton and Gamma Proton Scattering, and the Structure of the Nucleon. *Phys. Rev.*, 185:1975–1982, 1969.
- [11] K. Nakamura et al. Review of Particle Physics. *J. Phys.*, G37:075021, 2010.
- [12] S. D. Drell and T. Yan. Partons and their applications at high energies. *Ann. Phys.*, 66:578, 1971.

-
- [13] J. M. Campbell, J. W. Huston, and W. J. Stirling. Hard Interactions of Quarks and Gluons: A Primer for LHC Physics. *Rept. Prog. Phys.*, 70:89, 2007.
- [14] A. D. Martin, R. G. Roberts, W. J. Stirling, and R. S. Thorne. Parton distributions and the LHC: W and Z production. *Eur. Phys. J.*, C14:133–145, 2000.
- [15] Pavel M. Nadolsky et al. Implications of CTEQ global analysis for collider observables. *Phys. Rev.*, D78:013004, 2008.
- [16] M. Guzzi et al. CT10 parton distributions and other developments in the global QCD analysis. arXiv:1101.0561 [hep-ph].
- [17] A. D. Martin, W. J. Stirling, R. S. Thorne, and G. Watt. Parton distributions for the LHC. *Eur. Phys. J.*, C63:189–285, 2009.
- [18] R. D. Ball et al. A first unbiased global NLO determination of parton distributions and their uncertainties. *Nucl. Phys.*, B838:136–206, 2010.
- [19] S. Alekhin. The precise NNLO PDFs from the combined fit to the DIS and Drell-Yan data. *PoS*, HEP2005:042, 2006.
- [20] The H1 Collaboration. Combined Measurement and QCD Analysis of the Inclusive ep Scattering Cross Sections at HERA. *JHEP*, 01:109, 2010.
- [21] The UA1 Collaboration. Intermediate Vector Boson Cross-Sections at the CERN Super Proton Synchrotron Collider and the Number of Neutrino Types. *Phys. Lett.*, B198:271, 1987.
- [22] The UA2 Collaboration. A Measurement of the W and Z production cross-sections and a determination of $\Gamma(W)$ at the CERN $\bar{p}p$. *Phys. Lett.*, B276:365–374, 1992.
- [23] The CDF Collaboration. Measurement of $\sigma \cdot B(W \rightarrow e\nu)$ and $\sigma \cdot B(Z^0 \rightarrow e^+e^-)$ in $p\bar{p}$ collisions at $\sqrt{s} = 1.8$ TeV. *Phys. Rev. Lett.*, 76:3070, 1996.
- [24] The CDF Collaboration. Measurements of Inclusive W and Z Cross Sections in $p\bar{p}$ Collisions at $\sqrt{s} = 1.96$ TeV. *J. Phys.*, G34:2457–2544, 2007.
- [25] The DØ Collaboration. Extraction of the width of the W boson from measurements of $\sigma(p\bar{p} \rightarrow W + X) \times B(W \rightarrow e\nu)$ and $\sigma(p\bar{p} \rightarrow Z + X) \times B(Z \rightarrow ee)$ and their ratio. *Phys. Rev.*, D61:072001, 2000.
- [26] The DØ Collaboration. D0NOTE4403-CONF, D0NOTE4750-CONF.

- [27] The PHENIX Collaboration. Cross Section and Parity Violating Spin Asymmetries of W^\pm Boson Production in Polarized p+p Collisions at $\sqrt{s} = 500$ GeV. arXiv:1009.0505 [hep-ex].
- [28] The STAR Collaboration. Measurement of the parity-violating longitudinal single-spin asymmetry for W^\pm boson production in polarized proton-proton collisions at $\sqrt{s} = 500$ GeV. arXiv:1009.0326 [hep-ex].
- [29] R. Hamberg, W. L. van Neerven, and T. Matsuura. A Complete calculation of the order α_s^2 correction to the Drell-Yan K factor. *Nucl. Phys.*, B359:343–405, 1991.
- [30] C. Anastasiou, L. J. Dixon, K. Melnikov, and F. Petriello. High-precision QCD at Hadron Colliders: Electroweak Gauge Boson Rapidity Distributions at NNLO. *Phys. Rev.*, D69:094008, 2004.
- [31] R. Gavin, Y. Li, F. Petriello, and S. Quackenbush. FEWZ 2.0: A code for hadronic Z production at next-to-next-to-leading order. arXiv:1011.3540 [hep-ph].
- [32] G. Watt. PDF benchmarking for LHC processes. Paper in preparation. <http://projects.hepforge.org/mstwpdf/pdf4lhc/>.
- [33] E. L. Berger, F. Halzen, C. S. Kim, and S. Willenbrock. Weak-boson production at Fermilab Tevatron energies. *Phys. Rev. D*, 40(1):83–91, Jul 1989.
- [34] J. W. Stirling. Private communication.
- [35] The CDF Collaboration. Direct Measurement of the W Production Charge Asymmetry in $p\bar{p}$ Collisions at $\sqrt{s} = 1.96$ TeV. *Phys. Rev. Lett.*, 102:181801, 2009.
- [36] A. D. Martin, R. G. Roberts, W. J. Stirling, and R. S. Thorne. Physical gluons and high E(T) jets. *Phys. Lett.*, B604:61–68, 2004.
- [37] The DØ Collaboration. Measurement of the electron charge asymmetry in $p\bar{p} \rightarrow W + X \rightarrow e\nu + X$ events at $\sqrt{s} = 1.96$ TeV. *Phys. Rev. Lett.*, 101:211801, 2008.
- [38] The CDF Collaboration. Measurement of the lepton charge asymmetry in W boson decays produced in $p\bar{p}$ collisions. *Phys. Rev. Lett.*, 81:5754–5759, 1998.
- [39] The CDF Collaboration. Measurement of the forward-backward charge asymmetry of electron positron pairs in $p\bar{p}$ collisions at $\sqrt{s} = 1.96$ TeV. *Phys. Rev.*, D71:052002, 2005.

- [40] The DØ Collaboration. Measurement of the muon charge asymmetry from W boson decays. *Phys. Rev.*, D77:011106, 2008.
- [41] J. Pumplin et al. New generation of parton distributions with uncertainties from global QCD analysis. *JHEP*, 07:012, 2002.
- [42] A. D. Martin, W. J. Stirling, R. S. Thorne, and G. Watt. Update of Parton Distributions at NNLO. *Phys. Lett.*, B652:292–299, 2007.
- [43] A. Bodek, Y. Chung, B. Han, K. McFarland, and E. Halkiadakis. New analysis technique to measure the W production charge asymmetry at the Fermilab Tevatron. *Phys. Rev.*, D77:111301, 2008.
- [44] K. Lohwasser, J. Ferrando, and C. Issever. On direct measurement of the W production charge asymmetry at the LHC. *JHEP*, 09:079, 2010.
- [45] A. M. Cooper-Sarkar. Private communication.
- [46] K. Lohwasser. Private communication.
- [47] Kristin Lohwasser. *The W Charge Asymmetry: Measurement of the Proton Structure with the ATLAS Detector*. PhD thesis, Oxford University, 2009. CERN-THESIS-2010-069.
- [48] L. Evans and P. Bryant (eds.). LHC Machine. *JINST*, 3:S08001, 2008.
- [49] The ATLAS Collaboration. ATLAS Detector and Physics Performance. Technical Design Report. Vol. 1. CERN-LHCC-99-14.
- [50] The ATLAS Collaboration. ATLAS Detector and Physics Performance. Technical Design Report. Vol. 2. CERN-LHCC-99-15.
- [51] The ATLAS Collaboration. The ATLAS Experiment at the CERN Large Hadron Collider. *JINST*, 3:S08003, 2008.
- [52] ATLAS Experiment @ 2011 CERN. ATLAS Photos. <http://www.atlas.ch/photos/index.html>.
- [53] CERN MultiMedia Productions. LHC Machine Outreach. <http://lhc-machine-outreach.web.cern.ch/lhc-machine-outreach/>.
- [54] The ATLAS Collaboration. Luminosity Determination Using the ATLAS Detector. ATLAS-CONF-2010-060.
- [55] The ATLAS Collaboration. The ATLAS Muon Spectrometer Technical Design Report. CERN/LHCC/97-22.

-
- [56] The ATLAS Collaboration. Expected Performance of the ATLAS Experiment - Detector, Trigger and Physics. arXiv:0901.0512 [hep-ex].
- [57] E. Diehl. Private communication.
- [58] Y. Arai et al. ATLAS Muon Drift Tube Electronics. *JINST*, 3:P09001, 2008.
- [59] The ATLAS Collaboration. Commissioning of the ATLAS Muon Spectrometer with Cosmic Rays. *Eur. Phys. J.*, C70:875–916, 2010.
- [60] C. Amsler et al. Review of Particle Physics. *Phys. Lett.*, B667:1, 2008.
- [61] D. Adams et al. Track Reconstruction in the ATLAS Muon Spectrometer with MOORE. ATL-SOFT-2003-007, ATL-COM-MUON-2003-012.
- [62] S. Hassani et al. A Muon Identification and Combined Reconstruction Procedure for the ATLAS Detector at the LHC using the (MUONBOY, STACO, MuTag) Reconstruction Packages. *Nucl. Instrum. Meth.*, A572:77–79, 2007.
- [63] T. K. Gaisser. *Cosmic Rays and Particle Physics*. Cambridge University Press, 1990.
- [64] The OPERA Collaboration. Measurement of the atmospheric muon charge ratio with the OPERA detector. *Eur. Phys. J.*, C67:25–37, 2010.
- [65] The MINOS Collaboration. Measurement of the atmospheric muon charge ratio at TeV energies with MINOS. *Phys. Rev.*, D76:052003, 2007.
- [66] S. Haino et al. Measurements of Primary and Atmospheric Cosmic-Ray Spectra with the BESS-TeV Spectrometer. *Phys. Lett.*, B594:35–46, 2004.
- [67] The L3 Collaboration. Measurement of the Atmospheric Muon Spectrum from 20 GeV to 3000 GeV. *Phys. Lett.*, B598:15–32, 2004.
- [68] T. Hebbeker and C. Timmermans. A Compilation of High Energy Atmospheric Muon Data at Sea Level. *Astropart. Phys.*, 18:107–127, 2002.
- [69] B. Vulpesu et al. A Compact Detector for the Measurement of the Cosmic Ray Muon Charge Ratio. *Nucl. Instrum. Meth.*, A414:205–217, 1998.
- [70] A. Belloni et al. In-situ t0 calibration for MDT segments. ATL-COM-MUON-2009-006.
- [71] A. Salzburger. The ATLAS Track Extrapolation Package. ATL-SOFT-PUB-2007-005, ATL-COM-SOFT-2007-010.
- [72] M. Bianco, G. Cattani, and Chiodini G. Private communication.

- [73] The ATLAS Collaboration. Observation of $W \rightarrow l\nu$ and $Z \rightarrow ll$ production in proton-proton collisions at $\sqrt{s} = 7$ TeV with the ATLAS detector. ATLAS-CONF-2010-044.
- [74] The ATLAS Collaboration. Measurement of the $W \rightarrow l\nu$ production cross-section and observation of $Z \rightarrow ll$ production in proton-proton collisions at $\sqrt{s} = 7$ TeV with the ATLAS detector. ATLAS-CONF-2010-051.
- [75] T. Cornelissen et al. Concepts, Design and Implementation of the ATLAS New Tracking (NEWT). ATL-SOFT-PUB-2007-007, ATL-COM-SOFT-2007-002.
- [76] The ATLAS Collaboration. Charged-particle multiplicities in pp interactions measured with the ATLAS detector at the LHC. arXiv:1012.5104 [hep-ex].
- [77] G. Piacquadio, K. Prokofiev, and A. Wildauer. Primary vertex reconstruction in the ATLAS experiment at LHC. *J. Phys. Conf. Ser.*, 119:032033, 2008.
- [78] The ATLAS Collaboration. Performance of Primary Vertex Reconstruction in proton-proton Collisions at $\sqrt{s} = 7$ TeV in the ATLAS Experiment. ATLAS-CONF-2010-069.
- [79] The ATLAS Collaboration. Characterization of Interaction-Point Beam Parameters Using the pp Event-Vertex Distribution Reconstructed in the ATLAS Detector at the LHC. ATLAS-CONF-2010-027.
- [80] The ATLAS Collaboration. Alignment Performance of the ATLAS Inner Detector Tracking System in 7 TeV proton-proton collisions at the LHC. ATLAS-CONF-2010-067.
- [81] The ATLAS Collaboration. Alignment of the ATLAS Inner Detector Tracking System with 2010 LHC proton-proton collisions at $\sqrt{s} = 7$ TeV. ATLAS-CONF-2011-012.
- [82] W. Lampl et al. Calorimeter Clustering Algorithms: Description and Performance. ATL-LARG-PUB-2008-002.
- [83] T Barillari et al. Local Hadronic Calibration. ATL-LARG-PUB-2009-001, ATL-COM-LARG-2008-006.
- [84] The ATLAS Collaboration. Performance of the Missing Transverse Energy Reconstruction in Minimum Bias Collisions at center-of-mass Energy of 7 TeV with the ATLAS Detector. ATL-COM-PHYS-2010-248.
- [85] T. Sjostrand, S. Mrenna, and P. Skands. PYTHIA 6.4 Physics and Manual. *JHEP*, 05:026, 2006.

-
- [86] A. Sherstnev and R. S. Thorne. Parton Distributions for LO Generators. *Eur. Phys. J.*, C55:553, 2008.
- [87] S. Frixione, P. Nason, and C. Oleari. Matching NLO QCD computations with parton shower simulations:the POWHEG method. *JHEP*, 11:070, 2007.
- [88] P. Golonka and Z. Was. PHOTOS Monte Carlo: A Precision Tool for QED Corrections in Z and W Decays. *Eur. Phys. J.*, C45:97–107, 2006.
- [89] N. Davidson et al. Universal Interface of TAUOLA Technical and Physics Documentation. arXiv:1002.0543 [hep-ph].
- [90] The ATLAS Collaboration. ATLAS Monte Carlo tunes for MC09. ATLAS-PHYS-PUB-2010-002.
- [91] S. Agostinelli et al. GEANT4: A Simulation Toolkit. *Nucl. Instrum. Meth.*, A506:250–303, 2003.
- [92] The ATLAS Collaboration. The ATLAS Simulation Infrastructure. *Eur. Phys. J. C*, 70:787, 2010.
- [93] R. Bonciani, S. Catani, M. L. Mangano, and P. Nason. NLL Resummation of the Heavy-Quark Hadroproduction Cross-Section. *Nucl. Phys.*, B529:424, 1998.
- [94] The ATLAS Collaboration. Data-Quality Requirements and Event Cleaning for Jets and Missing Transverse Energy Reconstruction with the ATLAS Detector in Proton-Proton Collisions at a Center-of-Mass Energy of $\sqrt{s} = 7$ TeV. ATLAS-CONF-2010-038.
- [95] A. Belloni et al. Muon Definition for High-pT Physics: Algorithmic Fakes. ATL-COM-MUON-2010-009.
- [96] J. Barreiro Guimaraes da Costa et al. $W \rightarrow \mu\nu$ and $Z \rightarrow \mu\mu$ cross-sections measurements in proton-proton collisions at $\sqrt{s} = 7$ TeV with the ATLAS Detector. ATL-PHYS-INT-2011-019.
- [97] L. M. Kashif. *Measurement of the Z boson cross-section in the dimuon channel in pp collisions at $\sqrt{s} = 7$ TeV*. PhD thesis, Harvard University, 2010.
- [98] The ATLAS Collaboration. Muon Trigger Efficiency Measurements with Z bosons in proton-proton Collisions at $\sqrt{s} = 7$ TeV with the ATLAS Detector. ATL-COM-PHYS-2011-049.
- [99] The ATLAS Collaboration. Muon Definition for W, Z Analysis based on Athena Release 15. ATL-COM-PHYS-2010-1001.

-
- [100] The ATLAS Collaboration. Determination of the Muon Reconstruction Efficiency in ATLAS at the Z Resonance in proton-proton Collisions at $\sqrt{s} = 7$ TeV. ATLAS-CONF-2011-008.
- [101] M. Schott and M. Bellomo. Staco Efficiencies based on Z Bosons with L = 42 pb-1 and Release 15. <http://indico.cern.ch/conferenceDisplay.py?confId=110666>.
- [102] The ATLAS Collaboration. Muon Momentum Resolution in First Pass Reconstruction of pp Collision Data Recorded at $\sqrt{s} = 7$ TeV. ATLAS-CONF-2011-046.
- [103] The ATLAS Collaboration. Total inclusive W and Z boson cross-section measurements, cross-section ratios and combinations in the electron and muon decay channels at 7 TeV based on 300 nb^{-1} . ATL-COM-PHYS-2010-703.
- [104] S. Frixione and B. R. Webber. Matching NLO QCD Computations and Parton Shower Simulations. *JHEP*, 06:029, 2002.
- [105] J. Pumplin et al. Uncertainties of predictions from parton distribution functions. 2. The Hessian method. *Phys. Rev.*, D65:014013, 2001.
- [106] The CMS Collaboration. Measurement of the Lepton Charge Asymmetry in Inclusive W Production in pp Collisions at $\sqrt{s} = 7$ TeV. *JHEP*, 04:050, 2011.
- [107] A. Cooper-Sarkar. Proton Structure from HERA to LHC. arXiv:1012.1438 [hep-ph].
- [108] The NNPDF Collaboration. Reweighting NNPDFs: the W Lepton Asymmetry. arXiv:1012.0836 [hep-ph].
- [109] J. Rojo. Private communication.
- [110] Richard D. Ball et al. Impact of Heavy Quark Masses on Parton Distributions and LHC Phenomenology. arXiv:1101.1300 [hep-ph].